THÈSE POUR OBTENIR LE GRADE DE DOCTEUR DE L'UNIVERSITÉ DE MONTPELLIER

En Mathématiques et Modélisation

École doctorale I2S

Préparée à l'IFP Energies nouvelles

Un modèle proche paroi pour la prédiction des transferts thermiques dans les écoulements laminaires à haut nombre de Prandtl : application aux jets liquides impactants pour le refroidissement des moteurs électriques

Présentée par Adrien INGLES
Le 19 février 2026

Sous la direction de Professeur Franck Nicoud

Devant le jury composé de

Dr. Florent DUCHAINE	Chercheur senior	CERFACS	**Rapporteur**
Prof. Ronan VICQUELIN	Professeur des universités	CentraleSupélec, EM2C - CNRS	**Rapporteur**
Dr. Mélody CAILLER	Ingénieure de recherche	Safran Tech	**Examinatrice**
Prof. Luc VERVISCH	Professeur des universités	INSA Rouen Normandie, CORIA - CNRS	**Président du jury**
Prof. Franck NICOUD	Professeur des universités	Université de Montpellier, IMAG - CNRS	**Directeur de thèse**
Dr. Adèle POUBEAU	Ingénieure de recherche	IFP Energies nouvelles	**Co-encadrante**
Dr. Guillaume VINAY	Ingénieur de recherche	IFP Energies nouvelles	**Co-encadrant**

Title: A Near-Wall Model for Heat Transfer Prediction in Laminar Flows at High Prandtl Number: Application to Impinging Liquid Jets for Electric Motor Cooling

Abstract: A thermal wall model designed for high Prandtl number fluids and laminar flows is proposed to eliminate the need to finely mesh the thin laminar thermal boundary layer at the wall. The model is further extended to account for strong temperature dependence of viscosity, as encountered in oils used for electric motor cooling. The potential of the approach, based on the analytical solution developed by Lévêque in 1928, is first verified in a two-dimensional boundary layer development over a flat plat. It is then assessed by considering the two-phase flow configuration of an impinging jet with Prandtl numbers as high as 1000. Comparisons with wall-resolved simulations demonstrate accurate predictions of local heat transfer, even on under-resolved grids and with large viscosity variations. Consequently, computational time can be significantly reduced, especially as the Prandtl number increases, while preserving accurate results. Finally, the constant-viscosity version of the model is evaluated on a configuration representative of end-windings cooled by multiple impinging oil jets. Despite the complexity of the flow, the model gives promising results.

Keywords: High Prandtl number, Thermal wall model, Laminar flow, Oil cooling, Impinging liquid jet

Titre : Un modèle proche paroi pour la prédiction des transferts thermiques dans les écoulements laminaires à haut nombre de Prandtl : application aux jets liquides impactants pour le refroidissement des moteurs électriques

Résumé : Un modèle de paroi thermique, destiné aux fluides à nombre de Prandtl élevé et aux écoulements laminaires, est proposé afin d'éviter de mailler finement la mince couche limite thermique laminaire au voisinage de la paroi. Le modèle est ensuite étendu pour prendre en compte la forte dépendance en température de la viscosité, comme c'est le cas pour les huiles utilisées pour le refroidissement des moteurs électriques. Le potentiel de l'approche, fondée sur la solution analytique développée par Lévêque en 1928, est d'abord évalué sur le développement bidimensionnel d'une couche limite au-dessus d'une plaque plane. Elle est ensuite testée sur la configuration d'écoulement diphasique d'un jet impactant, pour des nombres de Prandtl pouvant atteindre 1000. Les comparaisons avec des simulations complètement résolues montrent que le modèle permet de prédire avec précision les transferts de chaleur locaux, y compris sur des maillages sous-résolus et en présence de fortes variations de viscosité. Le temps de calcul peut ainsi être fortement réduit, en particulier lorsque le nombre de Prandtl augmente, tout en conservant un niveau de précision similaire. Enfin, la version à viscosité constante du modèle est appliquée à une configuration représentative du refroidissement des têtes de bobines par plusieurs jets d'huile impactants. Malgré la complexité de l'écoulement, les résultats sont prometteurs.

Mots-clés : Nombre de Prandtl élevé, Modèle de paroi thermique, Écoulement laminaire, Refroidissement à huile, Jet liquide impactant

Remerciements

Je remercie en premier lieu mes encadrants, le Prof. Franck Nicoud de l'Université de Montpellier, ainsi que le Dr. Adèle Poubeau et le Dr. Guillaume Vinay de l'IFP Energies Nouvelles. Leurs conseils m'ont été d'une aide précieuse et ont constitué une source constante de motivation durant ces trois années de thèse.

Je souhaite adresser mes sincères remerciements aux membres du jury pour avoir accepté d'évaluer ce travail, ainsi que pour leurs remarques constructives et leurs questions pertinentes.

Je remercie également les chercheurs et le personnel administratif du département « Modélisation Numérique des Systèmes Énergétiques » de l'IFP Energies Nouvelles pour leur aide tout au long de ma thèse. J'éprouve une reconnaissance particulière envers les doctorants et post-doctorants que j'ai eu l'occasion de côtoyer durant ces trois années et qui ont grandement contribué à rendre cette expérience enrichissante et agréable.

Contents

Part I

Introduction

The first part introduces the industrial motivation, formulates the research problem and the approach to address it, and outlines the thesis structure. It then presents a literature review that informs the proposed solution and situates it within the context of related works.

CHAPTER 1

Industrial motivation

This chapter presents the overall industrial motivation, from the global context to the specific challenges addressed in this thesis. Then the problem statement, the solution proposed and the thesis structure are introduced.

1.1 Electric motor generalities

The automotive sector is currently undergoing a major transformation, particularly in China, US and European countries, in favor of electrification [1]. This shift is part of a global government strategy aiming to transition towards an electrified economy, reduce dependencies on fossil fuels, and decrease carbon emissions [2].

There are three main categories of electric vehicles in the market: battery electric vehicles, hybrid electric vehicles, and plug-in electric vehicles. Battery electric vehicles typically have a propulsion system powered by an electric motor connected to a gearbox through a driveshaft. The energy storage is fully electric, utilizing a battery pack. In hybrid electric vehicles, the propulsion system can be configured in parallel or series with an internal combustion engine, where the electric motor alone provides mechanical power to the wheels. The plug-in electric vehicle is a special type of hybrid electric vehicle that features larger batteries that can be connected to an external power source.

The primary goal of an electric motor (EM) is to convert electric power into mechanical power. More specifically, EMs for mobility are expected to meet specific requirements outlined in [3, 4], including for instance high power density, high and fast torque response, wide speed range, high efficiency and also reliability and low manufacturing cost. Typically, an EM includes a cylindrical rotor within a stator, both made from laminated sheets of ferromagnetic materials to minimize magnetic losses. The stator contains coils made of insulated copper wires inserted into dedicated slots. These coils connect at the stator's extremity, forming what is referred to as the end-windings (see Fig. 1.1). The rotor, mounted on a shaft, transmits torque to other powertrain components of the vehicle. All these components are embedded within the housing that protects internal parts and provides structural support. The principle of mechanical power production is based on

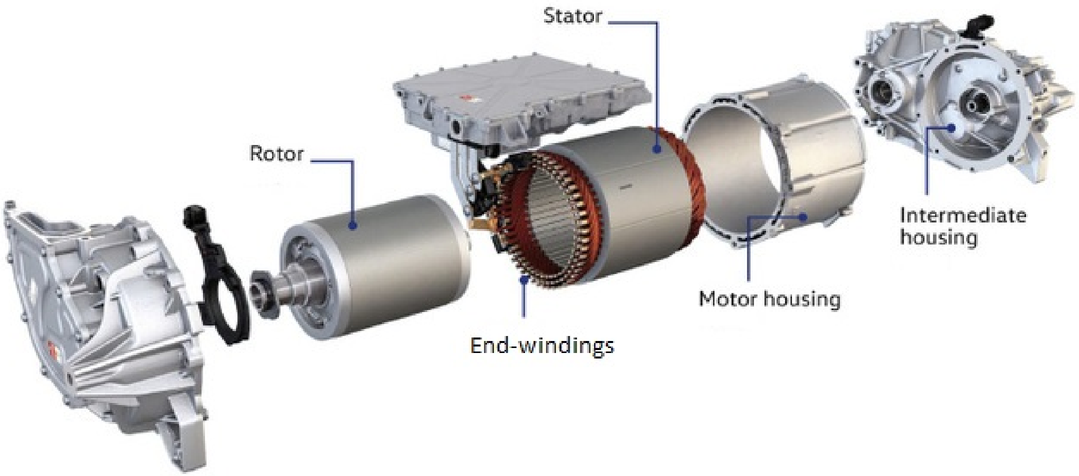

Figure 1.1: Main components of an electric motor [5].

generating momentum through the interaction of magnetic fields developed by both the stator and the rotor except for reluctance machine as detailed below. The different types of EM technology can be classified in four different categories [6]:

- Direct current electric motor: The stator and rotor conductors carry a Direct Current (DC), creating a magnetic field. To initiate motion, the rotor is connected to a commutator, which reverses the direction of its magnetic field during the rotation.
- Induction motor: The stator carries an Alternating Current (AC), creating a rotating magnetic field. The rotor, made up of short-circuited conductors, is subject to variations in magnetic flux from the stator. These variations induce an electric current

in the rotor, which in turn generates an induced magnetic field (Lenz law). This type of motor is called "asynchronous" because the rotor must rotate at a different mechanical frequency than the stator magnetic field to create an induced magnetic field.

- Synchronous motor with permanent magnet or wound rotor: Like for induction motor, the stator carries an alternating current, creating a rotating magnetic field. The difference is that a magnetic field is generated from the stator with either permanent magnet or wound rotor powered by alternating current.
- Synchronous reluctance motor: Like for induction motor, the stator is energized with an alternating current, establishing a rotating magnetic field. The rotor, here, is designed to create different reluctance paths within the rotor itself. As the stator's magnetic field rotates, the rotor seeks alignment with the lowest reluctance path of the magnetic circuit.

Nowadays, the automotive industry widely uses the synchronous motor with permanent magnet due to a high power and torque density and its lightness [7, 8, 9]. Induction motor is starting diffusing thanks to lower manufacturing cost and durability [10].

EMs have a high power efficiency compared to combustion engine (i.e., $> 90\%$ and $35 - 40\%$ respectively [11]) but they still lose heat, which needs to be evacuated to prevent high temperature that can deteriorate the motor.

1.2 Thermal management generalities on electric motors

1.2.1 Thermal constraints

The fraction of power in EMs not delivered to the shaft is what we call power loss, which is dissipated in the form of heat. The losses have different origins:

- Joule losses: This heat generation originates from the flow of electric current and is governed by Joule's law. They account for the majority of global losses [12] and mainly occur in the copper windings.
- Magnetic losses: Caused by the variability of the electromagnetic field, these take the form of eddy currents and magnetic hysteresis. They occur inside the ferromagnetic materials of the rotor and stator.

- Mechanical losses: Related to friction in the motor, notably coming from shaft bearings and air drag.

Given the severe temperature constraints on certain components, normal operation of EMs is constrained and heat losses must be managed to prevent temperature rise during normal operation of the machine. The main material constraints are as follows [13]:

- A maximum temperature of 180°C for the windings, due to the degradation of electrical insulation, which can expose the EM to short-circuit risks [14, 15].
- A maximum temperature of 140°C for the permanent magnet and ferromagnetic materials in the stator and rotor. Their magnetic properties can be temporarily or permanently deteriorated [16].
- A maximum temperature of 120°C for the lubricant, beyond which it degrades its lubricating characteristics and thereby increases mechanical loss [1].
- An increase in the electric resistivity of copper with temperature, which enhances the Joule effect in the copper windings.
- High and non-homogeneous temperatures cause material to dilate, deteriorating contact resistance and reducing lifetime [17].

Spatially nonuniform heat generation produces inhomogeneous temperature fields within the electric machine. The risk is the occurrence of a high-temperature localized peak. For instance, the highest source of heat generation in the copper windings, where the electric insulation is sensitive. The EM must be designed to prevent 'hot spots' with suitable heat conduction and cooling systems [11].

1.2.2 Cooling systems

The relatively low temperatures involved in an EM indicate low radiation emissions, with heat transfer occurring primarily by conduction (heat transfer through the machine elements) and convection (heat exchange with air and cooling liquids). There are two main methods to dissipate heat: the most commonly used is through the housing, as it is the easiest to set up. A complementary approach is local cooling, targeting specific critical components.

1.2.2.1 Cooling through the housing

The simplest method to dissipate heat is through the housing, offering the least complicated access with minimal impact on the electromechanical design [1]. An efficient cooling of the housing depends on the thermal resistivity of the EM materials being sufficiently low to allow efficient heat conduction from inside the EM towards the housing. This ensures overall low temperatures and minimal temperature gradients. This requirement poses a significant challenge in the design of the EM. For instance, the thermal conductivity along the copper wire (axially) is much higher than radially, with approximately a 100-fold difference, due to air gaps and electrical insulation materials [1]. Also, the stator and rotor, composed of laminated sheets of ferromagnetic materials, exhibit conductivity that is about 10 times lower in the axial direction [18, 19]. The interfaces between machine components involve contact resistance, further degrading the overall heat conduction [1]. Another aspect is air convection which also plays a non-negligible role in the heat-transfer inside the EM.

Effective cooling through the housing also requires low thermal resistance between the housing and the cooling source. One aspect is the general shape of the EM: maximizing the surface area relative to the volume, such as with a longer and thinner machine, significantly improves cooling efficiency [1, 20]. Regarding technical solutions, the simplest strategy involves using ambient air with fins on the housing to increase the exchange surface. Adding a fan can enhance heat transfer. However, this strategy is limited to environments with available space and a constant supply of cool air. A more effective but costly solution uses a liquid jacket inside the housing. This method necessitates an additional exchanger to cool down the water mixture, which is the most commonly used liquid [11].

1.2.2.2 Local cooling

Cooling through the housing faces challenges in the context of motors for electric vehicles, due to their high power density and rapid response requirements. Indeed, the concentration of high heat production within a smaller volume renders cooling solely through the housing insufficient for managing the temperature of sensitive components such as the end-windings, which are isolated from the housing. Therefore, supplement approaches have been studied: local cooling of heat sources. It is a "close-to-source heat removal" solution which involves the use of a cooling fluid and is designed to address specific critical components. However, its implementation can be challenging due to accessibility issues and potential impacts on the electrotechnical design and performance [11, 1].

The cooling fluid must be dielectric to avoid interaction with the electromagnetic field. The lubricating oil is an excellent candidate because it is dielectric, has a higher heat removal capacity than air, and is already present in the powertrain. This allows the use of an integrated cooling system to cool down the entire electric vehicle powertrain [21].

Several local cooling solutions have been explored. For example, Toyota has designed a system for which lubricating oil flows across the windings [1] and another configuration involving generating an oil fog inside the housing [18]. Some studies have investigated cooling by circulating oil directly in the winding slots [1]. Others have focused on cooling circuits printed directly in the ferromagnetic material of the stator [22] or in separate channels close to slot-windings and lamination steel [23]. Some closed-circuit solutions include cooling various components such as the shaft, stator, and end-windings [11].

1.3 Direct cooling of the end-windings

Cooling the end-windings is a relevant strategy as they can generate substantial heat. Moreover, the high thermal conductivity along copper wires means that cooling this part effectively impacts the overall windings temperature. Bertin [24] demonstrates the high sensitivity of the average temperature of the stator windings to heat transfer on the end-windings.

Owing to their accessibility, end-windings can be efficiently cooled down using direct cooling methods, a specific local cooling technique. Direct cooling involves direct contact between a cooling fluid and electrically active components. Previous experimental and numerical studies have explored various direct cooling configurations, including spray cooling [21, 25, 26, 27, 28], static impinging jets [21, 26, 27, 29, 30, 31] (see Fig. 1.2), and rotating jets exiting from the hollow shaft [25, 29, 32, 33, 34]. Among direct cooling strategies, jet and spray cooling hold significant promise, considering their effectiveness and low manufacturing cost [21]. These architectures aim to form a film covering the end-windings as extensively as possible to ensure maximal heat transfer [31]. Jet cooling, specifically addressed in the present work, is more reliable, easier to implement with reduced space requirements and offers minimal pressure losses with the ability to achieve extensive film coverage [21, 26, 27].

The implementation of jet cooling technology in the context of EM design necessitates finding a compromise between cooling efficiency, power-train integration, and cost [36]. The thermophysical properties of the oil can also be optimized and are closely related to oil temperature. Experimental studies (see Fig. 1.3) are complex and costly to set up

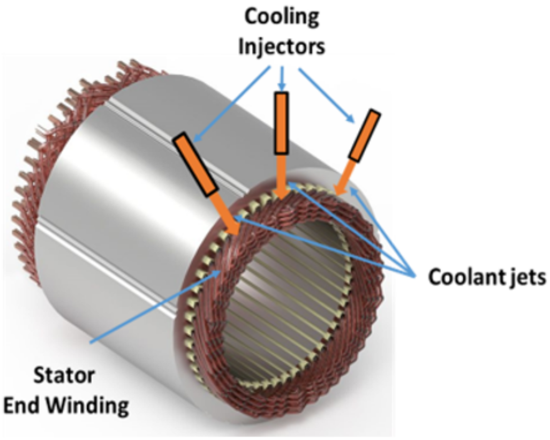

Figure 1.2: Simplified representation of end-windings jet cooling, adapted from [35].

and provide only a partial thermal assessment of the machine. High-fidelity numerical simulations therefore offer a powerful complement (see Fig. 1.4).

Three-dimensional (3D) computational fluid dynamics (CFD) simulations of direct oil-cooling systems for end-windings are well documented in the literature. In [30], a Reynolds-Averaged Navier–Stokes (RANS) study was conducted for a dozen impinging oil jets on end-windings under a single-phase, turbulent-flow assumption. In [25], a two-phase flow simulation using the Volume-of-Fluid (VoF) method was carried out; although the results agreed closely with local temperature measurements, each operating point required several days of computation. Grover et al. [34] (see Fig. 1.4) investigated two-phase rotating jets exiting the rotor shaft, modeling turbulence with both RANS and Large-Eddy Simulation (LES). They simulated jet breakup and film coverage using the VoF method, finding that mesh convergence with cell sizes down to 50 μm was necessary to resolve heat transfer accurately in the liquid film. In the work of Poubeau et al. [31], an impinging-jet configuration on a static end-winding geometry was simulated under the assumption of laminar two-phase flow using the VoF method. Mesh refinement studies indicated that cells as fine as 30 μm were required near impingement zones to capture heat transfer. This work also underscored the influence of the oil's strong temperature-dependent viscosity on heat transfer, highlighting the need to account for viscosity variation across the thermal boundary layer.

CFD, particularly the three-dimensional VoF method, has proved effective in modeling unsteady, laminar two-phase flows with heat transfer [31]. However, validation of both hydrodynamics and heat transfer remains rare and largely qualitative. Validation via local

Figure 1.3: Oil injection experiments on end-winding [27]

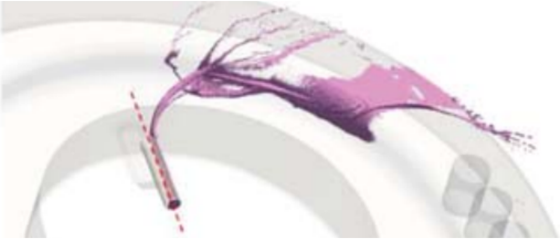

Figure 1.4: Modeling of oil flow from hollow shaft to the rotor end cap before it is slung onto the stator end-windings [34]

temperature measurements in solid elements, as carried out in [25, 30, 28, 37], is challenging due to uncertainties in the thermal modeling of solid parts. Moreover, computational cost is a criterion of paramount importance in EM optimization projects, especially when testing numerous configurations, including the computationally demanding cases of multiple jets impacting the end-windings and the overall EM modeling.

1.4 Oil jet cooling modeling

In the context of implementing oil-jet cooling, and given the flow rates, viscosity, and length scales characteristic of such systems, both the impinging liquid jets and the ensuing film flows remain laminar [26, 31]. Still, a comprehensive numerical modeling of impinging-jet oil cooling for end-windings must account for multiple complex phenomena (see Fig. 1.5):

- Destabilization of the liquid flow due to interaction with cross-air flow (air entrainment caused by the rotor),
- Splashing triggered by the jet impinging on the complex surface,
- Formation of a liquid film exhibiting different dynamic behavior in various regions,
- Surface wetting by the liquid film, dependent on the wettability of a complex surface,

- The impact of complex surfaces on the thermal exchanges between the liquid film and solid,
- Hydrodynamics of the liquid film and possible Kapitza and Marangoni instabilities [38] that can affect thermal exchanges,
- Thin thermal boundary layer relative to the film thickness and motor size, due to high Prandtl number (Pr) fluids ($100 < Pr < 1000$ for oils [31]),
- Strong coupling between the dynamic and thermal fields across the thin thermal boundary layer, due to fluids with high viscosity sensitivity to temperature (relative variation up to a factor of 15 for oils over the temperature range considered).

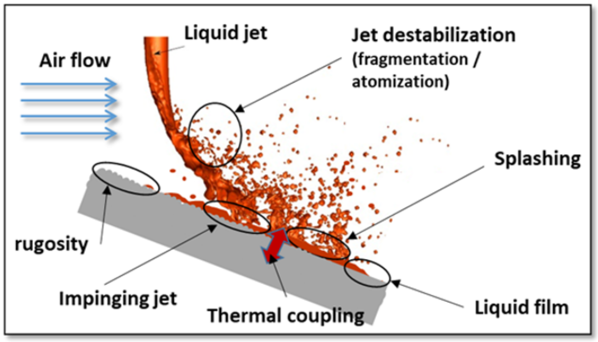

Figure 1.5: Multi-physics phenomena involved in the context of oil cooling of end-windings.

The complexity of validating hydrodynamic and heat transfer phenomena in EMs necessitates addressing each underlying mechanism separately to simplify numerical model validation and enhance overall understanding.

The two aspects addressed within the scope of this thesis are high Prandtl fluids and high viscosity sensitivity to temperature. Numerically, a high Pr entails resolving temperature gradients within a very thin thermal boundary layer, much thinner than the hydrodynamic boundary layer, both confined within the liquid film. Consequently, a single simulation must span two distinct physical scales: the thermal and the dynamic boundary layer thickness. Their ratio is well approximated by $Pr^{1/3}$ [39, 40], and is illustrated in Fig. 1.6. Accurately capturing heat transfer demands fine mesh resolution (yielding large cell counts) and small time steps for explicit integration, which together lead to prohibitive computational times. Therefore, developing strategies to reduce calculation time without compromising result fidelity is essential for EM cooling system design optimization.

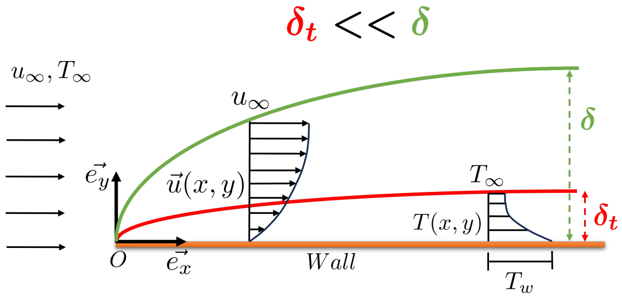

Figure 1.6: Illustration of the thermal and dynamic boundary layer for $Pr \gg 1$.

Oils generally exhibit a strong temperature dependence of kinematic viscosity, whereas their other thermophysical properties are much less sensitive. For the oils examined by Sindjui et al. [26] in the context of end-winding cooling with oil jets, increasing the bulk oil temperature from 30°C to 100°C changes the density by about 5%, the thermal conductivity by about 10%, and the specific heat capacity by about 15%. By contrast, the kinematic viscosity decreases by a factor of 5 or 7, depending on the oil. The variation of the kinematic viscosity with temperature for the different oils is shown in Fig. 1.7. The strong temperature dependence of oil viscosity implies that temperature can no longer be treated as a passive scalar, and the momentum and energy equations are therefore coupled. In particular, viscosity may vary substantially across the thin thermal boundary layer, modifying the near-wall shear and the velocity profile. The numerical study on impinging-jet cooling with oil [31] highlights the marked impact of viscosity variation on

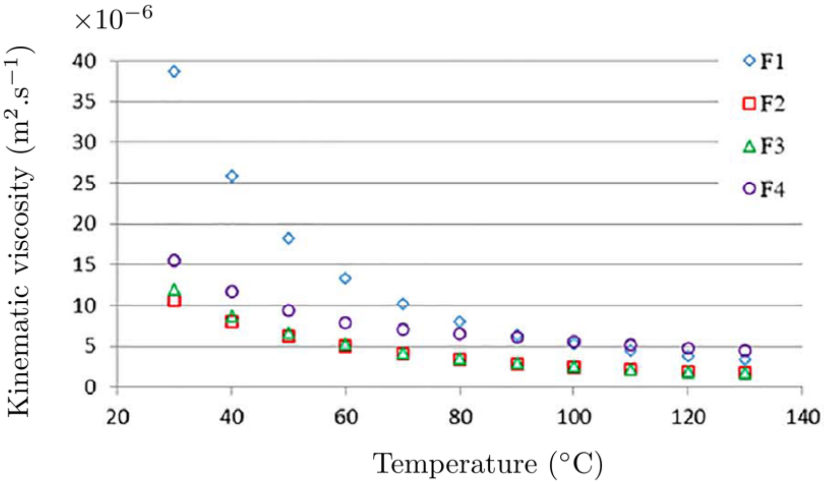

Figure 1.7: Kinematic viscosity as a function of temperature for 4 different oils (termed F1, F2, F3 and F4) considered in the end-winding cooling study [26].

near wall heat transfer. This fluid property must therefore be accounted for as an additional complexity on top of the high–Prandtl–number character of the fluid.

1.5 Objectives and structure of the thesis

The objective of this PhD thesis is to develop a modeling approach that overcomes the prohibitive cost of simulations with high–Prandtl–number fluids. The method must predict wall heat transfer accurately at low computational cost while accounting for the strong temperature dependence of oil viscosity. In particular, it must remain accurate in the near-impingement region, where the thermal boundary layer is thinnest, to enable the optimization of multi–jet cooling configurations [31]. To this end, a review of existing models in the literature that address reducing computational time in thin boundary layer modeling is presented in chapter 2. Building on that review, the proposed solution relies on a near-wall model, denoted thermal wall model (TWM), inspired by turbulent wall functions and subgrid-scale (SGS) models.

The thesis details the steps in developing and assessing the TWM. A first version of the model dedicated to fluids with low viscosity variation is presented (TWM-cst), followed by a more advanced version for fluids with strong temperature-dependent viscosity (TWM-var). Finally the TWM-cst is applied to a near-industrial configuration.

- Part II describes the first version of the proposed thermal wall model (TWM-cst), tailored for low viscosity variation fluids. The mathematical formulation and underlying assumptions are detailed, followed by the numerical implementation in a finite-volume framework. The model is then assessed on a two-dimensional thermal boundary-layer development case and on an academic impinging-jet configuration representative of the intended industrial application.
- Part III follows the same structure as Part II but for the improved version of the thermal wall model (TWM-var), which handles fluids with high viscosity sensitivity to temperature.
- Part IV presents an assessment of the TWM-cst on a configuration close to real end-winding geometry.
- In Part V, conclusions are drawn and perspectives for future work highlight potential model refinements.

CHAPTER 2

A state-of-the-art review of boundary layer modeling

In this chapter, the main characteristics of boundary layers (dynamic and thermal) are summarized with an emphasis on the high–Prandtl–number regime, where the thermal boundary layer is thinner than the dynamic boundary layer. Commonly used CFD approaches for treating thin thermal boundary layers are then reviewed. Both laminar and turbulent boundary layers characteristics and their associated treatments are outlined. Although the model developed here targets laminar flows, several ideas are adapted from turbulent wall modeling and inform the proposed methodology.

2.1 Boundary layer characteristics

When a fluid flows past a solid body, it adheres to the body's surface. Thus, a thin layer of varying velocity, small compared with the body size, is formed between the solid and the free stream of velocity $\vec{u}_\infty$. Regarding heat exchange between a solid and a fluid, when the wall temperature T_w differs from the free-stream temperature T_∞, a thermal boundary layer develops alongside the velocity boundary layer. boundary layers are well described in the literature; the main sources used here are [39, 41, 42, 43]. It is worth beginning the boundary layer description with a more general form of the Navier–Stokes equations to highlight the assumptions specific to boundary layer physics, which leads to the boundary layer equations. A few general remarks about laminar and turbulent flows are also provided, and the physics of boundary layer development over a flat wall (also called plate) is described. This canonical case helps understanding boundary layer characteristics and is the basic configuration for certain model developments.

2.1.1 Setup of the boundary layer equations

Considering the targeted industrial application (end-winding cooling by oil jets), temperature variations ΔT are moderate ($T \in [290, 390]\,\mathrm{K}$ and $\Delta T \approx 100\,\mathrm{K}$) and the flow operates at low Mach number, $Ma = \|\vec{u}_\infty\|/c \ll 1$, where $\|\vec{u}_\infty\| \approx 5\,\mathrm{m.s}^{-1}$ is used as a characteristic liquid velocity scale fixed equal to the jet injection velocity and c is the speed of sound in the oil. Under these conditions, compressibility effects are reasonably assumed negligible and the fluid density ρ can be taken as constant. Owing to the small temperature differences, radiative heat transfer is negligible and thus omitted. The mass conservation equation reads

$$\nabla \cdot \vec{u} = 0 \tag{2.1.1}$$

where $\vec{u}$ is the velocity vector. The momentum-conservation equation is

$$\rho \left(\frac{\partial \vec{u}}{\partial t} + (\vec{u} \cdot \nabla)\vec{u} \right) = -\nabla p + \nabla \cdot \overline{\overline{\tau}} + \rho \vec{g} \tag{2.1.2}$$

where p is the pressure and $\vec{g}$ the gravitational acceleration. Assuming a Newtonian fluid, the viscous stress tensor $\overline{\overline{\tau}}$ is given by Newton's law:

$$\overline{\overline{\tau}} = \mu \left(\nabla \vec{u} + (\nabla \vec{u})^T \right) \tag{2.1.3}$$

where μ is the dynamic viscosity. The gravitational body force $\rho \vec{g}$ is the only volumetric force considered here. The energy-conservation equation is

$$\rho c_p \left(\frac{\partial T}{\partial t} + \vec{u} \cdot \nabla T \right) = -\nabla \cdot \vec{q} + \Phi \tag{2.1.4}$$

where T is the temperature field and c_p the specific heat at constant pressure. The conductive heat flux $\vec{q}$ is given by Fourier's law,

$$\vec{q} = -k \nabla T \tag{2.1.5}$$

with k the thermal conductivity. The term Φ denotes viscous dissipation and is expressed as $\Phi = \overline{\overline{\tau}} : \nabla\vec{u}$.

To describe the boundary layer development on a plate, the following additional assumptions are made: steady and two-dimensional flow (i.e., no variation in the third direction). The fluid is assumed at first glance to have uniform properties ($\rho = \mathrm{cst}$, $c_p = \mathrm{cst}$, $\mu = \mathrm{cst}$, and $k = \mathrm{cst}$); the temperature field has thus no impact on the dynamic. The Eckert number Ec is small ($Ec = \frac{u_\infty^2}{c_p \Delta T} \ll 1$ with $c_p \approx 2000\,\mathrm{J.kg^{-1}.K^{-1}}$), which allows the viscous dissipation Φ to be omitted [43]. The boundary layer is very thin compared to the wall length; consequently, the streamwise velocity component u is generally much larger than the wall-normal component v, i.e., $u \gg v$ (see Fig. 2.1 for the axis definition). Moreover, streamwise gradients are small compared with wall-normal gradients across the boundary layer thickness, i.e., $\frac{\partial}{\partial x} \ll \frac{\partial}{\partial y}$. These last two hypotheses hold only sufficiently far from the plate leading edge. Finally, outside the boundary layer, $\vec{u}_\infty$ is assumed uniform with a weak pressure gradient, $\frac{\partial p_\infty}{\partial x} \approx 0$ where p_∞ is the pressure of the bulk flow. Following these assumptions, for a plat align with the x-axis, the incompressible Navier–Stokes equations detailed in Eq. 2.1.2, Eq. 2.1.1, and Eq. 2.1.4 simplify to the boundary layer equations:

$$\frac{\partial u}{\partial x} + \frac{\partial v}{\partial y} = 0 \tag{2.1.6}$$

$$\rho\left(u\frac{\partial u}{\partial x} + v\frac{\partial u}{\partial y}\right) = \frac{\partial}{\partial y}(\tau_{yx}) \tag{2.1.7}$$

$$\text{with } \tau_{yx} = \mu\frac{\partial u}{\partial y} \tag{2.1.8}$$

$$\rho c_p\left(u\frac{\partial T}{\partial x} + v\frac{\partial T}{\partial y}\right) = -\frac{\partial}{\partial y}(q_y) \tag{2.1.9}$$

$$\text{with } q_y = -k\frac{\partial T}{\partial y} \tag{2.1.10}$$

Here, u and v are the x and y components of $\vec{u}$, respectively; the shear stress τ_{yx} is the (y, x) component of the viscous stress tensor, and q_y is the y component of the heat flux vector $\vec{q}$. By simplifying the y-component of Eq. 2.1.2, the pressure is found to be uniform across the boundary layer ($\partial p/\partial y \approx 0$), and with the previously mentioned assumption $\partial p_\infty/\partial x \approx 0$, p does not appear explicitly in Eq. 2.1.7. To illustrate boundary layer flow, a velocity field representative of a laminar boundary layer developing over a flat plate is shown in Fig. 2.1.

The thickness of the velocity boundary layer δ (thermal boundary layer δ_t, respectively), is traditionally defined as the distance from the plate at which the normalized mean velocity

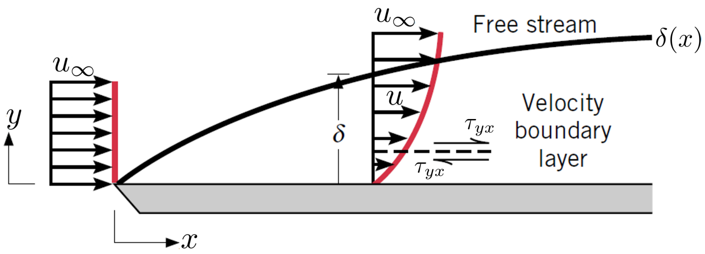

Figure 2.1: Laminar boundary layer development on a flat plate, adapted from [41].

parallel to the wall, $\frac{u}{u_\infty}$ (resp. the normalized mean temperature difference, $\frac{T-T_w}{T_\infty-T_w}$), reaches 0.99. Here $u_\infty = \|\vec{u}_\infty\|$, with $\vec{u}_\infty$ parallel to the plate. Formally,

$$\frac{u(y=\delta)}{u_\infty} = 0.99 \qquad \frac{T_w - T(y=\delta_t)}{T_w - T_\infty} = 0.99 \tag{2.1.11}$$

2.1.2 Solution of the laminar boundary layer

Boundary layers can be categorized into two types based on their flow characteristics: the *laminar* boundary layer, which exhibits a smooth flow pattern, and the *turbulent* boundary layer, characterized by the presence of vortices (eddies). Outside the boundary layer, a turbulent flow is marked by a strong dominance of inertial over viscous forces, in contrast to a laminar flow; this competition is measured by the Reynolds number (Re). Laminar flow is characterized by fluid particles following paths in layers, with adjacent layers sliding past one another widely without lateral mixing. Turbulent flow, on the other hand, is distinguished by a spectrum of coexisting vortices of different sizes; the kinetic energy contained in the largest eddies is transferred to progressively smaller ones until the Kolmogorov scale is reached, where viscous effects dissipate the motion and convert it into heat.

The academic situation of a flat plate in a free-stream parallel flow is considered where the first portion of the boundary layer is laminar, then it becomes fully turbulent after a transition region (see Fig. 2.2). The transition from laminar to turbulent boundary layer occurs within a range of Re that depends on the turbulence level of the free stream over the plate and on other plate characteristics. The Reynolds number is defined as

$$Re = \frac{x\,u_\infty}{\nu} \tag{2.1.12}$$

where x denotes a characteristic length equal to the streamwise distance from the leading edge to the position of interest. On a flat plate, below the critical Reynolds number of about 3.5×10^5, the boundary layer is always laminar, whereas above 4×10^6 the boundary layer is always turbulent [39].

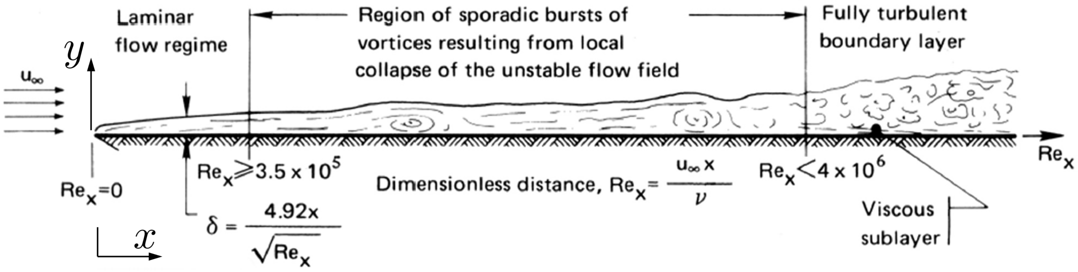

Figure 2.2: Development of a dynamic boundary layer on a flat plate, adapted from [39].

Along the plate, as x increases, the dynamic and thermal boundary layers thicken as momentum and temperature diffuse through the fluid (see Fig. 2.2). This leads to less sharp temperature and velocity gradients within the boundary layer, reducing wall heat flux and shear stress along the plate in both the fully laminar and fully turbulent boundary layer regions.

In the industrial application of interest, end-winding cooling by oil jets, the dynamic boundary layer remains laminar. Accordingly, the section focuses on the laminar region.

2.1.2.1 Dynamic boundary layer

To describe the velocity field in a laminar boundary layer over a flat plate, the boundary-layer equations (see Eq. 2.1.7–Eq. 2.1.9) were firstly solved by Blasius in 1908 [44]. Since the system has no characteristic length in the x direction, the velocity profile normal to the plate is assumed to be self-similar for all distances x from the leading edge, as confirmed experimentally [39]. This means that the dimensionless velocity profile, scaled by the boundary layer thickness, keeps the same shape $\forall x$. With this in mind, the velocity field can be expressed as

$$u = u_\infty \times \text{function}\left(\frac{y}{g(x)}\right), \tag{2.1.13}$$

where u_∞ is the free-stream velocity and $g(x)$ is proportional to the dynamic boundary layer thickness δ. To solve Eq. 2.1.7, since the flow is incompressible (divergence-free), two-dimensional, and steady, the stream function ψ, is introduced as first proposed by

Blasius:

$$u = \frac{\partial \psi}{\partial y} \qquad v = -\frac{\partial \psi}{\partial x} \tag{2.1.14}$$

With the self-similar form Eq. 2.1.13, ψ can be written as

$$\psi = u_\infty \, g(x) \, f\left(\frac{y}{g(x)}\right), \tag{2.1.15}$$

where f is an as-yet undetermined dimensionless function. A similarity variable

$$\eta = \frac{y}{g(x)} \tag{2.1.16}$$

is introduced via the change of variables $\frac{y}{g(x)} \to \eta$ in Eq. 2.1.15, with the proposed value $g(x) = \sqrt{\frac{\nu x}{u_\infty}}$. Substituting the resulting expression for ψ into Eq. 2.1.7, using Eq. 2.1.14, yields an ordinary differential equation independent of x:

$$f\frac{d^2 f}{d\eta^2} + 2\,\frac{d^3 f}{d\eta^3} = 0 \quad \text{with} \quad \begin{cases} u(y=0) = 0 & \Rightarrow \left.\frac{df}{d\eta}\right|_{\eta=0} = 0 \\ v(y=0) = 0 & \Rightarrow f(\eta = 0) = 0 \\ u(y \to \infty) = u_\infty & \Rightarrow \left.\frac{df}{d\eta}\right|_{\eta\to\infty} \to 1 \end{cases} \tag{2.1.17}$$

Eq. 2.1.17 can be solved numerically, e.g., using a shooting method with a fourth-order Runge–Kutta scheme. The dimensionless velocity profiles then follow from

$$u = u_\infty \frac{df}{d\eta} \qquad v = \frac{1}{2}\sqrt{\frac{\nu u_\infty}{x}}\left(\eta\,\frac{df}{d\eta} - f\right) \tag{2.1.18}$$

and can be extended to any x through the definition of η. The scaled velocity profiles are shown in Fig. 2.3.

From the dynamic boundary layer thickness δ definition in Eq. 2.1.11, η in Eq. 2.1.16 and the relation between u and f in Eq. 2.1.18, it follows that δ can be written as $\delta = \eta|_{f'=0.99}\; g(x)$[1]. The numerical solution gives $\eta|_{f'=0.99} \approx 4.91$, leading to

$$\delta \approx \; 4.91\left(\frac{\nu x}{u_\infty}\right)^{\frac{1}{2}} \approx 4.91\, x\, Re^{-1/2} \tag{2.1.19}$$

Thus, the dynamic boundary layer thickness increases with x and decreases with the Re.

---

[1] The notation $\eta|_{f'=0.99}$ corresponds to the value of η when $f' = \frac{u}{u_\infty} = 0.99$.

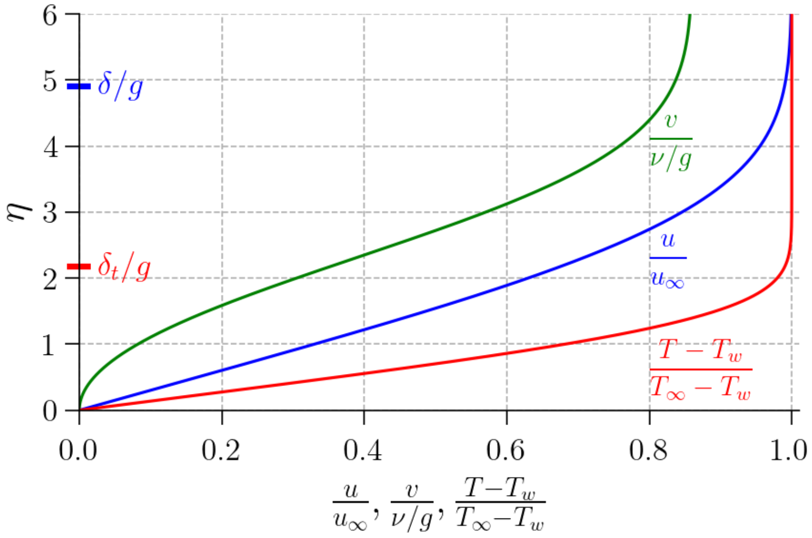

Figure 2.3: Scaled profiles solutions for laminar boundary layer on flat plate for Pr=10.

2.1.2.2 Thermal boundary layer

Analogously to the velocity profile, the thermal profile is self-similar and can be expressed as

$$\frac{T(x,y)-T_w}{T_\infty-T_w} = \Theta\left(\frac{y}{g(x)}\right) \tag{2.1.20}$$

Assuming a uniform wall temperature, introducing η and combining Eq. 2.1.9 with Eq. 2.1.20 yields

$$2\frac{d^2\Theta}{d\eta^2} + Pr\ f\frac{d\Theta}{d\eta} = 0 \quad \text{with} \quad \begin{cases} T(y=0) = T_w & \Rightarrow \Theta(0) = 0 \\ T(y\to\infty) = T_\infty & \Rightarrow \Theta(\eta\to\infty) = 1 \end{cases} \tag{2.1.21}$$

Eq. 2.1.21 can be solved numerically for a given Pr, e.g., using a shooting method with a fourth-order Runge–Kutta scheme. The temperature profile then follows from

$$T(x,y) = \Theta(T_\infty - T_w) + T_w \tag{2.1.22}$$

From the δ_t definition in Eq. 2.1.11, η in Eq. 2.1.16, and the definition of Θ in Eq. 2.1.20, it follows that δ_t can be written as $\delta_t = \eta|_{\Theta=0.99}\ g(x)$[2]. The value of $\eta|_{\Theta=0.99}$ depends on the Pr number. The Pr number, defined as the ratio of kinematic viscosity to thermal

---

[2] The notation $\eta|_{\Theta=0.99}$ corresponds to the value of η when $\Theta = 0.99$.

diffusivity, reads:

$$Pr = \frac{\nu}{\alpha} \tag{2.1.23}$$

The Pr has a crucial influence on the thermal thickness δ_t; in fact, the ratio $\frac{\delta_t}{\delta}$ depends only on Pr. For $Pr = 1$, the equations and boundary conditions for $f'(\eta)$ and $\Theta(\eta)$ are identical, so the scaled streamwise velocity and temperature profiles, along with boundary layers thickness, coincide. For $Pr > 1$, since the thermal diffusivity α is smaller than the momentum diffusivity ν, the thermal boundary layer is thinner than the dynamic one. This effect is confirmed by the Blasius solution, and the ratio can be accurately approximated [39] by

$$\frac{\delta_t}{\delta} \approx Pr^{-1/3} \tag{2.1.24}$$

Comparison with accurate numerical solutions shows that the correlation Eq. 2.1.24 is within 6% for $1 < Pr < 1000$. The effect for $Pr = 10$ on δ_t/δ and the resulting scaled temperature profile Θ are shown in Fig. 2.3.

2.1.2.3 Thermal boundary layer with very high Prandtl: Lévêque solution

The classical scaling given in Eq. 2.1.24 implies that the thermal boundary layer, in the limit $\text{Pr} \to \infty$, develops in a region where the velocity profile depends linearly on y, i.e., $u(x, y) = a(x)\ y$ with $a(x) = \frac{\tau_w(x)}{\mu}$ expressed in terms of the wall shear stress $\tau_w(x)$ and the uniform dynamic viscosity μ. The y-velocity component $v(x, y) = -\frac{d\tau_w}{dx}\frac{y^2}{2\mu}$ is derived from the continuity equation. This asymptotic regime leads to Lévêque's theory [45].

Lévêque solved Eq. 2.1.9 in 1928 under the additional assumption of a linear velocity profile [45]. Following Lévêque's assumptions, the boundary layer energy equation, Eq. 2.1.9, reads:

$$\rho c_p \left(\frac{\tau_w(x)}{\mu} y \frac{\partial T}{\partial x} - \frac{d\tau_w}{dx}\frac{y^2}{2\mu}\frac{\partial T}{\partial y} \right) = k\frac{\partial^2 T}{\partial y^2} \quad \text{with} \quad \begin{cases} T(y=0) = T_w \\ T(y \to \infty) = T_\infty \end{cases} \tag{2.1.25}$$

The temperature profile within the thermal boundary layer is assumed self-similar [45]. Hence, the dimensionless temperature can be written as a function Θ_L of the dimensionless wall-normal distance $y/g_L(x)$, where subscript L specifies quantities in the limit $Pr \to \infty$:

$$\frac{T(x, y) - T_w}{T_\infty - T_w} = \Theta_L \left(\frac{y}{g_L(x)} \right) \tag{2.1.26}$$

g_L is a function depending only on the streamwise coordinate x and is expected to be proportional to the thermal boundary layer thickness δ_t[3]. The function $g_L(x)$ is given by [45, 42]:

$$g_L(x) = \left(\frac{\tau_w(x)}{\mu}\right)^{-1/2} \left(9\alpha \int_0^x \sqrt{\frac{\tau_w(X)}{\mu}}\, dX\right)^{1/3} \tag{2.1.27}$$

where α is the thermal diffusivity. Eq. 2.1.25 and Eq. 2.1.26 are combining through the change of variables $y/g_L(x) \to \eta_L$, with the similarity variable η_L defined as

$$\eta_L = \frac{y}{g_L(x)} \tag{2.1.28}$$

As a result, Eq. 2.1.25 reduces to an ordinary differential equation:

$$\frac{d^2\Theta_L}{d\eta_L^2} + 3\eta_L^2 \frac{d\Theta_L}{d\eta_L} = 0 \quad \text{with} \quad \begin{cases} \Theta_L(\eta_L = 0) = 0 \\ \Theta_L(\eta_L \to \infty) = 1 \end{cases} \tag{2.1.29}$$

The scaled temperature profile $\Theta_L(\eta_L)$ expressed as a function of η_L, can be easily solved numerically using a fourth-order Runge-Kutta method in conjunction with the shooting method. Alternatively, the solution of Eq. 2.1.29 can be expressed in terms of incomplete gamma function, which gives:

$$\Theta_L(\eta_L) = \frac{\gamma\left(\frac{1}{3}, \eta_L^3\right)}{\Gamma(\frac{1}{3})} \tag{2.1.30}$$

where $\gamma(s,x) = \int_0^x t^{s-1} e^{-t}\, dt$ is the lower incomplete gamma function and $\Gamma(s) = \int_0^\infty t^{s-1} e^{-t}\, dt$ is the (complete) gamma function. The resulting scaled temperature profile is shown in Fig. 2.4, exhibiting a similar shape to the scaled temperature profile obtained for $Pr = 10$ in Fig. 2.3. The temperature field then follows from

$$T(x,y) = \Theta_L\left[T_\infty - T_w\right] + T_w = \frac{\gamma\left(\frac{1}{3}, \left(\frac{y}{g_L(x)}\right)^3\right)}{\Gamma(\frac{1}{3})}\left[T_\infty - T_w\right] + T_w \tag{2.1.31}$$

From the δ_t definition in Eq. 2.1.11, η_L in Eq. 2.1.28, and the definition of Θ_L in Eq. 2.1.26, the thermal boundary layer thickness can be written[4] as $\delta_t = \eta_L|_{\Theta_L=0.99}\ g_L(x)$, which highlights the proportionality between g_L and δ_t. The solution of Θ_L gives $\eta_L|_{\Theta_L=0.99} \approx 1.404$, leading to

$$\delta_t \approx 1.404\, g_L(x) \tag{2.1.32}$$

---

[3] The function g_L is only considered proportional to δ_t and not to δ as $\frac{\delta}{\delta_t} \to \infty$ when $\mathrm{Pr} \to \infty$

[4] The notation $\eta_L|_{\Theta_L=0.99}$ corresponds to the value of η_L when $\Theta_L = 0.99$.

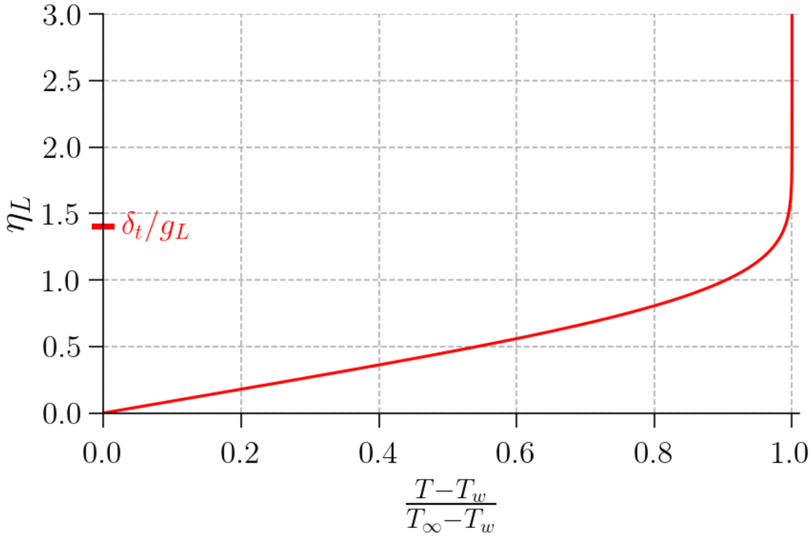

Figure 2.4: Scaled temperature profile solutions of Lévêque for a laminar boundary layer on a flat plate in the limit $Pr \to \infty$.

with $g_L(x)$ defined in Eq. 2.1.27.

2.1.3 Near wall flux

The wall shear stress τ_w and the wall heat flux q_w are given by

$$\tau_w = \mu \left.\frac{\partial u}{\partial y}\right|_{y=0} \qquad q_w = -\,k \left.\frac{\partial T}{\partial y}\right|_{y=0} \tag{2.1.33}$$

2.1.3.1 Laminar boundary layer

From Eq. 2.1.18 together with the similarity variable $\eta = y/g(x)$, the wall–normal velocity gradient at the wall reads

$$\left.\frac{\partial u}{\partial y}\right|_{y=0} = u_\infty\, f''(0)\, \frac{\partial \eta}{\partial y} = \frac{u_\infty\, f''(0)}{g(x)} \tag{2.1.34}$$

Similarly, from Eq. 2.1.22, the wall–normal temperature gradient at the wall is

$$\left.\frac{\partial T}{\partial y}\right|_{y=0} = (T_\infty - T_w)\, \Theta'(0)\, \frac{\partial \eta}{\partial y} = \frac{(T_\infty - T_w)\, \Theta'(0)}{g(x)} \tag{2.1.35}$$

Using $g(x) = \left(\frac{\nu\, x}{u_\infty}\right)^{1/2}$, both wall fluxes share the same streamwise scaling,

$$\tau_w \sim x^{-1/2} \qquad q_w \sim x^{-1/2} \tag{2.1.36}$$

since $\tau_w \sim 1/g(x)$ and $q_w \sim 1/g(x)$.

In the limit $Pr \to \infty$, using the Lévêque scaling $\eta_L = y/g_L(x)$ together with Eq. 2.1.26, the wall–normal temperature gradient takes the analogous form

$$\left.\frac{\partial T}{\partial y}\right|_{y=0} = \frac{(T_\infty - T_w)\,\Theta_L'(0)}{g_L(x)}, \tag{2.1.37}$$

With $\tau_w \sim x^{-1/2}$, Eq. 2.1.27 and Eq. 2.1.37 likewise yield

$$q_w \sim x^{-1/2} \tag{2.1.38}$$

2.1.3.2 Turbulent boundary layer

In the laminar boundary layer, momentum and heat are transferred solely by molecular diffusion. In contrast, within the turbulent boundary layer, large eddies initiate wall-normal motion, but only beyond a certain distance from the wall. The mixing induced by these eddies produces very steep near-wall gradients, where momentum and heat transport remain governed by molecular diffusion, which then weaken further from the wall. In the transition region along the plate from laminar to turbulent, an increase of $\tau_w(x)$ and $q_w(x)$ is observed. Indeed, gradients are typically steeper in a turbulent boundary layer than in a laminar one, as illustrated in Fig. 2.5a and Fig. 2.5b, which reflect the different flow characteristics of laminar and turbulent boundary layers. For the turbulent part of the boundary layer along the plate, experiments show that for $Re \lesssim 10^8$ (not too far from the plate edge), the turbulent boundary layer thickness grows much faster ($\delta \sim x^{4/5}$) than for the laminar boundary layer ($\delta \sim x^{1/2}$). However, the decay of $\tau_w(x)$ and $q_w(x)$ is more gradual in turbulence than in laminar [41]:

$$\tau_w \sim x^{-1/5} \qquad q_w \sim x^{-1/5} \tag{2.1.39}$$

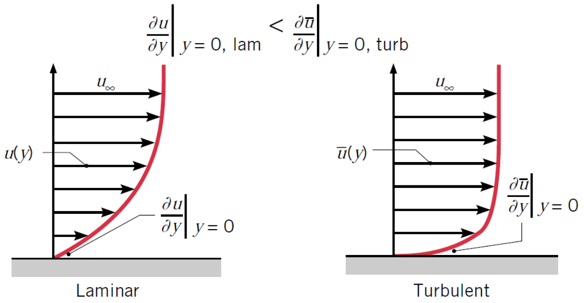

(a) u profile inside the laminar and turbulent boundary layer. $\overline{u}$ corresponds to a temporal mean velocity and in the laminar case $\overline{u} = u$.

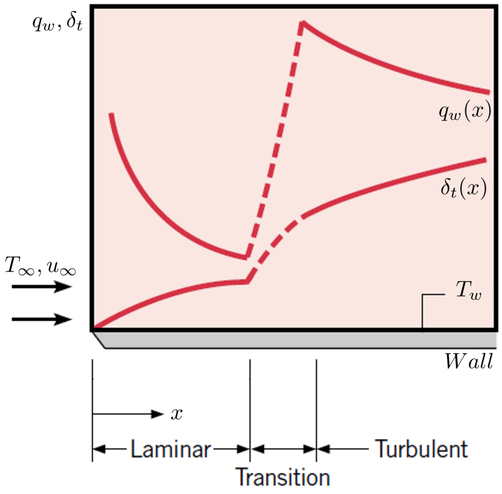

(b) q_w and δ_t along the wall inside the laminar and turbulent boundary layers

Figure 2.5: Effect of laminar–turbulent regime on (a) velocity profiles, (b) wall heat flux q_w and thermal boundary layer thickness δ_t. Adapted from [41].

2.2 Methods to model boundary layers in CFD

Several approaches have been proposed in the literature to model thin boundary layers (dynamic, thermal or mass boundary layers) so as to avoid finely meshing the near-wall region and thereby drastically reduce computational cost. Different approaches are detailed in this section, including the widely used and well-known “wall functions” described in section 2.2.2 with the aim of informing and inspiring the subsequent model development. To begin, the baseline method used by default without explicit boundary layer modeling is presented in the context of the finite–volume method in section 2.2.1.

The fluid treated here is assumed at first glance to have uniform fluid properties; the temperature exert no feedback on the dynamics and can therefore be treated as a passive scalar. Concentration field without feedback on the dynamics are analogous and can also be treated as passive scalars. Consequently, models designed for thin mass boundary layers can be leveraged for thermal boundary layer applications and are also treated in this section. The analogue of Pr for mass transfer is the Schmidt number (Sc), defined as the ratio of the kinematic viscosity ν to the mass diffusivity α_c:

$$Sc = \frac{\nu}{\alpha_c} \tag{2.2.1}$$

2.2.1 Default finite–volume method for near-wall flux calculation

In the context of the finite–volume method, the computational domain is divided into control volumes (cells). In the absence of boundary layer modeling, τ_w for a near–wall cell (denoted $cell_1$) is commonly evaluated by a linear interpolation between the wall and the cell center [46, 47]:

$$\tau_w \approx \mu \frac{u_1}{y_1} \tag{2.2.2}$$

where u_1 is the velocity at the first off–wall cell center and y_1 is its distance from the wall. $cell_1$ and its associated variables are illustrated on a Cartesian grid in Fig. 2.6. From Eq. 2.1.33, to capture τ_w accurately, the near–wall cell must be sufficiently fine so that

$$\frac{u_1}{y_1} \approx \left.\frac{\partial u}{\partial y}\right|_{y=0} \tag{2.2.3}$$

At high Re (see Eq. 2.1.19) the dynamic boundary layer is generally much thinner than the overall geometry thus practical meshes are often not fine enough and the approximation Eq. 2.2.2 becomes inaccurate.

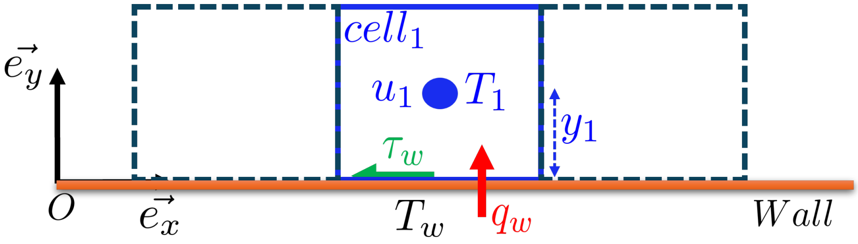

Figure 2.6: Illustration of a uniform Cartesian grid adjacent to a wall, highlighting the first off-wall $cell_1$; the filled dot marks its centroid.

A similar linear approximation is used for q_w [46, 47]:

$$q_w \approx -k \frac{T_1 - T_w}{y_1} \tag{2.2.4}$$

From Eq. 2.1.33, the above approximation holds provided that

$$\frac{T_1 - T_w}{y_1} \approx \left.\frac{\partial T}{\partial y}\right|_{y=0} \tag{2.2.5}$$

At high Pr, from Eq. 2.1.24, the thermal boundary layer is much finer than the dynamic boundary layer thus practical meshes are generally not fine enough and the approximation Eq. 2.2.4 becomes inaccurate.

2.2.2 Wall functions method approach

In CFD, laminar flows are generally fully resolved by solving the Navier–Stokes equations without a subgrid model. For turbulent flows, the analogous fully resolved approach is called *Direct Numerical Simulation* (DNS). Because the smallest eddies, of order the Kolmogorov scale, are very small, and become smaller as Re increases, DNS requires an extremely fine mesh to resolve all scales, making it computationally prohibitive and largely limited to academic cases. Two other approaches are therefore common: *Large Eddy Simulation* (LES), in which only the larger turbulent scales are resolved and the smaller ones are modeled, and *Reynolds–Averaged Navier–Stokes* (RANS), in which all turbulence scales are modeled. In these approaches, the mesh does not need to resolve the entire eddy spectrum, which greatly reduces the computational cost. The RANS approach is widely used, especially for practical engineering flows. Within RANS, a main class of turbulence models relies on the Boussinesq eddy-viscosity hypothesis [48], notably the well-known k–ϵ model [49] and k–ω model [50].

To evaluate the near-wall fields and wall fluxes within the RANS framework, two methods are commonly used. The first is the *wall integration method*, which requires a Low-Reynolds-number (LRN) turbulence model. Examples include the k-ω model and the k-ϵ model augmented with viscous damping functions. This class of models includes a near-wall modification of the equations solved to account for turbulence behavior close to the wall and requires a finely resolved mesh in the near-wall region, where gradients are steeper.

The second approach is the *wall function method*, used with a High-Reynolds-number (HRN) turbulence model such as the standalone k-ϵ model. This approach does not capture near-wall modifications of turbulence, even if the mesh is refined, and therefore requires a dedicated near-wall modeling strategy. Wall functions are applied to bridge the region between the wall and the fully turbulent core based on the *law of the wall.* As a result, HRN turbulent models with wall functions enable the estimation of wall fluxes on a coarser mesh and at lower computational cost, albeit with some loss of information and accuracy. In general, the *wall function method* is less accurate than the *wall integration method.*

A hybrid approach between the *wall integration method* and the *wall function method*, while still using an LRN turbulence model, is a possible strategy and has been developed or used, for instance, in [51, 52, 53]. In such approaches, a wall function bridges the near-wall region when the mesh is too coarse and switches to resolving the boundary layer with the LRN turbulence model when the mesh is sufficiently fine.

It is useful to examine in more detail how wall functions treat the thin dynamic and thermal boundary layers as a source of inspiration for the present work, especially to understand how high Pr impact this approach. With this objective in mind, the law of the wall used to bridge the near-wall region is detailed in the following section, followed by the implementation strategy.

2.2.2.1 Law of the wall

The wall–function approach relies on universal velocity and temperature profiles, collectively called the *law of the wall*, to bridge the near–wall region between the wall and the first off–wall node. Profiles for other transported turbulent quantities are also required; see

[51] for details. The profile expressions are derived from the boundary layer equations (see Eq. 2.1.6 - Eq. 2.1.9) rewritten in terms of the Reynolds–Averaged Navier–Stokes (RANS) equations. The RANS approach consists of decomposing each instantaneous variable into a mean and a fluctuating part, e.g. $u = \overline{u} + u'$, where an overbar denotes a mean and a prime a fluctuation, and then averaging in time (appropriate here because the mean fields are steady). This yields the following forms of the boundary layer equations:

$$\frac{\partial \overline{u}}{\partial x} + \frac{\partial \overline{v}}{\partial y} = 0 \tag{2.2.6}$$

$$\rho\left(\overline{u}\,\frac{\partial \overline{u}}{\partial x} + \overline{v}\,\frac{\partial \overline{u}}{\partial y}\right) = \frac{\partial}{\partial y}\left(\tau_{yx}^{tot}\right) \tag{2.2.7}$$

$$\text{with} \;\; \tau_{yx}^{tot} = \mu\,\frac{\partial \overline{u}}{\partial y} - \rho\,\overline{u'v'} \tag{2.2.8}$$

$$\rho c_p\left(\overline{u}\,\frac{\partial \overline{T}}{\partial x} + \overline{v}\,\frac{\partial \overline{T}}{\partial y}\right) = -\,\frac{\partial}{\partial y}\left(q_y^{tot}\right) \tag{2.2.9}$$

$$\text{with} \;\; q_y^{tot} = -\,k\,\frac{\partial \overline{T}}{\partial y} - \rho c_p\,\overline{v'T'} \tag{2.2.10}$$

Under the eddy–diffusivity assumption, the shear stress τ_{yx} can be written as

$$\tau_{yx}^{tot} \;=\; \rho\,(\nu + \nu_t)\,\frac{\partial \overline{u}}{\partial y} \tag{2.2.11}$$

where ν is the kinematic viscosity and ν_t the eddy viscosity for momentum, with the turbulent contribution

$$-\rho\,\overline{u'v'} \;=\; \rho\,\nu_t\,\frac{\partial \overline{u}}{\partial y} \tag{2.2.12}$$

Analogously, the heat flux q_y^{tot} is modeled as

$$q_y^{tot} \;=\; -\,\rho c_p\left(\frac{\nu}{Pr} + \frac{\nu_t}{Pr_t}\right)\,\frac{\partial \overline{T}}{\partial y} \tag{2.2.13}$$

where Pr_t is the turbulent Prandtl number. The turbulent component of the wall–normal heat flux is then

$$-\,\rho c_p\,\overline{v'T'} \;=\; -\,\rho c_p\,\frac{\nu_t}{Pr_t}\,\frac{\partial \overline{T}}{\partial y} \tag{2.2.14}$$

Dimensionless velocity profile

According to Prandtl's mixing–length theory, the turbulent component of the shear stress (see Eq. 2.2.12) can be expressed in terms of a mixing length l_m. This approach is analogous to kinetic–gas theory, where the mixing length plays a role similar to the mean free path [42]:

$$-\rho\,\overline{u'v'} \;=\; \rho\, l_m^2 \left|\frac{\partial \overline{u}}{\partial y}\right| \frac{\partial \overline{u}}{\partial y} \tag{2.2.15}$$

Consequently, combining Eq. 2.2.12 and Eq. 2.2.15, the eddy viscosity takes the form

$$\nu_t \;=\; l_m^2 \left|\frac{\partial \overline{u}}{\partial y}\right|. \tag{2.2.16}$$

Measurements show that, near the wall ($y/\delta \leq 0.2$), the mixing length can be approximated by the linear law with von Kármán constant[5] $\kappa \approx 0.41$:

$$l_m \;=\; \kappa\, y \tag{2.2.17}$$

The analytical description of the velocity profile is established in the inner region of the turbulent boundary layer, $y/\delta \leq 0.2$, where the convective term is negligible[6] [39]. Consequently, from Eq. 2.2.7 the shear stress τ_{yx}^{tot} is uniform and equal to τ_w along the y-direction sufficiently close to the wall. Hence, from Eq. 2.2.8 we write

$$\tau_w \;=\; \tau_{yx}^{tot} \;=\; \rho\,(\nu + \nu_t)\,\frac{\partial \overline{u}}{\partial y} \tag{2.2.18}$$

A dimensional analysis shows that only two dimensionless groups arise, based on the friction velocity $u_\tau = \left(\tau_w/\rho\right)^{1/2}$:

$$y^+ = \frac{y\,u_\tau}{\nu} \tag{2.2.19}$$

$$u^+ = \frac{\overline{u}}{u_\tau} \tag{2.2.20}$$

The velocity profile can be determined by integrating Eq. 2.2.18. Moreover, depending on the position within the inner layer, additional simplifications apply. Three regions are identified (see Fig. 2.7):

- **Viscous (linear) sublayer** ($y^+ \lesssim 7$): the eddy size l_m is very small and the turbulent contribution to the shear stress is negligible compared with the viscous one

---

[5] This approximation is not accurate very near the wall, i.e. for $y^+ \lesssim 30$

[6] Near the wall ($y/\delta \leq 0.2$), the mean velocities are sufficiently small that the convective term in Eq. 2.2.7 can be neglected.

($\nu_t \ll \nu$). From Eq. 2.2.18,

$$\overline{u} = \frac{\tau_w}{\rho}\int_0^y \frac{dy}{\nu} = \frac{u_\tau^2\, y}{\nu}$$
$$u^+ = y^+ \tag{2.2.21}$$

- **Inertial (Log–law) sublayer** ($y^+ \gtrsim 30$): l_m is larger and the turbulent contribution dominates ($\nu_t \gg \nu$). Using the mixing–length form Eq. 2.2.16 in Eq. 2.2.18 and $l_m = \kappa y$,

$$\overline{u} = \sqrt{\frac{\tau_w}{\rho}}\int_0^y \frac{dy}{l_m} = \frac{u_\tau}{\kappa}\ln(y) + \text{constant}$$
$$u^+ = \frac{1}{\kappa}\ln(y^+) + B, \tag{2.2.22}$$

  with experimental data giving $B \approx 5.5$.

- **Buffer layer** ($7 \lesssim y^+ \lesssim 30$): transition region between the linear sublayer and the log–law region.

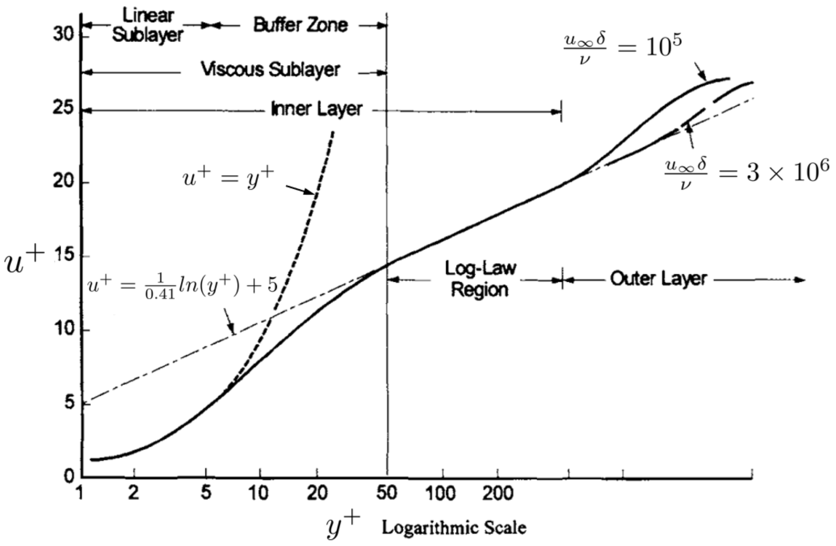

Figure 2.7: Different regions in a turbulent boundary layer over a flat plate, adapted from [54].

In the outer part of the turbulent boundary layer ($y/\delta > 0.2$), turbulent mixing is the dominant transport mechanism. The gradients are weak and do not directly set the wall transport. Nevertheless, this region contributes to the momentum balance within the boundary layer and governs how τ_w and δ vary along the wall.

Dimensionless temperature profile

The thermal boundary layer has universal properties when it is contained within the dynamic boundary layer, which is the case for $Pr > 0.5$ [42]. In this case, the Reynolds analogy used in most CFD codes assumes a similar structure between the thermal and dynamic boundary layers with an inner and an outer region. The inner region contains a linear sublayer governed by heat conduction and a logarithmic layer where turbulent mixing is the dominant mode of heat transport. With a Prandtl number Pr close to unity, the mean temperature and velocity profiles overlap; if $Pr > 1$, the thermal linear sublayer becomes thinner. Following the Reynolds analogy and assuming Pr close to unity for the discussion below, a dimensionless temperature is defined as

$$T^+ = \frac{T_w - \overline{T}}{q_w/(\rho C_p u_\tau)} \tag{2.2.23}$$

As for the dynamic boundary layer, in the inner thermal sublayer ($y/\delta < 0.2$), the convective term in Eq. 2.2.9 can be neglected. Thus, the heat flux across the inner thermal sublayer is taken as uniform and equal to the wall heat flux:

$$q_w \;=\; q_y^{tot} \;=\; -\,\rho C_p \left(\frac{\nu}{Pr} + \frac{\nu_t}{Pr_t} \right) \frac{\partial \overline{T}}{\partial y} \tag{2.2.24}$$

The turbulent Prandtl number Pr_t varies with position in the boundary layer; it depends on Pr and also on the flow field. The Reynolds analogy, commonly used in CFD, assumes similar thermal and momentum turbulent diffusivity and thus takes Pr_t as approximately constant and close to unity [51]. Given the similar structures of the thermal and dynamic boundary layers, it is natural to express the dimensionless temperature T^+ as a function of y^+ (see Eq. 2.2.19). Three regions are identified in the thermal boundary layer:

- **Thermal linear sublayer** ($y^+ \lesssim 7$) [39]

$$\begin{aligned} T_w - \overline{T} &= \frac{q_w}{\rho C_p} \frac{Pr}{\nu} \int_0^y dy = \frac{q_w}{\rho C_p} \frac{Pr\, y}{\nu} \\ T^+ &= Pr\, y^+ \end{aligned} \tag{2.2.25}$$

- **Thermal Log-law sublayer** ($y^+ \gtrsim 30$)

$$\begin{aligned} T_w - \overline{T} &= \frac{q_w}{\rho C_p}\, Pr_t \int_0^y \frac{dy}{\nu_t} \\ T^+ &= \frac{Pr_t}{\kappa}\, \ln(y^+) + A(Pr) \end{aligned} \tag{2.2.26}$$

  or, using the P–function representation:

$$T^+ = Pr_t\Big(\frac{1}{\kappa}\, \ln(y^+) + B + P(Pr)\Big) \tag{2.2.27}$$

$$T^+ = Pr_t\big(u^+ + P(Pr)\big) \tag{2.2.28}$$

- **Thermal buffer layer** ($7 \lesssim y^+ \lesssim 30$): the transition region between the thermal linear sublayer and the thermal log layer.

The relation above holds if the velocity log layer overlaps the temperature log layer, which implies a Prandtl number not too far from unity. The P–function, $P(\mathrm{Pr})$, can be viewed as an additional resistance accounting for Prandtl number effects. Various resistance functions exist in the literature. For example, Kader [55] proposed the following analytically derived formulation:

$$P \;=\; \big(3.85\,\mathrm{Pr}^{1/3} - 1.3\big)^2 \;+\; 2.12\,\ln(\mathrm{Pr}) \tag{2.2.29}$$

Another P–function widely used in CFD codes is that of Jayatilleke [56], derived from a fit to experimental data and typically used with $Pr_t \approx 0.9$:

$$P \;=\; 9.24\left[\left(\frac{Pr}{Pr_t}\right)^{0.75} - 1\right]\left[1 + 0.28\,\exp\!\left(-0.007\,\frac{Pr}{Pr_t}\right)\right]. \tag{2.2.30}$$

An example of a dimensionless temperature profile for air reported by [57] is shown in Fig. 2.8. A fit to experimental results gives $\mathrm{Pr}_t = 0.85$, $\mathrm{Pr} = 0.7$, and $A(\mathrm{Pr}) = 3.9$. q_w is governed primarily by heat transfer in the sublayer, where the Prandtl number plays a key role. For Prandtl numbers far from unity, the foregoing approach with a traditional P-formulations, such as Kader's (Eq. 2.2.29), can lead to large errors in predicting the temperature profile [58].

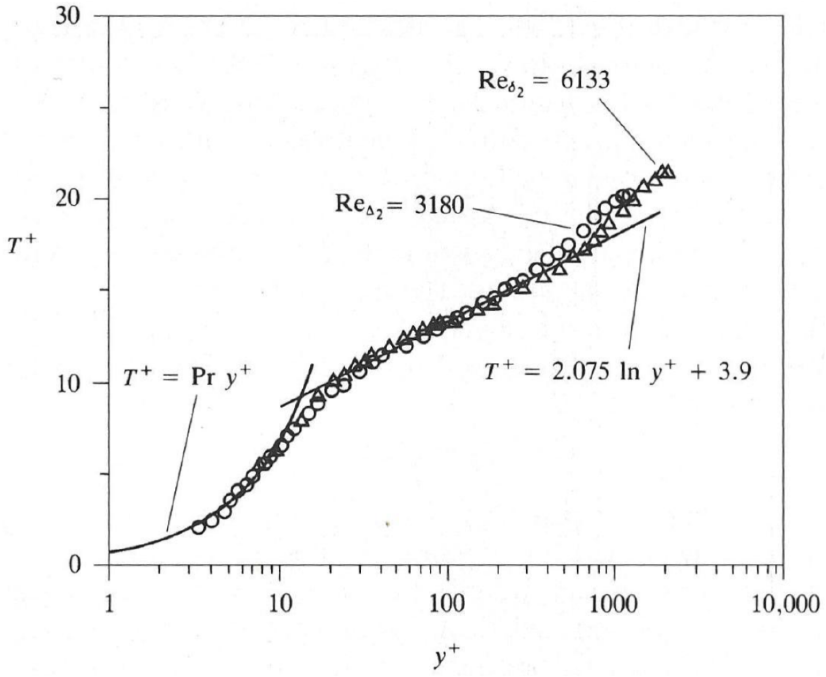

Figure 2.8: Example of thermal wall law for air [57]

2.2.2.2 Numerical implementation of the wall functions

Wall functions replace the linear finite–volume approximation (see section 2.2.1) with a non–linear relation based on the law of the wall, that links u_1 to τ_w. Similarly, for near–wall heat transfer, a wall function provides a non–linear relation linking the first–cell temperature T_1 to the wall heat flux q_w.

The most commonly used wall–function approach is the "standard wall function", proposed by Launder and Spalding [59]. The model uses the universal, dimensionless, two-layer velocity profile provided by the law of the wall (see section 2.2.2.1): a linear profile up to the transition distance $y^+ < y^+_{\text{trans},u}$, followed by a logarithmic profile for $y^+_{\text{trans},u} < y^+ < 200$. The transition distance $y^+_{\text{trans},u}$ is obtained from the intersection of the linear and logarithmic profiles and is taken to be approximately 11. Originally, the wall function assumed that the near-wall cell center falls in the log region, using only the logarithmic part of the velocity profile; however, in many CFD codes (e.g., [47]), the two-layer approach is preferred. For the standard wall function, τ_w is computed from the first off–wall cell values u_1 and y_1 using the relations below, derived from Eq. 2.2.21 and Eq. 2.2.22 and the definition

$u_\tau = \sqrt{\tau_w/\rho}$:

$$\tau_w = \begin{cases} \mu \, \dfrac{u_1}{y_1} & \text{if } y_1^+ \leq y^+_{trans,u} \\ \dfrac{\rho \, u_1 \, u_\tau}{\dfrac{1}{\kappa} \ln(y_1^+) + B} & \text{if } y_1^+ \geq y^+_{trans,u} \end{cases} \tag{2.2.31}$$

with $y_1^+ = \dfrac{u_\tau \, y_1}{\nu}$ (see Eq. 2.2.19). From the thermal wall–law relations (see Eq. 2.2.25 and Eq. 2.2.28), an analogous expression is used for q_w:

$$q_w = \begin{cases} \dfrac{\mu \, c_p \, (T_w - T_1)}{Pr \, y_1} & \text{if } y_1^+ \leq y^+_{trans,T} \\ \dfrac{\rho \, c_p \, u_\tau \, (T_w - T_1)}{Pr_t \left(\dfrac{1}{\kappa} \ln(y_1^+) + B + P(Pr) \right)} & \text{if } y_1^+ \geq y^+_{trans,T}. \end{cases} \tag{2.2.32}$$

Here $y^+_{trans,T}$ depends on Pr and is obtained from the intersection of the linear and logarithmic temperature profiles. The forms in Eq. 2.2.31 and Eq. 2.2.32 follow directly because τ_w and q_w are used in the scalings to nondimensionalize the velocity and temperature profiles. Note that y_1^+ depends on τ_w through u_τ, therefore, τ_w must be obtained iteratively.

To obtain a smooth transition of the profile between the two layers, in the buffer layer, and thus improve the wall–flux prediction if the near–wall point falls in this zone, it is classical to use a blending function. For instance, the function proposed by Kader (1981) [55] for the temperature wall function has the following form:

$$T^+ = Pr \, y^+ \, e^{-\Gamma} + Pr_t \left(\frac{1}{\kappa} \ln(y^+) + B + P \right) e^{-1/\Gamma} \tag{2.2.33}$$

with Pr_t set to a value near unity, and with Γ defined as a function of Pr and y^+:

$$\Gamma(Pr, y^+) = 10^{-3} \, \frac{(Pr \, y^+)^4}{1 + 5 \, Pr^3 \, y^+}. \tag{2.2.34}$$

Two numerical strategies can be used to inject wall function information into the main flow solution:

- The newly calculated τ_w from the wall function is provided to the CFD solver, and the near–wall velocity u_1 is calculated by the solver.
- A second approach is to compute τ_w with the linear approximation in Eq. 2.2.2 but replaces the molecular viscosity by an effective value μ_w. If the first off-wall node

lies in the logarithmic sublayer, $\mu_w = \mu \frac{u_1^+}{y_1^+}$, so that Eq. 2.2.2 reproduces the target τ_w given by Eq. 2.2.31 [51]. If the first node lies in the linear sublayer, $\mu_w = \mu$.

- Finally, one can introduce a source term directly into the transport equation of the variable considered [51].

To be more consistent with the finite–volume approach, turbulent quantities can be computed from the dimensionless profiles as cell–average quantities across the cell height, rather than as point values at the cell center. This strategy is, for example, used in the well–known wall functions of Launder and Spalding [59].

2.2.2.3 Wall functions with high–Prandtl–number fluids

Wall heat transfer modeling for high Pr fluids within the RANS framework has been found to be challenging, even without accounting for temperature dependent properties. As the thermal linear sublayer becomes thinner with increasing Pr, wall integration approaches using LRN turbulence models (without wall functions) require very fine near-wall cells and become less practical. Consequently, the wall function method, used together with either LRN or HRN turbulence models, becomes necessary.

Wall functions for high Pr (or high Sc) fluids have received little attention. For $Pr \gtrsim 100$, only a limited number of studies are available, notably those by Suga et al. [60, 61] and, more recently, by Saric et al. [53, 62]. The latter authors show that classical wall functions suffer from mesh dependence and a lack of accuracy at high Pr. Part of the discrepancy stems from deficiencies in the P-function (e.g., Kader's, see Eq. 2.2.29, and Jayatilleke's, see Eq. 2.2.30), together with the common assumption of a uniform turbulent Prandtl number Pr_t near the wall [58]. A further source of error arises from blending functions (e.g., Kader's, see Eq. 2.2.33), which may behaves poorly in the buffer layer and deteriorates as Pr increases [52, 53].

Irrenfried and Steiner [58] proposed an improved P-function, applicable for all y^+ and eliminating the need for a blending function. Their formulation was derived from DNS of a turbulent heated pipe flow with Pr up to 20 at $Re = 5300$ (based on pipe diameter). Saric and Basara [62] noted that the Irrenfried–Steiner formulation requires numerical integration to evaluate P in each near-wall cell, which is not appealing for industrial application in CFD. They therefore introduced a simple two-layer model, the Prandtl Thermal-Layer (PRTL) model, without a blending function. As in [58], the proposed $T^+(y^+)$ profile implicitly takes into account a near-wall non-uniform Pr_t at high Pr:

- For $y^+ \leq 40$:

$$T^+(y^+) \;=\; \frac{2}{\sqrt{4c\big(\mathrm{Pr}^{-1}+a\big)-b^2}}\,\arctan\left(\frac{2c\,y^+ + b}{\sqrt{4c\big(\mathrm{Pr}^{-1}+a\big)-b^2}}\right)\Bigg|_0^{y^+} \tag{2.2.35}$$

- For $y^+ \geq 40$:

$$T^+ \;=\; Pr_t\,\big(u^+ + f_{TL}\,P\big) \tag{2.2.36}$$

where P is Jayatilleke's P-function (see Eq. 2.2.30), and the coefficients a, b, c, and f_{TL} are specified for different Pr ranges in [62]. The PRTL model is applicable across a wide range of Prandtl numbers ($1 < Pr < 2900$) [62].

Fig. 2.9 presents an a priori assessment of the dimensionless temperature profile $T^+(y^+)$ obtained from the two-layer PRTL model (Eq. 2.2.35 and Eq. 2.2.36) against DNS data for channel flow from [63]. In this a priori test, DNS information is directly injected into Eq. 2.2.36 to compute the model profile $T^+(y^+)$. The resulting profile shows clear added value at high Pr (up to 500) compared with the classical approach (Jayatilleke's P-function with Kader's blending), yielding a closer fit to the DNS data.

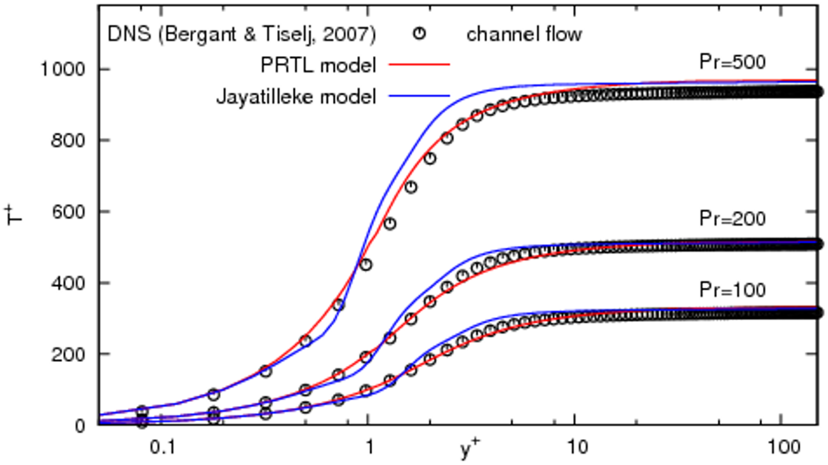

Figure 2.9: From [62]. A priori evaluation of PRTL against the DNS data from [63] and the classical Jayatilleke approach.

Finally, applying the PRTL model to heated pipe flow at $Re = 5\,000$–$20\,000$ (based on diameter), [62] reported improved wall heat-flux predictions up to $Pr = 200$, together with a substantially reduced mesh dependence.

2.2.2.4 Discussion on wall functions applicability for laminar situations

Regarding laminar flow, as seen in section 2.1, the thermal boundary layer becomes significantly thinner than the dynamic boundary layer at high Pr. This leads to a two scale simulation problem, similar to turbulent boundary layer simulations. A wall function like approach, using a universal, dimensionless temperature profile to bridge the region between the wall and the first off–wall cell center, therefore seems appealing. For modeling purposes, some hypotheses used to build the "laws of the wall", as well as the numerical implementation strategies detailed in section 2.2.2.2, should be considered.

The turbulent "law of the wall" is not directly usable in a laminar context for the following reasons:

- Its temperature profile relies critically on turbulent (eddy) diffusivity in the logarithmic region, which shapes the profile and is absent in laminar flow.
- These wall laws are typically derived for fully developed turbulent boundary layers; in such configurations, the thermal boundary layer penetrates into a region where the molecular thermal diffusion contribution to the heat flux, $-k\,\frac{\partial \overline{T}}{\partial y}$, becomes negligible compared to the turbulent contribution, $-\rho c_p\,\overline{v'T'}$ (see Eq. 2.2.10). Hence, these relations cannot be extrapolated to laminar regimes: the eddy diffusivity impacts the temperature field even at very high Pr. The DNS database with high Pr fluid used by [62] (originally from [63]) illustrates this point: a symmetric channel with periodic inlet–outlet conditions enforces both hydrodynamically and thermally developed flow [63].
- Finally, the assumption of a negligible convective term across the inner turbulent boundary layer in Eq. 2.2.24 (for $y/\delta < 0.2$), used to build the temperature wall law, implies that q_y^{tot} is uniform across the inner turbulent boundary layer. This, in turn, constrains the mesh choice: the near-wall cell must lie where q_y^{tot} is uniform. This is not suitable for our high Pr laminar application, since q_y is not expected to be uniform across the thermal boundary layer[7] and thus the near-wall cell may lie in a region of non-uniform q_y.

---

[7] q_y is not uniform across the thermal boundary layer, as shown by the nonlinear Lévêque temperature profile in Fig. 2.4.

2.2.3 Sub-grid scale model approach

An appealing and simple sub–resolution correction method for thin scalar boundary layers is the sub–grid–scale (SGS) model introduced by Bothe, Kröger and Warnecke in [64]. It relies on a dimensionless near-wall profile, similar to wall functions, but adapted to laminar flows with slip boundaries (e.g., no–shear liquid–gas interfaces). The model has been used in [65, 66, 67, 68] to investigate thin mass boundary layers around bubbles, including cases with high Sc ($10^1 < Sc < 10^7$) and high Péclet (Pe) numbers ($10^2 < Pe < 10^4$). It was recently extended to bilateral concentration boundary layers [69]. At high Pe, tangential advection dominates over wall–normal advection, so the scalar boundary layer becomes much thinner than the chosen characteristic length (for instance the bubble diameter). The Pe number is an appropriate metric to treat scalar boundary layer along slip interfaces such as for gas bubbles inside a liquid. It is defined as $Pe = Re\,Sc$ for species (mass) transfer and $Pe = Re\,Pr$ for heat transfer. In bubble flows with a slip interface, the liquid viscosity has a reduced impact on the near–interface shear, and the scalar boundary layer thickness is therefore primarily governed by Pe rather than by Re and Sc (or Pr) separately [39, 67].

To determine a universal dimensionless profile, consider the scalar transport equation in a simplified 2D setting:

$$\frac{\partial c}{\partial t} = -\left(u\,\frac{\partial c}{\partial x} + v\,\frac{\partial c}{\partial y}\right) + \alpha_c\left(\frac{\partial^2 c}{\partial x^2} + \frac{\partial^2 c}{\partial y^2}\right) \tag{2.2.37}$$

where x is the direction tangential (parallel) and y the direction normal (perpendicular) to the interface; c is the concentration, α_c is the mass diffusivity of the considered species. The concentration boundary layer equation follows from Eq. 2.2.37 under the standard boundary layer assumptions detailed in section 2.1. The resulting form mirrors the laminar thermal boundary layer energy equation Eq. 2.1.9 upon replacing $T \to c$ and $\alpha \equiv k/(\rho c_p) \to \alpha_c$. Moreover, for a slip boundary and a high Péclet numbers ($Pe \gg 1$), tangential advection dominates over wall–normal advection. In that limit, Eq. 2.2.37 simplifies to

$$u\,\frac{\partial c}{\partial x} \;=\; \alpha_c\,\frac{\partial^2 c}{\partial y^2} \tag{2.2.38}$$

Unlike turbulent wall functions, the tangential (parallel) advection of the scalar is retained and not neglected. Moreover, given the high Pe, the scalar boundary layer is assumed not to extend far into the bulk flow. Consequently, for a slip interface (no shear), the tangential velocity u must be taken uniform across the scalar boundary layer. The dimensionless solution of Eq. 2.2.38 then reads

$$\frac{c - c_w}{c_\infty - c_w} = \operatorname{erf}\left(\frac{y}{\delta_c(x)}\right) \tag{2.2.39}$$

with the concentration boundary layer thickness

$$\delta_c(x) = \sqrt{\frac{4\,\alpha_c\,x}{u}} \tag{2.2.40}$$

where c_w and c_∞ denote, respectively, the concentration at the interface and in the bulk flow.

The model must provide the wall mass flux q_{w_c}. Unlike turbulent wall functions, where q_w directly scales the profile and can be obtained analytically (see Eq. 2.2.32), here q_{w_c} must be derived from the gradient of the profile $c(y)$ using the relation

$$q_{w_c} = \alpha_c \left.\frac{\partial c}{\partial y}\right|_{y=0} \tag{2.2.41}$$

To evaluate Eq. 2.2.41 from $c(y)$, the profile parameter δ_c must be determined beforehand to get $c(y)$ from Eq. 2.2.39 (with c_w and c_∞ known). As the model is applied locally, x isn't known to deduce δ_c from Eq. 2.2.40, but δ_c can be determined from the near–wall cell concentration c_1. Following the finite–volume philosophy, a strategy already mentioned in wall function implementation (see section 2.2.2.2) treats c_1 as a cell–average across the cell height rather than as a point value [67]. Let y_1 be the half-height of the first off–wall cell, c_1 is then expected to follow the relation

$$c_1 = \frac{1}{2y_1}\int_0^{2y_1} c(y)\,dy = \frac{1}{2y_1}\int_0^{2y_1}\left[(c_\infty - c_w)\operatorname{erf}\left(\frac{y}{\delta_c}\right) + c_w\right] dy \tag{2.2.42}$$

δ_c is then identified to make the profile $c(y)$ accommodate the integral quantity c_1. Once δ_c is known, the wall scalar flux $q_{w,c}$ can be obtained from Eq. 2.2.41 and Eq. 2.2.39 as:

$$q_{w,c} = \alpha_c\,(c_\infty - c_w)\left.\frac{\partial \operatorname{erf}\left(\frac{y}{\delta_c}\right)}{\partial y}\right|_{y=0} = \alpha_c\,(c_\infty - c_w)\,\frac{2}{\sqrt{\pi}\,\delta_c}. \tag{2.2.43}$$

This SGS approach mirrors wall–function ideas while remaining computationally inexpensive and easy to implement, making it an appealing template for modeling thin scalar boundary layers in a laminar context. However, its applicability is limited to scalar transfer at slip walls.

2.2.4 Integrated quantity solving approach

A different modeling strategy was proposed by Hansen and Shadden in [70] for near-wall mass transport in cardiovascular flows. By integrating the scalar transport equation across the concentration boundary layer thickness, a surface transport equation for an integral quantity is solved along the interface. Similar approaches are used for concentration or temperature diffusion in bubble flow contexts, where the mass or energy contained in the scalar boundary layer is tracked along the bubble interface [71, 70, 68].

This approach separates the resolution of the bulk flow from that of the near-wall region. It therefore requires solving an additional transport equation along the surface and is applicable only for thin scalar boundary layers [70]. In [70], ϕ, the integral amount of scalar stored in the boundary layer, is defined assuming a flat wall. For simplicity, the surface is taken as a 1D wall aligned with the x direction:

$$\phi = \int_0^{\delta_c} c(y)\, dy \tag{2.2.44}$$

where δ_c is the concentration boundary layer thickness, y the wall-normal coordinate, and c the concentration. The governing advection–diffusion equation is recalled below from Eq. 2.2.37:

$$\frac{\partial c}{\partial t} = -\left(u\frac{\partial c}{\partial x} + v\frac{\partial c}{\partial y}\right) + \alpha_c\left(\frac{\partial^2 c}{\partial x^2} + \frac{\partial^2 c}{\partial y^2}\right) \tag{2.2.45}$$

with α_c the scalar diffusion coefficient. Integrating Eq. 2.2.45 across the boundary layer thickness yields the surface equation for the integral quantity:

$$\frac{\partial \phi}{\partial t} = -\frac{\partial}{\partial x}\left(\int_0^{\delta_c} c\, u\, dy\right) + \alpha_c\frac{\partial^2 \phi}{\partial x^2} + q_{w_c} \tag{2.2.46}$$

where the first and second terms on the right–hand side represent, respectively, advection and diffusion of the integral quantity along the surface, and q_{w_c} is the mass wall flux.

The Lévêque approximation [45] is adopted for the near-wall velocity field along the no-slip wall. For very large Schmidt numbers ($Sc \gg 1$), the scalar boundary layer is confined deep inside the dynamic boundary layer, so the shear stress can be taken uniform across the scalar layer, $\tau_{yx}(y) = \mu\,\frac{\partial u}{\partial y} = \tau_w$. Note that the same assumption underlies the inner part of the dynamic law of the wall $y/\delta \lesssim 0.2$ (see section 2.2.2.1). With uniform viscosity

μ and a laminar flow assumption, the velocity is therefore assumed linear across the scalar boundary layer, $u(y) = \dfrac{\tau_w}{\mu}\, y$. The advective term then simplifies to

$$\frac{\partial}{\partial x}\left(\int_0^{\delta_c} c\, u\, dy\right) = \frac{\partial}{\partial x}\left(\frac{\tau_w}{\mu}\int_0^{\delta_c} c\, y\, dy\right) \tag{2.2.47}$$

Similarly to wall functions and the SGS approach, information is extracted from the main 3D flow solution. Here, the wall shear stress τ_w is taken from the CFD solution and used in Eq. 2.2.46 via Eq. 2.2.47. As in wall functions/SGS, an auto-similar scalar profile (a "law of the wall") is assumed across the concentration boundary layer. This allows both the advective term in Eq. 2.2.47 and the wall flux term q_{w_c} to be expressed in terms of the integral quantity ϕ rather than the local firstly unknown field c. The parameters needed to reconstruct the field $c(x, y)$ along the interface from the dimensionless profile can be inferred from ϕ.

The resulting surface equation for ϕ is solved along the interface, yielding a map of the integral quantity and, at low cost, the associated wall flux map q_{w_c}. In this framework, the wall flux map q_{w_c} replaces the traditional finite volume method approximation (see section 2.2.1), which evaluates q_{w_c} using a linear approximation across the near-wall cell.

2.2.5 Radial sub-resolution approach

The laminar radial sub-resolution (LRS) method [72] was developed for heat transfer across bubble interfaces when the thermal boundary layer is thin or moderately thin relative to the bubble size. In this approach, the fields are numerically solved on a Cartesian mesh.

As in the integral-quantity approach, the LRS strategy separates the resolution of the bulk flow from that of the near-wall region: in addition to the main Eulerian coarse Cartesian mesh, LRS solves a one-dimensional advection–diffusion equation for temperature along discretized 1D segments normal to the interface. The coarse mesh temperature solution is used as boundary conditions at the tips of each segment. Source terms are added in the 1D equation to account for tangential effects, and the local interface curvature is incorporated into the one-dimensional formulation.

An interesting numerical feature of this approach is its ability to treat the system in a local coordinate frame perfectly aligned with the interface and with the main direction of variation. Consequently, the discretization is not influenced by the collinearity between the interface normal vectors and the Cartesian directions. The LRS approach has demonstrated better performance than the sub-grid-scale (SGS) model approach and the integral quantity solving approach for the configurations tested in [72]. However, this method appears more complex to develop.

2.2.6 Dual-grid approach

One class of methods relies on two distinct grids. In [73], the velocity field is solved on a coarse mesh and interpolated onto a finer, secondary grid dedicated to the temperature field. Thus, this dual-grid strategy captures the thin thermal boundary layer with only moderate additional cost. However, this method is less flexible and involves a high level of effort to set up.

2.3 Literature review conclusion

To fulfill the objectives of this PhD, outlined in section 1.5, we propose a solution informed by the state-of-the-art review: a near-wall model, denoted the thermal wall model (TWM). Two variants are proposed: TWM-cst, tailored for flows with negligible viscosity variation with temperature (constant properties), and TWM-var, an extension that accounts for strongly temperature-dependent viscosity.

The TWM follows the core philosophy of subgrid-scale (SGS) models (see section 2.2.3) and turbulent wall functions (see section 2.2.2), but is expressly tailored for laminar, high Prandtl number flows adjacent to no-slip walls and, concerning its extension, for fluids with strongly temperature-dependent viscosity. In the spirit of classical wall functions and SGS models, and for the sake of simplicity, the formulation relies on local near-wall variables and on the dimensionless temperature profile proposed by Lévêque (see section 2.1.2.3), tailored for high Prandtl number laminar flows. To the best of our knowledge, no comparable model has been reported in the literature.

Part II

Thermal wall model for fluids with constant viscosity

In this part, the thermal wall model (TWM-cst), tailored for fluids with weak viscosity variation, is described. The model is then assessed on a two-dimensional thermal boundary layer development case and on an academic impinging-jet configuration representative of the intended industrial application.

CHAPTER 3

Thermal wall model description and implementation

The thermal wall model, TWM, given a wall temperature T_w, should predict accurately the surface wall heat flux, q_w, while reducing the number of grid cells required within the thermal boundary layer. This chapter presents the foundation of the constant-viscosity variant of the model (TWM-cst) upon which the extension for variable viscosity (TWM-var) will subsequently be built and presented in Part III. It is first described mathematically, followed by a detailed discussion of its numerical implementation within the finite volume framework.

3.1 Mathematical Formulation

The development of both the thermal and dynamic boundary layer is considered in the classical configuration of laminar boundary layer flow over a flat plate maintained at a uniform T_w, in contact with a free-stream at temperature T_∞ (see Fig. 3.1). The flow is assumed to be steady, incompressible, and two-dimensional, with negligible pressure gradients, viscous dissipation, and property variations.

The thermal boundary layer, in the limit $\mathrm{Pr} \to \infty$ is much thinner than the dynamic boundary layer according to Eq. 2.1.24. Similarly to wall function practice (see section 2.2.2), it is assumed that the thermal boundary layer resides well inside the dynamic boundary layer, allowing us to drop the convective term in the boundary layer momentum equation[1] across and in the vicinity of δ_t. From Eq. 2.1.7, across and near δ_t this yields

$$\tau_w = \tau_{yx} = \mu \frac{\partial u}{\partial y} \tag{3.1.1}$$

which is analogous to the wall function treatment when using Eq. 2.2.18. From Eq. 3.1.1, an expression for u follows:

$$u(x, y) = \int_0^y \frac{\tau_w(x)}{\mu} dY \tag{3.1.2}$$

As the dynamic viscosity μ is assumed uniform, the thermal boundary layer develops in a region where the velocity profile depends linearly on y, i.e., $u(x, y) = \frac{\tau_w(x)}{\mu}\ y$ and $v(x, y) = -\frac{d\tau_w}{dx}\frac{y^2}{2\mu}$ (see Fig. 3.1). This asymptotic regime leads to Lévêque's theory [45] whose the solution for the auto-similar temperature profile across the thermal boundary layer is described in section 2.1.2.3. The Lévêque profile solution serves as the foundation for the development of the model targeting high Pr number fluids.

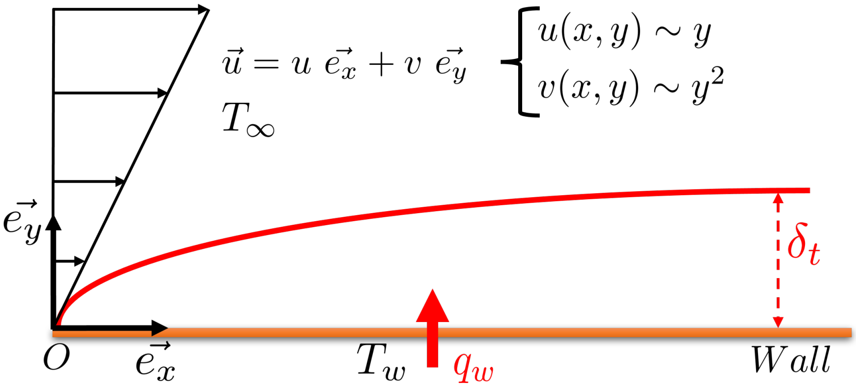

Figure 3.1: Thermal boundary layer development for a high Prandtl number fluid, in the classical configuration of laminar boundary layer flow over a flat plate maintained at a uniform wall temperature T_w, in contact with a uniform, wall-parallel free-stream at temperature T_∞.

For convenience and clarity in the subsequent model description and implementation, we adopt a scaling different from η_L: δ_t is used in place of g_L to nondimensionalize the

---

[1] The convective term in the boundary layer energy equation cannot be neglected, since convective and conductive effects are of comparable magnitude at a distance δ_t from the wall.

wall-normal distance y. We introduce the dimensionless distance from the wall y^* as

$$y^* = \frac{y}{\delta_t(x)} \tag{3.1.3}$$

From Eq. 2.1.32, plus the definition of η_L and y^* in Eq. 2.1.28 and Eq. 3.1.3, the linear relation between η_L and y^* is given by:

$$y^* \approx \frac{\eta_L}{1.404}. \tag{3.1.4}$$

The dimensionless temperature $\frac{T-T_w}{T_\infty - T_w}$ is denoted for convenience T^*[2]. The profile of T^* expressed as a function of y^* is written $T^* = P_T(y^*)$. It is deduced from Eq. 3.1.4 using the known solution of $T^* = \Theta_L(\eta_L)$ (see Fig. 2.4) and appears as the blue curve in Fig. 3.2. P_T is referred to as the Lévêque profile. It is worth noting that the profile P_T is independent of the wall shear stress τ_w.

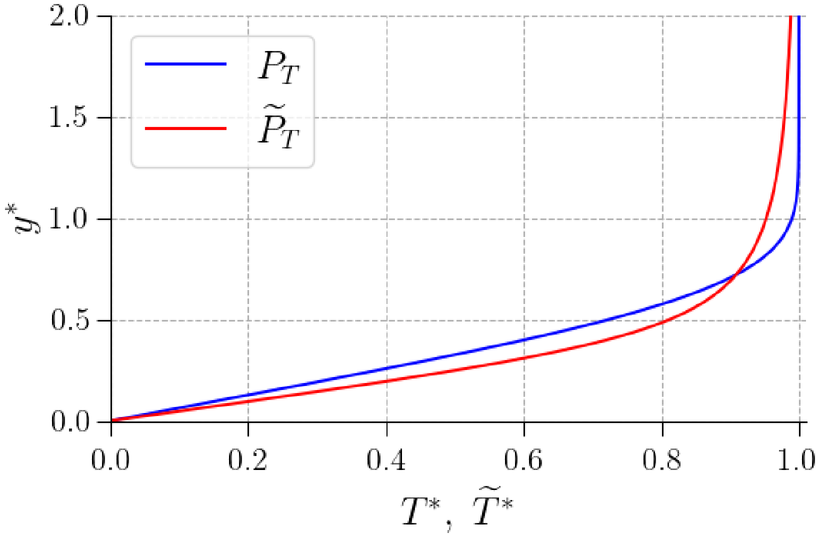

Figure 3.2: Comparison of P_T, the denoted Lévêque temperature profile across the thermal boundary layer, and $\widetilde{P}_T$ (introduced, along with $\widetilde{T}$, in section 3.2), the flow temperature profile derived from P_T (see Eq. 3.3.11).

The thermal wall model aims to calculate the surface wall heat flux $q_w(x)$. By applying Fourier's law together with the definition of y^* (see Eq. 3.1.3) and T^*, a relation between

---

[2] From the definition of δ_t in Eq. 2.1.11, δ_t can be also defined as the distance from the wall at which $T^* = 0.99$.

δ_t and q_w can be derived:

$$q_w = -k \left.\frac{\partial T^*}{\partial y^*}\right|_{(y^*=0)} \frac{(T_\infty - T_w)}{\delta_t} \tag{3.1.5}$$

Then, using the numerical approximation of the profile P_T near the wall, it rises:

$$q_w \approx 1.572 \; k \; \frac{(T_w - T_\infty)}{\delta_t} \tag{3.1.6}$$

The expression of q_w in Eq. 3.1.6, along with the Lévêque profile P_T, form the basis of the model.

The implementation of the model in a finite volume formulation context is detailed in the next section.

3.2 Numerical implementation

When using the thermal wall model, the user prescribes T_w as a Dirichlet boundary condition. The free-stream temperature T_∞ is assumed to be uniform outside the thermal boundary layer and is also prescribed by the user. The model then provides the associated surface wall heat flux q_w to the CFD solver for each near-wall cell using local information.

For the following we consider the near-wall cell, denoted $cell_1$. The proposed model can be expressed as a function f_1 of the relevant input parameters:

$$q_w = f_1 \left(T_1, T_w, T_\infty, y_1, k\right) \tag{3.2.1}$$

where T_1 represents the discretized temperature calculated at the near-wall cell center and y_1 is the distance from the wall to the center of the first cell. The location of these variables in the framework of a Cartesian mesh is illustrated in Fig. 3.3. In addition to the input parameters listed above, the function f_1 makes use of a dimensionless temperature profile that bridges the near-wall region. For this purpose, the Lévêque profile P_T is employed (see Fig. 3.2).

For the near-wall cell, $cell_1$, q_w can be assessed using the theoretical relation Eq. 3.1.6 provided that δ_t is known. Determining δ_t for $cell_1$ is equivalent to determining y_1^*, the dimensionless distance from the wall to the cell center, as they are related by Eq. 3.1.3. In theory, the value of y_1^* can be deduced from T_1^* using the Lévêque profile P_T (see Fig. 3.2). In practice, however, P_T cannot be directly applied due to a particularity of the finite

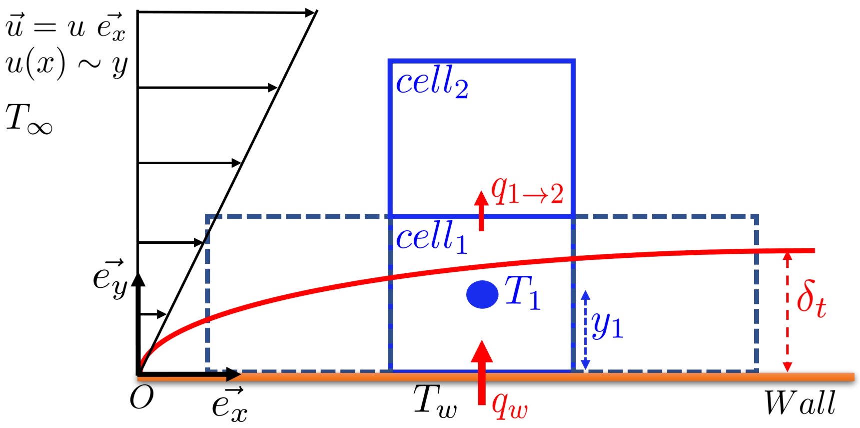

Figure 3.3: Illustration of a uniform Cartesian grid adjacent to a wall, highlighting the first off-wall control volume $cell_1$; the filled dot marks its centroid. The thermal boundary layer, shown in red, is illustrated for a coarse mesh relative to a thin thermal boundary layer.

volume formulation. To account for this, a modified profile, denoted as $\widetilde{P}_T$, is derived from P_T (see section 3.3). This adjusted profile is then used to determine y_1^* from T_1^* as follows:

$$y_1^* = \widetilde{P}_T^{-1}(T_1^*) \tag{3.2.2}$$

where $\widetilde{P}_T^{-1}$ represents the inverse function of $\widetilde{P}_T$. The dimensionless near-wall cell temperature, T_1^*, obtained from the CFD calculation, is computed using T_∞, T_w, and T_1 as follows[3]:

$$T_1^* = \frac{T_1 - T_w}{T_\infty - T_w} \tag{3.2.3}$$

All necessary implementation steps have been described so far and are summarized in Fig. 3.4. The equations stated in this section are collected in Tab. 3.1. Additional details regarding the calculation of $\widetilde{P}_T$ are provided in section 3.3.

---

[3] The usual dimensionless relation can be applied to T_1 in this finite volume context; the justification is given in section 3.3 (see, in particular, Eq. 3.3.8).

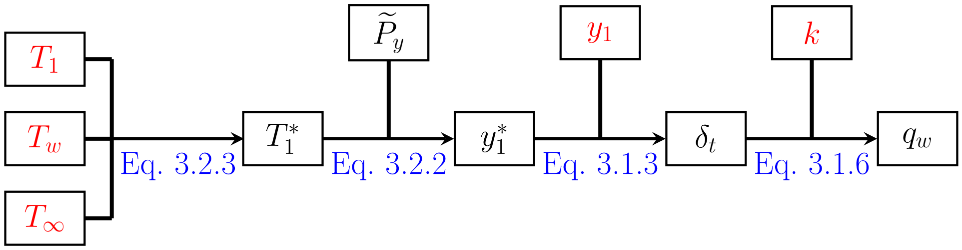

Figure 3.4: Overview of the steps involved in the thermal wall model. Input parameters are highlighted in red.

Reference	**Expression**
Dimensionless temperature	
Eq. 3.3.8	$\widetilde{T}^* = \dfrac{\widetilde{T} - T_w}{T_\infty - T_w}$
Dimensionless wall-normal coordinate	
Eq. 3.1.3	$y^* = \dfrac{y}{\delta_t(x)}$
Wall heat flux	
Eq. 3.1.6	$q_w \approx 1.572\, k\, \dfrac{T_w - T_\infty}{\delta_t}$

Table 3.1: Summary of the equations stated in section 3.2.

3.3 Effective Lévêque temperature profile in finite volumes method

In a finite volume approach, the computational domain is divided into control volumes (cells). The energy equation is integrated over each cell, leading to a discretized formulation that ensures integral energy conservation over any group of cells [46]. Consequently, in a steady-state configuration, T_1 should not be interpreted as the temperature at the cell center, but rather as a value that ensures the surface heat fluxes at the cell interfaces are consistent with energy conservation, particularly in cases with an under-resolved grid.

To properly define $\widetilde{P}_y$, we examine energy conservation within a control volume composed of a group of near-wall cells including $cell_1$. From a heat balance perspective, a row of near-wall cells, each of height $2y_1$, can be treated as a one-dimensional (1D) system. In this system, under the additional assumption of a velocity field parallel to the wall across the near-wall cells (aligned with the x-axis in our case, i.e., $v = 0$), the flow transports the thermal energy accumulated upstream.

The discretized advective heat flux Q_{a_1} along this 1D system at the $cell_1$ center position x_1, depicted in Fig. 3.5, can be approximated using local cell information and assuming uniform fluid properties as[4]:

$$Q_{a_1} = \dot{m}_1 c_p T_1 \tag{3.3.1}$$

where $\dot{m}_1$ is the discretized mass flow rate through the 1D system at the cell center x_1 and is given by

$$\dot{m}_1 = 2y_1 \rho u_1 \tag{3.3.2}$$

with u_1 denoting the velocity associated with $cell_1$[5]. The discrete approximation of Q_{a_1} should reproduce the exact advective heat flux through a section of height $2y_1$ at the same streamwise location x_1,

$$Q_a(x_1, y_1) = \int_0^{2y_1} \rho c_p u(Y) T(x_1, Y)\, dY \tag{3.3.3}$$

so that $Q_{a_1} = Q_a(x_1, y_1)$ when the discrete approximation is correct. Here, $u(y)$ and $T(x, y)$ represent the exact velocity and temperature distributions within the entire domain (see

---

[4] Throughout this section, Q_{a_1} and all other advective heat and mass fluxes discussed are expressed per meter of depth along the third spatial coordinate.

[5] As we aim to express the advective heat flux along the x-axis at the cell center position rather than at an interface between control volumes, T_1 and other variables associated with the $cell_1$ are directly used to approximate Q_{a_1}.

Tab. 3.2 for an overview of the key variables and their definitions). Specifically, $T(x_1, y)$ is the exact temperature profile at $x = x_1$, which is conceptually illustrated along with $u(y)$ in Fig. 3.5. Moreover, an accurately calculated advective mass flux $\dot{m}_1$ should correspond to the exact formulation:

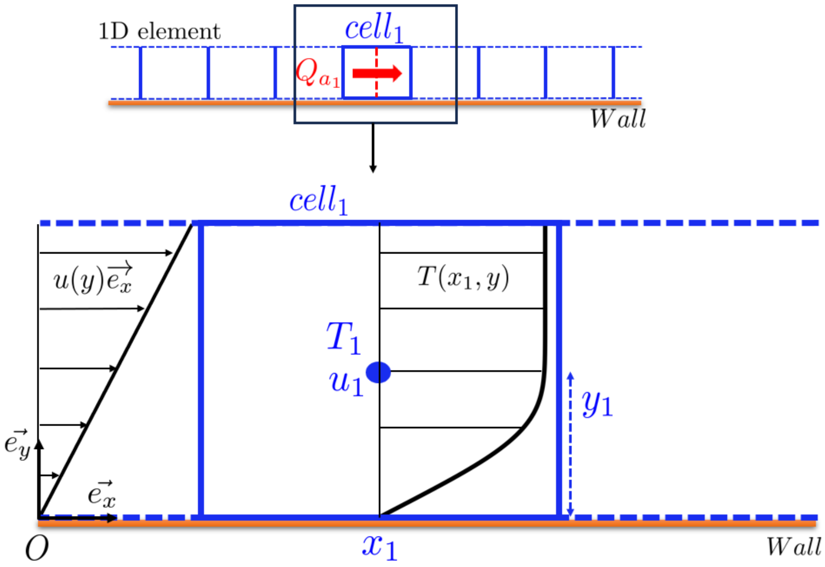

Figure 3.5: Discretized advective heat flux Q_{a_1} along the 1D system at $x = x_1$. It can be approximated using T_1 and u_1 from cell$_1$ (see Eq. 3.3.1), or computed exactly from the profiles $u(y)$ and $T(x_1, y)$ (see Eq. 3.3.3).

$$\dot{m}(x_1, y_1) = \int_0^{2y_1} \rho u(Y) \, dY \tag{3.3.4}$$

Combining Eq. 3.3.1 with the corresponding exact expressions for Q_{a_1} and $\dot{m}_1$ given in Eq. 3.3.3 and Eq. 3.3.4, one shows that T_1 must coincide with the flow temperature $\widetilde{T}(x_1, y_1)$, defined as

$$\widetilde{T}(x_1, y_1) = \frac{\int_0^{2y_1} \rho c_p u(Y) \; T(x_1, Y) \; dY}{c_p \int_0^{2y_1} \rho u(Y) \; dY} \tag{3.3.5}$$

Physically, $\widetilde{T}(x_1, y_1)$ at a given section x_1 of the 1D system represents the mean temperature weighted by the velocity profile along that section. As the fluid properties are assumed uniform, $\widetilde{T}(x_1, y_1)$ can be written as follows:

$$\widetilde{T}(x_1, y_1) = \frac{\int_0^{2y_1} u(Y) \; T(x_1, Y) \; dY}{\int_0^{2y_1} u(Y) \; dY} \tag{3.3.6}$$

A dimensionless flow temperature $\widetilde{T}^*(x_1, y_1)$ can be introduced by rewriting Eq. 3.3.6 in terms of the dimensionless temperature $T^*(x_1, y)$ instead of $T(x_1, y)$. This leads to the following expression:

$$\widetilde{T}^*(x_1, y_1) = \frac{\int_0^{2y_1} u(Y)\ T^*(x_1, Y)\ dY}{\int_0^{2y_1} u(Y)\ dY} \tag{3.3.7}$$

Substituting the definition $T^* = \dfrac{T - T_\infty}{T_w - T_\infty}$ into Eq. 3.3.7 and using Eq. 3.3.6 gives:

$$\widetilde{T}^* = \frac{\widetilde{T} - T_w}{T_\infty - T_w} \tag{3.3.8}$$

For convenience, the exact flow temperature $\widetilde{T}(x_1, y_1)$ is denoted as $\widetilde{T_1^e}$, while the exact temperature at the position (x_1, y_1), denoted as $T(x_1, y_1)$, is abbreviated as T_1^e (see Tab. 3.2).[6]

Since, in our context, the computed dimensionless temperature T_1^* is expected to match the flow temperature $\widetilde{T_1^e}^*$, a modified profile from Lévêque theory, denoted as $\widetilde{P}_T$, must be introduced so that the proper y_1^* is predicted from T_1^* (see Fig. 3.4). The profile $\widetilde{T}^* = \widetilde{P}_T(y^*)$ is derived from $T^* = P_T(y^*)$ in a similar manner to Eq. 3.3.7 after introducing the change of variable $y/\delta_t(x) \rightarrow y^*$, which yields:

$$\widetilde{P}_T(y^*) = \frac{\int_0^{2y^*} u(Y^*) P_T(Y^*)\, dY^*}{\int_0^{2y^*} u(Y^*)\, dY^*} \tag{3.3.9}$$

where $u(y^*)$ denotes the same physical field as $u(y)$, but expressed in terms of the coordinate y^* instead of y for notational convenience. Under the additional assumption of a linear velocity profile $u(y)$ across cell$_1$, it raises:

$$\widetilde{P}_T(y^*) = \frac{\int_0^{2y^*} Y^* P_T(Y^*)\, dY^*}{\int_0^{2y^*} Y^*\, dY^*} \tag{3.3.10}$$

$$= \frac{1}{2y^{*2}} \int_0^{2y^*} Y^* P_T(Y^*)\, dY^* \tag{3.3.11}$$

---

[6] It is worth noting that for sufficiently high n_{δ_t}, with $n_{\delta_t} = \frac{\delta_t(x_1)}{2y_1}$ the number of cells across $\delta_t(x_1)$ for an uniform mesh, both T_1^{e*} and $\widetilde{T_1^e}^*$ evolve as $\sim n_{\delta_t}^{-1}$ (or $\sim y_1$ for a given δ_t). Thus, the differences between the two temperatures become smaller as the near-wall cell becomes finer for a given δ_t. However, their ratio remains constant (see Appendix A for more details).

Fig. 3.2 compares the two profiles P_T and $\widetilde{P}_T$.

The accuracy of the model methodology is assessed in the next two sections.

Symbol	**Unit**	**Definition**
Uniform parameters		
k	$\mathrm{W \cdot m^{-1} \cdot K^{-1}}$	Thermal conductivity of the fluid.
T_w	K	Wall temperature.
T_∞	K	Temperature of the free-stream.
Continuous fields		
$\delta_t(x)$	m	Thickness of the thermal boundary layer
$q_w(x)$	$\mathrm{W \cdot m^{-2}}$	Surface wall heat flux.
$T(x, y)$	K	Exact local temperature.
$\widetilde{T}(x, y)$	K	Exact flow temperature calculated along a height $2y$ from the wall (see Eq. 3.3.6).
Discrete parameters		
$x_1,\ y_1$	m	Coordinates of the center of $cell_1$ (see Fig. 3.3).
T_1	K	Temperature of $cell_1$.
T_1^e	K	Shorthand for $T(x_1, y_1)$: exact temperature at the center of $cell_1$.
$\widetilde{T_1^e}$	K	Shorthand for $\widetilde{T}(x_1, y_1)$: exact flow temperature calculated along the $cell_1$ height.
Universal dimensionless profiles (see Fig. 3.2)		
$*$	–	Generic dimensionless indicator.
$P_T(y^*)$	–	Relation[7] between y^* and $T^*(x, y^*)$, valid $\forall x$; termed the Lévêque profile.
$\widetilde{P}_T(y^*)$	–	Relation between y^* and $\widetilde{T}^*(x, y^*)$, valid $\forall x$ (see Eq. 3.3.11).

Table 3.2: List of the main symbols, their units, and definitions.

---

[7] $T(x, y^*)$ denotes the same physical field as $T(x, y)$, but expressed in terms of the coordinate (x, y^*) instead of (x, y) for notational convenience.

CHAPTER 4

Verification of the thermal wall model under Lévêque conditions

This chapter presents the results of the evaluation of the TWM-cst on a simple configuration that satisfies all the model assumptions. Before assessing the model, the numerical setup is described, along with the need for mesh refinement to accurately capture q_w without model, particularly under the challenging conditions of a thin thermal boundary layer.

4.1 Numerical set-up

The configuration is designed to reproduce the steady-state development of the thermal boundary layer over a flat wall at infinite Prandtl numbers, i.e., to resolve the thermal boundary layer development within a velocity field that varies linearly with the wall-normal distance. As illustrated in Fig. 4.1, the numerical setup consists in a two-dimensional domain with a length of $L = 10^{-1}$ m and a height H of 10^{-3} m. The maximum thermal boundary layer thickness within the domain, occurring at the domain exit, is determined using Lévêque's analytical solution [45] and is found to be 0.75 mm. Since this value is smaller than the 1 mm domain height, the top boundary is sufficiently distant from the wall to ensure negligible interaction with the thermal boundary layer.

Velocity boundary conditions are applied such that a linear velocity profile with a slope of $\frac{\partial u}{\partial y} = \frac{\tau_w}{\mu} = 60$ s^{-1}, zero velocity at the wall (no-slip wall), and no vertical component

($v = 0$ m.s^{-1}) is maintained uniformly throughout the domain. At the inlet and bottom wall, Dirichlet boundary conditions are imposed for the temperature, while at the top and outlet boundaries, zero heat flux is applied.

To solve the boundary layer equation, only the following fluid properties are required[1]: density $\rho = 10^3$ kg.m^{-3}, specific heat capacity at constant pressure $c_p = 4.185\times10^3$ J.kg^{-1}.K^{-1}, and thermal conductivity $k = 4\times10^{-2}$ W.m^{-1}.K^{-1}. These values correspond to a thermal diffusivity $\alpha = 10^{-8}$ m^{2}s^{-1}.

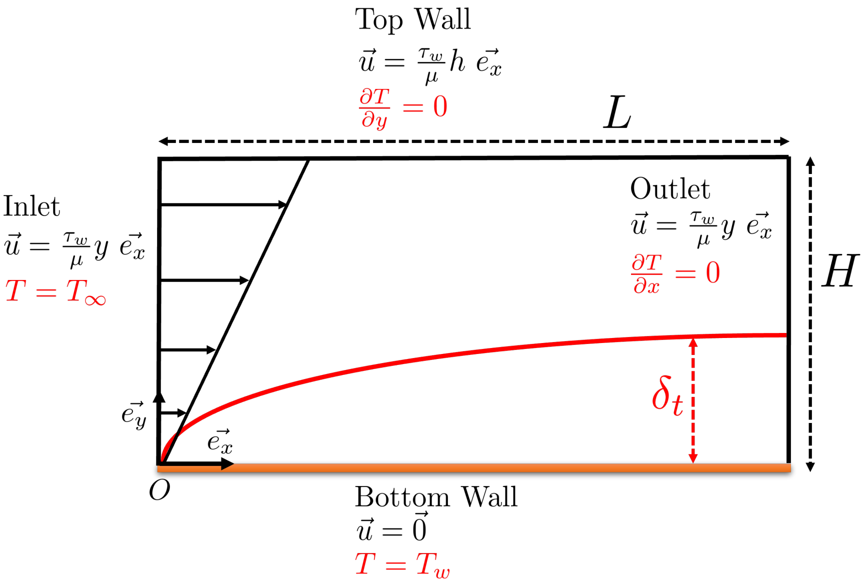

Figure 4.1: Geometry and boundary conditions of the computational domain.

The simulation aims to solve the steady-state thermal boundary layer development. Mass, momentum and energy equations are solved numerically using a finite volume method implemented in the CFD code CONVERGE [47]. The finite volume method is employed with a pressure-velocity coupling algorithm based on the PISO scheme. For pressure, momentum, and energy terms, a second-order upwind scheme is used. A transient semi-implicit solver is employed, with the maximum time step constrained by the Courant–Friedrichs–Lewy (CFL) number fixed at 0.75 and the Fourier number fixed at 5.

A Cartesian, uniform mesh is used. The most refined case, referred to as the wall-resolved reference mesh (WR), consists of an x-cell size of 5×10^{-5} m and a y-cell size of 1×10^{-5} m. This results in a total of 2000×100 cells. The thermal boundary layer exhibits a significantly higher gradient in the y-direction than in the x-direction, i.e., $\frac{\partial}{\partial x} \ll \frac{\partial}{\partial y}$,

---

[1] The viscosity value is not relevant here, since the steady-state velocity field is independent of μ.

except in the vicinity of the wall edge at the inlet. Consequently, the mesh is optimized by employing flattened cells, where the x-cell size is larger than the y-cell size, while maintaining a low enough aspect ratio to ensure numerical accuracy. Additionally, 3 coarser meshes along the y-axis, denoted A, B and C in Tab. 4.1, are considered. To keep the maximum aspect ratio below 5, the refinement in the x-direction is reduced but kept identical across all coarser meshes.

	Mesh A	**Mesh B**	**Mesh C**	**WR**
x-cell size	5×10^{-4} m	5×10^{-4} m	5×10^{-4} m	5×10^{-5} m
y-cell size	5×10^{-4} m	2×10^{-4} m	1×10^{-4} m	1×10^{-5} m
number of cells	400	1000	2000	200 000

Table 4.1: Meshes used to evaluate the impact of mesh refinement on q_w prediction at infinite Prandtl number.

To verify that the WR reference case is well resolved, it is compared to Lévêque's theoretical predictions by analyzing the evolution of the boundary layer thickness δ_t and the surface wall heat flux q_w along the wall, as shown in Fig. 4.2 and Fig. 4.3, respectively. The relative errors in δ_t and q_w, displayed on the right y-axis, are defined as follows: $\delta_t^{error} = \left|\frac{\delta_t - \delta_t^{theo}}{\delta_t^{theo}}\right|$ and $q_w^{error} = \left|\frac{q_w - q_w^{theo}}{q_w^{theo}}\right|$ where the subscript "*theo*" denotes the Lévêque theoretical solution.

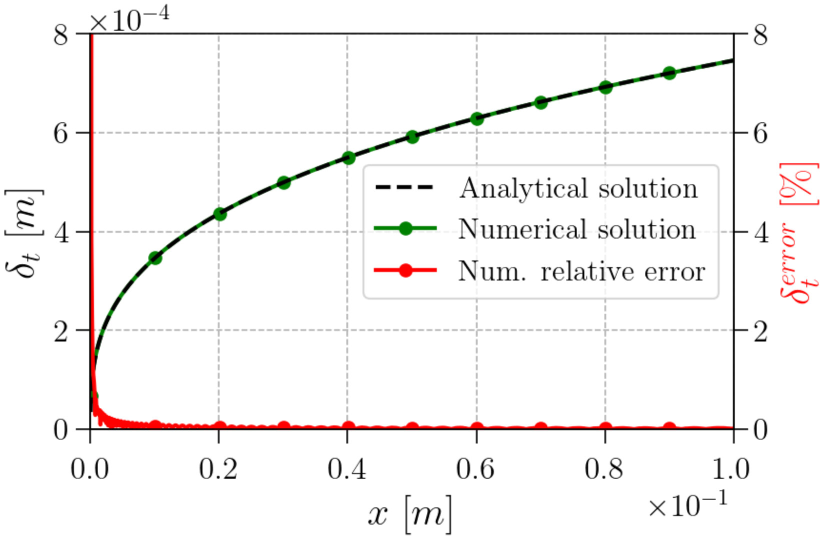

Figure 4.2: Numerical prediction of the thermal boundary layer thickness δ_t using the WR mesh, compared with the analytical Lévêque solution.

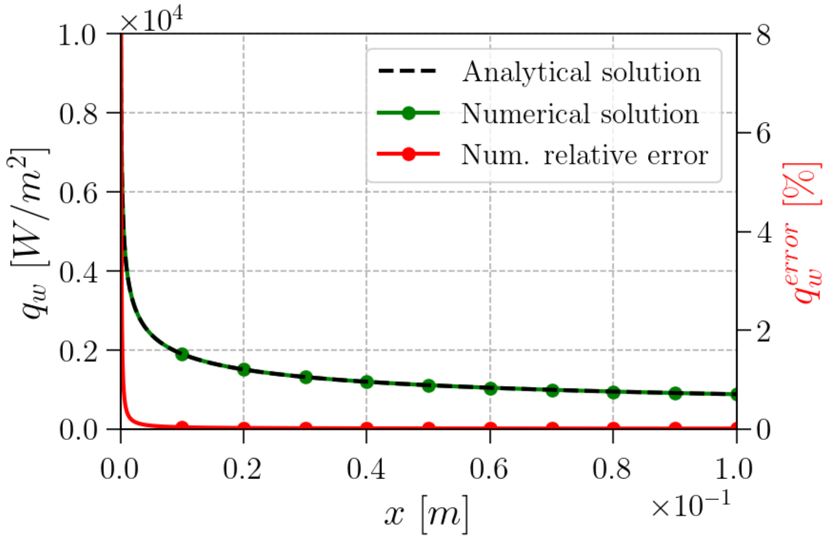

Figure 4.3: Numerical prediction of the surface wall heat flux q_w using the WR mesh, compared with the analytical Lévêque solution.

The comparison with the Lévêque analytical solution demonstrates good agreement, validating the numerical approach. It is important to note that the assumptions underlying the Lévêque solution, and more generally boundary layer theory, include the condition $\frac{\partial}{\partial y} \gg \frac{\partial}{\partial x}$. Thus, the range of x-positions where the analytical solution is applicable can be expressed as: $\frac{x}{\delta_t(x)} > 10$. In the present case, this criterion translates to $x > 2 \times 10^{-3}$ mm. Consequently, the first 40 near-wall cells immediately downstream of the inlet, which represent 2% of the plate length, cannot be directly compared with the Lévêque analytical solution.

4.2 Grid sensitivity analysis

The impact of coarser meshes on q_w prediction is now investigated to quantify the influence of the number of cells across the thermal boundary layer. For this purpose, the relative error in the wall heat flux, q_w^{error}, defined as:

$$q_w^{\text{error}} = \frac{q_w - q_w^{\text{ref}}}{q_w^{\text{ref}}} \tag{4.2.1}$$

is plotted in Fig. 4.4 as a function of the number of cells in the thermal boundary layer: $n_{\delta_t} = \frac{\delta_t}{2y_1}$[2]. Here, q_w^{ref} corresponds to the wall heat flux obtained from the wall-resolved reference simulation (WR). The results obtained with the three coarser meshes (Mesh A, B, and C) are presented in Fig. 4.4. For a given n_{δ_t}, the wall heat flux error q_w^{error} remains consistent across different coarse meshes, indicating that the accuracy of the wall heat flux computation is primarily determined by the number of cells within the thermal boundary layer. As expected, for low values of n_{δ_t} (less than 0.7), the prediction of q_w is poor, and it further degrades as n_{δ_t} is reduced (with an error of 75% for $n_{\delta_t} = 0.2$). This is due to the highly nonlinear temperature profile between the wall and the center of the near-wall cell. In the finite volume method, the solver computes q_w under the assumption of a linear temperature variation across the near-wall cell. Specifically, q_w is computed as (see section 2.2.1):

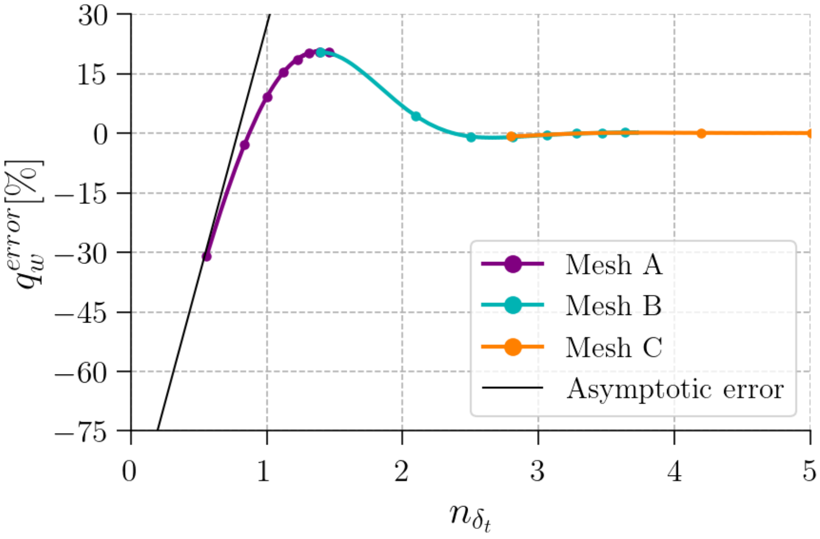

Figure 4.4: q_w^{error} sensitivity to mesh resolution. Three uniform Cartesian meshes with different cell sizes are used to construct the curves, demonstrating that q_w^{error} primarily depends on n_{δ_t}. The black curve, whose equation is given by Eq. 4.2.3, represents the asymptotic error observed for very coarse meshes.

$$q_w = -k_1 \frac{T_1 - T_w}{y_1} \tag{4.2.2}$$

For a very coarse mesh ($y_1 \gg \delta_t$), the proportion of the cell volume with temperature above T_∞ is minimal, and thus $T_1 \approx T_\infty$. The tangent equation at the origin can then be derived

---

[2] The exact δ_t from the WR case is used to calculate n_{δ_t} for all meshes. n_{δ_t} is expected to increase with the x-position due to the Cartesian mesh structure and the growth of δ_t along the plate.

from the Lévêque theoretical solution Eq. 3.1.6, which gives: $q_w^{\text{ref}} \approx k(T_w - T_\infty)\ 1.572\ \delta_t^{-1}$. Combining this equation with Eq. 4.2.2 and the definition of q_w^{error} given in Eq. 4.2.1, leads to the following asymptotic error expression:

$$q_w^{\text{error}} \approx 1.27 n_{\delta_t} - 1 \tag{4.2.3}$$

as illustrated in Fig. 4.4. For more refined meshes, the numerical wall heat flux q_w gives a good prediction, with an error below 1% for $n_{\delta_t} = 3$.

4.3 Thermal wall model assessment

The surface wall heat flux q_w calculated by the CFD tool for each near-wall cell is now modified by the TWM-cst, indirectly impacting the temperature field and the heat flux between cells inside the domain. The free stream temperature T_∞ needed by the model (see Fig. 3.4) is set equal to the inlet temperature. The model is tested on the same meshes as those used in section 4.2. Additionally, supplementary cases with lower thermal diffusivity values, $\alpha = 10^{-10}\ \text{m}^2{\cdot}\text{s}^{-1}$ and $\alpha = 10^{-9}\ \text{m}^2{\cdot}\text{s}^{-1}$, have been simulated to complement the previous cases at $\alpha = 10^{-8}\ \text{m}^2{\cdot}\text{s}^{-1}$ and to cover a broader range of n_{δ_t} in the results presented below.

Fig. 4.5 compares the relative errors on q_w with and without the model. For $n_{\delta_t} < 2$, a significant improvement is observed when the thermal wall model is activated (blue curve in Fig. 4.5), as the wall heat flux error drops to nearly zero.

Fig. 4.6 presents the temperature profiles for two values of n_{δ_t}. As for q_w^{error}, the dimensionless numerical temperature profiles depend only on n_{δ_t}. The exact temperature for the near-wall cell, $\widetilde{T_1^e}^*$, is computed based on the WR case and marked by a green triangle. For the two profiles shown, the temperature predicted by the model for the near-wall cell appears to deviate from the exact local temperature profile $T^*(x_1, y^*)$ (obtained from the WR case[3]). While this may initially seem paradoxical, it is actually consistent with expectations. As explained in chapter 3, a correct estimation of the heat fluxes for each cell along the wall ensures that T_1^* aligns with $\widetilde{T_1^e}^*$ and not $T^*(x_1, y_1^*)$, also referred to as T_1^{e*} (see Tab. 3.2).

For both profiles, the agreement between the numerical results obtained with the model

---

[3] With this numerical-setup where Lévêque's theory holds, one has $\widetilde{P}_T(y_1^*) = \widetilde{T}^*(x_1, y_1)$ and $P_T(y_1^*) = T^*(x_1, y_1)$ with $T(x, y)$ obtained from the wall-resolved mesh; in shorthand, $\widetilde{P}_T(y_1^*) = \widetilde{T_1^e}^*$ and $P_T(y_1^*) = T_1^{e*}$.

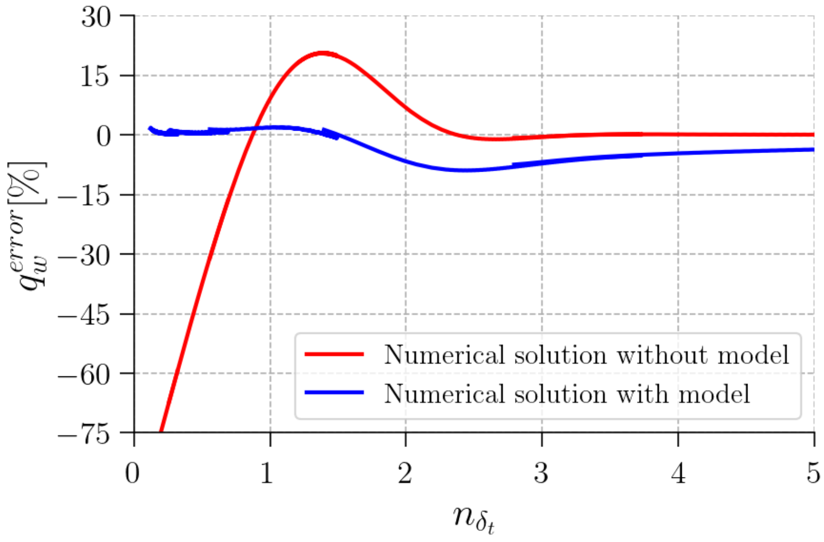

Figure 4.5: Relative error on q_w vs. n_{δ_t} with and without model correction. The curves are constructed from cases with different meshes and thermal diffusivities.

and $\widetilde{T_1^e}^*$ is quite satisfactory, with only a slight offset observed in Fig. 4.6b. This offset explains the q_w error for the same range of n_{δ_t} seen in Fig. 4.5. Further details on the near-wall cell temperature and its dependence on n_{δ_t} are provided in Appendix A.

For $n_{\delta_t} > 2$ (see Fig. 4.5), the q_w predictions with the thermal wall model deteriorate slightly, becoming marginally less accurate than those without the model. Nevertheless, the error remains below 10% and gradually decreases toward zero as the mesh resolution is refined. The degradation in q_w can be attributed to errors in T_1^*, which in turn originate from inaccuracies in the heat flux between the first and second cells, $q_{1\to2}$, where $cell_2$ is the adjacent cell to $cell_1$, located further from the wall (see Fig. 3.3). These inaccuracies have no impact for lower n_{δ_t}, as $q_{1\to2}$ becomes negligible in comparison to q_w.

The error in $q_{1\to2}$ arises from a slight inconsistency between the discretization scheme used to compute the heat flux between cells [47] and the near-wall cell temperature T_1 obtained from an exact q_w. In the solver, this flux is evaluated with a second-order central differencing scheme,

$$q_{1\to2} = -k\frac{T_2 - T_1}{2y_1} \tag{4.3.1}$$

where $2y_1$ equals to the distance between the two cell centers, since the Cartesian mesh is uniform. For this expression to be consistent, it is implicitly assumed a linear temperature variation between neighboring cells. Additionally, it is assumed that the cells' temper-

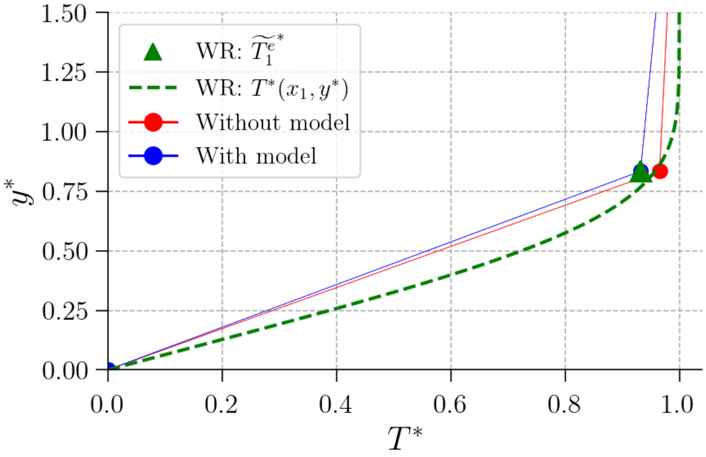

(a) Temperature profile for $n_{\delta_t} = 0.6$

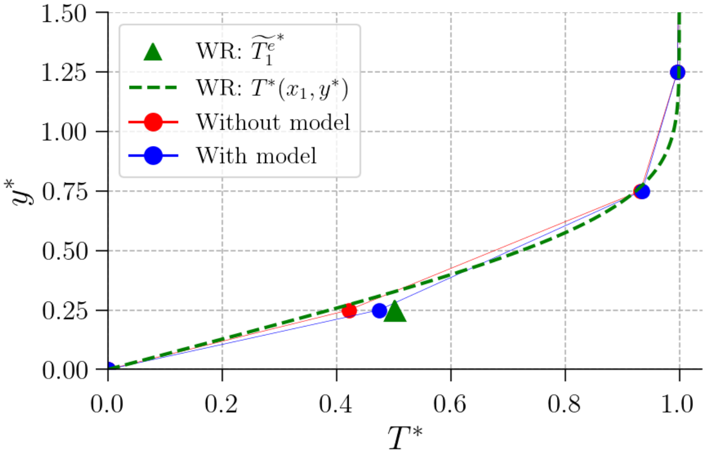

(b) Temperature profile for $n_{\delta_t} = 2$

Figure 4.6: Temperature profiles normal to the wall, with and without the model. The circles represent the numerical solutions at the cell-center positions. The results obtained using the model align well with the exact solution, represented by black triangles.

atures, T_1 and T_2, are equal to the exact temperature values at their geometric centers, namely T_1^e and T_2^e. Under this assumptions, $q_{1\to 2} = -k\frac{T_2^e - T_1^e}{2y_1}$. However, with q_w accurately computed along the wall, the temperature of near-wall cells tends to approximate $\widetilde{T_1^e}$, not T_1^e. Consequently, the discrete flux actually computed is $q_{1\to 2} = -k\frac{\widetilde{T_2^e} - \widetilde{T_1^e}}{2y_1}$ which is not correct. Further details about $q_{1\to 2}$ and q_w errors and their impacts on T_1 are provided in Appendix B.

The next step is to assess the thermal wall model in more complex and challenging flows.

CHAPTER 5

Evaluation of the thermal wall model under jet impingement configuration

This section evaluates the thermal wall model tailored for constant viscosity fluids (TWM-cst), for a liquid jet (high Prandtl number) impinging on a heated flat wall, a configuration representative of real electric motor cooling systems. In this scenario, some assumptions underlying the model, such as the linear velocity profile and parallel velocity to the wall, may no longer hold. Nevertheless, following the philosophy of classical wall-function approaches, the model may remain useful and effective even beyond its strict domain of validity.

The jet impingement configuration follows the experimental set-up described in [74] and previously simulated in Poubeau et al. [36]. A wide range of Pr and Re numbers were tested while maintaining laminar and stable flow conditions. One advantage of this experimental set-up is the limited radial extension of the heated flat wall, which allows full resolution of the physics within a reasonable computational time. Moreover, the radial extension is too short to observe the formation of a hydraulic jump [36], thereby limiting the assessment of the model to the supercritical part of the impinging jet (between the impingement point and the hydraulic jump).

In [36], the numerical setup was validated by comparing wall-resolved simulations with experimental results from [74] for various Re and Pr numbers. Building on this, a simplified numerical configuration is derived from the validated setup and is used to evaluate the TWM-cst. The corresponding cases are summarized in Tab. 5.2. The improvements introduced by the thermal wall model are discussed across different characteristic flow regions and the sensitivity of the model to the Pr and Re numbers is investigated.

5.1 Numerical set-up description

The experimental set-up, which forms the basis for the numerical simulations, is detailed in [74] and [36], and illustrated in Fig. 5.1. A jet of oil is injected through a nozzle of diameter $d = 2.06$ mm, positioned at a distance $H = 10$ mm from a heated wall. The inlet liquid temperature T_∞, flow rate $\dot{V}$, and heated wall temperature T_w are precisely controlled and measured. The heated wall is part of an assembly consisting of a cylindrical copper block surrounded by thermal insulation, with a resistance heater at its base. By measuring temperatures at various heights within the assembly, the mean surface wall heat flux, $\overline{q_w}$, is determined.

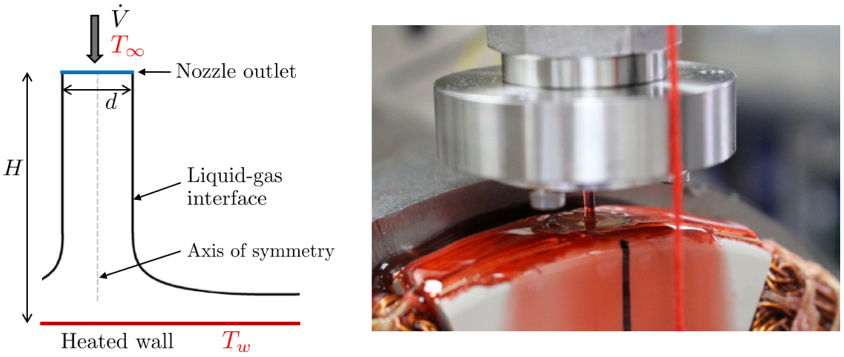

Figure 5.1: Experimental setup [74]: photograph of the liquid jet impinging on a heated wall, with an accompanying schematic of the jet.

Fluid properties vary with temperature according to the correlations given in [36]. The liquid density ρ_l varies weakly with temperature, showing a maximum relative variation of 6% between 323 K and 393 K. In the numerical set-up, it is assumed uniform and set equal to the liquid inlet density, $\rho_l = \rho_l(T_\infty)$. From the density correlation given in [36], the inlet density is written as

$$\rho_l = -0.64\,T_\infty + 1027.6 \tag{5.1.1}$$

The surface tension σ_l was estimated from a typical oil [36]. σ_l shows a maximum variation of 21%, and its variation with temperature is described by

$$\sigma_l(T) = -8.0 \times 10^{-5}\, T + 0.0582 \tag{5.1.2}$$

The correlations for heat capacity, thermal conductivity, and viscosity were fitted in [36] to measurements provided by the oil manufacturer[1]. The variation of the specific heat capacity $c_{p,l}$ is given by

$$c_{p,l}(T) = 3.829\, T + 907.13 \tag{5.1.3}$$

$c_{p,l}$ displays a maximum variation of 13%. The thermal conductivity $k_l = 0.13\ \mathrm{W.m^{-1}.K^{-1}}$ is constant. Oil viscosity exhibits a strong dependence on temperature. The dynamic and kinematic viscosities, μ_l and ν_l respectively, can vary by a factor of 5 between the bulk flow and the near-wall region. To represent this temperature dependence, measurements were fitted, and the kinematic viscosity $\nu_l(T)$ is expressed using Walther's equation [75]:

$$\ln\!\big(\ln(\nu_l \times 10^6 - 0.7)\big) \;=\; C + m\, \ln(T) \tag{5.1.4}$$

with $m = -3.1987$ and $C = 19.595$, yielding a coefficient of determination $R^2 = 0.993$ for $T_l \in [300\,\mathrm{K}, 440\,\mathrm{K}]$. The viscosity law is depicted in Fig. 5.2 (blue curve).

The Reynolds and Prandtl numbers are computed based on fluid properties evaluated at the film temperature T_f, defined as $\frac{T_\infty + T_w}{2}$, assuming a uniform wall temperature T_w. The nozzle diameter d is chosen as the characteristic length scale. These numbers are then defined as follows:

$$Re = \frac{4\rho_l \dot{V}}{\pi \mu_l d} \tag{5.1.5}$$

$$Pr = \frac{c_{p,l}\mu_l}{k_l} \tag{5.1.6}$$

Experimental measurements [74] and the corresponding validation cases [36] were conducted for several combinations of T_∞, T_w and $\dot{V}$, covering Prandtl numbers in the range $74 \leq Pr \leq 158$ and Reynolds numbers $220 \leq Re \leq 2844$.

Due to the high thermal conductivity of copper and the surrounding thermal insulation of the solid assembly, heat transfer can be reasonably assumed to be one-dimensional, with T_w remaining nearly uniform. It was confirmed in [36] that temperature variations across the heated wall surface remain below 1 K. Based on this observation, the computational

---

[1] Ford Motor Company

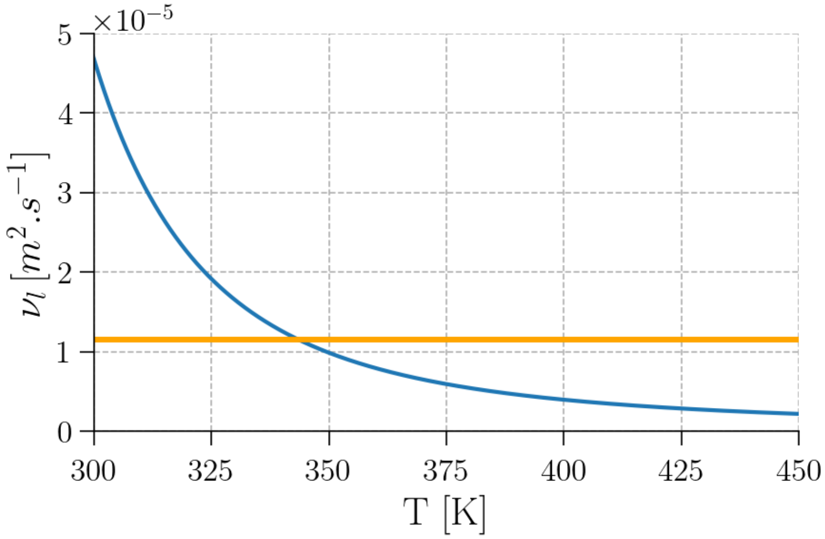

Figure 5.2: Oil viscosity laws used for the impinging-jet configuration. The blue line represents the realistic temperature-dependent viscosity law. The orange line represents the uniform viscosity used for model validation.

domain used in [36], which included the whole assembly, has been simplified in our study. The domain now consists only of ambient air, the cooling liquid jet, and the liquid film, excluding the solid assembly beneath the heated wall. The simplified computational domain is illustrated in Fig. 5.3. It extends radially up to $r = R$, where $R = 6.3$ mm is the radius of the heated wall. The fluid domain includes a nozzle of length $l = 3$ mm, with its exit positioned at a distance H from the heated wall. The jet impingement point is set at the origin of the domain, $(x, y, z) = (0, 0, 0)$. To reduce computational cost while maintaining a 3D approach, only one-quarter of the geometry is simulated, with symmetry boundary conditions applied on the planes spanned by $(\vec{e}_x, \vec{e}_z)$ and $(\vec{e}_y, \vec{e}_z)$ (i.e., on $y = 0$ and $x = 0$). The gravity vector $\vec{g}$ is directed along the unit vector $-\vec{e}_z$.

At the nozzle inlet, a mass flow rate, $\dot{m} = \rho_l \dot{V}$, with uniform velocity field at temperature T_∞ is imposed[2]. The nozzle walls are subject to no-slip and adiabatic conditions. Given the nozzle's length and the Reynolds number, the velocity profile at the nozzle exit corresponds to a partially developed Poisseuille profile [36]. An outlet boundary condition is applied at $r = R$ where the pressure is set to an exit value $P_{exit}(z)$, equal to the atmospheric value augmented by the local hydrostatic head. At the heated wall, a no-slip condition is imposed along with a Dirichlet condition for temperature, which is set to T_w.

---

[2] Since only one quarter of the geometry is simulated, the inlet mass flow is set to $\dot{m}/4$.

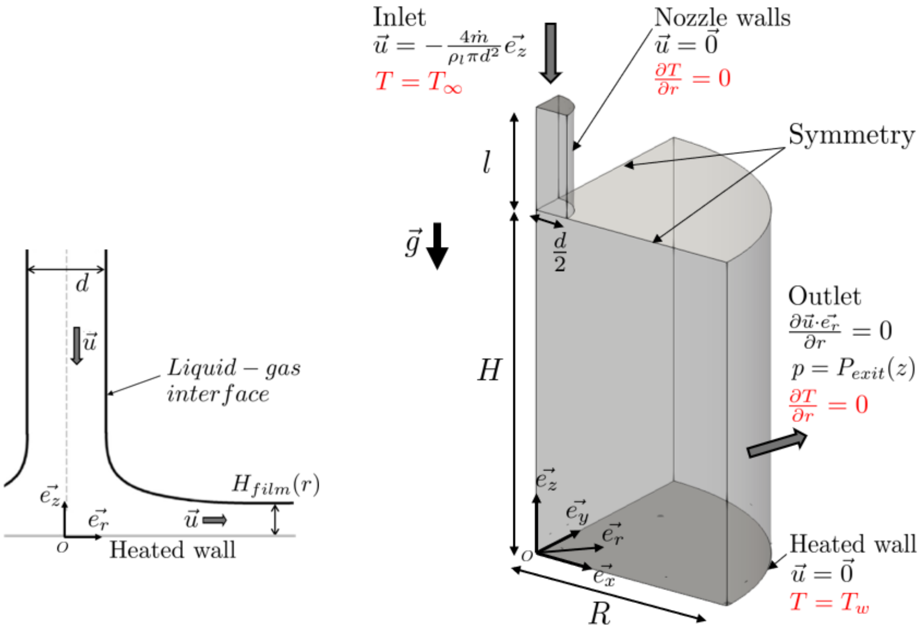

Figure 5.3: Computational domain of the asymmetric liquid jet impinging on a flat wall. The radial direction in polar coordinates is denoted by the unit vector $\vec{e}_r$.

Regarding the meshes used, two categories of grids are considered: wall-resolved and coarse meshes, which mainly differ in their refinement near the wall. Wall-resolved meshes ensure accurate resolution of the thermal and dynamic boundary layers, as well as of the liquid film. In the film region including the liquid–air interface, the radial cell size is about $100\,\mu$m. Near the heated wall, the grid is refined with a minimum cell height ranging from $2\,\mu$m to $5\,\mu$m, depending on the Pr number, and an expansion ratio of 1.04. This guarantees at least 30 cells between the wall and the liquid–air interface, and a minimum of 5 cells within the thermal boundary layer, ensuring accurate results even in the stagnation zone which is particularly challenging to resolve due to the extremely thin thermal boundary layer, as highlighted in [36]. In contrast, the coarse meshes are specifically designed to assess the thermal wall model. They do not fully resolve the thermal boundary layer over the entire radial range, but they are sufficiently fine to capture the dynamic behavior and film thickness. In the film region including the liquid–air interface, the near-wall grid has a minimum cell height ranging from $40\,\mu$m to $56\,\mu$m depending on the film thickness. The expansion ratio and radial cell size are kept identical to those of the wall-resolved mesh. This refinement ensures a minimum of 5 cells across the liquid film. In the nozzle and jet regions, both meshes are identical, matching that used in [36]: a fixed grid cell size of $62.5\,\mu$m is employed, with near-nozzle wall refinement consisting of six layers of cells of

31 μm and a first off-wall cell of 10 μm.

The CFD code CONVERGE [47], previously used in chapter 4, is employed to solve this two-phase incompressible flow configuration. The maximum time step is constrained by the CFL number fixed at 0.75 and the Fourier number fixed at 2. Specifically, the mass and momentum equations solved (written in index notation with $i, j = 1, 2, 3$ and using Einstein's summation convention) are:

$$\frac{\partial u_i}{\partial x_i} = 0 \tag{5.1.7}$$

$$\rho \left[\frac{\partial u_i}{\partial t} + u_j \frac{\partial u_i}{\partial x_j} \right] = -\frac{\partial p}{\partial x_i} + \frac{\partial}{\partial x_j} \left[\mu \left(\frac{\partial u_i}{\partial x_j} + \frac{\partial u_j}{\partial x_i} \right) \right] + \rho g_i + \sigma \kappa n_i \tag{5.1.8}$$

Here, $\vec{g}$ is the gravitational acceleration, μ the dynamic viscosity, ρ the density, σ the surface tension of the liquid, κ the curvature, and $\vec{n}$ the unit normal vector to the liquid-air interface. For the surface-tension term in Eq. 5.1.8, the interface curvature is computed as $\kappa = -\frac{\partial n_i}{\partial x_i}$ with $n_i = \frac{\partial \alpha}{\partial x_i}(\|\frac{\partial \alpha}{\partial x_i}\|)^{-1}$. The energy equation solved is:

$$\rho c_p \left[\frac{\partial T}{\partial t} + u_j \frac{\partial T}{\partial x_j} \right] = \frac{\partial}{\partial x_j} \left(k \frac{\partial T}{\partial x_j} \right) \tag{5.1.9}$$

The flow is assumed to be laminar, therefore, no turbulence model is applied. The two-phase flow is modeled using the Volume of Fluid (VoF) approach. Both phases are treated as incompressible and share the same mass, momentum and energy equations. The volume fraction α is transported to capture the evolution of the free surface:

$$\frac{\partial \alpha}{\partial t} + u_j \frac{\partial \alpha}{\partial x_j} = 0 \tag{5.1.10}$$

Here, $\alpha = 0$ indicates the presence of liquid, while $\alpha = 1$ represents gas. The fluid properties are defined as:

$$\rho = \rho_l \alpha + \rho_g (1 - \alpha), \quad \mu = \mu_l \alpha + \mu_g (1 - \alpha) \tag{5.1.11}$$

Where the subscript g is used to denote gas properties, which, in our case, correspond to air. To discretize the convective term in Eq. 5.1.10, the High-Resolution Interface Capturing scheme is used [76].

All cases are initialized with a liquid film to ensure a fully wetted surface. Steady state is supposed to be achieved when temporal variations of the wall heat flux fall below 0.2%, which occurs before 0.2 s of physical time. Defining the characteristic development time for the radial flow as

$$t_c = \frac{R\,(\pi d^2/4)}{\dot{V}} \tag{5.1.12}$$

this corresponds to approximately $40\,t_c$ to $200\,t_c$, depending on the configuration.

5.2 Numerical set-up validation

Prior to evaluating the thermal wall model, the numerical setup is validated by comparison with experiments using wall-resolved cases that include temperature-dependent properties. Cases P (see Tab. 5.1) cover a wide range of Pr and Re and serve exclusively for the numerical setup validation. Additional information on the temperature-dependent properties of cases P is given in [36].

Cases	Parameters								
	$\dot{V}$ (m^3·s^{-1})	T_∞ (K)	T_w (K)	Re	Pr	Mesh size	Min. cells number		
							H_{film}	δ	δ_t
$\mathbf{P_{1_r}}$	2.50×10^{-5}	323	363	1319	158	365 900	43	29	6.6
$\mathbf{P_{2_r}}$	0.42×10^{-5}	323	363	220	158	346 400	35	24	6.2
$\mathbf{P_{3_r}}$	0.42×10^{-5}	323	393	317	111	346 400	34	24	5.5
$\mathbf{P_{4_r}}$	2.50×10^{-5}	363	393	2844	74	366 100	43	28	10.3
$\mathbf{P_{5_r}}$	0.42×10^{-5}	363	393	474	74	379 400	40	25	8.8
$\mathbf{P_{6_r}}$	2.50×10^{-5}	323	393	1900	111	410 000	42	27	6.0

Table 5.1: Summary of the numerical cases P, only used to validate the numerical setup, which are wall-resolved with temperature-dependent liquid properties. The *Min. cells number* column reports the minimum number of cells across the film, the dynamic and thermal boundary layer, respectively.

The evaluation is based on the mean Nusselt number, $\overline{Nu}$, which represents the ratio of $\overline{q_w}$ to the heat flux obtained from pure conduction. It is defined as:

$$\overline{Nu} = \frac{\overline{q_w}}{k_l \frac{(T_w - T_\infty)}{d}} \tag{5.2.1}$$

with k_l evaluated at T_f. Fig. 5.4 presents a comparison between experimental and numerical results. The $\overline{Nu}$ values exhibit good agreement with measurements across the entire range of Pr and Re tested, validating the numerical set-up. It is worth noting that the impinging-jet and induced liquid film show no instabilities.

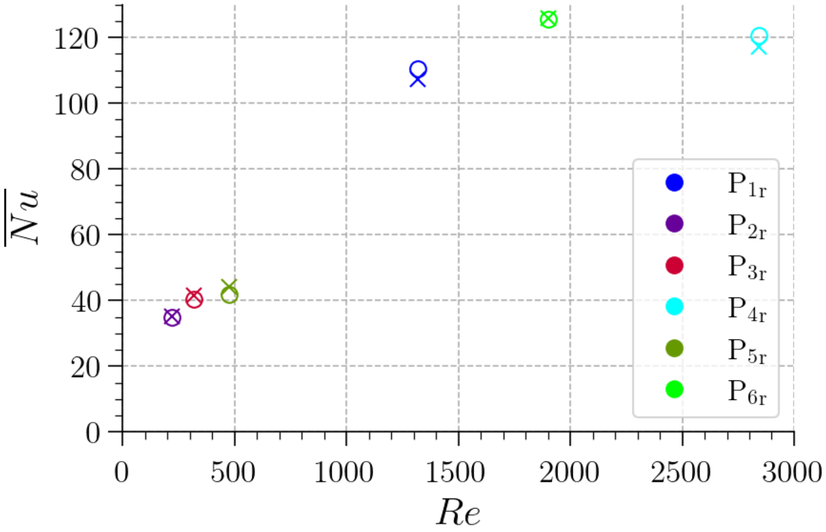

Figure 5.4: Comparison of $\overline{Nu}$ from experimental (circles) and numerical results (crosses) for the wall-resolved cases P (without thermal wall model) listed in Tab. 5.1.

5.3 Thermal wall model assessment

Oil exhibits a strong viscosity dependence on the temperature and therefore does not satisfy the model assumption of uniform properties. The dynamic viscosity can vary by a factor 5 between the bulk flow and near the wall. For model validation purpose, the numerical set-up in [36] is simplified by imposing uniform fluid properties. Therefore, the uniform-property assumption used by TWM-cst (see chapter 3) remains valid for the present assessment.

The TWM-cst is assessed on configurations with Re and Pr numbers comparable to those used to validate the numerical set-up (see Tab. 5.1), but with uniform properties. These configurations, used as baseline validation cases for the model, are summarized in Tab. 5.2. Following the temperature–dependence correlations detailed in section 5.1, the properties are evaluated at the film temperature $T_f = \frac{T_\infty + T_w}{2} = 343\,\mathrm{K}$, which is identical for each configuration (see Tab. 5.2). This yields $\rho_l = 0.808 \times 10^3\,\mathrm{kg\,m^{-3}}$, $c_{p,l} = 2.221 \times$

$10^3\,\mathrm{J\,kg^{-1}\,K^{-1}}$, $\sigma_l = 3.08 \times 10^{-2}\mathrm{N.m^{-1}}$ and $\nu_l = 1.147 \times 10^{-5}\,\mathrm{m^2\,s^{-1}}$ (see the orange line in Fig. 5.2). In contrast, k_l is adjusted to achieve the desired Pr number, with for instance $k_l = 1.3 \times 10^{-1}\,\mathrm{W\,m^{-1}\,K^{-1}}$ for $Pr = 158$ and $k_l = 2.05 \times 10^{-2}\,\mathrm{W\,m^{-1}\,K^{-1}}$ for $Pr = 1000$.

The different configurations used to validate the thermal wall model are summarized in Tab. 5.2. Cases with a coarse mesh, indicated by a subscript "c", are used with model (superscript "m") or without model. Wall-resolved cases are indicated by a subscript "r" and always used without model. The configurations are carried out to evaluate the model on a wide range of Pr and Re numbers.

Cases	Parameters								
	$\dot{V}$ ($\mathrm{m^3 \cdot s^{-1}}$)	T_∞ (K)	T_w (K)	Re	Pr	Mesh size	Min. cells number		
							H_{film}	δ	δ_t
$\mathbf{A_c}$, $\mathbf{A_c^m}$	1.67×10^{-5}	323	363	898	158	209 300	5.4	2.7	0.5
$\mathbf{A_r}$						335 200	36	22	5.9
$\mathbf{B_c}$, $\mathbf{B_c^m}$	1.67×10^{-5}			898	1000	209 300	5.4	2.7	0.3
$\mathbf{B_r}$						389 700	50	35	6.3
$\mathbf{C_c}$, $\mathbf{C_c^m}$	1.67×10^{-5}			898	10	209 300	5.4	2.7	1.3
$\mathbf{C_r}$						335 200	36	22	13
$\mathbf{D_c}$, $\mathbf{D_c^m}$	1.67×10^{-5}			898	1	209 300	5.4	2.7	3.0
$\mathbf{D_r}$						335 200	36	22	25
$\mathbf{E_c}$, $\mathbf{E_c^m}$	0.42×10^{-5}			225	158	186 800	4.7	2.8	0.6
$\mathbf{E_r}$						335 200	43	29	10
$\mathbf{F_c}$, $\mathbf{F_c^m}$	2.50×10^{-5}			1348	158	209 300	4.8	2.4	0.44
$\mathbf{F_r}$						335 200	34	21	5.3
$\mathbf{G_r}$	0.42×10^{-5}	323	393	317	111	346 000	36	26	7.3

Table 5.2: Summary of numerical cases with uniform liquid properties, used to evaluate the thermal wall model. For each configuration, two grids are considered: a wall-resolved mesh (subscript "r") and a coarse mesh (subscript "c"). Wall-resolved cases are simulated only without model, while coarse meshes are simulated with (superscript "m") and without model. The *Min. cells number* column reports the minimum number of cells across the film, the dynamic and thermal boundary layers over the entire radial domain.

5.3.1 Wall-resolved case analysis

In this section, before showing model results, the wall-resolved configuration $\mathrm{A_r}$ is analyzed. The case is detailed in Tab. 5.2 and characterized by a high Pr number ($Pr = 158$) and an intermediate Re number ($Re = 898$).

The results are presented in Fig. 5.5 which displays the radial profiles of the film thickness H_{film} along with the dynamic boundary layer thickness δ, defined as the location where the radial velocity $\vec{u} \cdot \vec{e_r}$ is maximal, and the thermal boundary layer thickness δ_t (see definition section 3.1). Moreover, the non-dimensional wall shear stress τ_w along the radial direction, expressed as

$$\tau_w^* = \tau_w \frac{\rho_f \pi d^4}{8\dot{m}^2} \tag{5.3.1}$$

is depicted in Fig. 5.6. The results for the local Nusselt number Nu, defined as

$$Nu = \frac{q_w}{\frac{k_l (T_w - T_\infty)}{d}} \tag{5.3.2}$$

are also shown in the same figure. These two figures highlight the different regions encountered in a liquid jet impinging on a flat wall for a laminar flow, as observed in [36, 77, 78]. Near the jet axis, Region 1, called the stagnation zone, extends up to a distance of approximately $0.7d$ from the jet axis [77, 79], where the dimensionless wall shear stress τ_w^* reaches its maximum. In this zone, both the dynamic and thermal boundary layer, δ and δ_t, are very thin. The local Nusselt number Nu attains its maximum farther from the impingement point, owing to the jet's non-parabolic near-wall velocity profile [36]. In Region 2, the dynamic boundary layer expands radially until it reaches the liquid-air interface, which occurs at approximately $1.7d$, a value which aligns with the literature [77, 78]. Region 3 is the viscous similarity region, where the dynamic boundary layer spans the full film thickness. In these last two regions, τ_w and Nu decrease at a progressively lower rate as the distance from the jet axis increases (see Fig. 5.6). No hydraulic jump is observed in the film thickness profile due to the limited radial extent of the computational domain.

The three distinct regions exhibit different flow characteristics, which in turn affect the thermal behavior. To comply with the model's assumptions, the velocity profile is expected to be parallel to the wall across the near-wall cell and to vary linearly across both the near-wall cells and the thermal boundary layer (see chapter 3). Specifically, for the axisymmetric impinging jet configuration, this implies $u_r(z) \sim z$ and $u_z = 0\ \mathrm{m \cdot s^{-1}}$ within these zones, where $u_r = \vec{u} \cdot \vec{e_r}$ and $u_z = \vec{u} \cdot \vec{e_z}$ denote the velocity components parallel and normal to the wall (see Fig. 5.3). However, in an impinging jet configuration, these assumptions may be violated due to the complex flow behavior near the stagnation point, in region 1 and 2.

Velocity profiles $u_r(z)$ obtained from both the wall-resolved ($\mathrm{A_r}$) and coarse mesh ($\mathrm{A_c}$), are shown in Fig. 5.7a for three different positions on the plate. The distance z from

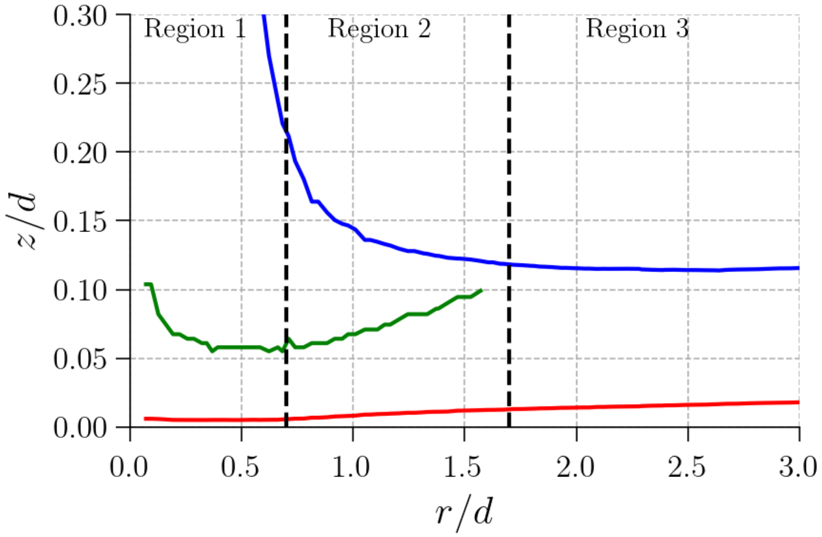

Figure 5.5: Radial profiles of H_{film} (blue line), δ (green line), and δ_t (red line) from the wall-resolved configuration A_r.

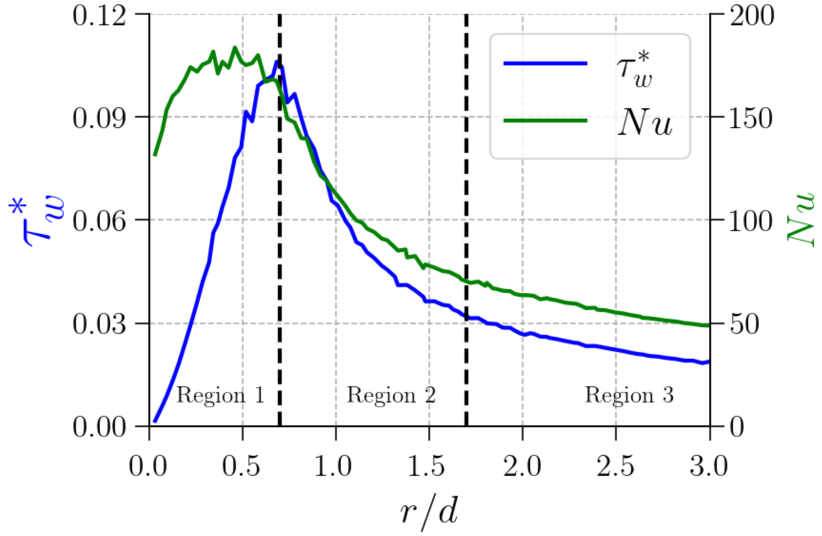

Figure 5.6: Dimensionless wall shear stress and Nusselt number along the radial direction of the wall-resolved case A_r.

the wall is scaled by δ_t to highlight the extent of the thermal boundary layer. The exact temperature profiles, from the wall-resolved case, are nearly linear up to $z^* = 1$ for the three radial positions. Consequently, the assumption $u_r(z) \sim z$ across δ_t holds true at least from $\frac{r}{d} = 0.1$.

In Fig. 5.7a, the case $\mathrm{A_r}$ is also used to assess the linearity of the velocity profile across the near-wall cell heights of the coarse mesh, on which the model is expected to be apply. The cell centers of the coarse mesh are indicated by red markers. It is observed that, over a distance equal to twice the height of the near-wall cell center, the resolved profiles (green curves) deviate slightly from linearity near the jet impingement point. This deviation from a core model assumption may lead to errors in the model's prediction of the wall heat flux q_w. Furthermore, the coarse mesh used with the thermal wall model must be sufficiently refined to capture the velocity gradient accurately. The velocity gradient estimated from the coarse mesh is not entirely accurate near the jet impinging area, where the dynamic boundary layer is the thinnest, potentially leading to errors in the model predictions.

Fig. 5.7b allows to assess the model assumption that the velocity field is parallel to the wall across the near wall cell. It shows that the ratio $\frac{u_z}{u_r} < 0.3$ at $\frac{r}{d} = 0.1$ and becomes negligible further from the jet across the near-wall cell height of the coarse mesh. Therefore, the thermal wall model assumption, $u_z = 0$ m.s^{-1}, is considered valid for $\frac{r}{d} > 0.1$.

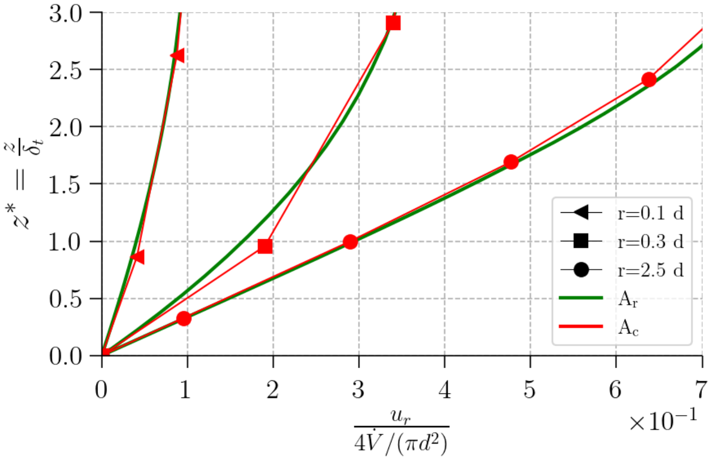

(a) Wall-parallel velocity component

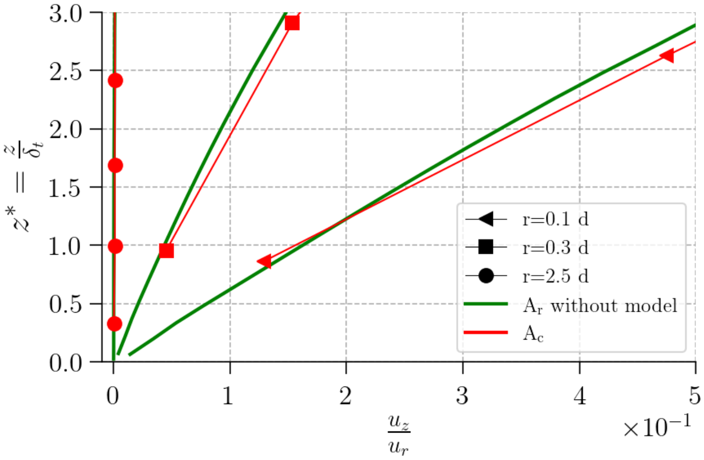

(b) Ratio of the wall-normal to wall-parallel velocity components

Figure 5.7: Profiles of the radial and normal velocity components to the wall in the impinging jet configuration A using the coarse-mesh case (A_c) without model and the wall-resolved reference (A_r). The red markers indicate the position of the cell centers of the case A_c.

5.3.2 Assessment with uniform viscosity

In this section, the thermal wall model is first evaluated for three different Pr numbers $(10, 158,$ and $1000)$ at fixed Re (898), corresponding to the configurations C, A and B in Tab. 5.2. The Pr variation is obtained by modifying only the liquid conductivity k_l while keeping all other parameters identical. The free stream temperature T_∞ needed by the model (see Fig. 3.4) is set equal to the inlet temperature.

Predictions from the coarse mesh, with and without the model, are assessed via the radial evolution of the Nu number (see Fig. 5.8), by comparing with the wall-resolved reference. The error in Nu for the coarse mesh without the model reaches a maximum of 70% at $Pr = 1000$ (case $\mathrm{B_c}$), 40% at $Pr = 158$ (case $\mathrm{A_c}$) and 15% for $Pr = 10$ (case $\mathrm{C_c}$) in Region 1, where the thermal boundary layer is thinnest and therefore least resolved. With the model (cases $\mathrm{A_c^m}$, $\mathrm{B_c^m}$ and $\mathrm{C_c^m}$), the numerical results show significant improvements for all cases, even though the jet configuration differs from the parallel shear flow used to develop the model. Note however the slight underestimation in Region 1 for cases $\mathrm{A_c^m}$ and $\mathrm{B_c^m}$. Indeed, a thinner dynamic boundary layer in Region 1 may leads to imperfectly resolved velocity profile, which is a source of error for Nu prediction, though it still represents a notable improvement compared to the corresponding cases without model. A small overestimation is also noticeable for $\frac{r}{d} > 1$. This slight errors may be due to a velocity field that is not perfectly parallel to the wall or linear across the near-wall cells.

For clearer comparison with the results obtained under Lévêque conditions, summarized in Fig. 4.5, the n_{δ_t} range covered by each configuration is listed in Tab. 5.3. The configurations, characterized by different Pr, span the range of n_{δ_t} from 0.3 for case $\mathrm{B_c}$ to 3.8 for case $\mathrm{C_c}$.

Cases	Min. n_{δ_t}	Max. n_{δ_t}
$\mathbf{A_c}$, $\mathbf{A_c^m}$	0.5	1.7
$\mathbf{B_c}$, $\mathbf{B_c^m}$	0.3	0.9
$\mathbf{C_c}$, $\mathbf{C_c^m}$	1.3	3.8
$\mathbf{D_c}$, $\mathbf{D_c^m}$	3.0	8.8
$\mathbf{E_c}$, $\mathbf{E_c^m}$	0.6	3.2
$\mathbf{F_c}$, $\mathbf{F_c^m}$	0.4	1.4

Table 5.3: Minimum and maximum number of cells across the thermal boundary layer over the entire radial domain.

For case $\mathrm{B_c}$ ($Pr = 1000$), n_{δ_t} remains below unity across the plate. In this regime,

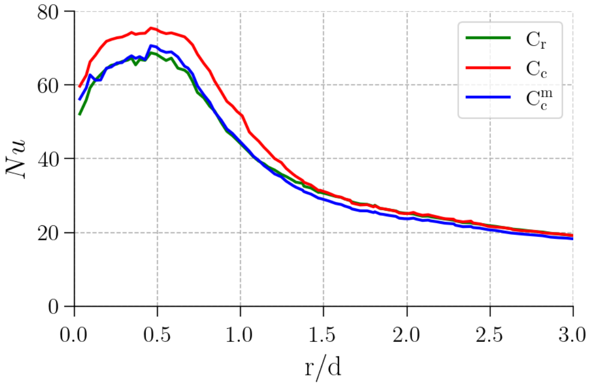

(a) Configuration C ($Pr = 10$)

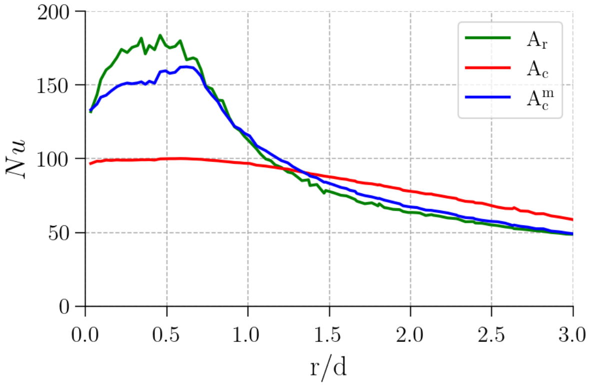

(b) Configuration A ($Pr = 158$)

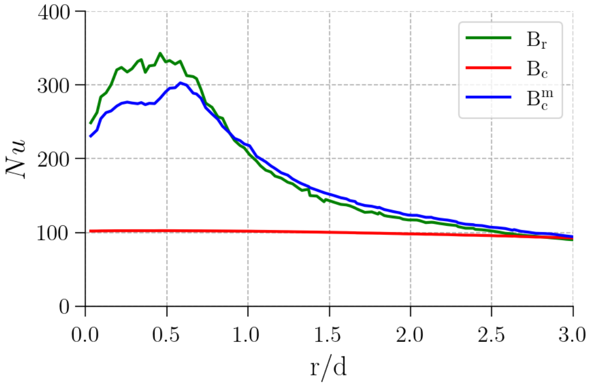

(c) Configuration B ($Pr = 1000$)

Figure 5.8: Radial profiles of Nu obtained using the coarse mesh cases, with (A_c^m, B_c^m and C_c^m) and without the thermal wall model (A_c, B_c and C_c), compared to their respective wall-resolved cases (A_r, B_r and C_r).

the solution without model strongly underestimates q_w under Lévêque conditions, while the model delivers a large improvement. A trend that persists in the impinging jet configuration. Case $\mathrm{A_c}$ ($Pr = 158$) shows the same trend in Region 1, owing to similar n_{δ_t} values. For case $\mathrm{A_c}$, the prediction without model overestimates the wall-resolved result around Region 3, near $n_{\delta_t} \approx 1.5$; the model noticeably reduces the error. This results are consistent with the trends obtained under Lévêque conditions in Fig. 4.5 for similar n_{δ_t}. Case $\mathrm{C_c^m}$ ($Pr = 10$), representative of a moderate Pr, is employed to examine the model at higher n_{δ_t}. Without the model, the prediction overestimates the wall-resolved reference in Regions 1–2, with the over-prediction occurring where $n_{\delta_t} \approx 1.5$. The model yields an improvement, mirroring the behavior seen for $\mathrm{A_c^m}$ in Regions 3 with similar n_{δ_t}. Farther from the jet, the model shows a mild underestimation ($\sim 5\%$), coincident with $n_{\delta_t} \in [2, 4]$, a range already associated with model underestimation under Lévêque conditions.

To evaluate the results by region, the dimensionless integrated wall heat flux Q_w^* is introduced, normalized by the total wall flux from the wall-resolved case, giving

$$Q_w^*(r_1, r_2) = \frac{\int_{r_1}^{r_2} q_w \; r \; dr}{\int_0^R q_w^{res} \; r \; dr} \tag{5.3.3}$$

where r_1 and r_2 represent arbitrary radial positions between 0 and R. The results for Q_w^* are presented in Fig. 5.9c for the cases B ($Pr = 1000$), distinguishing between regions 1, 2 and 3 [3]. The results without the thermal wall model show a clear underestimation of Q_w^* in all regions, along with a pronounced improvement when using the model. These observations are consistent with the results obtained under Lévêque conditions in Fig. 4.5, where lower values of n_{δ_t} lead to large improvements with the model. Results for the cases A ($Pr = 158$) are shown in Fig. 5.9b. Without the thermal wall model, the error in the integral wall heat flux appears to balance out between these regions but remains nonzero when considered individually. Incorporating the model (case $\mathrm{A_c^m}$) improves Q_w^* predictions for each region. Concerning results for case $\mathrm{C_c^m}$ with a moderate Pr number ($Pr = 10$) in Fig. 5.9a, a slight improvement is observed in Regions 1 and 2, offset by a slight deterioration in Region 3 where the thermal boundary layer is thicker. As already mentioned, this trend is consistent with Fig. 4.5, which indicates a moderate underestimation for $n_{\delta_t} \gtrsim 2$. Even if the error marginally increases in this range of n_{δ_t}, the model largely improves the prediction where the thermal boundary layer is under-resolved ($n_{\delta_t} \lesssim 2$). Therefore, the prediction with the model shows low sensitivity to flow regions and n_{δ_t}, consistently reducing the error to a value close to zero. These results demonstrate the robustness of the thermal wall model to

---

[3] Regions 1 and 2 span the radial interval $r_1 = 0$ mm to $r_2 = 1.4$ mm and $r_1 = 1.4$ mm to $r_2 = 3.5$ mm. The region 3 extends from $r_1 = 3.5$ mm to $r_2 = R = 6.3$ mm

the mesh thickness, provided the velocity profile is well resolved.

Finally, the cases D (see Tab. 5.2) with $Pr = 1$ have been carried out to demonstrate the flexibility of the model in a context where δ_t becomes as thick as δ and even thicker than H_{film} across the entire plate. In this configuration, the coarse mesh almost resolves the thermal boundary layer throughout the radial domain, achieving at least three cells across the thermal boundary layer in the stagnation zone (see Tab. 5.2). Fig. 5.10 compares the local Nu results obtained with and without the model to the wall-resolved case $\mathrm{D_r}$ along the radial direction. As the thermal boundary layer is thicker, case $\mathrm{D_c}$ without model provides accurate results not only for the dynamic quantities but also for the N_u. The thermal wall model demonstrates good predictive capabilities for N_u even in the presence of a thick thermal boundary layer, highlighting the flexibility of the model.

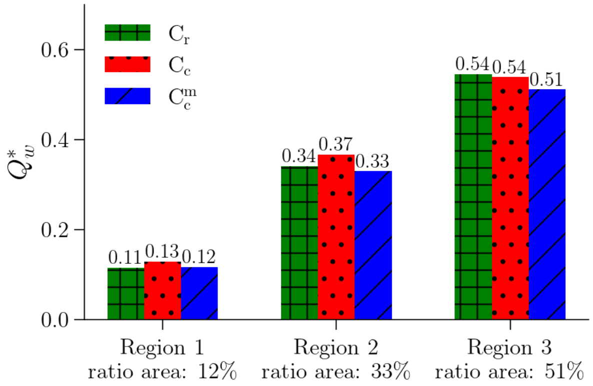

(a) Configuration C ($Pr = 10$)

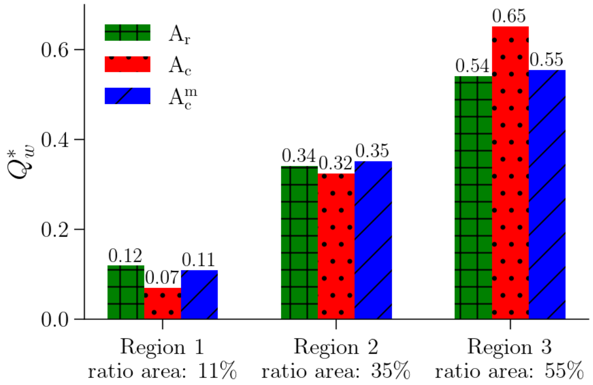

(b) Configuration A ($Pr = 158$)

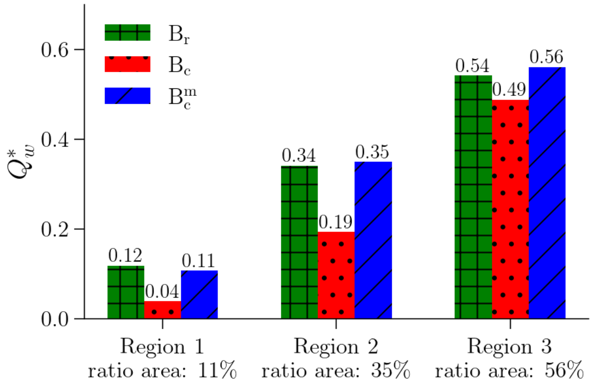

(c) Configuration B ($Pr = 1000$)

Figure 5.9: Dimensionless integral wall heat flux Q_w^* extracted by region (see Eq. 5.3.3). Comparisons are made between the coarse mesh cases without model ($\mathrm{A_c}$, $\mathrm{B_c}$ and $\mathrm{C_c}$), to cases with model ($\mathrm{A_c^m}$, $\mathrm{B_c^m}$ and $\mathrm{C_c^m}$), and their respective wall-resolved cases ($\mathrm{A_r}$, $\mathrm{B_r}$ and $\mathrm{C_r}$).

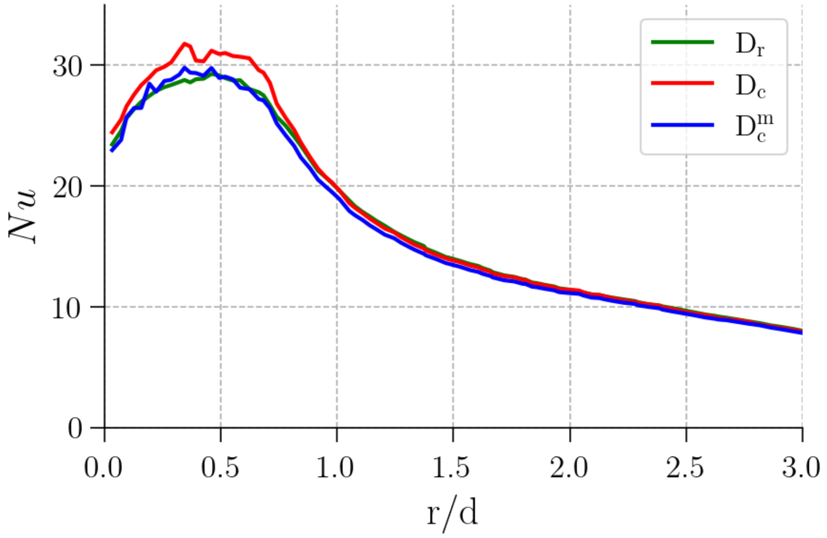

Figure 5.10: Radial profile of Nu obtained from the cases D ($Pr = 1$), with (D_c^m) and without the thermal wall model (D_c), compared to the wall-resolved case (D_r).

The sensitivity of the model to the Re number is now evaluated at $Pr = 158$ by considering cases E and F, which correspond to $Re = 225$ and $Re = 1348$, respectively. Results in Fig. 5.11 show substantial improvement at both Reynolds number extremes, which corroborates the ability of the thermal wall model to handle laminar flow over a wide range of Re. The high Re case, F_c^m in Fig. 5.11b, exhibits a slight underestimation of the heat flux beneath and very near the jet, as observed for the similar but lower Re cases, A_c^m and B_c^m in Fig. 5.8. Conversely, the low Re case, E_c^m in Fig. 5.11a, shows a better estimate of Nu in the same region. This difference may be related to a slightly less accurate representation of the near-jet velocity profile at higher Re numbers, even when ensuring at least five cells across the film thickness, as the momentum boundary layer becomes thinner. In addition, the assumption of linear velocity profile up to the first-cell height can be more strongly violated at higher Re. To illustrate this hypothesis, radial velocity profiles in region 1 for cases E_r and F_r are plotted in Fig. 5.12, along with coarse meshes results without model: E_c and F_c. The exact profiles (from wall-resolved cases) show that the velocity across the near-wall cell height of the coarse meshes is nearly linear in case E (low Re), which is not the case for case F (high Re). Also a slightly better prediction of the near-wall velocity is noticeable in case E (low Re).

Results for all configurations in terms of q_w^{error} (see Eq. 4.2.1 for definition) as a function of n_{δ_t} are shown in Fig. 5.13 for cases without the model (red dots) and with the model (blue dots). The configurations span n_{δ_t} from about 0.3 for case B to values > 5 for case

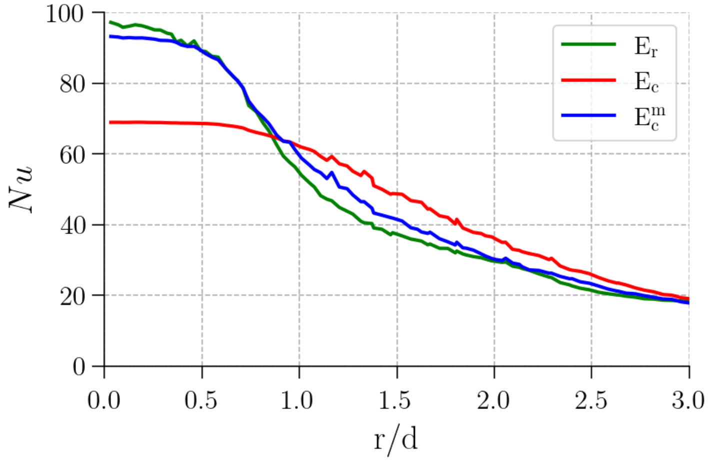

(a) Configuration E ($Re = 225$)

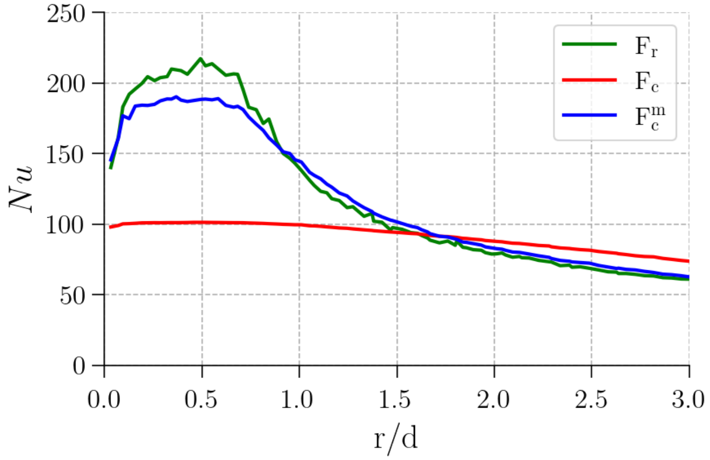

(b) Configuration F ($Re = 1348$)

Figure 5.11: Radial profiles of Nusselt number obtained using the coarse-mesh cases, with ($\mathrm{E_c^m}$ and $\mathrm{F_c^m}$) and without the thermal wall model ($\mathrm{E_c}$ and $\mathrm{F_c}$), compared with their respective wall-resolved references ($\mathrm{E_r}$ and $\mathrm{F_r}$).

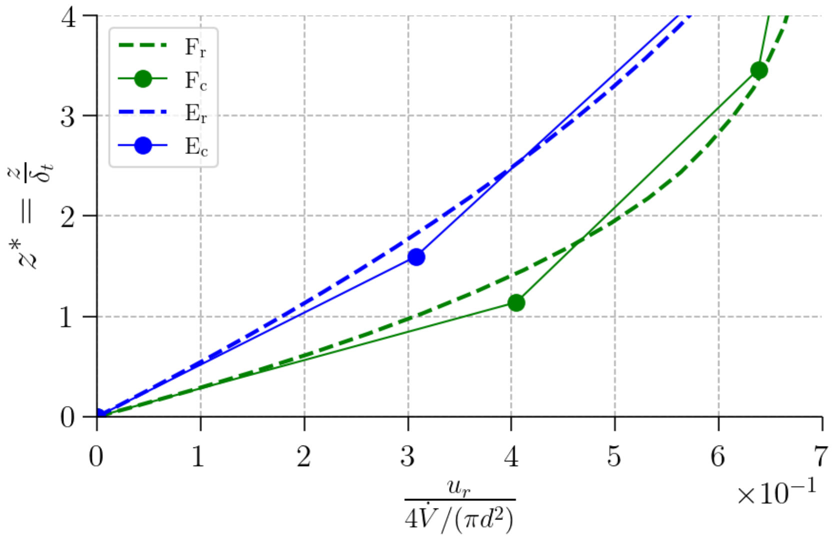

Figure 5.12: Profiles of the radial velocity components u_r near the wall at $r = 0.5d$, obtained using the coarse-mesh cases ($\mathrm{E_c}$ and $\mathrm{F_c}$) without model, with their respective wall-resolved references ($\mathrm{E_r}$ and $\mathrm{F_r}$). The markers indicate the position of the coarse mesh's cell centers.

D; the range reached by each configuration is detailed in Tab. 5.3. Errors are compared against the Lévêque condition trends (red and blue lines) from chapter 4. In the impinging jet configuration, the error is influenced by factors beyond near-wall mesh resolution, as the error curves do not collapse onto a single curve, unlike under Lévêque conditions. Nevertheless, n_{δ_t} remains a useful parameter for anticipating the model's impact. The model delivers a marked improvement for coarse meshes with $n_{\delta_t} < 1$, consistent with the Lévêque results. At intermediate n_{δ_t}, it either reduces the error or yields a marginal increase. For $n_{\delta_t} \gtrsim 3$, its impact is negligible, as errors are already low with or without the model. Hence, despite differences between the impinging-jet and Lévêque cases, the benefit of the model should be interpreted primarily through the degree of refinement within the thermal boundary layer.

Results for all configurations in terms of the relative error in the integrated wall heat flux Q_w^{error}, defined as $Q_w^{error} = \frac{Q_w^* - Q_w^{*\,res}}{Q_w^{*\,res}}$ with $Q_w^{*\,res}$ the integral heat flux of the corresponding wall-resolved case, are summarized[4] in Tab. 5.4. The error is drastically reduced with the model in Regions 1 for high Pr cases (cases A, B, E and F), for which the n_{δ_t} range includes

---

[4] The comparison between coarse meshes with and without the model must be interpreted with care: depending on the distance from the jet, positive and negative errors may compensate each other, which can reduce the apparent overall error.

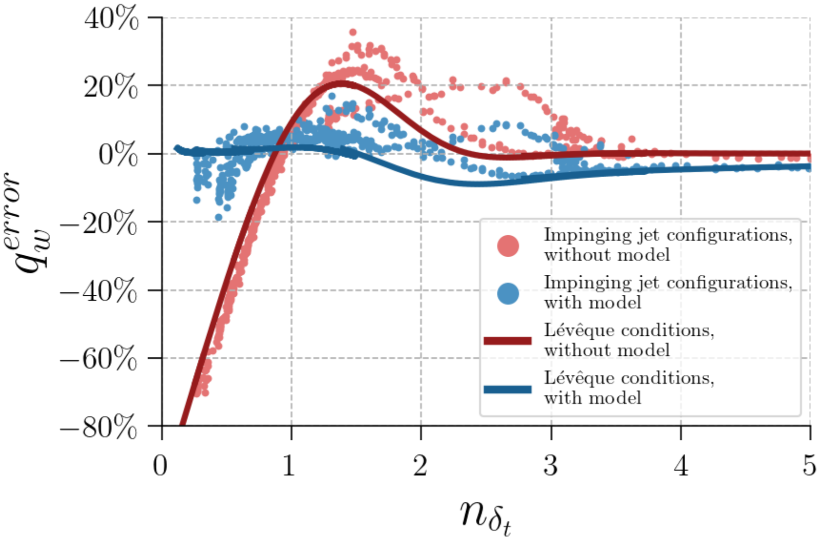

Figure 5.13: Relative error on q_w vs. n_{δ_t} for all impinging jet configurations, without (blue dots) and with the model (red dots) (see Tab. 5.2). Red and blue lines show the trends under Lévêque conditions (see chapter 4).

values below unity (see Tab. 5.3). For case E ($Pr = 10$) the model still demonstrate a notable improvement in region 1, and for case D ($Pr = 1$), errors are already near zero. Overall, errors in Regions 2 and 3 and over the entire plate are reduced or remain close to zero.

The gain in terms of computational cost is reported in Tab. 5.5 for all configurations. The CPU time is dominated by the mesh resolution, with no additional cost introduced by activating the thermal wall model. Hence, similar q_w distributions (and by extension Q_w^*) can be obtained at a fraction of the computational expense compared to wall-resolved cases. For instance, the computational cost is reduced by 68% for case A ($Pr = 158$, $Re = 898$). The benefit is more pronounced as the thermal boundary layer becomes thinner, as illustrated by case B ($Pr = 1000$), where the computation time is reduced by 93%. Under the constraints imposed by the CFL and Fourier numbers (for advection and diffusion, respectively), the speedup is strongly influenced by the increase in time step. For case B ($Pr = 1000$), which uses a very fine wall-resolved mesh, the time step increases by a factor of about 7 when switching to the coarse mesh, much larger than the factor 2 observed in the lower Pr configurations. This large increase is driven by a much stronger growth of the near-wall cell height. For case F, a high Re and high $\dot{V}$ configuration, the time step increases by only a factor of 1.3, as the global time step may be constrained by the high velocity in a cell away from the wall, a point that remains to be confirmed.

Cases	Regions			
	1	2	3	All regions
$\mathbf{A_c}$	-41	-4.9	20	3.9
$\mathbf{A_c^m}$	-8.4	3.1	2.6	1.5
$\mathbf{B_c}$	-67	-43	-10	-29
$\mathbf{B_c^m}$	-9.5	2.3	3.5	1.4
$\mathbf{C_c}$	12	7.6	-1.2	3.5
$\mathbf{C_c^m}$	1.9	-3.4	-6.2	-4.3
$\mathbf{D_c}$	7.0	-0.1	-1.4	0.0
$\mathbf{D_c^m}$	-0.4	-4.1	-3.2	-3.3
$\mathbf{E_c}$	-24	2.1	20	12
$\mathbf{E_c^m}$	-1.3	4.6	5.5	4.7
$\mathbf{F_c}$	-50	-14	16	-5.5
$\mathbf{F_c^m}$	-9.2	2.7	3.0	1.5

Table 5.4: Relative error Q_w^{error} [%] for the coarse mesh cases, with and without the thermal wall model, separated by flow regions.

Cases	Coarse mesh with model
A	$-69\,\%$
B	$-93\,\%$
C	$-62\,\%$
D	$-65\,\%$
E	$-93\,\%$
F	$-52\,\%$

Table 5.5: Reduction of the calculation time (CPU time) relatively to the wall-resolved case. Calculation times are identical with and without the model.

5.3.3 Assessment with temperature-dependent viscosity

The model was designed under the assumption of uniform liquid properties. In this section, it is evaluated in a more demanding configuration, where properties vary with temperature. The viscosity is particularly sensitive to temperature (see Fig. 5.2), which is common for oils, the target coolant for the industrial application. For configuration $\mathrm{P}_{3_\mathrm{r}}$, with an injection temperature $T_l = 323\,\mathrm{K}$ and a wall temperature $T_w = 393\,\mathrm{K}$, the viscosity ratio satisfies $\frac{\mu_l(T_\infty)}{\mu_l(T_w)} \approx 5$, that is, the viscosity varies by a factor of 5 across the thin thermal boundary layer.

In this realistic, viscosity-dependent case $\mathrm{P}_{3_\mathrm{r}}$, the model is evaluated on a coarse mesh with at least five cells across the film thickness, denoted $\mathrm{P}_{3_\mathrm{c}}^{\mathrm{m}}$. The resulting Nusselt number, Nu, is shown in Fig. 5.14. The error remains large, with only a slight improvement in the impingement zone compared with the coarse mesh without the model $\mathrm{P}_{3_\mathrm{c}}$.

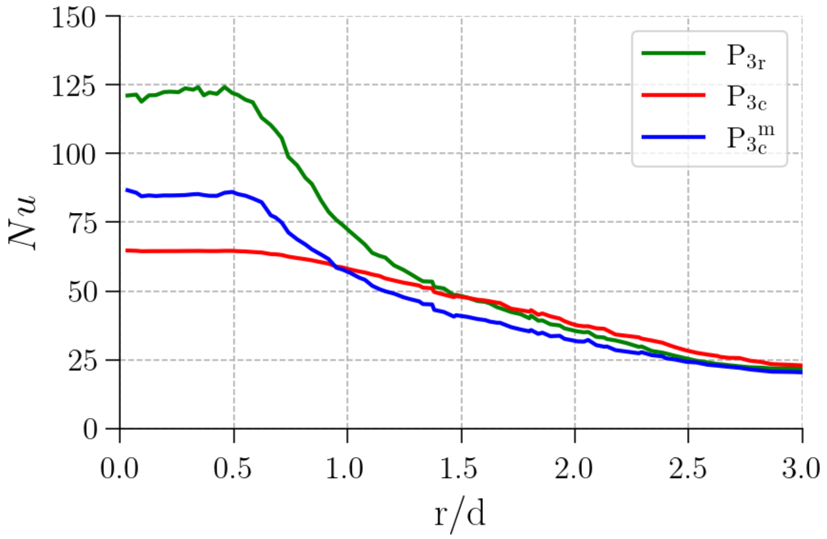

Figure 5.14: Radial profile of Nu obtained with the coarse-mesh case P_6, with ($\mathrm{P}_{6_\mathrm{c}}^{\mathrm{m}}$), and without the thermal wall model ($\mathrm{P}_{6_\mathrm{c}}$), compared with the wall-resolved case $\mathrm{P}_{6_\mathrm{r}}$.

This behavior stems from the non-linear velocity field across the first near-wall cell of the coarse mesh (denoted cell_1) and across δ_t, which contradicts a core model assumption, together with under-resolution of the velocity field on the coarse mesh. As shown in Fig. 5.15, when viscosity varies strongly across a thin thermal boundary layer (case $\mathrm{P}_{3_\mathrm{r}}$), the near-wall velocity is no longer linear within δ_t, and by extension across cell_1. The coarse mesh cannot capture this curvature near the wall (case $\mathrm{P}_{3_\mathrm{c}}$). By contrast, in the uniform viscosity case $\mathrm{G_r}$, identical to $\mathrm{P_{3r}}$ except that all properties are fixed at the film temperature $T_f = \frac{T_\infty + T_w}{2} = 358\,\mathrm{K}$, the velocity profile remains essentially linear within δ_t (and across $\mathrm{cell_1}$). Since the thermal wall model presumes that the near-wall velocity field is already resolved and linear, applying it when the velocity is under-resolved and non-linear leads to inaccurate predictions of the temperature field and of the wall heat flux q_w[5].

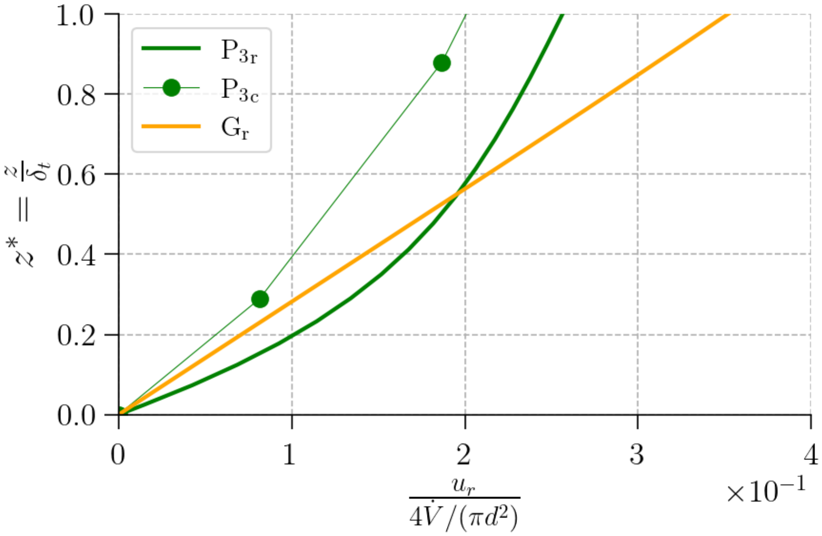

Figure 5.15: Profiles of the near-wall radial velocity in the impinging-jet configuration $\mathrm{A_{3r}}$ and in the companion case $\mathrm{G_r}$ with uniform properties fixed at T_f.

An extended version of the thermal wall model, capable of handling fluids with strongly temperature-dependent viscosity, is therefore of clear interest for the industrial context considered. The next section, Part III, deals with the extension of the TWM, TWM-var, tailored for fluids with strong temperature-dependent viscosity.

---

[5] Refining the mesh to make the model applicable is not a practical remedy, because the resolution needed to capture the velocity field within the thermal boundary layer is comparable to that required to resolve the temperature field. With such a mesh, q_w is already accurately obtained without a model.

Part III

Thermal wall model extended to fluids with temperature-dependent viscosity

The oil used in the impinging-jet configuration (chapter 5) exhibits a strong viscosity–temperature dependence. The temperature range, between 293 K and 393 K, is representative of the temperatures reached in the realistic context of cooling end windings, which can lead to a viscosity reduced by a factor 15 near the wall. Although temperature sensitivity can vary significantly between oils [26], a strong dependence on temperature is usually observed over the temperature range relevant to the industrial application.

TWM-cst was designed for flows with a uniform viscosity. Its assessment on the impinging-jet configuration (see section 5.3.3), using realistic oil properties and temperature range (leading to a viscosity variation up to a factor of 5 between wall and bulk viscosity), revealed a significant error in the wall heat-flux prediction. It is therefore necessary to address the large viscosity variation by introducing an extension of the model, denoted TWM-var. This extension is described in chapter 6, and results with a temperature-dependent viscosity law are presented for a 2 dimensional thermal boundary layer development in chapter 7 and the impinging-jet configuration in chapter 8.

CHAPTER 6

Thermal wall model for variable viscosity: description and implementation

This chapter describes the extension of the thermal wall model (TWM-var) to handle high viscosity variations induced by temperature within the thermal boundary layer. Specifically, the mathematical development and the implementation within the finite-volume framework are detailed.

6.1 Mathematical formulation

As with the TWM-cst, the TWM-var must also provide the wall heat flux q_w for each near–wall cell. The working context and hypotheses are the same as for the TWM-cst, except that the assumption of negligible viscosity variation with temperature is dropped. In particular, viscosity may vary substantially across the thermal boundary layer, thereby influencing the velocity field; as a result, temperature can no longer be treated as a passive scalar and the momentum and energy equations become coupled.

As a reminder, the academic context considered here is a thermal boundary layer developing over a flat wall at infinite Pr. The impact of temperature dependent viscosity on the laminar boundary layer development has been study in [80] but for moderate Pr

number. Since the thermal boundary layer lies deep inside the dynamic boundary layer, the streamwise velocity outside and near the thermal layer evolves approximately linearly. However, this does not hold inside the thermal boundary layer, where viscosity variations with temperature invalidate the linear–velocity assumption of TWM-cst as highlighted by case P_{3r} in Fig. 5.15. Consequently, a coarse mesh across the thermal boundary layer that cannot resolve the temperature profile will fail to capture the resulting nonlinear velocity profile (see case P_{3c} in Fig. 5.15) and the associated wall shear stress τ_w. The TWM-var applied on a coarse mesh must therefore account for the nonlinear near-wall velocity profile to predict τ_w accurately, in addition to q_w, which is also influenced by this profile.

Guided by wall–function practice (see section 2.2.2), it is assumed that the thermal boundary layer resides well inside the dynamic boundary layer, allowing us to drop the convective term in the boundary–layer momentum equation across and in the vicinity of δ_t[1]. From Eq. 2.1.7, across and near δ_t this yields

$$\tau_w = \tau_{yx} = \mu \left(T(y)\right) \frac{\partial u}{\partial y} \tag{6.1.1}$$

which is analogous to the wall–function treatment when using Eq. 2.2.18. From Eq. 6.1.1, an expression for u follows:

$$u(x, y) = \int_0^y \frac{\tau_w(x)}{\mu \left(T(x, Y)\right)} dY \tag{6.1.2}$$

A common assumption is the existence of self-similar velocity and temperature profiles so that, both fields, when written in scaled form, depend only on a single wall-normal dimensionless coordinate. We adopt this assumption across and beyond δ_t. First, the scaled temperature profile is assumed to match the Lévêque proposition (see section 3.1),

$$T^* = P_T(y^*) \tag{6.1.3}$$

even though the velocity field is not strictly linear across δ_t (one of Lévêque's original hypotheses). The resulting temperature profile is shown in Fig. 6.1 and this simplification will be assessed a posteriori.

Secondly, the velocity must be scaled to obtain a dimensionless profile with self-similar and thus universal characteristics. It is natural to scale the wall–normal distance by the thermal thickness δ_t, defining $y^* = y/\delta_t$. Indeed, u should depend primarily on the position

---

[1] The convective term in the boundary layer energy equation cannot be neglected, since convective and conductive effects are of comparable magnitude at a distance δ_t from the wall.

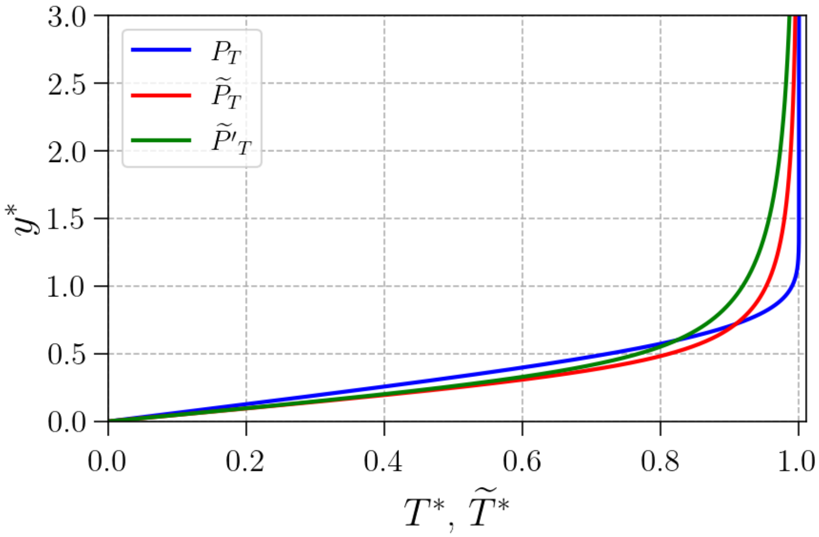

Figure 6.1: Comparison of P_T, the Lévêque temperature profile across the thermal boundary layer (see section 3.1), $\widetilde{P}'_T$, the flow temperature profile used in the TWM-var (introduced in section 6.2.1), and $\widetilde{P}_T$, the flow temperature profile used in the iso–viscosity model TWM-cst (see Eq. 3.3.11).

relative to the thermal boundary layer, since u varies nonlinearly only where μ varies (i.e., within the thermal layer) and reverts to an approximately linear trend for $y > \delta_t$. Using Eq. 6.1.2, the velocity written in terms of $y^* = y/\delta_t$ is

$$u(x, y^*) \;=\; \tau_w(x)\, \delta_t(x) \int_0^{y^*} \frac{1}{\mu(T(x, Y^*))}\, dY^* \tag{6.1.4}$$

where $u(x, y^*)$ and $T(x, y^*)$ denote the same physical fields as $u(x, y)$ and $T(x, y)$, but expressed in the coordinates (x, y^*) instead of (x, y) for notational convenience. The expression above shows that the integral is independent of τ_w and δ_t, which factor out of the integral. It is therefore natural to scale u by a quantity that removes any dependence on τ_w and δ_t from the dimensionless velocity. A straightforward choice is the velocity at the edge of the thermal layer, $u(x, y^* = 1)$. This leads to the scaled velocity

$$u^*(x, y^*) = \frac{u(x, y^*)}{u(x, y^* = 1)} \tag{6.1.5}$$

and, using Eq. 6.1.2, $u^*(x, y^*)$ can be written as

$$u^*(x, y^*) = \frac{\displaystyle\int_0^{y^*} \frac{1}{\mu(T(x, Y^*))} \, dY^*}{\displaystyle\frac{1}{\mu_{eq}}} \tag{6.1.6}$$

$$\text{with} \quad \frac{1}{\mu_{eq}} = \int_0^1 \frac{1}{\mu(T(x, Y^*))} \, dY^* \tag{6.1.7}$$

The quantity $u^*(x, y^*)$ is independent of τ_w and δ_t, so the dimensionless profile remains valid regardless of the values of these two variables. It still depends, however, on the viscosity law $\mu(T)$ and on the temperature profile $T(x, y^*)$. Since $T^*(x, y^*)$ is assumed known, equal to the Lévêque profile P_T $\forall x$, we write from the definition of T:

$$T(x, y^*) = T_w(x) - P_T(y^*)\big(T_w(x) - T_\infty\big) \tag{6.1.8}$$

Hence, $u^*(x, y^*)$ ultimately depends only on $T_w(x)$, T_∞, $\mu(T)$ and y^*. In other words, for uniform T_w and T_∞ and a fixed viscosity law $\mu(T)$, the profile $u^*(x, y^*)$ can be regarded as universal, i.e. a function of y^* only, but must be recomputed if any of these inputs change. This is convenient because these three parameters are typically easy to obtain even on under–resolved meshes, unlike τ_w and δ_t. Typically, T_∞ is taken as the inlet temperature of the coolant; the law $\mu(T)$ is tied to the coolant and thus well-defined; and T_w may vary from one near-wall cell to another. In what follows, we consider a single set of parameters; consequently, $u^*(x, y^*)$ is treated as a universal dimensionless profile[2], denoted P_u, depending only on y^*:

$$u^* = P_u(y^*) \tag{6.1.9}$$

$P_u(y^*)$ is computed from Eq. 6.1.6 and the solution is illustrated in Fig. 6.2 using a typical oil viscosity law $\mu(T)$, represented by the kinematic viscosity $\nu_l(T)$ in Fig. 5.2 (blue curve; $\rho_l = 0.808 \times 10^3\,\mathrm{kg\,m^{-3}}$). The temperatures $T_w = 393\,\mathrm{K}$ and $T_\infty = 323\,\mathrm{K}$ are chosen so that $\mu_\infty/\mu_w \approx 5$, with $\mu_\infty = \mu(T_\infty)$ and $\mu_w = \mu(T_w)$, a value representative of the industrial application.

Analogously to the scaled velocity profile, the equivalent viscosity μ_{eq} defined in Eq. 6.1.7 depends only on T_w, T_∞, and the law $\mu(T)$. Using its definition together with Eq. 6.1.4,

---

[2] For a spatially varying T_w, one possible approach is to precompute the dimensionless profiles for a discrete set of wall temperatures, or alternatively to compute and regularly update a dedicated profile for each near-wall cell.

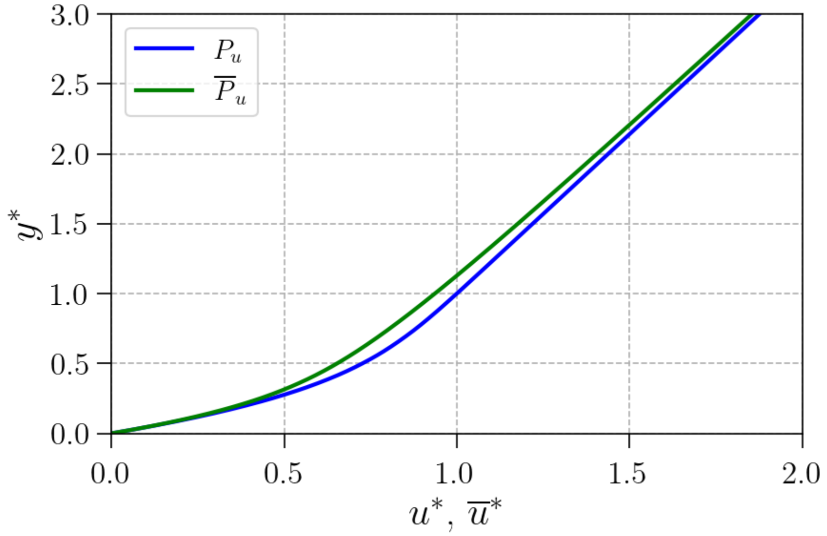

Figure 6.2: P_u, the universal dimensionless velocity profile across the thermal boundary layer, for a typical oil viscosity law $\mu(T)$ and a realistic set of $T_w = 393\,\mathrm{K}$ and $T_\infty = 323\,\mathrm{K}$ in the industrial context ($\mu_\infty/\mu_w = 5$). Also shown is $\overline{P}_u$, the mean (cell–averaged) velocity profile derived from P_u (see Eq. 6.2.17).

the wall shear stress can be written as

$$\tau_w(x) = \mu_{eq}\frac{u(x, y = \delta_t)}{\delta_t(x)} = \mu_{eq}\frac{u(x, y^* = 1)}{\delta_t(x)} \tag{6.1.10}$$

Thus, μ_{eq} has a clear physical interpretation: it is the viscosity that would yield the same τ_w if the velocity varied linearly across the thermal boundary layer thickness δ_t.

6.2 Numerical implementation

As with the thermal wall model for constant viscosity, the extended version must also provide the wall heat flux q_w for each near–wall cell. Because temperature and velocity are strongly coupled through the temperature–dependent viscosity $\mu(T)$, both fields must be captured accurately. If the mesh does not resolve the temperature within the thermal boundary layer, it will likewise fail to resolve the velocity profile, which is non-linear inside the thermal layer. Consequently, the extended model should also correct the dynamics by supplying a consistent wall shear stress τ_w for each near–wall cell.

For what follows, we consider the near–wall cell $cell_1$. The proposed model is expressed through two functions, f_1 and f_2, of the relevant input parameters:

$$q_w = f_1\left(T_1, T_w, T_\infty, y_1, k\right) \tag{6.2.1}$$

and

$$\tau_w = f_2\left(u_1, \delta_t, y_1^*, \mu_{eq}\right) \tag{6.2.2}$$

where $y_1^* = y_1/\delta_t$. The locations of these variables in a Cartesian mesh are illustrated in Fig. 6.3.

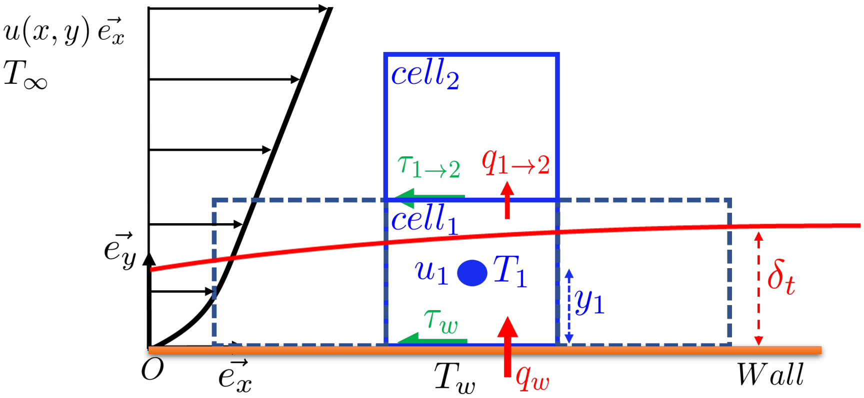

Figure 6.3: Illustration of a uniform Cartesian grid adjacent to a wall, highlighting the first off–wall control volume $cell_1$; the filled dot marks its centroid. The thermal boundary layer, shown in red, is sketched for a coarse mesh relative to a thin thermal boundary layer The velocity profile is given as an example for a typical oil.

6.2.1 Wall heat flux calculation

The numerical steps behind f_1 (see Eq. 6.2.1) to determine q_w for the near-wall cell, $cell_1$, are the same as in the TWM-cst and are detailed in section 3.2. The different steps are summarized in Fig. 6.4 and the equations stated in this section are collected in Tab. 6.1. The only difference with TWM-cst is that the modified profile, denoted $\widetilde{P'}_T$, is used instead of $\widetilde{P}_T$ to determine y_1^* from T_1^*:

$$y_1^* = \widetilde{P'}_T^{-1}\left(T_1^*\right) \tag{6.2.3}$$

Indeed, as in the TWM-cst, f_1 relies on a dimensionless temperature profile where the Lévêque profile P_T is employed here as well. To remain consistent with the finite–volume method, a cell–averaged profile $\widetilde{P'}_T$ based on P_T is used. In the TWM-cst, $\widetilde{P}_T$ was computed from Eq. 3.3.11 under a linear–velocity assumption across the near-wall cell. Since this assumption no longer holds, we replace it with the more general relation derived from Eq. 3.3.9:

$$\widetilde{P}'_T(x, y^*) = \frac{\int_0^{2y^*} u(x, Y^*)\, P_T(Y^*)\, \mathrm{d}Y^*}{\int_0^{2y^*} u(x, Y^*)\, \mathrm{d}Y^*} \tag{6.2.4}$$

Introducing u^* via Eq. 6.1.5 and denoting the dimensionless velocity profile by $P_u(y^*)$ (see Eq. 6.1.9), this becomes

$$\widetilde{P'}_T(y^*) = \frac{\int_0^{2y^*} P_u(Y^*)\, P_T(Y^*)\, \mathrm{d}Y^*}{\int_0^{2y^*} P_u(Y^*)\, \mathrm{d}Y^*} \tag{6.2.5}$$

Using the numerically calculated profile P_u from Eq. 6.1.6 in Eq. 6.2.5 yields the profile $\widetilde{P'}_T$, shown in green in Fig. 6.1.

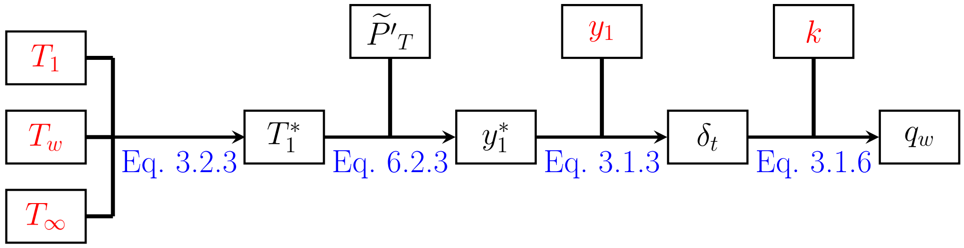

Figure 6.4: Overview of the steps involved in the TWM-var. Input parameters are highlighted in red.

6.2.2 Wall shear stress calculation

The numerical steps underlying f_2 (see Eq. 6.2.2) to determine τ_w for the near-wall cell, $cell_1$, are summarized in Fig. 6.5, and the equations stated in this section are collected in Tab. 6.2.

Following the steps summarized in Fig. 6.5, the relative position y_1^* is used and already available from the q_w computation (see Fig. 6.4).

The equivalent viscosity μ_{eq} must be evaluated in advance from Eq. 6.1.7, given the viscosity law $\mu(T)$ and the temperature profile $T(x_1, y^*)$. The latter is obtained from Eq. 6.1.8 using T_w, T_∞, and the Lévêque profile $P_T(y^*)$. The free-stream temperature T_∞ is assumed uniform (coolant inlet temperature), whereas T_w may vary from cell to cell, so μ_{eq} can be cell-dependent.

Reference	**Expression**
Dimensionless temperature	
Eq. 3.2.3	$T_1^* = \dfrac{T_1 - T_w}{T_\infty - T_w}$
Universal dimensionless profiles	
Eq. 3.3.9	$\widetilde{P}_T(y^*) = \frac{\int_0^{2y^*} u(Y^*) P_T(Y^*) \, dY^*}{\int_0^{2y^*} u(Y^*) \, dY^*}$
Eq. 3.3.11	$\widetilde{P}_T(y^*) = \frac{1}{2y^{*2}} \int_0^{2y^*} Y^* P_T(Y^*) \, dY^*$
Eq. 6.1.9	$u^* = P_u(y^*)$
Dimensionless velocity	
Eq. 6.1.5	$u^*(x, y^*) = \frac{u(x,y^*)}{u(x,y^*=1)}$
Eq. 6.1.6	$u^*(x, y^*) = \dfrac{\displaystyle\int_0^{y^*} \frac{1}{\mu(T(x, Y^*))} \, \mathrm{d}Y^*}{1/\mu_{eq}}$
Dimensionless wall-normal coordinate	
Eq. 3.1.3	$y^* = \dfrac{y}{\delta_t(x)}$
Wall heat flux	
Eq. 3.1.6	$q_w \approx 1.572 \, k \, \dfrac{T_w - T_\infty}{\delta_t}$

Table 6.1: Summary of the equations stated in section 6.2.1.

The dimensionless velocity u_1^* is then determined from y_1^*. To this end, the self-similar velocity profile $P_u(y^*)$ is first constructed using Eq. 6.1.6, once μ_{eq}, the viscosity law $\mu(T)$, and the temperature profile $T(x_1, y^*)$ from Eq. 6.1.8 are known. To be consistent with the finite-volume method (see section 6.2.3), a cell-average version of this profile, denoted $\overline{P}_u(y^*)$, is then used to relate the first-cell position y_1^* to u_1^* as:

$$y_1^* = \overline{P}_u^{-1}(u_1^*), \tag{6.2.6}$$

where $\overline{P}_u^{-1}$ denotes the inverse function of $\overline{P}_u$.

The velocity u_1 is used together with the dimensionless value u_1^* to determine $u(x_1, y = \delta_t)$, i.e. the velocity at a distance δ_t from the wall. However, the relation defining the dimensionless velocity (see Eq. 6.1.5), recalled here for $cell_1$,

$$u(x_1, y^* = 1) = \frac{u(x_1, y_1^*)}{u^*(x_1, y_1^*)} \tag{6.2.7}$$

cannot be directly used, because in the finite-volume framework u_1 cannot be considered equal to $u(x_1, y_1^*)$. Since the computed velocity u_1 is expected to match the exact mean velocity $\overline{u}(x_1, y_1^*)$ (see section 6.2.3), the cell-averaged version of this relation is used instead, which is found to have a similar form (see Eq. 6.2.16). From Eq. 6.2.16, it yields

$$u(x_1, y^* = 1) = \frac{u_1}{u_1^*} \tag{6.2.8}$$

Finally, τ_w follows from Eq. 6.1.10. The equivalent viscosity μ_{eq} is used, and the thermal thickness δ_t is also required to determine τ_w; δ_t is obtained during the q_w calculation procedure (see Fig. 6.4).

Further details on the construction of $\overline{P}_u(y^*)$ and on the link between $u(x_1, y^* = 1)$ and u_1 are provided next.

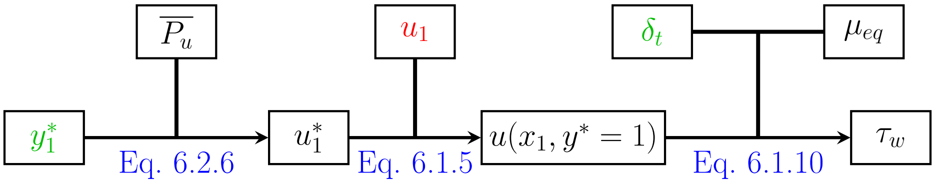

Figure 6.5: Overview of the steps involved in the thermal wall model extension to get τ_w. Input parameters are highlighted in red. Parameters that have already been calculated to determine the wall heat flux (see Fig. 6.4) are highlighted in green.

Reference	Expression
Temperature field	
Eq. 6.1.8	$T(x,y^*) = T_w(x) - P_T(y^*)\big(T_w(x) - T_\infty\big)$
Equivalent viscosity	
Eq. 6.1.7	$\dfrac{1}{\mu_{eq}} = \displaystyle\int_0^1 \frac{1}{\mu(T(x,Y^*))}\,\mathrm{d}Y^*$
Dimensionless velocity	
Eq. 6.1.5	$u^*(x,y^*) = \dfrac{u(x,y^*)}{u(x,y^*=1)}$
Eq. 6.2.16	$\overline{u}^*(x,y^*) = \dfrac{\overline{u}(x,y^*)}{u(x,y^*=1)}$
Eq. 6.1.6	$u^*(x,y^*) = \dfrac{\displaystyle\int_0^{y^*} \frac{1}{\mu(T(x,Y^*))}\,\mathrm{d}Y^*}{1/\mu_{eq}}$
Wall shear stress	
Eq. 6.1.10	$\tau_w(x) = \mu_{eq}\dfrac{u(x,y=\delta_t)}{\delta_t(x)} = \mu_{eq}\dfrac{u(x,y^*=1)}{\delta_t(x)}$

Table 6.2: Summary of the equations stated in section 6.2.2.

6.2.3 Effective velocity profile in finite-volumes methods

Similarly to f_1, The finite-volume context must be taken into account for f_2, when determining u_1^* from y_1^* using the universal dimensionless velocity profile (see Fig. 6.5). In the same spirit as section 3.3, and under the assumption that the velocity is parallel to the wall up to the near-wall cell height (aligned with the x-axis, i.e., $v = 0$), mass and momentum conservation are examined along a one-dimensional (1D) stack of near-wall cells that includes $cell_1$. The discretized advective mass flux $\dot{m}_1$ through this 1D line at the $cell_1$ center position x_1 (see Fig. 6.6) reads, as in Eq. 3.3.2:

$$\dot{m}_1 = 2y_1\rho u_1 \tag{6.2.9}$$

Likewise, the discretized advective momentum flux Q_{m_1} at x_1 is

$$Q_{m_1} = 2y_1\rho u_1^2 \tag{6.2.10}$$

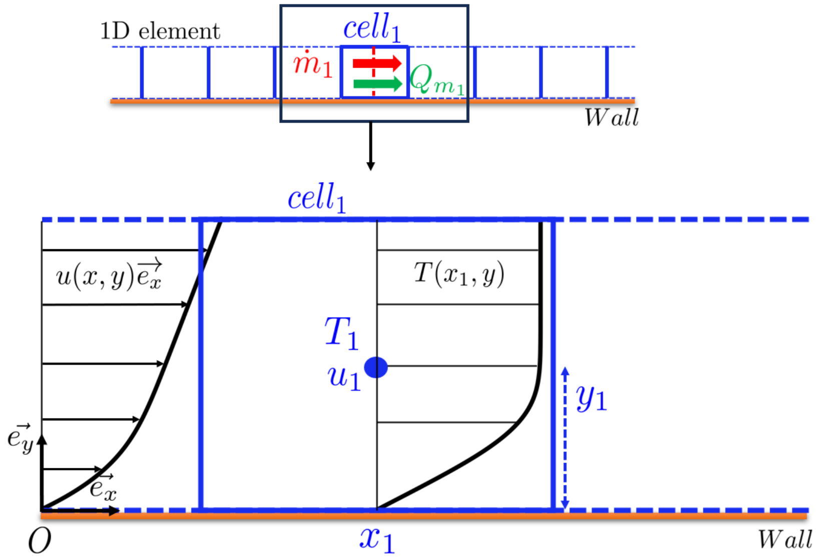

Figure 6.6: Discretized momentum flux Q_{m_1} and mass flux $\dot{m}_1$ along the 1D system at $x = x_1$. They can be approximated using u_1 from $cell_1$ (see Eq. 6.2.9 and Eq. 6.2.10), or computed exactly from the profile $u(x_1, y)$ (see Eq. 6.2.11 and Eq. 6.2.13). The velocity profile shown corresponds to a typical oil with a fivefold viscosity variation between the wall and the bulk flow.

The accurately computed advective mass flux $\dot{m}_1$ should coincide with the exact expression recalled below:

$$\dot{m}(x_1, y_1) = \int_0^{2y_1} \rho\, u(x_1, Y)\, dY \tag{6.2.11}$$

so that $\dot{m}_1 = \dot{m}(x_1, y_1)$ when the numerical solution is accurately resolved. Here, $u(x, y)$ and $T(x, y)$ denote the exact velocity and temperature fields in the domain, in particular, $u(x_1, y)$ and $T(x_1, y)$ are the exact profiles at $x = x_1$ (see Fig. 6.6). Comparing Eq. 6.2.11 with the discrete expression Eq. 6.2.9 shows that the discretized cell velocity u_1 must equal the cell–average velocity

$$\overline{u}(x_1, y_1) = \frac{1}{2y_1} \int_0^{2y_1} u(x_1, Y)\, dY \tag{6.2.12}$$

Similarly the discretized advective momentum flux Q_{m_1} should correspond to the exact formulation

$$Q_m(x_1, y_1) = \int_0^{2y_1} \rho u^2(x_1, Y)\, dY \tag{6.2.13}$$

Combining Eq. 6.2.10 with the corresponding exact expression for Q_{m_1} given in Eq. 6.2.13, shows that u_1 must coincide with the flow velocity $\widetilde{u}(x_1, y_1)$, defined as

$$\widetilde{u}(x_1, y_1) = \left(\frac{\int_0^{2y_1} u^2(x_1, Y)\ dY}{2y_1} \right)^{1/2} \tag{6.2.14}$$

For the numerical solution to be consistent with the exact solution in terms of both mass and momentum, u_1 must be equal to both $\overline{u}(x_1, y_1)$ and $\widetilde{u}(x_1, y_1)$ which is not possible except for the particular case $u(x, y) = 0$. From a thermal point view, predict the good mass flux is critic to be consistent in term of advective heat flux. Thus, u_1 is expected to be consistent with $\overline{u}(x_1, y_1)$.

A dimensionless mean velocity $\overline{u}^*(x_1, y_1)$ can be introduced by rewriting Eq. 6.2.12 in terms of the dimensionless velocity $u^*(x_1, y)$ instead of $u(x_1, y)$:

$$\overline{u}^*(x_1, y_1) = \frac{1}{2y_1} \int_0^{2y_1} u^*(x_1, Y)\, dY. \tag{6.2.15}$$

Substituting the definition of $u^*(x, y^*) = \frac{u(x,y^*)}{u(x,y^*=1)}$ (Eq. 6.1.5) into Eq. 6.2.15 gives:

$$\overline{u}^*(x, y^*) = \frac{\overline{u}(x, y^*)}{u(x, y^* = 1)} \tag{6.2.16}$$

Following the same convention used for the exact flow temperature in section 3.3, the exact mean velocity $\overline{u}(x_1, y_1)$ is denoted as $\overline{u_1^e}$, while the exact velocity at the position (x_1, y_1), denoted as $u(x_1, y_1)$, is abbreviated as u_1^e (see Tab. 6.3 for an overview of the key variables and their definitions).

A modified profile derived from $P_u(y^*)$, denoted $\overline{P}_u(y^*)$, is introduced so that the proper u_1^* is produced from y_1^* (see Fig. 6.5). The profile $\overline{P}_u(y^*)$ follows from $P_u(y^*)$ by the same averaging as in Eq. 6.2.15 after the change of variable $y/\delta_t(x) \to y^*$:

$$\overline{P}_u(y^*) = \frac{\int_0^{2y^*} P_u(Y^*)\, dY^*}{\int_0^{2y^*} dY^*}. \tag{6.2.17}$$

Fig. 6.2 compares the two profiles $P_u(y^*)$ and $\overline{P}_u(y^*)$.

Symbol	**Unit**	**Definition**
Continuous fields		
$\mu(x, y)$	$\mathrm{Pa \cdot s}$	Dynamic viscosity of the fluid.
$\tau_w(x)$	Pa	Wall shear stress.
$u(x, y)$	$\mathrm{m.s^{-1}}$	Exact local velocity.
$\overline{u}(x, y)$	$\mathrm{m.s^{-1}}$	Exact mean velocity calculated along a height $2y$ from the wall (see Eq. 6.2.12).
Discrete parameters		
$x_1,\ y_1$	m	Coordinates of the center of $cell_1$ (see Fig. 6.3).
u_1	$\mathrm{m.s^{-1}}$	velocity of $cell_1$.
u_1^e	$\mathrm{m.s^{-1}}$	Shorthand for $u(x_1, y_1)$: exact velocity at the center of $cell_1$.
$\overline{u_1^e}$	$\mathrm{m.s^{-1}}$	Shorthand for $\overline{u}(x_1, y_1)$: exact mean velocity calculated along the $cell_1$ height.
Universal dimensionless profiles (see Fig. 6.2)		
$*$	–	Generic dimensionless indicator.
$P_u(y^*)$	–	Relation between y^* and $u^*(x, y^*)$[3], valid $\forall x$; derived from the Lévêque profile.
$\overline{P}_u(y^*)$	–	Relation between y^* and $\overline{u}^*(x, y^*)$, valid $\forall x$ (see Eq. 6.2.17).
$\widetilde{P'}_T(y^*)$	–	Relation between y^* and $\widetilde{T}^*(x, y^*)$, valid $\forall x$ (see Eq. 6.2.5).

Table 6.3: Additional main symbols, their units, and definitions, complementing Tab. 3.2.

---

[3] $u(x, y^*)$ denotes the same physical field as $u(x, y)$, but expressed in terms of the coordinate (x, y^*) instead of (x, y) for notational convenience.

6.3 Asymptotics behavior

This section examines the behavior of the model in limiting cases, namely when the viscosity is nearly uniform and when the mesh is either very coarse (relative to δ_t) or very fine. This analysis makes it possible to verify that the model behaves correctly in these limiting configurations.

6.3.1 Uniform viscosity

In the limiting case of uniform viscosity μ, and under the model hypothesis that τ_{yx} is uniform across the near–wall cell, the dimensionless velocity profile is linear within $cell_1$. Consequently, the wall shear stress should be taken as

$$\tau_w = \mu \frac{u_1}{y_1} \tag{6.3.1}$$

In the context of the TWM-cst, τ_w is computed by the solver according to Eq. 6.3.1, since no model correction is applied and the finite–volume discretization is used (see section 2.2.1).

In the TWM-var, for a uniform viscosity μ, the dimensionless velocity obtained from Eq. 6.1.6 yields

$$u^*(y^*) = y^* \tag{6.3.2}$$

so that u^* depends only on y^* and the profile $u^* = P_u(y^*)$ is linear with unit slope. From Eq. 6.2.17 it follows that $\overline{P}_u = P_u$, i.e. the cell-averaged profile has the same linear shape. Hence, in the uniform viscosity limit, the calculation step for u_1^* reduces to,

$$u_1^* = y_1^* \tag{6.3.3}$$

and, by the definitions of u_1^* in Eq. 6.2.8 and y_1^*,

$$\frac{u_1}{y_1} = \frac{u(x_1, y = \delta_t)}{\delta_t} \tag{6.3.4}$$

with $u(x_1, y = \delta_t) = u(x_1, y^* = 1)$. Using this relation, the final step for τ_w in Eq. 6.1.10 can be rewritten as

$$\tau_w = \mu_{eq} \frac{u_1}{y_1} \tag{6.3.5}$$

With the definition Eq. 6.1.7, one has $\mu_{eq} = \mu$. Therefore τ_w is computed exactly as in

Eq. 6.3.1, recovering the correct asymptotic limit.

Concerning the q_w calculation, the only difference between the extension and the constant viscosity model lies in how $\widetilde{P}_T$ is obtained from P_T: the TWM-var uses Eq. 6.2.5, whereas the TWM-cst uses Eq. 3.3.11. In the uniform viscosity limit, since the dimensionless velocity profile becomes linear, these two relations coincide. Consequently, the q_w computed by the extension is consistent with that of the TWM-cst. Because both τ_w and q_w are corrected in an identical manner in this limit, the two model versions yield identical q_w (and τ_w).

6.3.2 Very coarse near-wall cell

The asymptotic case of a very coarse near–wall cell relative to the thermal boundary layer thickness translates mathematically as

$$y_1^* \gg 1 \tag{6.3.6}$$

In this limit, the dimensionless velocity profile P_u can be simplified. From Eq. 6.1.6, the scaled velocity can be written as

$$u^*(x, y^*) = 1 + \frac{\int_1^{y^*} \frac{1}{\mu_\infty}\, dY^*}{\frac{1}{\mu_{eq}(x)}} \tag{6.3.7}$$

where μ_∞ is the viscosity evaluated at the temperature beyond the thermal boundary layer For $y^* \gg 1$, the following approximation holds:

$$u^*(x, y^*) \approx \frac{\int_1^{y^*} \frac{1}{\mu_\infty}\, dY^*}{\frac{1}{\mu_{eq}(x)}} \tag{6.3.8}$$

This relation simplifies to

$$u^* \approx \frac{\mu_{eq}}{\mu_\infty}\, y^* \tag{6.3.9}$$

Accordingly, in this limiting case, $u^* = P_u(y^*)$ can be approximated by a linear relation in y^* with slope μ_{eq}/μ_∞. Using the relation between P_u and $\overline{P}_u$ given in Eq. 6.2.17, it follows that $\overline{P}_u$ is also linear in y^* with the same slope. Hence, u_1^* is predicted from y_1^* (see Fig. 6.5) as

$$u_1^* = \frac{\mu_{eq}}{\mu_\infty}\, y_1^* \tag{6.3.10}$$

Using the definitions of u_1^* (see Eq. 6.2.8) and $y_1^* = \frac{y_1}{\delta_t}$, it follows that

$$\frac{u_1}{y_1} = \frac{\mu_{eq}}{\mu_\infty} \frac{u(x_1, y^* = 1)}{\delta_t} \tag{6.3.11}$$

Given this relation, the final step to compute τ_w using Eq. 6.1.10 can be rewritten as

$$\tau_w = \mu_\infty \frac{u_1}{y_1} \tag{6.3.12}$$

In Eq. 6.3.12, τ_w is obtained exactly as with a linear approximation of the velocity profile across the near–wall cell, but using the viscosity μ_∞. This is consistent with the limiting case of an infinitely thin thermal boundary layer, for which the thermal layer's influence on τ_w becomes negligible. Indeed, the near–wall cell is assumed to lie well inside the dynamic boundary layer, so the hypothesis of a uniform τ_{yx} across the cell holds. With a uniform temperature T_∞ (and thus uniform μ_∞) across $cell_1$ due to the negligible influence of the thermal boundary layer, it follows that τ_w must be given by Eq. 6.3.12.

6.3.3 Very fine near-wall cell

The asymptotic case of a very thin near–wall cell relative to the thermal boundary layer translates mathematically as

$$y_1^* \ll 1 \tag{6.3.13}$$

In this limit, the dimensionless velocity profile P_u can be simplified. From Eq. 6.1.6, the scaled velocity becomes

$$u^*(x, y^*) \approx \frac{\int_0^{y^*} \frac{1}{\mu_w} \, dY^*}{\frac{1}{\mu_{eq}(x)}} \tag{6.3.14}$$

where μ_w is the viscosity at the wall temperature T_w. Hence,

$$u^* \approx \frac{\mu_{eq}}{\mu_w} y^* \tag{6.3.15}$$

Accordingly, in this limiting case, $u^* = P_u(y^*)$ can be approximated by a linear relation in y^* with slope μ_{eq}/μ_w. Using the relation between P_u and $\overline{P}_u$ given in Eq. 6.2.17, it follows that $\overline{P}_u$ is also linear in y^* with the same slope. Hence, u_1^* is predicted from y_1^* (see Fig. 6.5) as

$$u_1^* = \frac{\mu_{eq}}{\mu_w} y_1^* \tag{6.3.16}$$

Using the definitions of u_1^* (see Eq. 6.2.8) and $y_1^* = \frac{y_1}{\delta_t}$, it follows that,

$$\frac{u_1}{y_1} = \frac{\mu_{eq}}{\mu_w} \frac{u(x_1, y^* = 1)}{\delta_t} \tag{6.3.17}$$

Inserting this into Eq. 6.1.10 yields

$$\tau_w = \mu_w \frac{u_1}{y_1} \tag{6.3.18}$$

In Eq. 6.3.18, τ_w is evaluated exactly as in a linear approximation across the near–wall cell, but with the wall viscosity μ_w. This matches the expected limit for a cell placed deep inside the thermal boundary layer: the viscosity is essentially uniform and equal to μ_w over the cell height, the shear τ_{yx} is uniform, and thus τ_w must takes the form of Eq. 6.3.18.

CHAPTER 7

Thermal wall model for variable viscosity: verification under Lévêque conditions

This section assesses the TWM-var using a simple thermal boundary layer development over a flat wall in a single-phase flow that satisfies the model assumptions. Throughout, the setup adheres to Lévêque conditions except for the uniform-properties assumption, i.e. a uniform shear stress across a thin thermal boundary layer, so that the underlying assumptions of the TWM-var remain valid. The test case closely mirrors that of chapter 4, used to validate the constant-viscosity model (TWM-cst), but includes viscosity variations with temperature and several modifications required to meet the hypotheses.

The numerical setup is first detailed. Then, a wall-resolved reference case is introduced to isolate and quantify the impact of temperature-dependent viscosity. Finally, the performance of the TWM-var on this configuration is evaluated.

7.1 Numerical set-up

The configuration consists of the development of the thermal boundary layer over a flat wall at infinite Pr, with a temperature-dependent viscosity. The numerical setup is a two-dimensional domain of length $L = 1$ m and height $H = 4 \times 10^{-2}$ m, as illustrated in

Fig. 7.1.

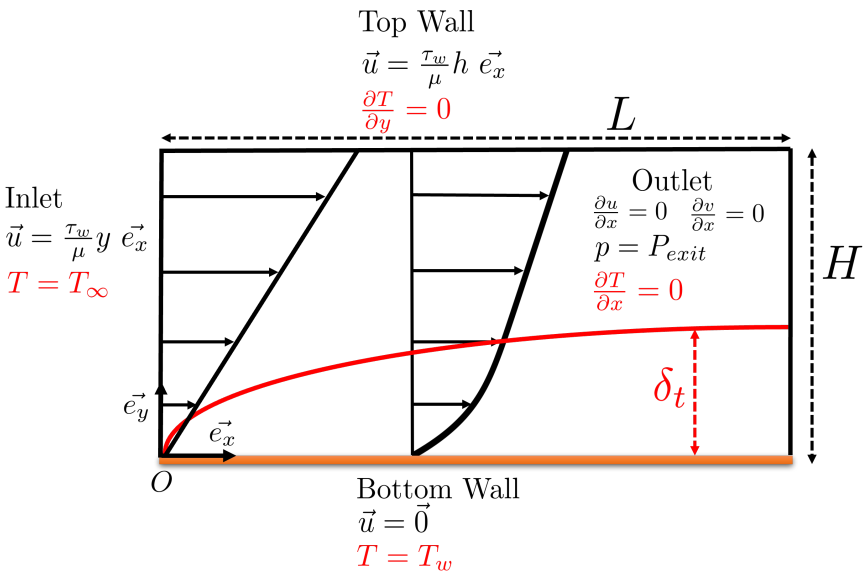

Figure 7.1: Computational domain and boundary conditions.

The top wall is adiabatic and Dirichlet temperature boundary conditions are imposed at the inlet and at the bottom wall: $T_\infty = 323$ K at the inlet and $T_w = 393$ K at the wall. At the inlet, a linear velocity profile parallel to the wall is prescribed with a slope $\left.\frac{\partial u}{\partial y}\right|_{y=0} = 1.5\ \mathrm{s}^{-1}$. No slip is enforced at both walls, with $u = 0$ at the bottom wall and $u = 6 \times 10^{-2}\ \mathrm{m\,s^{-1}}$ at the top wall, which is consistent with the inlet linear velocity profile. A Dirichlet pressure condition is prescribed at the outlet.

To satisfy the infinite Pr assumption, the numerical setup must reproduce the shear-dominated regime that prevails well inside the momentum boundary layer, where the shear stress τ_{yx} is approximately uniform in the wall-normal direction. To obtain this type of shear flow, first, the streamwise pressure gradient is kept negligible relative to the viscous and inertial terms of the momentum equation[1]. This requires limiting the influence of the thermal boundary layer on the core flow, which is achieved by enforcing $\delta_t \ll H$[2], that is,

---

[1] As in the derivation of the boundary layer momentum equation Eq. 2.1.7 from the Navier–Stokes equations Eq. 2.1.2, the streamwise pressure gradient must remain negligible compared with viscous and inertial terms.

[2] The top and bottom wall kinematic conditions are chosen to induce a nearly uniform τ_{yx} across the domain, which is consistent with the imposed linear velocity profile at the inlet, where $\delta_t = 0$ and $\mu(x = 0, y)$ uniform. The flow rate is set by the inlet velocity profile. For $x > 0$, the viscosity profile $\mu(x, y)$ evolves normal to the wall because of the developing thermal boundary layer, which would naturally reshape the velocity profile and alter the flow rate if the pressure gradient remained zero. Since the inlet flow rate is

by operating at a sufficiently large Péclet number[3],

$$Pe = \frac{Q}{\alpha} \tag{7.1.1}$$

where $Q = \displaystyle\int_{y=0}^{y=H} \left.\frac{\partial u}{\partial y}\right|_{y=0} y \, dy$ (with units [m^2.s^{-1}]) is the inlet flow (kept uniform along the domain) expressed for one meter of depth along the third spatial coordinate and α the thermal diffusivity. Second, the inertial term must be negligible compared with the viscous term[4], which is ensured by keeping the Reynolds number small,

$$Re = \frac{Q}{\nu} \tag{7.1.2}$$

with ν the kinematic viscosity. These constraints guide the choice of fluid properties and size of the domain.

Accordingly to these constraints, the following fluid properties are specified: density $\rho = 10^3$ kg m^{-3}, specific heat at constant pressure $c_p = 4.185 \times 10^3$ J kg^{-1} K^{-1}, and thermal conductivity $k = 7 \times 10^{-3}$ W m^{-1} K^{-1}. These property values imply a small thermal diffusivity $\alpha = \frac{k}{\rho c_p} = 1.67 \times 10^{-9}$ m^2 s^{-1}. This, in turn, yields a large Péclet number, $Pe \approx 7 \times 10^5$, and a thin thermal boundary layer relative to the channel height, with $\frac{\delta_t(L)}{H} = 6 \times 10^{-2}$ at the outlet, where δ_t is thickest.

All properties are taken as uniform[5], except for viscosity, in accordance with the model assumptions. The viscosity law is the same as that used for the oil in the impinging jet configuration (see Fig. 5.2) but increased by a factor 10 so that $Re \leq 40$, where the maximum Re is evaluated with $\mu(T_\infty)$, the lowest dynamic viscosity in the domain. In this configuration, the viscosity varies by a factor of $\frac{\mu_\infty}{\mu_w} = 5$ across the thermal boundary layer where $\mu_\infty = \mu(T_\infty)$ and $\mu_w = \mu(T_w)$.

Finally, to satisfy the model assumptions, the wall-normal velocity component v should remain negligible throughout the domain, so that v is negligible compared to u within the

---

fixed, a non-zero streamwise pressure gradient can emerge to enforce global mass conservation. Therefore, the effect of the thermal boundary layer on the bulk flow must be restricted to maintain a low streamwise pressure gradient.

[3] Computing a Pr here is not particularly meaningful, since Pr quantifies the ratio δ/δ_t (see Eq. 2.1.24), and no dynamic boundary layer develops in this configuration. Nevertheless, by enforcing an almost uniform shear stress that mimics the flow deep inside the momentum boundary layer, the case effectively corresponds to an infinite Pr.

[4] This assumption is used to obtain Eq. 6.1.1 from Eq. 2.1.7 and is therefore employed in the TWM-var.

[5] All fluid properties, except for the viscosity, depend only weakly on temperature and therefore vary little over a realistic temperature range (see section 1.4).

near-wall cell. This condition holds when $\frac{\partial \delta_t}{\partial x}$ is sufficiently small[6]. In the present setup, $\frac{\partial \delta_t}{\partial x}$ decreases with x as the thermal boundary layer grows, and over 95% of the domain the normalized gradient satisfies $\frac{\partial \delta_t}{\partial x}/\delta_t < 1\%$. Hence, the assumption is satisfied everywhere except over the first 5% of the wall near the inlet.

The same numerical methods are used as in chapter 4. A uniform, Cartesian mesh is also adopted. The wall-resolved reference mesh (WR-var) uses an x-cell size of 5×10^{-4} m and a y-cell size of 5×10^{-5} m, giving 2000×800 cells in the x and y directions, respectively, for a total of 1 600 000 cells[7]. In addition, four coarser meshes along y, denoted A, B, C, D and E in Tab. 7.1, are considered. To keep the maximum aspect ratio below 5, the x spacing is relaxed for the coarser mesh sets.

Mesh	**A**	**B**	**C**	**D**	**E**	**WR-var**
x-cell size (m)	2.5×10^{-3}	2.5×10^{-3}	2.5×10^{-3}	2.5×10^{-3}	2.5×10^{-3}	5×10^{-4}
y-cell size (m)	4×10^{-3}	2×10^{-3}	1.25×10^{-3}	0.8×10^{-3}	0.5×10^{-3}	5×10^{-5}
Number of cells	4 000	8 000	12 800	20 000	32 000	1 600 000

Table 7.1: Meshes used to evaluate the impact of TWM-var on q_w prediction at high Prandtl number with temperature-dependent viscosity. WR-var denotes the wall-resolved reference mesh.

7.2 Impact of a temperature-dependent viscosity

The development of the thermal boundary layer along the wall is analyzed using the WR-var reference case. To quantify the effect of a non-uniform viscosity, we compare it with a similar case, WR-cst, which uses a uniform viscosity $\mu = \mu_\infty$. The two wall-resolved cases are summarized in Tab. 7.2.

	WR-var	**WR-cst**
μ law	$\mu(T)$	$\mu = \mu_\infty$
μ_∞/μ_w	5	1

Table 7.2: Wall-resolved cases used to evaluate the impact of a non-uniform viscosity.

---

[6] If $\partial \delta_t/\partial x$ is small, then $\partial u/\partial x$ is small across the domain, and by mass conservation Eq. 2.1.6 the wall-normal velocity $v(x, y) = -\int_0^y \frac{\partial u}{\partial x}\,\mathrm{d}y$ becomes small compared to u.

[7] As explained in chapter 4, the thermal boundary layer exhibits much steeper gradients in the y direction than in x over most of the wall, so the mesh is optimized with flattened cells while maintaining a sufficiently low aspect ratio.

In the WR-var case, the viscosity inside the thermal boundary layer is lower, with a maximum reduction by a factor of 5 near the wall. A direct consequence is an approximately 25% thinner thermal boundary layer along the plate, see Fig. 7.2. This trend is corroborated by the green solid line in Fig. 7.3, where the near wall flow has lower temperature (for a given y) and a steeper gradient. The reduction follows from higher velocities within δ_t, which strengthen convection, as indicated by the red solid line. The impact of temperature-dependent viscosity on the velocity and temperature profiles corroborates the observations reported in [80] for laminar boundary layers at moderate Prandtl numbers. It is worth noting that, as the shear stress τ_{yx} is almost kept uniform (see section 7.3 for more details about τ_{yx}), the velocity gradient in WR-cst is also uniform. Whereas in the WR-var case, as μ vary, the velocity gradient is non-uniform, with $\left.\frac{\partial u}{\partial y}\right|_{y=0} = \frac{\mu_\infty}{\mu_w} \left.\frac{\partial u}{\partial y}\right|_{y>\delta_t}$, so the product $\mu\frac{\partial u}{\partial y} = \tau_{yx}$ remains uniform.

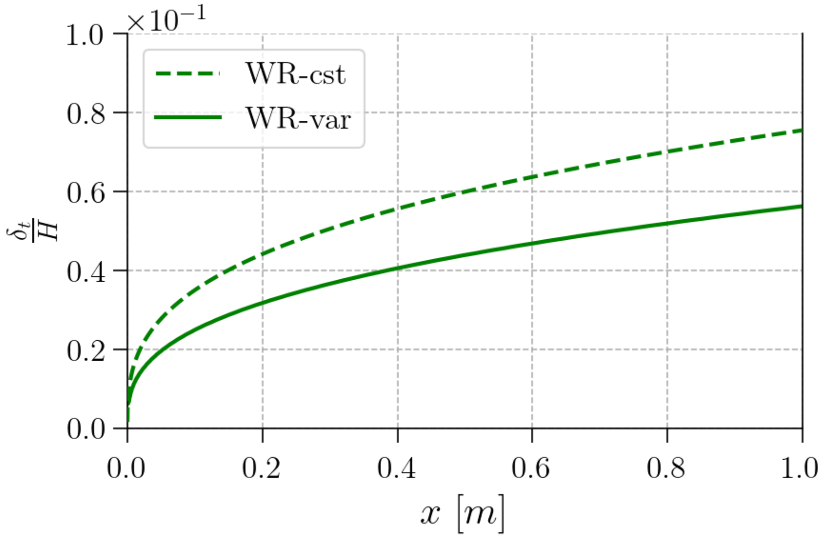

Figure 7.2: Normalized thermal boundary layer thickness along the bottom wall, comparison between cases WR-var and WR-cst.

In the WR-var case, the fluid adjacent to the wall is cooler. Accordingly, the near-wall temperature gradient $\left.\frac{\partial T}{\partial y}\right|_{y=0}$ is larger, so the wall heat flux[8] increases, $q_w = -k \left.\frac{\partial T}{\partial y}\right|_{y=0}$, as seen in Fig. 7.4. The wall shear stress τ_w decreases slightly in the WR-var configuration compared with WR-cst (see Fig. 7.4), consistent with the higher velocity at $y = \delta_t$ in WR-var. With an identical top-wall velocity between cases, an almost linear profile between

---

[8] Throughout this chapter, q_w and τ_w are expressed per meter of depth along the third spatial coordinate.

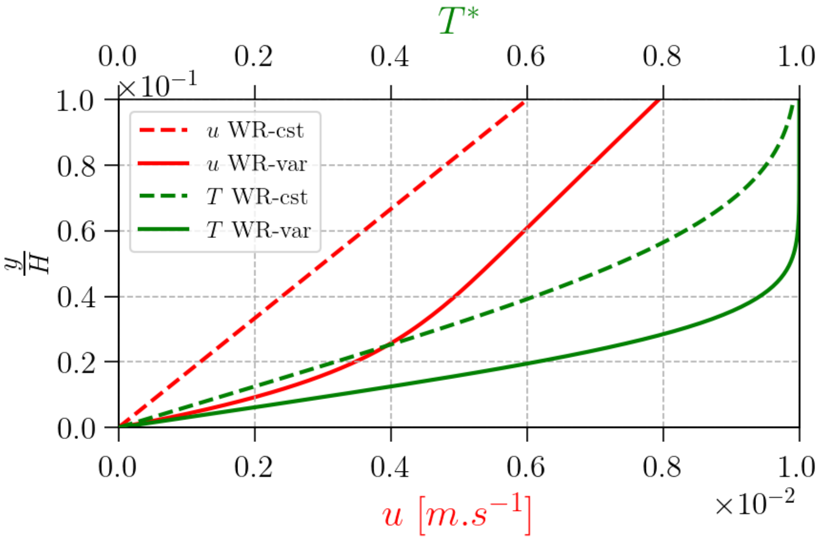

Figure 7.3: Temperature and velocity profiles near the bottom wall, taken at $x = 0.8\,m$, comparison between cases WR-var and WR-cst.

δ_t and H then implies a slightly smaller uniform slope $\frac{\partial u}{\partial y}\Big|_{y>\delta_t}$ in WR-var. Because τ_{yx} is approximately uniform in the wall-normal direction, $\tau_w \approx \mu_\infty \left.\frac{\partial u}{\partial y}\right|_{y>\delta_t}$, hence τ_w is slightly lower in WR-var. The effect remains small, since $\delta_t \ll h$. Along the plate, as δ_t increases, τ_w declines mildly with x. Near the inlet, where δ_t is very thin, τ_w is essentially identical between both cases.

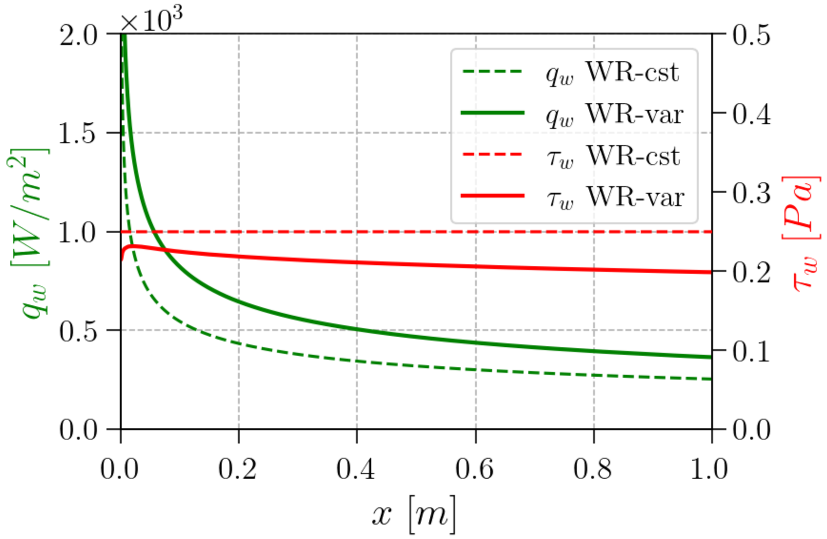

Figure 7.4: Wall heat flux and wall shear stress along the bottom wall, comparison between cases WR-var and WR-cst.

7.3 Fulfillment of model assumptions

The TWM-var assumptions, (see section 6.1), are expected to hold in the present configuration. Before assessing the model, these assumptions are verified in the wall-resolved results.

The model assumes a self-similar temperature profile whose shape is close to the Lévêque profile P_T. Fig. 7.5 shows five profiles of the WR-var case at different streamwise positions. When the wall-normal coordinate y is scaled by δ_t, and the temperature is nondimensionalized with T_w and T_∞, the profiles collapse onto a single curve, which indicates self-similarity across δ_t. The collapsed profile lies very close to P_T. Thus, although a strictly linear velocity profile (one of the prerequisites of Lévêque theory) is not satisfied under variable viscosity, the dimensionless temperature profile remains close to the Lévêque profile, and the corresponding TWM-var hypothesis is considered valid with the proposed numerical set-up.

Given that the temperature profiles are close to the P_T profile, the viscosity evolution $\mu(T(y))$ across δ_t is expected to follow $\mu(P_T(y))$. This is confirmed in Fig. 7.6 by plotting $\frac{\mu(P_T(y))}{\mu_w}$ as a black line and comparing it with several viscosity profiles extracted across the domain.

The model assumes a uniform τ_{yx} across δ_t, which is satisfied with the proposed nu-

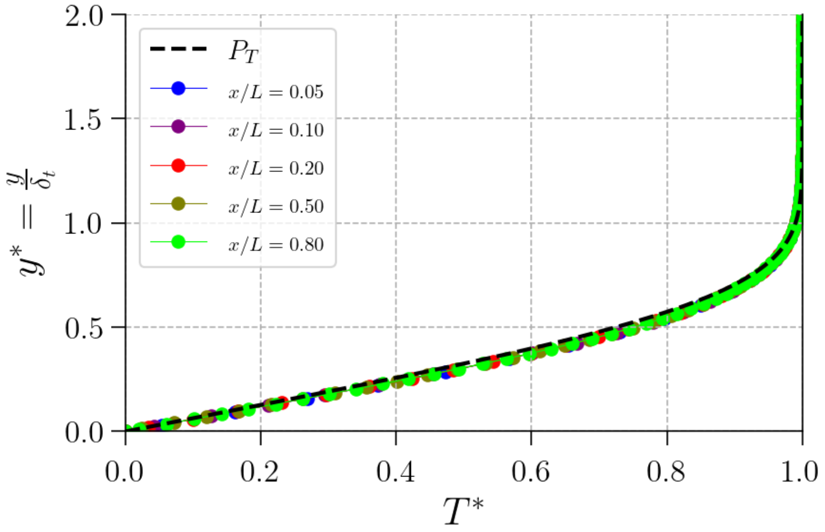

Figure 7.5: Near-wall dimensionless temperature profiles of the wall-resolved case WR-var. Comparison with the theoretical profile P_T.

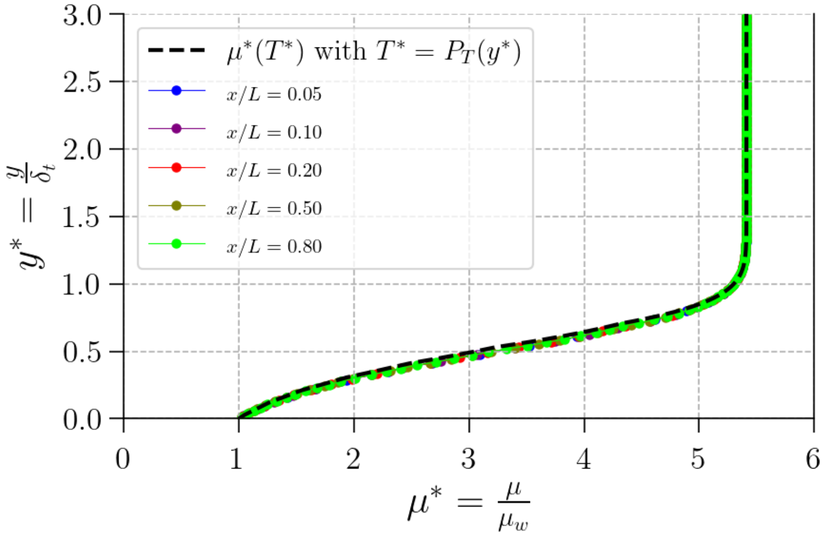

Figure 7.6: Distribution of near-wall dimensionless viscosity profiles. Comparison with the theoretical distribution.

merical set-up as shown in Fig. 7.7. However, the stronger model assumption of a uniform τ_{yx} across the near-wall cells is potentially not fully met. The ratio $\frac{\tau_{yx}}{\tau_w}$ varies and reaches about 1.2 at $y = 10\,\delta_t$, so a near-wall cell with height $2y_1 = 10\,\delta_t$, or larger, corresponding to $n_{\delta_t} = 0.1$, may introduce an error. This non-uniformity of τ_{yx} may stem from a residual streamwise pressure gradient, or from a Reynolds number that is not sufficiently low.

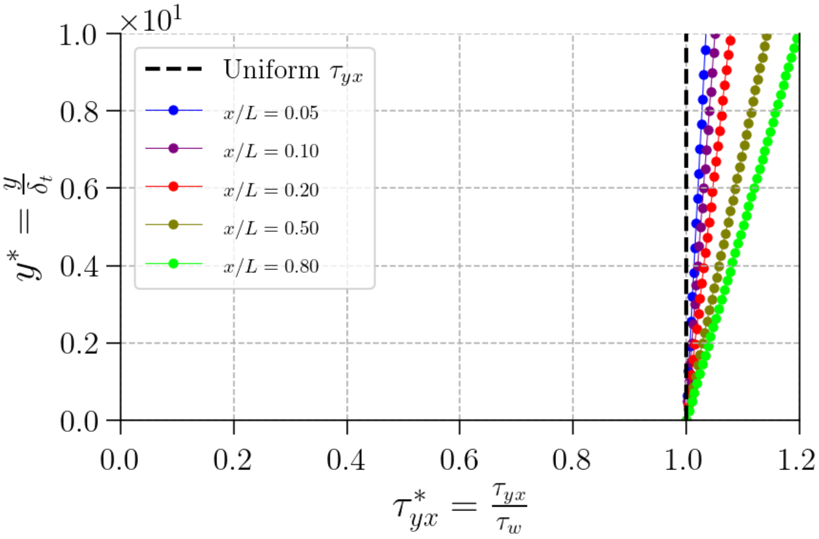

Figure 7.7: Distribution of near-wall dimensionless shear-stress profiles of the wall-resolved case WR-var. Comparison with the uniform shear stress assumption.

Finally, the model assumes a self-similar velocity profile, denoted P_u, shown as a black line in Fig. 7.8. The dimensionless velocity profiles from the wall-resolved case collapse onto a single curve, which confirms self-similarity, and they agree well with the theoretical profile P_u for $y < 2\,\delta_t$. At larger y, a slight offset appears, which likely reflects the small departure from a perfectly uniform τ_{yx} across the domain.

These results from the WR-var case validate the assumptions of TWM-var in the context of the proposed numerical set-up, with only a potential error for very coarse meshes ($n_{\delta_t} \lesssim 0.25$), for which τ_{yx} varies by more than 10 % across the near-wall cell and hence deviates from the assumption of uniform shear stress.

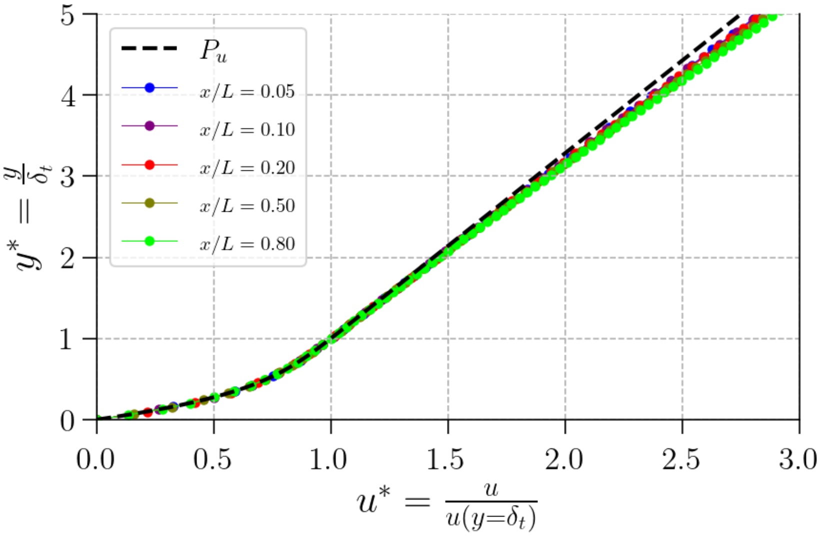

Figure 7.8: Near-wall dimensionless velocity profiles of the wall-resolved case WR-var. Comparison with the theoretical profile P_u.

7.4 TWM-var assessment

The TWM-var is now assessed on the coarse meshes summarized in Tab. 7.1. Results are compared with the corresponding coarse-grid solutions without a model, with TWM-cst, and they are validated against the wall-resolved (WR-var) reference.

7.4.1 Dynamic analysis

We first examine the streamwise evolution of the wall shear stress τ_w using coarse mesh A. This choice enables assessment on a relatively coarse grid. On this grid, the number of cells across the thermal boundary layer thickness satisfies $0.1 < n_{\delta_t} < 0.6$ for $0.025 < \frac{x}{L} < 1$, where n_{δ_t} denotes the cell count across δ_t. Fig. 7.9 plots τ_w versus the x position. The results show that TWM-var drastically improves the prediction relative to both the case without a model and TWM-cst, which yield similar trends and errors.

Fig. 7.10 shows the dimensionless velocity profile for $n_{\delta_t} \approx 0.5$ (obtained at $x = 0.9\,m$ with mesh A), since the numerical outcome depends primarily on n_{δ_t}. The TWM-var results give a near-wall velocity u_1 consistent with the expected value $\overline{u_1^e}$ (see Tab. 6.3 for variable definitions) computed from the WR-var results and indicated by the green

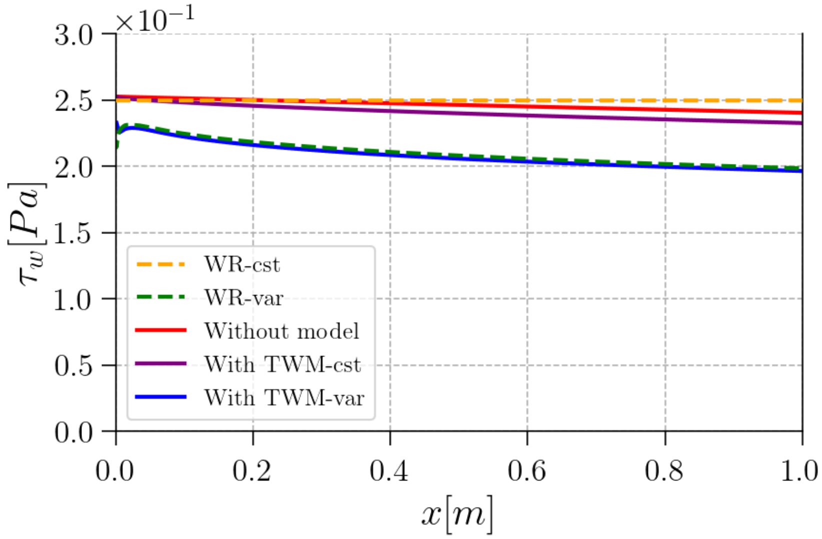

Figure 7.9: Dimensionless wall shear stress along the wall for coarse mesh A, with and without models, compared with the wall-resolved (WR-var) reference.

triangle[9]. The quantity u_1 depends on τ_w and on τ_{1-2}, the shear stress between the first and second cells (see Fig. 6.3). Since both τ_w (see Fig. 7.9) and u_1 are correctly predicted, this implies that τ_{1-2} has also been well estimated. The term τ_{1-2} is not provided by the model, it is evaluated by the solver using a finite-volume approximation[10]. Its impact on u_1 is significant since τ_w and τ_{1-2} are of the same order of magnitude.

To determine τ_w without a model, the finite–volume method (see section 2.2.1) uses the relation $\tau_w \approx \mu \frac{u_1}{y_1}$. In [47], it is effectively assumed that $\mu = \mu_1$ (another option would be to set $\mu = \mu_w$) and that the velocity profile between the wall and the center of cell$_1$ is linear. Under these assumptions, τ_w can be written as

$$\tau_w \approx \mu_1 \frac{u_1}{y_1} \tag{7.4.1}$$

For a coarse mesh with $n_{\delta_t} \ll 1$, $T_1 \approx T_\infty$, hence $\mu_1 \approx \mu_\infty$ in Eq. 7.4.1. Consequently, Fig. 7.10 shows that the coarse mesh without a model produces a velocity profile similar

---

[9] With the numerical set-up considered here, the underlying assumptions are reasonably well satisfied, meaning one can write $\overline{u}^*(x_1, y_1^*) \approx \overline{P_u}(y_1^*)$; in shorthand, $\overline{u_1^e}^* \approx \overline{P_u}(y_1^*)$ with $\overline{u_1^e}^*$ computed from the WR-var case.

[10] In the finite-volume scheme, τ_{1-2} is computed assuming a linear velocity variation between the centers of cell$_1$ and cell$_2$, and that u_1 equals the exact value at the center of cell$_1$ [47]. These assumptions are not strictly satisfied, which can introduce an error in τ_{1-2} and, by extension, in u_1 and τ_w, whether or not a model is used.

to the case WR-cst. Likewise, the relative error on τ_w without a model is comparable to the WR-cst case in Fig. 7.9.

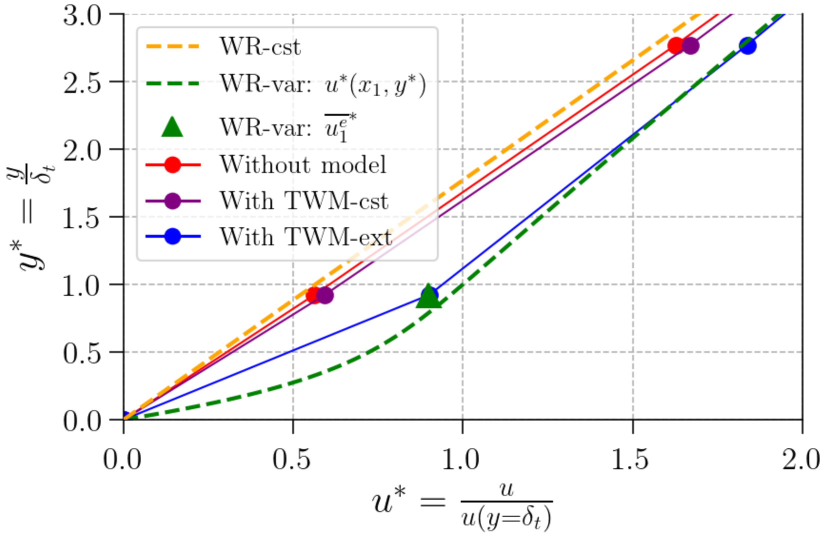

Figure 7.10: Dimensionless velocity profile at $n_{\delta_t} = 0.5$ for coarse mesh A, with and without models. Comparison with the wall-resolved reference (WR-var) and the WR-cst.

The conclusions drawn for the near-wall cell velocity in Fig. 7.10 also hold for Fig. 7.11, which shows its streamwise evolution. The case without model, or with TWM-cst, incurs large errors in the prediction of u_1, reaching up to 37% near the outlet. With TWM-var, the near-wall velocity u_1 agrees closely with the wall-resolved reference[11] on the entire domain. This improvement is crucial from a thermal standpoint, because the prediction of T_1, and consequently of q_w, is primarily governed by the near-wall mass flow rate through the near-wall cells. The thermal results are analyzed in the next section.

---

[11] The expected values of u_1 are computed for each near-wall cell of the coarse mesh from the WR-var solution using Eq. 6.2.12

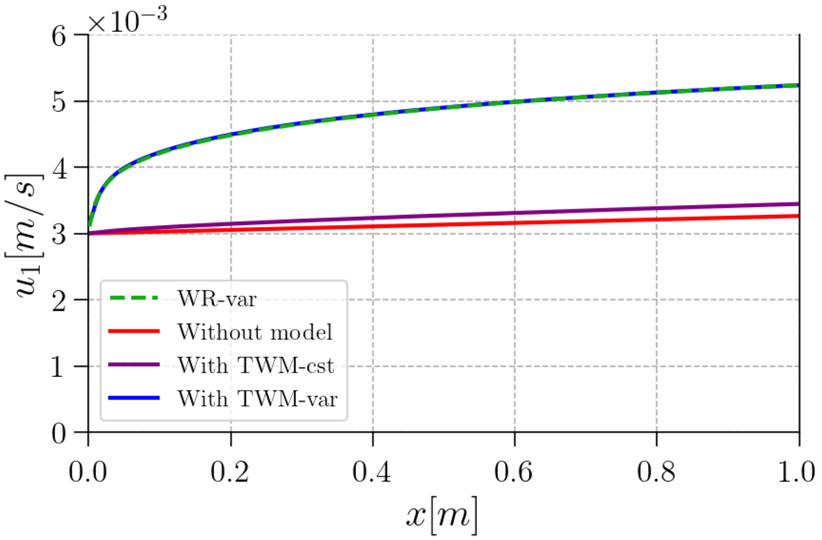

Figure 7.11: Near-wall cell velocity along the wall for coarse mesh A, with and without models, compared with the wall-resolved (WR-var) reference.

7.4.2 Thermal analysis

The evolution of the wall heat-flux prediction, q_w, along the wall for the mesh A is shown in Fig. 7.12. TWM-var provides results that are consistent with the wall-resolved reference, whereas TWM-cst improves upon the no-model case but retains a noticeable offset.

As in the uniform-viscosity cases (see chapter 4), the relative error q_w^{error} (see Eq. 4.2.1 for definition) primarily depends on n_{δ_t}. An overview of all meshes results from Tab. 7.1 is given in Fig. 7.13. For $n_{\delta_t} < 1.5$, TWM-var yields a marked improvement, and the wall heat-flux error drops to nearly zero. For $n_{\delta_t} > 1.5$, the q_w predictions with TWM-var deteriorate slightly and become marginally less accurate than those without a model as the error remains below 10% and decreases toward zero as the mesh is refined. These results are similar with the trends obtained with TWM-cst under the assumption of constant viscosity (see Fig. 4.5). With a variable viscosity, TWM-cst reduces only partially the error, which further decreases with mesh refinement. With the chosen viscosity ratio, $\frac{\mu_\infty}{\mu_w} = 5$, and $n_{\delta_t} = 0.5$, the errors are about 50% without a model, 30% with TWM-cst, and 3.5% with TWM-var. If the viscosity ratio increases, the TWM-cst error is expected to grow due to the increasing discrepancy between the actual velocity profile and the linear profile assumed by TWM-cst[12].

---

[12] This test case is carried out in the impinging-jet context in the next chapter (see chapter 8)

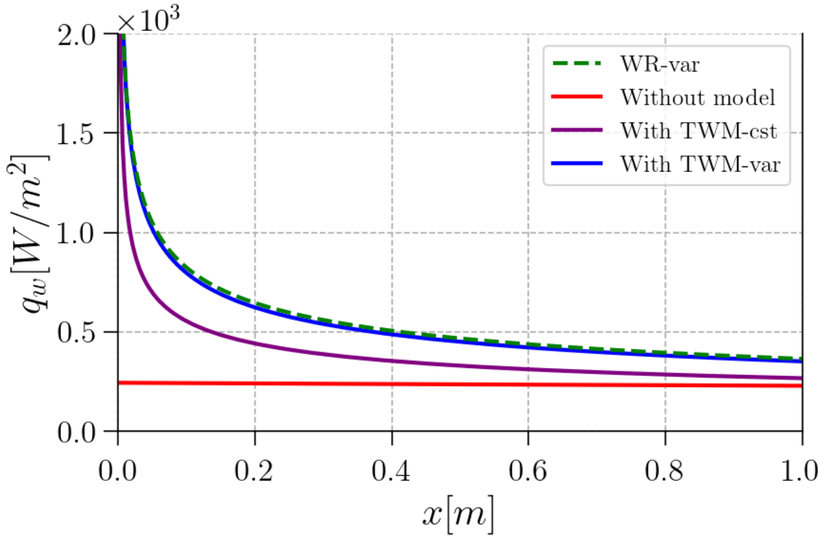

Figure 7.12: Dimensionless wall heat flux along the wall for coarse mesh A, with and without models, compared with the wall-resolved (WR-var) reference.

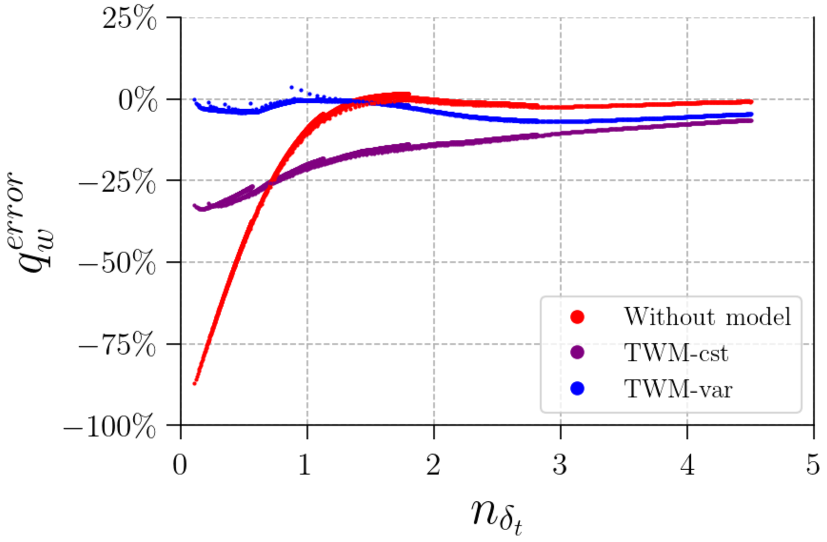

Figure 7.13: Relative error in q_w versus n_{δ_t}, with and without model corrections. The curves combine results from meshes A, B, C, D and E.

Similarly to q_w, results for τ_w expressed in terms of τ_w^{error} as a function of n_{δ_t} are provided in Appendix C.

The temperature profile is shown in Fig. 7.14 at $n_{\delta_t} = 0.5$ for case A. The differences between TWM-var and TWM-cst solutions, and between the solution without model, are small in terms of near wall temperature T_1, yet they translate into large variations of q_w. With TWM-var, T_1 is consistent with the expected flow temperature $\widetilde{T_1^e}^*$ computed from the WR-var results (see Tab. 3.2 for variable definitions). Although TWM-cst appears to reproduce correctly T_1, the evaluation of q_w with TWM-cst relies on a different $\widetilde{P_T}$ which leads to a biased q_w (see Fig. 6.1) .

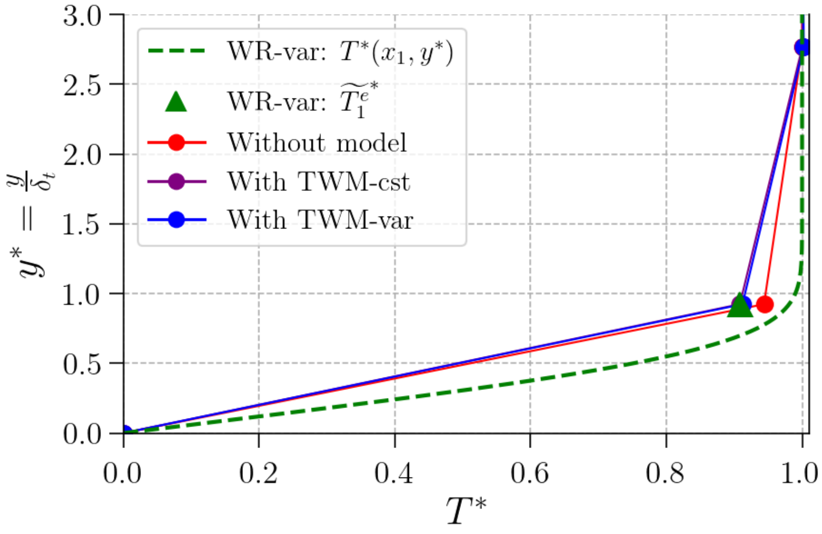

Figure 7.14: Dimensionless temperature profile with and without models at $n_{\delta_t} = 0.5$ for coarse mesh A. Comparison with the wall-resolved (WR-var) reference.

As in the uniform-viscosity assessment of TWM-cst, the next step is to evaluate TWM-var in the impinging-jet configuration with variable viscosity.

CHAPTER 8

Thermal wall model for variable viscosity: evaluation under jet impingement configuration

TWM-var is evaluated on the impinging-jet configuration presented in chapter 5 but with the realistic viscosity law of variation with the temperature depicted in Fig. 5.2 by the blue line. The actual experimental configurations presented in section 5.2 are directly used to assess the model. Moreover, the sensitivity of the model to the Prandtl and Reynolds numbers and viscosity law is investigated.

8.1 Numerical setup

In chapter 5, TWM-cst was evaluated using wall-resolved cases with uniform viscosity as a reference, while the numerical set-up had been validated beforehand for temperature-dependent viscosity by comparison with experimental data. We now evaluate TWM-var directly on the temperature-dependent configurations, using cases P summarized in Tab. 8.1, which correspond to real experimental conditions. The cases not covered experimentally, namely H, I, and J, are nonetheless based on the validated numerical set-up and are used to assess the sensitivity of the model to the Prandtl and Reynolds numbers, as well as to the viscosity variation.

The coarse meshes are sufficiently refined to resolve the velocity field outside the thermal boundary layer, while the temperature and velocity profiles are under-resolved inside the thermal boundary layer. When TWM-var is activated, the influence of the thermal boundary layer on the near wall heat flux and wall shear stress is modeled by TWM-var.

Cases	Parameters									
	μ_l (Pa·s)	$\dot{V}$ ($m^3 \cdot s^{-1}$)	T_l (K)	T_w (K)	Re	Pr	Mesh size	Min. cells number		
								H_{film}	δ	δ_t
$\mathbf{P_{1_c}}$ $\mathbf{P_{1_c}^{mv}}$ $\mathbf{P_{1_c}^{mc}}$	$\mu_l(T)$	2.50×10^{-5}	323	363	1319	158	209 000	5.1	2.7	0.4
$\mathbf{P_{1_r}}$							366 000	43	29	6.6
$\mathbf{P_{2_c}}$ $\mathbf{P_{2_c}^{mv}}$ $\mathbf{P_{2_c}^{mc}}$		0.42×10^{-5}	323	363	220	158	216 000	5.7	3.2	0.6
$\mathbf{P_{2_r}}$							346 000	35	24	6.2
$\mathbf{P_{3_c}}$ $\mathbf{P_{3_c}^{mv}}$ $\mathbf{P_{3_c}^{mc}}$		0.42×10^{-5}	323	393	317	111	216 000	5.4	3.2	0.5
$\mathbf{P_{3_r}}$							346 000	34	24	5.5
$\mathbf{P_{4_c}}$ $\mathbf{P_{4_c}^{mv}}$ $\mathbf{P_{4_c}^{mc}}$		2.50×10^{-5}	363	393	2844	74	220 000	5.2	2.8	0.5
$\mathbf{P_{4_r}}$							366 000	34	22	5.2
$\mathbf{P_{5_c}}$ $\mathbf{P_{5_c}^{mv}}$ $\mathbf{P_{5_c}^{mc}}$		0.42×10^{-5}	363	393	474	74	228 000	5.2	2.5	0.6
$\mathbf{P_{5_r}}$							379 000	40	25	8.8
$\mathbf{P_{6_c}}$ $\mathbf{P_{6_c}^{mv}}$ $\mathbf{P_{6_c}^{mc}}$		2.50×10^{-5}	323	393	1900	111	234 000	4.9	2.4	0.3
$\mathbf{P_{6_r}}$							410 000	42	27	6.0
$\mathbf{H_c}$ $\mathbf{H_c^{mv}}$ $\mathbf{H_c^{mc}}$	$\mu_l(T = T_\infty)$	0.42×10^{-5}	323	393	124	292	216 000	6.0	3.6	0.7
$\mathbf{H_r}$							346 000	36	26	7.3
$\mathbf{I_c}$ $\mathbf{I_c^{mv}}$ $\mathbf{I_c^{mc}}$	$\mu_l(T)$	0.42×10^{-5}	323	393	317	1	216 000	4.2	2.2	3.0
$\mathbf{I_r}$							346 000	29	18	23
$\mathbf{J_c}$ $\mathbf{J_c^{mv}}$ $\mathbf{J_c^{mc}}$	$\mu_l(T)$	0.42×10^{-5}	293	393	220	158	201 000	5.5	3.2	0.3
$\mathbf{J_r}$							343 000	43	31	5.5

Table 8.1: Summary of numerical case parameters. For each configuration, two grids are considered: a wall-resolved mesh (subscript "r") and a coarse mesh (subscript "c"). Wall-resolved cases are simulated only without model, while coarse meshes are simulated with TWM-var (superscript "mv") or with TWM-cst (superscript "mc") or without model. The *Min. cells number* column reports the minimum number of cells across the film, the dynamic and thermal boundary layer over the entire radial domain. Cases P correspond to real experimental conditions. Cases H, I, and J evaluate TWM-var on configurations without experimental data.

Before assessing the model in section 8.4, the impact of a non-uniform viscosity on the flow and temperature fields is first examined, and then the model assumptions are confronted with the results obtained using a wall-resolved mesh.

8.2 Impact of a non-uniform viscosity

The case P_{3_r} (see Tab. 8.1) is compared with H_r in Fig. 8.1, a similar configuration with a uniform viscosity $\mu_l = \mu_l(T_\infty)$, $\forall T$. In the configuration P_3, the viscosity very near the wall is lower by a factor of 5, that is, $\frac{\mu_\infty}{\mu_w} = 5$ (where $\mu_w = \mu_l(T_w)$ and $\mu_\infty = \mu_l(T_\infty)$). This reduction yields a thinner thermal boundary layer, which is explained by weaker near-wall friction and a higher local velocity. The higher velocity within the film, together with flow-rate conservation, leads to a reduced film thickness. Similar results was observed in [81] for a Pr slightly above 1.

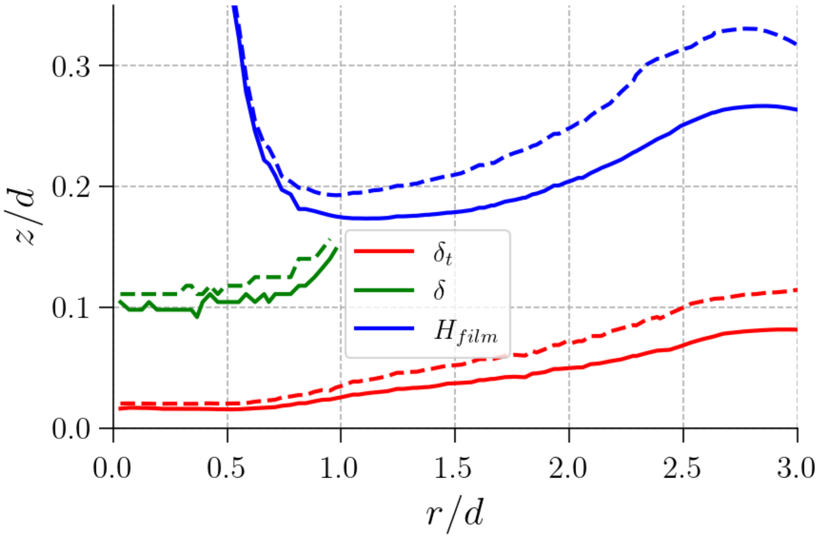

Figure 8.1: Radial profiles of H_{film}, δ, and δ_t for wall-resolved configurations with (case P_{3_r}, plain lines) and without viscosity variation (case H_r, dashed lines).

The wall-flux variation (τ_w and q_w), whose indirect effects were observed on H_{film} and δ_t, are visualized in Fig. 8.2 via the friction coefficient τ_w^* and the Nusselt number Nu (see Eq. 5.3.1 and Eq. 5.3.2 for definitions). A lower near-wall viscosity increases convective intensity, hence Nu rises. Conversely, τ_w^* decreases, while the location of its peak remains at the same radial distance from the impingement point.

The velocity profiles at three radial locations are shown in Fig. 8.3, highlighting the increase in velocity due to the reduced near-wall viscosity. With a uniform viscosity, the near-wall profile is approximately linear. As already shown in Fig. 5.15, a non-uniform viscosity produces a non-linear profile within the thermal boundary layer; just outside δ_t, the profile becomes nearly linear again.

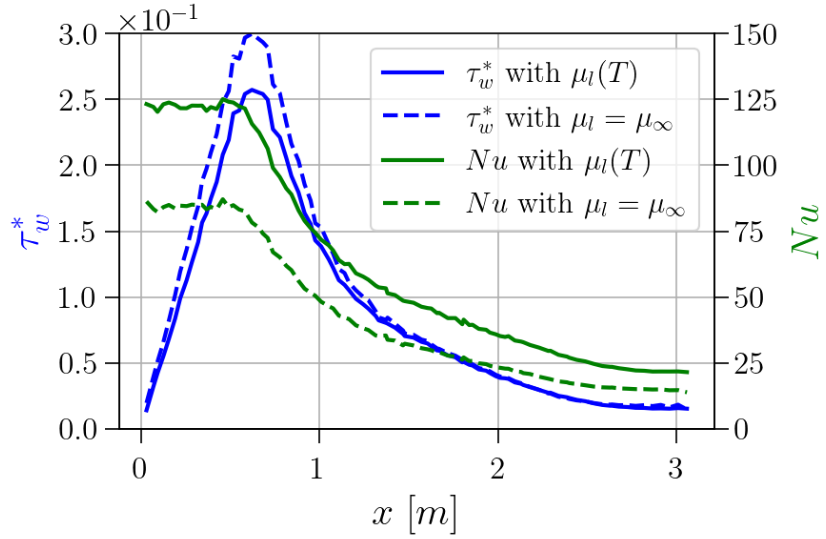

Figure 8.2: Friction coefficient and Nusselt number along the radial direction of the wall-resolved case, with and without viscosity variation.

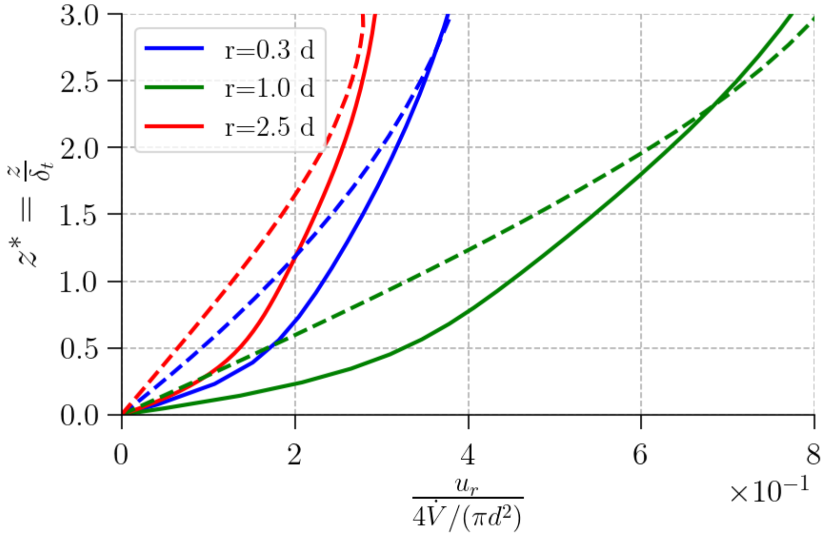

Figure 8.3: Profiles of the radial velocity component near the wall for the wall-resolved case, with (plain lines) and without (dashed lines) viscosity variation.

The next section assesses whether the main assumptions hold for the academic jet configuration.

8.3 Confrontation of model assumptions

The academic jet configuration is challenging for TWM-var, because the model assumptions are not perfectly satisfied by the nature of the flow, even for Pr up to 158. Several key assumptions, namely the temperature profile shape P_T, the near-uniformity of the shear stress, and the velocity profile shape P_u, are assessed by comparison with the wall-resolved case $\mathrm{P}_{3_\mathrm{r}}$. Configuration P_3 features a strong viscosity variation, with $\frac{\mu_\infty}{\mu_w} = 5$, and a high Prandtl number, $Pr = 111$.

The profile P_T is examined in Fig. 8.4 at three positions spanning the different regions of the film. The numerical profiles are close to the theory within and near the thermal boundary layer, collapsing onto a single curve close to the Lévêque solution.

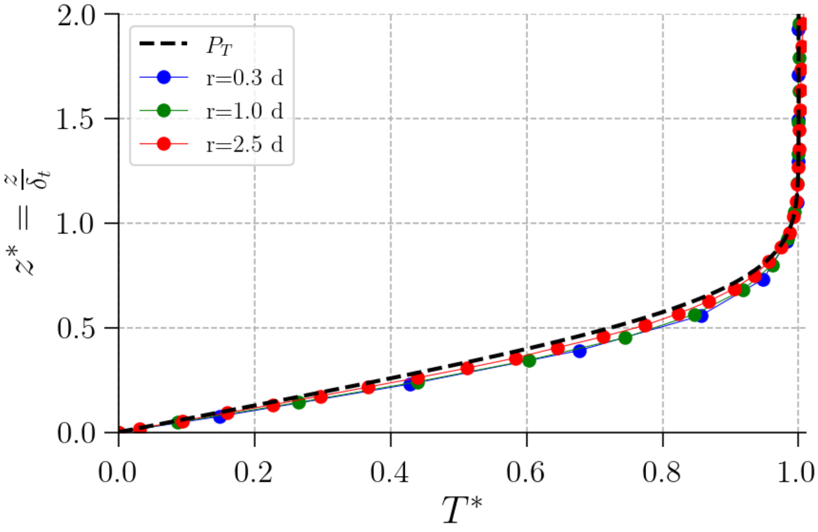

Figure 8.4: Near-wall dimensionless temperature profiles of the wall-resolved case $\mathrm{P}_{3_\mathrm{r}}$, compared with the theoretical model profile P_T.

Regarding τ^*_{yx} in Fig. 8.5, uniformity is not perfectly satisfied, especially beneath the jet ($r < d$), where at $z^* = 1$ a 20% variation of the shear stress is observed. At $r = d$ and $r = 2.5\,d$, the variation across δ_t remains within 10%, which appears acceptable. For $z > \delta_t$, the departure from τ_w increases and becomes significant for large z. Increasing

Pr, and thus reducing δ_t, should help decrease the offset between τ_{yx} and τ_w within the thermal layer, as the latter will then be closer to the wall.

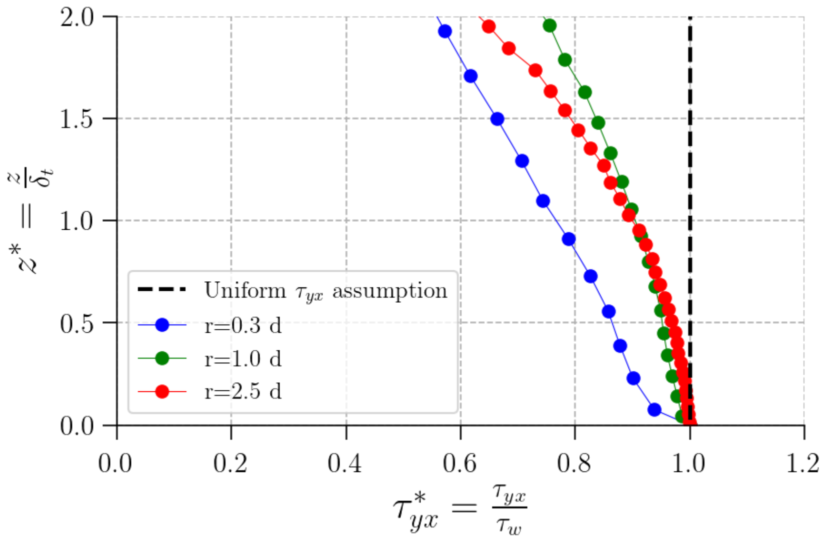

Figure 8.5: Near-wall dimensionless shear stress profiles of the wall-resolved case P_{3_r}. Comparison with the uniform shear stress assumption.

Nevertheless, the theoretical model profile P_u, based on the assumption of an approximately uniform τ_{yx} across and near δ_t, shows good agreement with the numerical results. In Fig. 8.6, within the thermal boundary layer, the computed profiles superimpose well on P_u, with a higher offset for $r < d$. The offset increases only slightly outside the thermal layer, since the profiles are not perfectly linear beyond δ_t.

The profile P_u is expected to hold across the entire height of the first near-wall cell. Therefore a first cell that is too high could yield a non-linear velocity variation within the cell when $z > \delta_t$. However, the coarse meshes considered are designed to resolve the velocity field outside δ_t, which implies an almost piecewise-linear variation across each cell away from the thermal layer.

Overall, the assumptions underpinning TWM-var appear to be reasonably well satisfied in this academic jet configuration. The model is assessed in the next section.

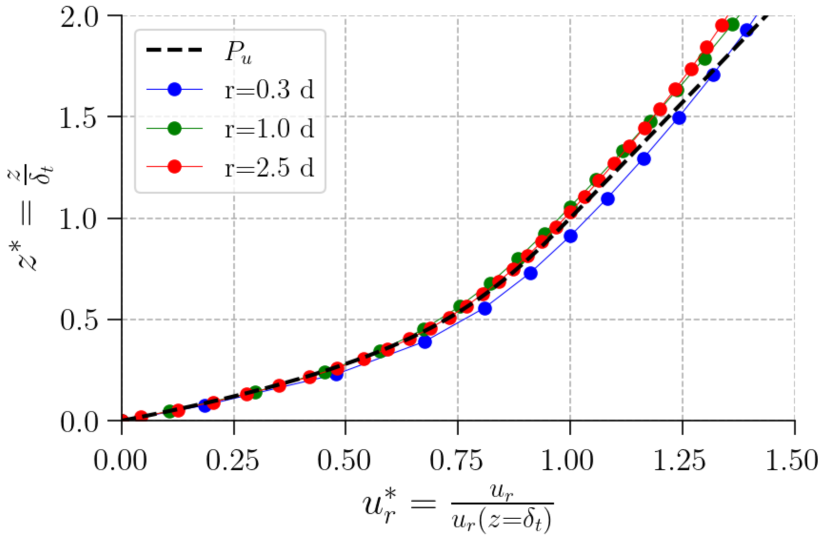

Figure 8.6: Near-wall dimensionless velocity profiles of the wall-resolved case $\mathrm{P}_{3_\mathrm{r}}$, compared with the theoretical model profile P_u.

8.4 Model validation

TWM-var is assessed on coarse meshes by comparison with the wall-resolved references, and also against TWM-cst and the coarse mesh without a model. For clearer comparison with the results obtained under Lévêque conditions, summarized in Fig. 7.13, the n_{δ_t} range covered by each configuration is listed in Tab. 8.2.

Fig. 8.7 reports the local Nusselt number Nu as a function of the radial distance r for configuration P_3 with $\frac{\mu_l}{\mu_w} = 5$. TWM-var matches the wall-resolved result very closely in all regions. It also delivers a substantial improvement over TWM-cst and the no-model baseline, especially near the jet, regions 1 and 2[1], where the thermal boundary layer is thinnest and n_{δ_t} is close to 0.5. This is consistent with the results obtained in the Lévêque configuration, where a strong improvement with TWM-var is observed for $n_{\delta_t} < 1$ (see Fig. 7.13). For example, at $r = 0.4\,d$ in region 1, the error is about 50% without a model, 30% with TWM-cst, and 5% with TWM-var. For $r > d$, the TWM-var slightly overpredicts q_w. This errors may be due to a velocity field that is not perfectly parallel to the wall or linear across the near-wall cells. A similar trend has already been observed with TWM-cst at uniform viscosity in the impinging jet configuration Fig. 5.8. Farther from the jet, as δ_t

---

[1] The limit between regions 1 and 2 is set at $r = 0.6d$ to match the peak position of τ_w^* in Fig. 8.8. The limit between regions 2 and 3 is set using the correlation $r = 0.1773\,Re^{1/3}\,d$ given in [77, 78].

Cases	Min. n_{δ_t}	Max. n_{δ_t}
$\mathbf{P_{1c}}$	0.4	1.3
$\mathbf{P_{2c}}$	0.6	3.4
$\mathbf{P_{3c}}$	0.5	2.7
$\mathbf{P_{4c}}$	0.5	1.5
$\mathbf{P_{5c}}$	0.6	2.5
$\mathbf{P_{6c}}$	0.3	1.1
$\mathbf{H_c}$	0.7	3.8
$\mathbf{I_c}$	3.0	14
$\mathbf{J_c}$	0.3	1.9

Table 8.2: Minimum and maximum number of cells across the thermal boundary layer over the entire radial domain for the coarse mesh. Values are identical with or without model.

and n_{δ_t} grow, the differences among cases diminish.

In Fig. 8.8, TWM-var brings an improvement in the prediction of τ_w^*. At the location of the τ_w^* peak, the error is about 14% without a model and about 5% with TWM-var. The errors without a model, and with TWM-cst, remain relatively small overall, consistent with the observations and explanation in section 7.4.

It is also noteworthy that the film thickness in Fig. 8.9, which is noticeably overestimated when using the coarse mesh without a model (and with TWM-cst), is markedly improved with TWM-var across all regions. Without a model, the error is about 10% at the location of minimum thickness, whereas it drops to about 1% with TWM-var. This improvement in H_{film} likely results from a more accurate prediction of τ_w and of the near-wall velocity, which ultimately governs the overall film thickness.

Indeed, the velocity profiles show a significant improvement in Fig. 8.10. With TWM-var, the near-wall cell velocities, and those farther from the wall, are much more consistent with the wall-resolved reference. For example, at $r = 1.0\,d$, the near-wall cell velocity error is reduced from 50% with TWM-cst to 10% with TWM-var. The velocity error without model explains the large discrepancies in Nu reported in Fig. 8.7. Note that the near-wall cell velocity, whose center is (r_1, z_1), is expected to be consistent with $\overline{P_u}(z_1)$, and therefore close to, but not exactly equal to, the wall-resolved value $u(r_1, z_1)$[2]. On this basis, the results can be reasonably compared with the $\mathrm{P_{3r}}$ profiles.

---

[2] $\overline{P_u}(z_1)$ is a cell-averaged counterpart of $P_u(z_1)$, and $P_u(z_1)$ is expected to match the wall-resolved velocity $u(r_1, z_1)$, see Fig. 6.1.

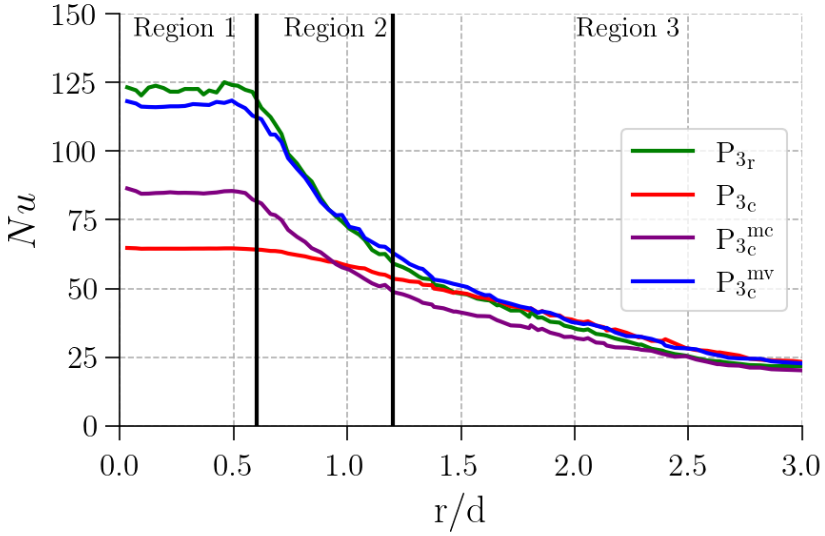

Figure 8.7: Radial profiles of Nu obtained with the coarse mesh from configuration P_3, with TWM-cst ($P_{3_c}^{mc}$), with TWM-var ($P_{3_c}^{mv}$) and without model corrections (P_{3_c}), compared to the wall-resolved reference (P_{3_r}).

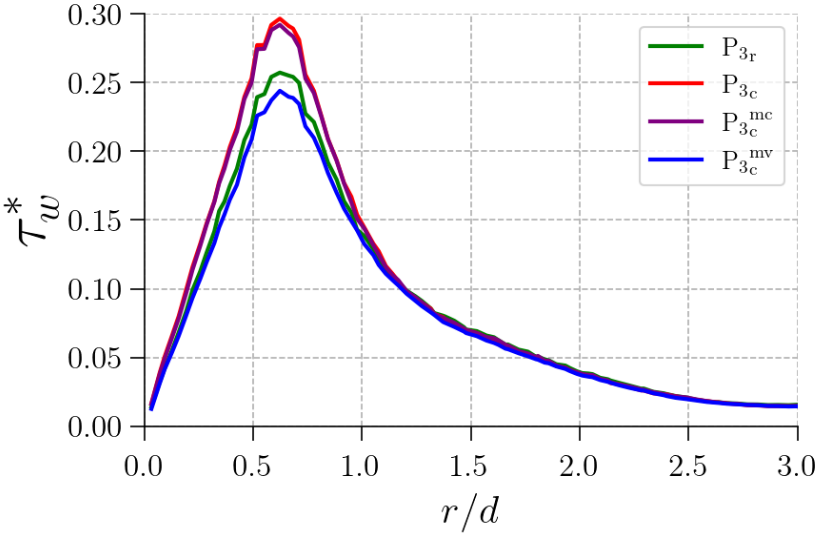

Figure 8.8: Radial profiles of τ_w^* obtained with the coarse mesh from configuration P_3, with TWM-cst ($P_{3_c}^{mc}$), with TWM-var ($P_{3_c}^{mv}$) and without model corrections (P_{3_c}), compared to the wall-resolved reference (P_{3_r}).

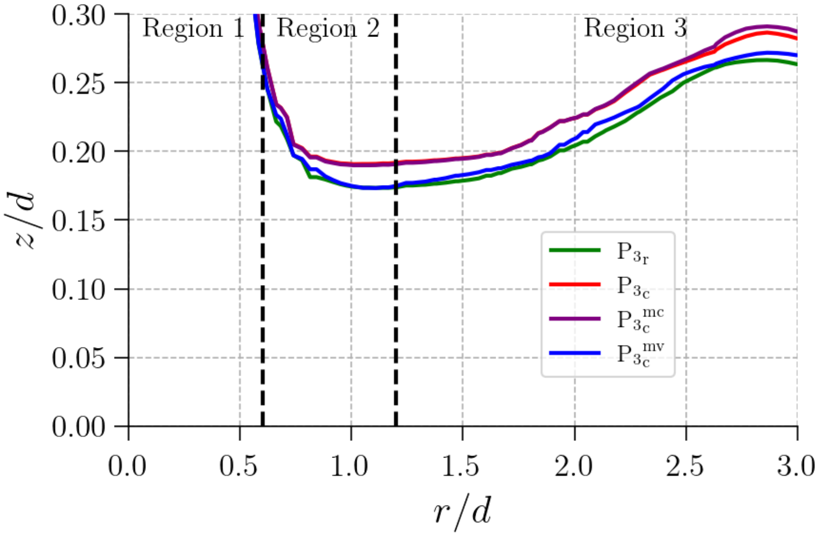

Figure 8.9: Radial profiles of H_{film} obtained with the coarse mesh from configuration P_3, with TWM-cst ($P_{3_c}^{mc}$), with TWM-var ($P_{3_c}^{mv}$) and without model corrections (P_{3_c}), compared to the wall-resolved reference (P_{3_r}).

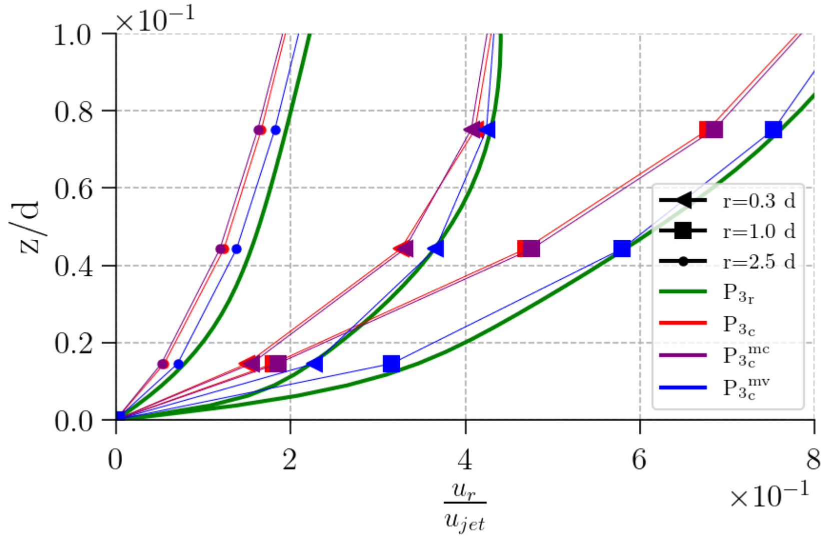

Figure 8.10: Profiles of the radial velocity component obtained with the coarse mesh from configuration P_3, with TWM-cst ($P_{3_c}^{mc}$), with TWM-var ($P_{3_c}^{mv}$) and without model corrections (P_{3_c}), compared to the wall-resolved reference (P_{3_r}). Markers indicate coarse-mesh cell-center locations.

Finally, Fig. 8.11 reports the dimensionless integral wall heat flux Q_w^* (see Eq. 5.3.3) for all configurations P that were also covered experimentally. For each case, Q_w^* is decomposed into the contribution from the near-jet region, $0 < r < d$ (bottom of each bar), and that from the remainder of the plate (upper part of each bar). This split highlights that, without a model, opposite errors in the two regions partially compensate, therefore plate-integrated values must be interpreted carefully. TWM-var brings substantial improvements in the near-jet zone, where the thermal boundary layer is thinnest, and it also shows good agreement with the wall-resolved references for the plate-integrated flux. Over the wide ranges of viscosity ratio, Reynolds number, and Prandtl number that were tested, the model produces consistent results.

The prediction obtained with TWM-var in Fig. 8.11 shows low sensitivity to the flow region and to the mesh thickness, as n_{δ_t} varies along the plate from about 0.3 cells across the thermal boundary layer for case $\mathrm{P}_{6_\mathrm{c}}^{\mathrm{mc}}$ to a maximum of 3.4 cells for case $\mathrm{P}_{2_\mathrm{c}}^{\mathrm{mc}}$, spanning the intervening range (see Tab. 8.2). By contrast, the no-model and TWM-cst predictions exhibit strong mesh dependence, despite all cases sharing the same minimum number of cells across the minimum film thickness.

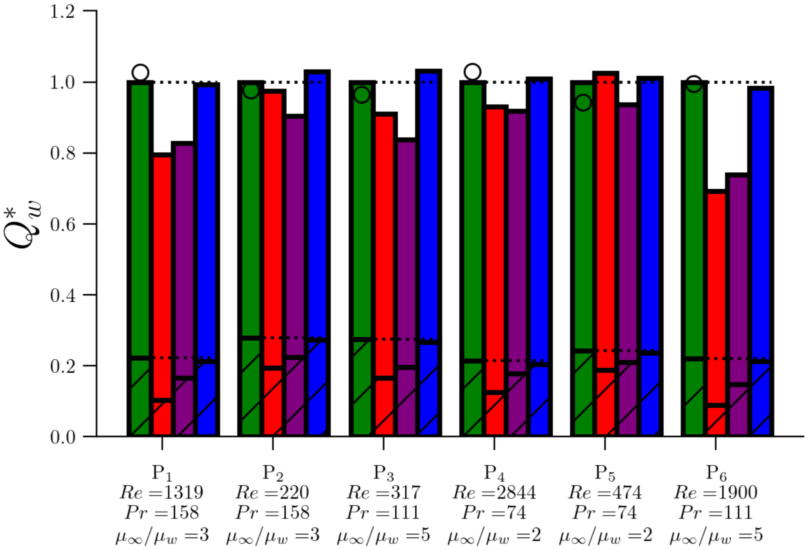

Figure 8.11: Dimensionless integral wall heat flux Q_w^* (see Eq. 5.3.3) over the entire plate, distinguishing between the near-jet region $0 < r < d$ and the remainder of the plate. Comparisons are shown for the P cases with TWM-var (blue), without TWM-var (red), and their respective wall-resolved references (green). Results obtained with TWM-cst (purple) are also included. Experimental measurements are indicated by black rings.

Further details on how the model behaves across different ranges of viscosity ratio, Re and Pr numbers are provided below.

8.4.1 Sensitivity to the viscosity-ratio

The sensitivity to the viscosity ratio is examined using configurations J and H, both derived from P_3. Case J employs a lower liquid temperature T_∞ while keeping T_w unchanged, which increases the viscosity ratio from $\mu_\infty/\mu_w = 5$ in P_3 to $\mu_\infty/\mu_w = 15$. Configuration H, by contrast, uses a uniform viscosity equal to $\mu_l = \mu_l(T_\infty)$, $\forall T$.

The results for J in Fig. 8.12 show that the TWM-cst error increases compared to the wall-resolved case, as the viscosity varies strongly within the thermal boundary layer. This highlights the growing benefit of TWM-var for large viscosity contrasts.

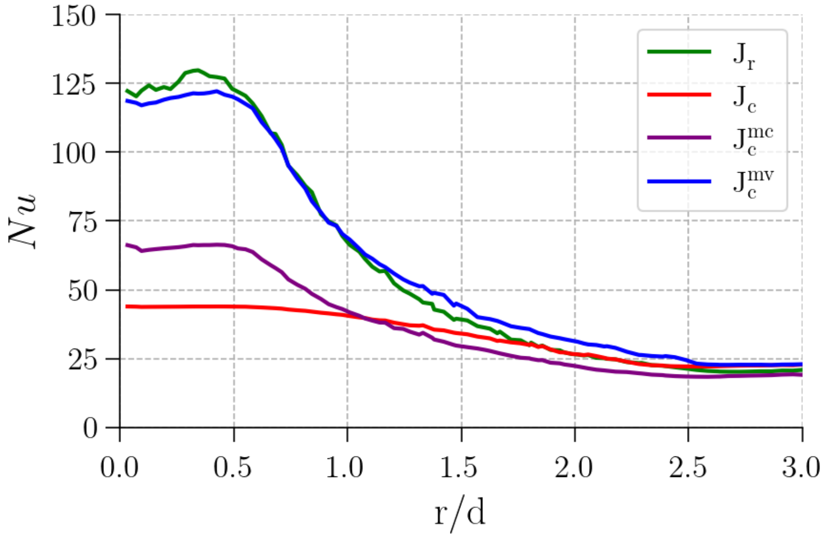

Figure 8.12: Radial profiles of Nu obtained with the coarse mesh from configuration J, with TWM-cst ($\mathrm{J_c^{mc}}$), with TWM-var ($\mathrm{J_c^{mv}}$) and without model corrections ($\mathrm{J_c}$), compared to the wall-resolved reference ($\mathrm{J_r}$).

Conversely, Fig. 8.13 shows, using configuration H with a uniform viscosity, that TWM-var produces results identical to TWM-cst, and both are consistent with the wall-resolved case. These findings corroborate the asymptotic uniform-viscosity limit demonstrated in section 6.3.1.

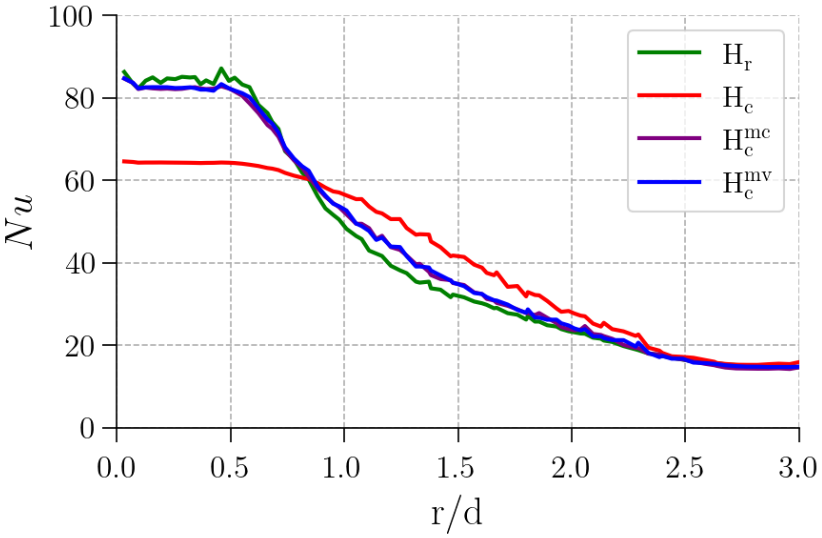

Figure 8.13: Radial profiles of Nu obtained with the coarse mesh from configuration H, with TWM-cst (H_c^{mc}), with TWM-var (H_c^{mv}) and without model corrections (H_c), compared to the wall-resolved reference (H_r).

8.4.2 Sensitivity to Reynolds number

The behavior of the model at higher Reynolds number is illustrated with case P_6 ($Re = 1900$) in Fig. 8.14. The local Nusselt number Nu is well predicted by the TWM-var in all regions, with only a slight offset in region 1, larger than for the lower Re equivalent case P_3 ($Re = 317$, see Fig. 8.7).

It is worth noting that the benefit provided by TWM-var is greater in configuration P_6 (see Fig. 8.14) than in P_3 (see Fig. 8.7), since the range of n_{δ_t} is shifted toward lower values in P_6 (see Tab. 8.2).

The scaled $u_r(z)$ profiles of the low and high Re configurations (respectively P_3 and P_6) are shown in Fig. 8.15 at $r = 0.5\,d$. The less accurate representation of the near-jet velocity profile by the model at high Re (${P_6}_c^{mv}$) compared to the low Re configuration (${P_3}_c^{mv}$), may be the reason for the slight Nu error obtained with ${P_6}_c^{mv}$ in Region 1 (see Fig. 8.14 at $r = 0.5\,d$)[3]. Indeed, the wall-resolved solution (${P_6}_r$) shows that part of the velocity profile outside δ_t is not fully linear across the coarse near-wall cell. As a result, the model assumption of a linear $u_r(z)$ profile across the near-wall cell (outside δ_t) is not

---

[3] The near-wall cell velocity, whose center is (r_1, z_1), is expected to be consistent with $\overline{P_u}(z_1)$, and therefore close to, but not exactly equal to, the wall-resolved value $u(r_1, z_1)$.

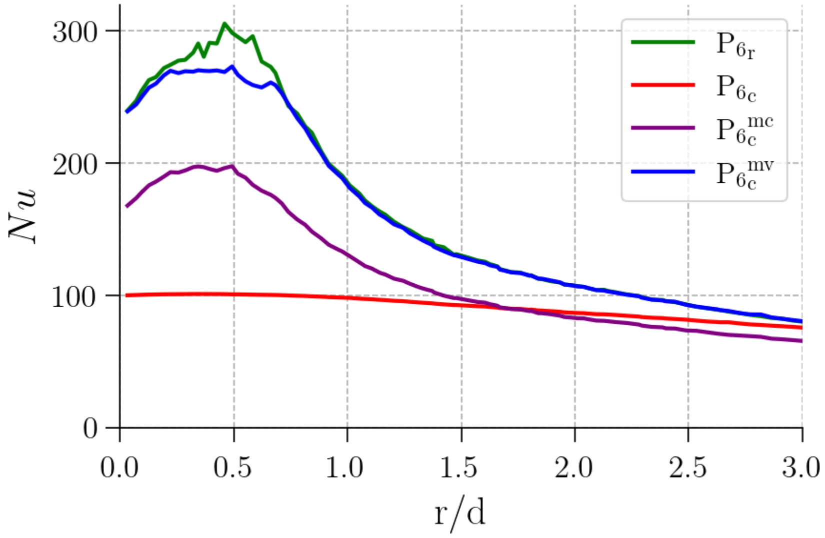

Figure 8.14: Radial profiles of Nu obtained with the coarse mesh from configuration P_6, with TWM-cst ($P_{6_c}^{mc}$), with TWM-var ($P_{6_c}^{mv}$) and without model corrections (P_{6_c}), compared to the wall-resolved reference (P_{6_r}).

strictly satisfied. Moreover, the non-linearity of $u_r(z)$ between the near-wall cell and the adjacent cell can introduce an error in the solver's estimate of τ_{12}[4] and, consequently, in u_1. A reduced near-wall cell height (i.e. a less coarse near-wall mesh) would therefore likely improve the prediction.

Thus, TWM-var exhibits satisfactory performance over a broad range of Reynolds numbers, approximately $Re \in [327, 1900]$.

8.4.3 Sensitivity to Prandtl number

A low Pr corresponds to a configuration in which the thermal boundary layer δ_t is thick relative to the momentum boundary layer δ and becomes a substantial fraction of the film thickness H_{film}, and, by extension, of the first near-wall cell height. This situation can arise even at moderately high Pr if the wall, and thus the film, extends far enough for the thermal boundary layer to intersect the free surface far from the jet. To examine how the model behaves when the thin thermal boundary layer assumption is not met, we consider configuration I with $Pr = 1$ in Fig. 8.16. The I_c case without a model already performs

---

[4] In the finite-volume method, a linear variation of $u_r(z)$ between adjacent cell centers is assumed to compute τ_{12}.

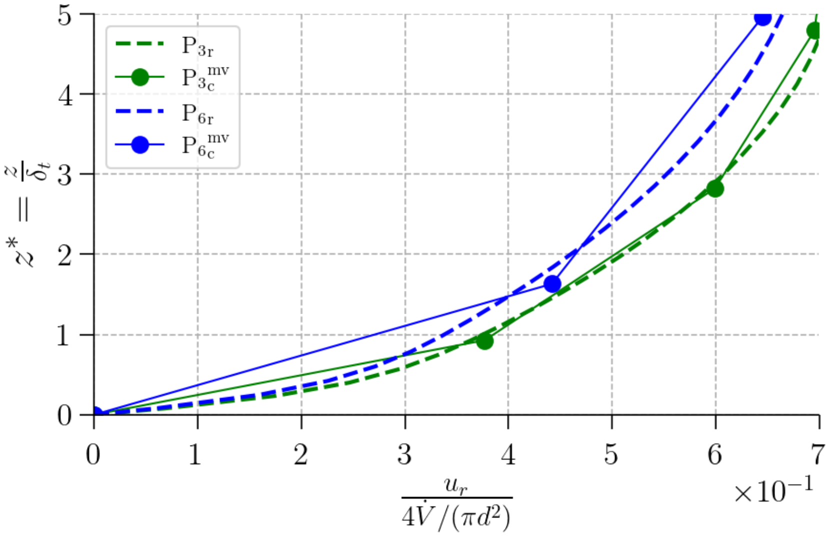

Figure 8.15: Profiles of the radial velocity components u_r near the wall at $r = 0.5\,d$, obtained with the coarse meshes from configurations P_3 and P_6, with TWM-var ($P_{3_c}^{mv}$ and $P_{6_c}^{mv}$), compared to the wall-resolved references (P_{3r} and P_{6r}). Markers indicate coarse-mesh cell-center locations.

well, because the thick thermal boundary layer is well resolved. TWM-var also shows very good agreement with the wall-resolved case I_r, which demonstrates the robustness of TWM-var in this regime.

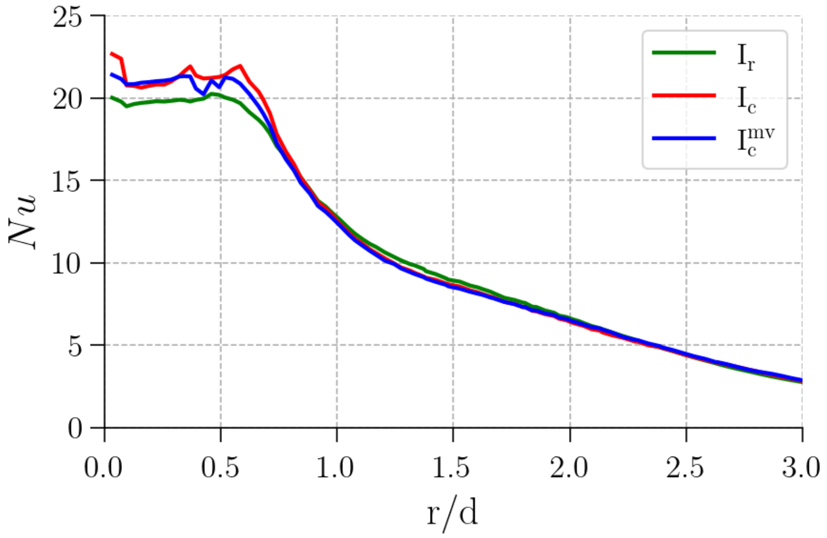

Figure 8.16: Radial profiles of Nu obtained with the coarse mesh from configuration I, with TWM-var ($\mathrm{I_c^{mv}}$) and without model corrections ($\mathrm{I_c}$), compared to the wall-resolved reference ($\mathrm{I_r}$).

8.5 Concluding remarks on the model

The conclusions obtained for TWM-var in the impinging-jet configuration with variable viscosity are similar to those obtained for TWM-cst under constant-viscosity conditions (see section 5.3.2). The TWM-var provides a substantial improvement in the prediction of q_w compared with both TWM-cst and the no-model case, especially when $n_{\delta_t} < 1$, or only leads to a marginal deterioration. The benefit of the model should thus be interpreted primarily in terms of the degree of refinement within the thermal boundary layer, since the largest gains are obtained for $n_{\delta_t} < 1$, that is, when n_{δ_t} approaches zero. Finally, TWM-var shows low sensitivity to the flow regions, which confirms its robustness.

The computational-cost savings for all configurations are reported in Tab. 8.3. CPU time is primarily governed by mesh resolution and activating TWM-var introduces no measurable overhead. The smaller speedup observed for configurations $\mathrm{P_4}$ and I, arises because the time step remains identical in the wall-resolved and coarse mesh cases despite the coarser near-wall resolution. This suggests that, under the constraints imposed by the CFL and Fourier numbers, the global time step is controlled by a cell away from the wall, a point that remains to be confirmed. Even so, the overall reduction in calculation time remains substantial.

Cases	Coarse mesh with model
$\mathbf{P_1}$	−82 %
$\mathbf{P_2}$	−72 %
$\mathbf{P_3}$	−79 %
$\mathbf{P_4}$	−35 %
$\mathbf{P_5}$	−80%
$\mathbf{P_6}$	−81 %
H	−83 %
I	−41 %
J	−77 %

Table 8.3: Reduction of the calculation time (CPU time) relatively to the wall-resolved case. Calculation times are identical with (TWM-var and TWM-cst) and without the models.

Part IV

Advance application case of the thermal wall model

CHAPTER 9

Industrial application

This chapter presents results for the application of TWM-cst to a realistic end-winding cooling configuration, under the approximation of a fluid with uniform viscosity. Only TWM-cst is considered in this work due to time constraints, while the variable-viscosity case to assess TWM-var is left as a perspective for future work.

9.1 Numerical set-up

A realistic representation of a commercial traction electric machine was previously designed to experimentally evaluate the effectiveness of direct oil jet cooling [26]. Various jet injection designs, oils, and operating conditions were investigated. The study demonstrated that adding an oil jet cooling system significantly decreases the end-winding temperature, confirming the relevance of this cooling approach. Building on this experimental configuration, a complementary numerical study of one specific jet injection design was carried out by Poubeau et al. [31]. Since the experiments provided only partial thermal characterization of the machine without direct flow measurements, the numerical analysis complements the experimental data by providing detailed insight into the local heat transfer at the end-winding surface. The numerical study in [31] aimed to identify best practices for grid definition and flow validation, and to investigate the sensitivity of the cooling performance to oil properties, flow rate, and oil temperature. Fig. 9.1 illustrates the type of simulation performed in [31], featuring five impinging jets striking the top of the end-windings. These jets form a liquid film that flows downward by gravity, partially wetting the solid surfaces. The red zones, corresponding to the impingement regions, indicate areas of highest surface heat flux q_w extracted from the wall.

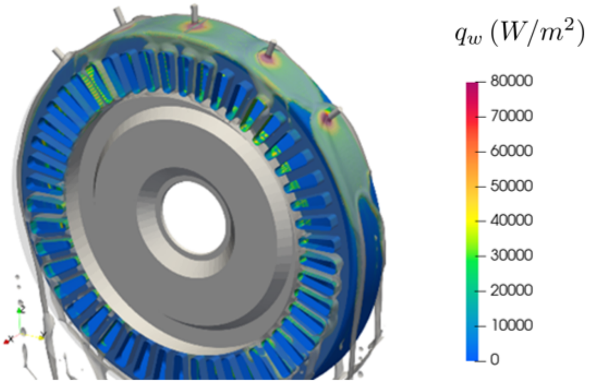

Figure 9.1: Oil jet impingement over the end-windings simulated by [31] using a realistic geometry and impingement conditions consistent with the experimental setup of [26]. The red regions indicate zones of high surface heat flux beneath the impinging jets.

9.1.1 Geometry, boundary conditions and fluid properties

The numerical setup used here is based on the configuration presented in [31]. To isolate the key physical mechanisms and ensure reasonable computational cost, the geometry shown in Fig. 9.2 has been simplified from the original configuration in [26]: rotation effects and solid thermal conduction are neglected, and the end-windings surface is modeled as smooth. The geometry consists of five jets impinging on the upper part of the outer surface of the end-windings. This configuration allows the formation of a gravity-driven liquid film that covers most of the end-windings surface. Owing to geometric symmetry, only half of the domain is simulated. The outer surface of the end-windings, highlighted in Fig. 9.3, has a ring shape with a radius of 9.7 cm, yielding a total perimeter of 61 cm. The outer surface depth (along the $\vec{e_x}$ direction) is approximately 2.6 cm and the jet nozzles have a diameter of 3.2 mm.

For the assessment of the TWM-cst, the analysis focuses exclusively on the outer surface, which is directly impacted by the jets. This region exhibits the largest wetted area and the highest local heat fluxes. More specifically, the upper portion of the outer surface, above the red line in Fig. 9.3, is used as the primary zone of analysis, as it is almost completely wet.

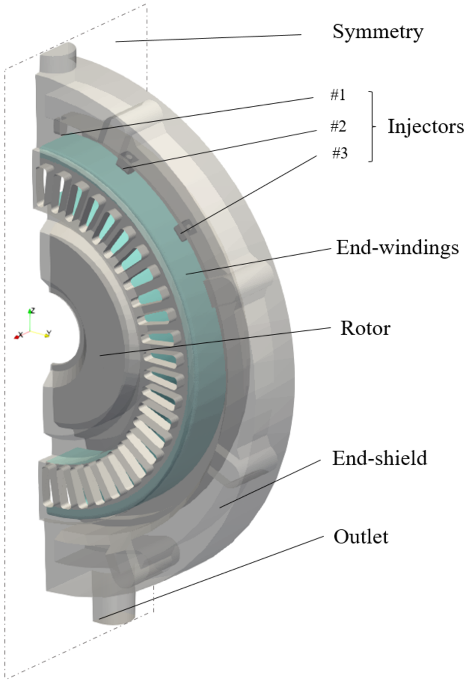

Figure 9.2: Geometry of the end-windings used for the TWM-cst assessment, obtained from [31].

Concerning the boundary conditions, no-slip and Dirichlet conditions with a fixed wall temperature are imposed on all solid surfaces and kept constant throughout the simulation with $T_w = 340\,\mathrm{K}$ for the end-windings surface (including the outer surface) and $T_w = 313\,\mathrm{K}$ on other surfaces. An outlet boundary condition is defined at the bottom of the domain (see Fig. 9.2). The imposed flow rate at injector 1 is $1.08 \times 10^{-5}\,\mathrm{m^3\,s^{-1}}$ (halved due to the symmetry plane), while injectors 2 and 3 each deliver $0.92 \times 10^{-5}\,\mathrm{m^3\,s^{-1}}$. The inlet oil temperature is set to $T_\infty = 313\,\mathrm{K}$.

Initially, the domain is filled with air at $T_g = 293\,\mathrm{K}$. The oil properties are assumed uniform and evaluated at the inlet temperature T_∞, with values detailed in [31]. The thermal diffusivity of the oil is $\alpha_l = 8.05 \times 10^{-8}\,\mathrm{m^2\,s^{-1}}$, and the kinematic viscosity used is $\nu_l = 1.5 \times 10^{-5}\,\mathrm{m^2\,s^{-1}}$. The density is $\rho_l = 0.814 \times 10^3\,\mathrm{kg\,m^{-3}}$ and the specific heat capacity used is $c_{p,l} = 2090\,\mathrm{J\,kg^{-1}\,K^{-1}}$. The surface tension is fixed at $\sigma_l = 30 \times 10^{-3}\,\mathrm{N\,m^{-1}}$, and the static contact angle is set to $\theta_s = 30°$, which affects the momentum balance at the triple line (solid–oil–air interface). A sensitivity study presented in [31] showed that both

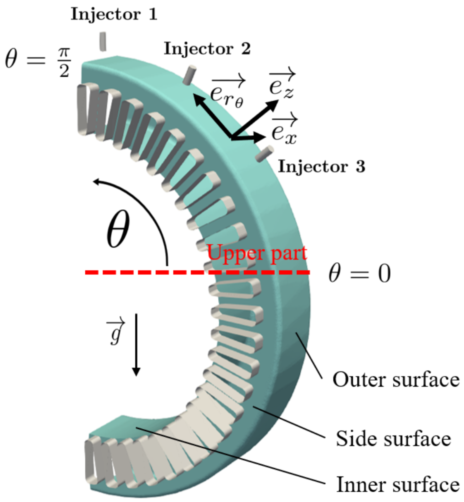

Figure 9.3: Focus on the outer surface of the end-windings. The zone analyzed for the TWM-cst assessment corresponds to the upper part located above the red line. A local cylindrical coordinate system, illustrated here as an example, is used for further local analyses.

parameters have a significant influence on the film extension.

For comparison with the TWM-cst assessment on the academic impinging jet (see Tab. 5.2 in chapter 5), the Reynolds number is calculated for each injector independently, following the same formulation as in the academic configuration. The corresponding relations are recalled below:

$$Re = \frac{4\rho_l \dot{V}}{\pi \mu_l d} \tag{9.1.1}$$

$$Pr = \frac{\nu_l}{\alpha_l} \tag{9.1.2}$$

where $\dot{V}$ is the volumetric flow rate of the considering jet and d the jet diameter. The resulting Re and Pr are summarized in Tab. 9.1. The Pr numbers fall within, and the Re numbers remain only slightly below, the range of conditions previously tested for the TWM-cst in chapter 5. Therefore, the TWM-cst is expected to provide accurate predictions in the near-jet regions.

The CFD code CONVERGE [47] is used to solve the two-phase flow configuration. The numerical setup follows the methodology described for the academic impinging jet in chapter 5.

	Re	*Pr*
Jet 1	287	186
Jets 2 & 3	243	186

Table 9.1: *Re* and *Pr* numbers characterizing the near-jet liquid films.

9.1.2 Meshing strategy

The reference grid, considered as a wall-resolved configuration, together with the coarse meshes used to assess the model, are presented in this section. Since the model is evaluated on the upper outer part of the end-windings, the mesh description focuses on this specific region. The reference mesh was illustrated in [31] near injector 1 and is shown in Fig. 9.4.

The computational domain is automatically discretized using the cut-cell Cartesian method implemented in CONVERGE [47]. The Adaptive Mesh Refinement (AMR) technique is employed to automatically refine the grid at the liquid–gas interface, as shown in Fig. 9.4. A minimum cell size of 0.3 mm is adopted. A sensitivity analysis performed in [31] demonstrated a weak sensitivity of the results for a minimum cell size of 0.3 mm in terms of mean wall heat flux and wetted surface extent.

A dedicated boundary layer mesh is generated near the solid walls of the end-windings to accurately capture the boundary layer behavior while optimizing the number of cells. This refined near-wall grid is composed of flattened cells, as illustrated in Fig. 9.4. The height of the first cell adjacent to the wall is $\Delta_{\text{min}} = 35\,\mu\text{m}$, with an expansion ratio of 1.4. The total thickness of the boundary layer mesh region is $\Delta_{\text{tot}} = 380\,\mu\text{m}$, corresponding to five cells across this zone. This configuration corresponds to the finest near-wall resolution tested in [31]. Results obtained in [31] with a $35\,\mu\text{m}$ first-cell height (compared to $100\,\mu\text{m}$) showed a weak mesh dependency on the outer surface in terms of wetted area and mean heat flux, except in the local stagnation region. A finer mesh is not accessible due to prohibitive calculation times. Nevertheless, validation in the stagnation zone for the mesh using $35\,\mu\text{m}$ was ensured using the Nusselt correlation proposed in [36].

The wall-resolved configuration was thus defined with a minimum AMR cell size of 0.3 mm and a near-wall cell height of $35\,\mu\text{m}$ for the boundary layer grid. To evaluate the model performance, coarser meshes are employed such that the velocity field remains well resolved while the temperature field becomes under-resolved. For this purpose, the AMR refinement was maintained, and the boundary layer grid was progressively coarsened. Three coarse meshes were generated, with respective near-wall cell heights Δ_{min} of $100\,\mu\text{m}$, $200\,\mu\text{m}$, and $300\,\mu\text{m}$, while keeping a similar total boundary layer mesh thickness ($\Delta_{\text{tot}} \approx$

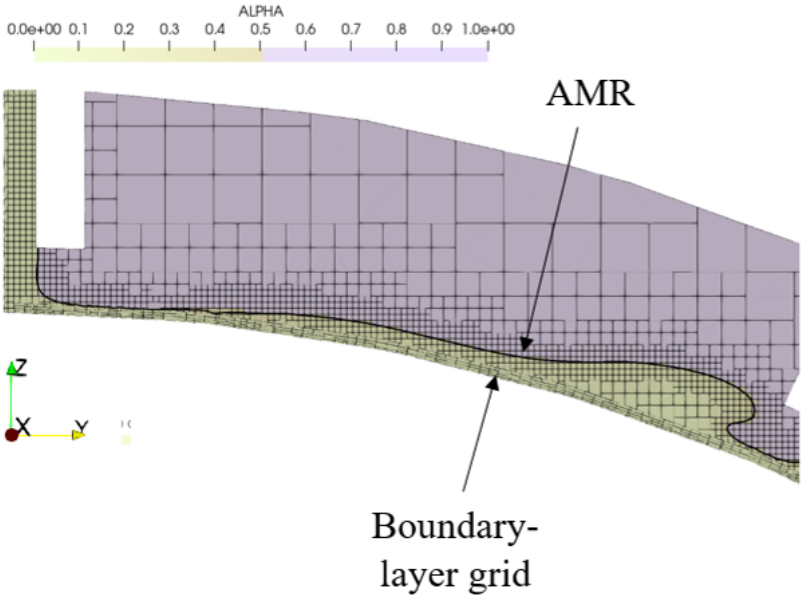

Figure 9.4: Two-dimensional view of the computational mesh near the outer surface, showing the boundary layer refinement and the AMR zones at the liquid–gas interface.

380 μm) across all cases. The different boundary layer mesh configurations and their main parameters, used in this study and described in [31], are summarized in Tab. 9.2 and illustrated in Fig. 9.5.

The total number of cells in the wall-resolved mesh is approximately 3.1×10^6. The reduction in cell count achieved with the coarser meshes remains modest (about 13%), as AMR refinement at the liquid–gas interface has a more significant impact on the total number of cells. However, since the solver employs a semi-implicit approach, the minimum cell size constrains the maximum allowable time step through the CFL condition and the Fourier number. Accordingly, the CFL number is fixed at 0.5 and the Fourier number is set to 10. Increasing the minimum cell size therefore could allow a larger time step and reduce further the overall computational time.

Simulations are carried out with and without TWM-cst for each meshes (except for the wall-resolved mesh, only simulated without model). Their convergences and the analysis of the flow are described in section 9.2.

Mesh	Mesh parameters				
	Δ_{min} (μm)	Expansion ratio	Δ_{tot} (mm)	No. of cells within Δ_{tot}	Total no. of cells in the boundary layer grid
Wall-resolved	35	1.4	0.38	5	737 000
Mesh A	100	1.14	0.40	4	637 000
Mesh B	200	1.00	0.40	2	436 000
Mesh C	300	1.00	0.30	1	334 000

Table 9.2: Summary of the different boundary layer mesh configurations used for the model assessment.

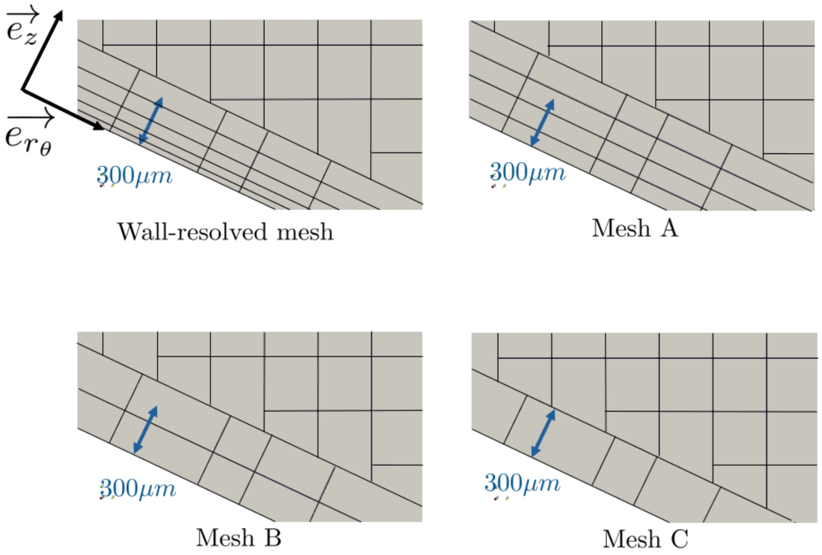

Figure 9.5: Comparison of the different boundary layer mesh strategies adopted for the assessment of the TWM-cst, from the wall-resolved grid (upper left) to the coarsest configuration (lower right).

9.1.3 Model activation condition on a partially wet surface

In this configuration, the model is applied to a partially wetted surface. Consequently, an activation condition for the model has been implemented in CONVERGE CFD [47], ensuring that the model operates exclusively in regions where the liquid phase is in contact with solid walls. The activation criterion in a given near-wall cell is based on the local gas volume fraction, denoted by the variable α in the Volume of Fluid (VoF) framework (see chapter 5 for additional details on the governing equations). The TWM-cst is activated only when the gas volume fraction $\alpha < 10^{-3}$ ($\alpha = 0$ indicates the presence of liquid).

For the moment, no detailed analysis of the TWM–cst interaction with the three-phase contact line using the VoF method has been conducted. Further investigation on this aspect would be a valuable direction for future work.

9.2 Simulation convergence and steady-state analysis

9.2.1 Convergence analysis

The flow convergence is analyzed for all meshes, with and without the TWM-cst (except for the wall-resolved mesh), focusing on the upper outer part of the end windings. To evaluate convergence, the parameter ξ is introduced to represent the ratio between the liquid-covered surface area S_{film} and the total outer surface area S_{total}:

$$\xi = \frac{S_{\text{film}}}{S_{\text{total}}} \tag{9.2.1}$$

The time evolution of ξ for the upper part of the outer end-windings is presented in Fig. 9.6. All the coarse meshes reach a steady value of ξ after approximately 1 s, while the total simulated physical time extends to 15 s. As expected, the model has a negligible effect, since it only (indirectly) modifies the temperature field, which acts as a passive scalar in the present configuration. The most refined mesh requires roughly twice as long (in physical time) to reach steady film coverage compared to the coarser ones. As discussed in [31], this behavior is related to the mesh-dependent viscous stresses near the contact line, which arise from the modeling approach combining a static contact angle and a no-slip wall condition. Although this dependency does not affect the final steady-state solution, using a coarser mesh reduces the time required to achieve steady-state convergence.

The macroscopic variable used to evaluate the global thermal convergence is the spa-

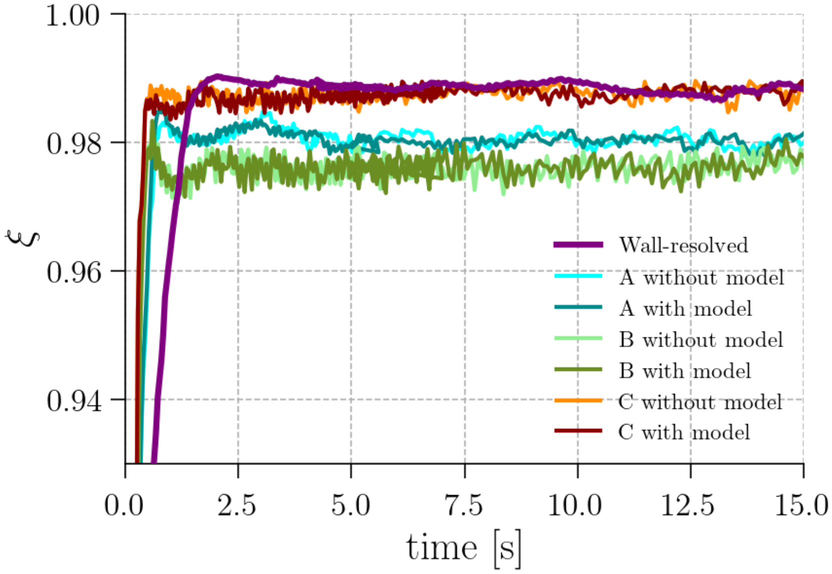

Figure 9.6: Time evolution of the surface liquid coverage ratio ξ for the upper outer surface of the end-windings. All meshes reach a steady-state value after approximately 2.5 s.

tially averaged surface heat flux over the upper outer end-winding surface, denoted by $\overline{q_w}$. The time evolution of $\overline{q_w}$ is presented in Fig. 9.7. The results show that $\overline{q_w}$ reaches a steady value after approximately 10 s for all meshes, with only negligible fluctuations observed between 10 s and 15 s. The simulations can therefore be considered converged from a thermal standpoint and no degradation of the convergence is noticeable with the TWM-cst. It is not particularly informative to assess the model solely on the basis of the averaged wall heat flux $\overline{q_w}$, since local errors in q_w may compensate. It is therefore more pertinent to analyse the model using the local heat-flux q_w or by distinguishing between different zones. In the following sections, all results presented correspond to instantaneous fields sampled at a physical time of 15 s.

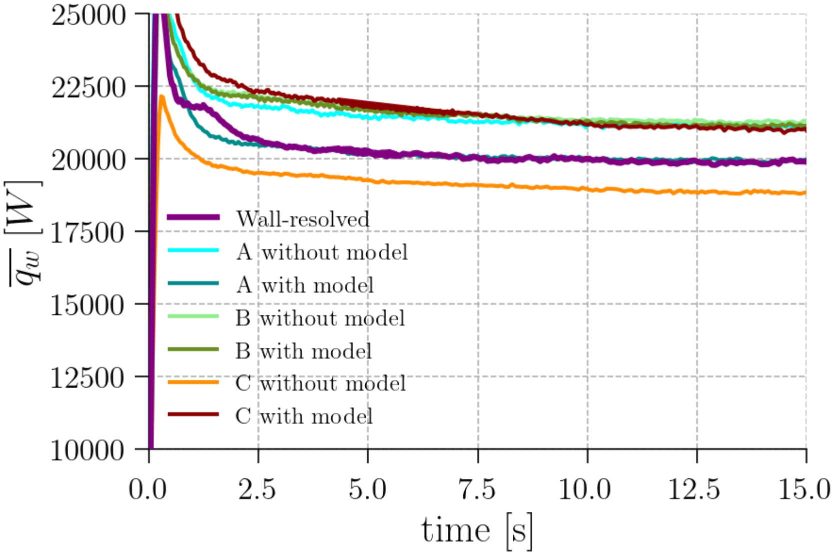

Figure 9.7: Time evolution of the mean wall heat flux $\overline{q_w}$ over the upper outer surface of the end-windings for all meshes.

9.2.2 Flow and thermal analysis

A detailed analysis of the steady-state flow over the upper part of the outer end-windings surface is carried out using the wall-resolved case. Fig. 9.8 illustrates the liquid film shape (in green), which covers the vast majority of the surface, together with the liquid velocity field at the liquid–gas interface. The results show the formation of pronounced bumps between the impinging jets, particularly upstream of jets 2 and 3. These bumps result from the collision between liquid streams flowing in opposite directions. Their position between jets is likely due to the influence of gravity or a differential flow rate between jets, which induces a preferential downstream position of the bumps[1]. The bumps start very close to jets 2 and 3 and extend over more than half of the circumferential length around each jet. The effect of the bump extends up to approximately 4 jet diameters upstream of jets 2 and 3.

Fig. 9.9 presents a cross-sectional slice passing through the jet centers (normal to the $\vec{e_x}$ direction), colored by the gas volume fraction α. The figure highlights the bump, where the velocity field reveals the presence of recirculation zones and a stagnation (collision) point along the wall.

---

[1] A downstream position means downstream relatively to the gravity, which means for lower values of θ (see Fig. 9.3)

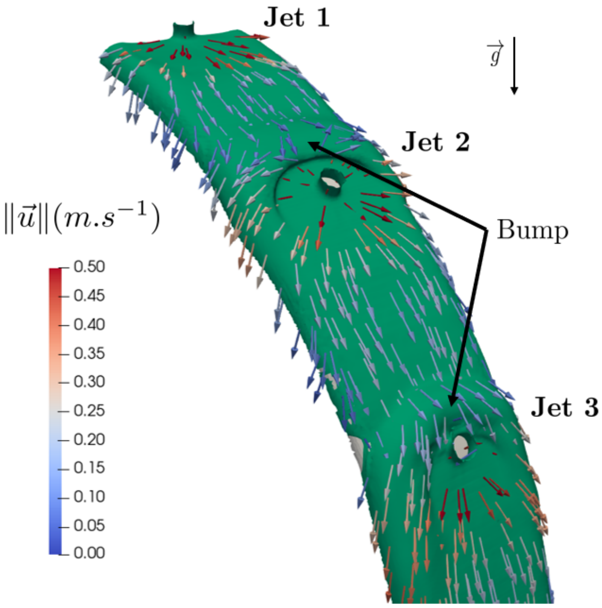

Figure 9.8: Liquid film (in green, represented with an iso-contour $\alpha = 0.5$) over the upper outer surface of the end-windings and liquid velocity magnitude at the liquid–gas interface for the wall-resolved configuration. The color scale saturates for $\|\vec{u}\| > 0.5\,\mathrm{m.s^{-1}}$.

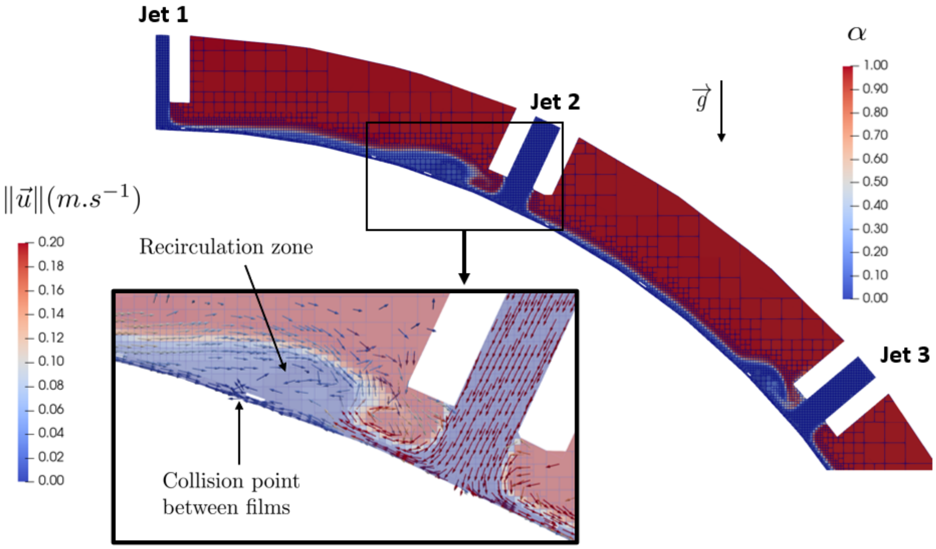

Figure 9.9: Cross-sectional slice through the jet centers, colored by gas volume fraction. Recirculation zone and a stagnation point appear in the film bump. The velocity-magnitude color scale is applied only to the velocity arrows and saturates for $\|\vec{u}\| > 0.2\,\mathrm{m\,s^{-1}}$.

The evolution of the film thickness along this cross-sectional slice is shown in Fig. 9.10, which clearly identifies the recirculation zones where the local film height H_{film} reaches approximately 3 mm, compared to about 1 mm in the upstream film. Within these recirculation regions, the near-wall velocity decreases, resulting in weaker convective heat transfer and a corresponding reduction in the local Nusselt number. This is visible in Fig. 9.10, where Nu reaches a minimum at the collision point. The figure also highlights the much higher Nu values directly beneath the impinging jets, followed by a sharp decay in their immediate vicinity. Results from the academic impinging jet configuration presented in chapter 5 show a pronounced decrease in Nu up to the upper radial limit of region 2, located for example at $1.1\,d$ for jet 2. Beyond region 2, the Nu value continues to decrease gradually until the film collision point is reached.

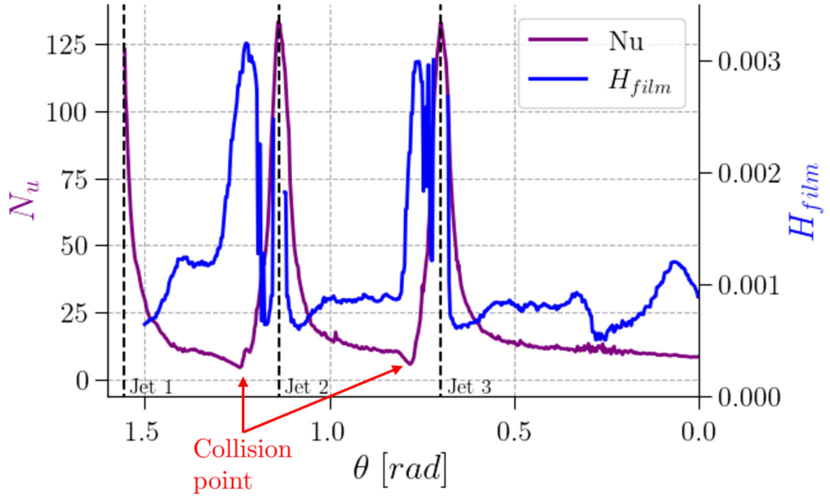

Figure 9.10: Azimuthal evolution of film thickness H_{film} and Nusselt number Nu along the upper outer surface. The recirculation zones correspond to thicker films and reduced local Nu.

The azimuthal velocity u_θ, defined as the projection $u_\theta = -\vec{u} \cdot \vec{e_{r_\theta}}$, is shown upstream jet 2 in Fig. 9.11a along profiles in the $\vec{e_z}$ direction and contained inside the plane passing through the jets. The profiles up to $r_\theta = -1.5d$ from the jet, exhibit a dynamic boundary layer development shape, as expected within the near-jet film. Beyond this distance, at $r_\theta = -2d$, $r_\theta = -3d$, and $r_\theta = -4d$, u_θ approaches zero. In this region, a non-negligible wall-normal velocity component relatively to the azimuthal component may develop[2], which

---

[2] In the plane passing through the jets, the parallel component of the velocity to the wall, $\vec{u} - (\vec{u} \cdot \vec{e_z})\,\vec{e_z}$, is nearly identical to the azimuthal component $-u_\theta\,\vec{e_{r_\theta}}$, since the $\vec{e_x}$ component of $\vec{u}$ is negligible.

falls outside the assumptions of the TWM-cst model. The corresponding temperature profiles, shown in Fig. 9.11b, depart from the Lévêque-type behavior, exhibiting a quasi-linear near-wall profile at $r = -4d$, which can be attributed to the non–wall-parallel flow and to the dominance of conduction over convection[3].

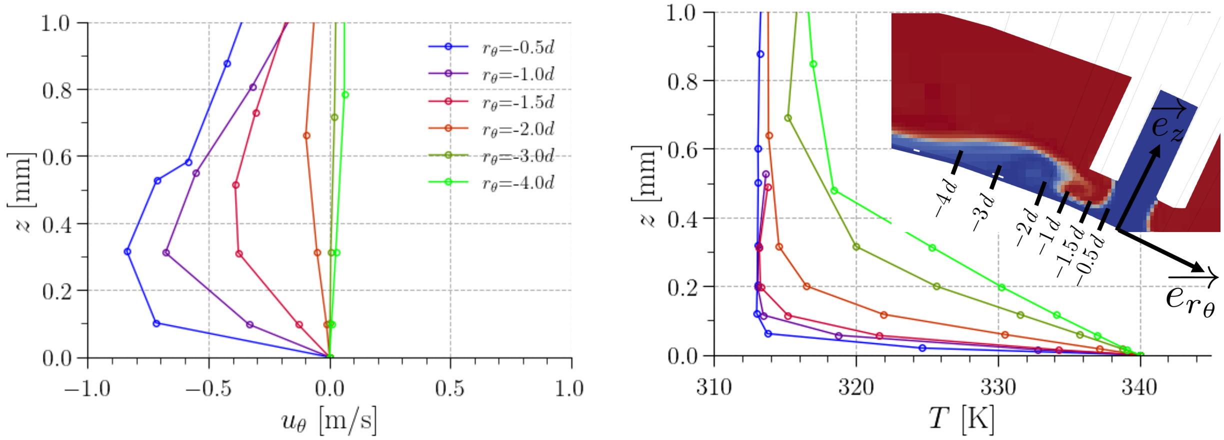

(a) Azimuthal velocity profiles.

(b) Temperature profiles.

Figure 9.11: Azimuthal velocity (a) and temperature (b) profiles, at several distances upstream from jet 2, inside the liquid film, for the wall-resolved configuration.

On the downstream side, the velocity profiles shown in Fig. 9.12a exhibit a parabolic shape from and beyond $r_\theta = 2d$, characteristic of film flow in the region 3 (see chapter 5). Conversely, the near-wall temperature profiles downstream, presented in Fig. 9.12b, seem to follow the Lévêque-type distribution. It is worth noting that the temperature at the liquid–gas interface increases with distance from the jet. This rise may result from diffusive heat transfer from the hotter surrounding air (with $T_g \approx 316\,K$ neat jet 2) toward the liquid film. However, due to the low thermal diffusivity of the liquid (α_l), this effect is expected to have only a minor influence on the near-wall temperature field. The order of magnitude of the penetration height H_p of the heat diffusion from the gas phase inside the liquid film at a distance of $5d$ from the jet axis can be estimated as:

$$H_p = \sqrt{\alpha_l t_p} \tag{9.2.2}$$

---

[3] In the conduction-dominated regime, the notion of a thermal boundary layer, which is intrinsically linked to convective transport, becomes meaningless.

where t_p is the characteristic time for the flow to travel $5d$:

$$t_p = \frac{5d}{u_{r_\theta}^{\text{interf}}} \approx \frac{0.015}{0.2} = 0.075 \text{ s} \tag{9.2.3}$$

with $u_{r_\theta}^{\text{interf}}$ a representative azimuthal velocity at the liquid–gas interface taken at $r = 3d$. This gives $H_p \approx 0.1\,\text{mm}$. Considering that the film thickness is approximately $0.5\,\text{mm}$, this order of magnitude suggests that heat diffusion from the interface can noticeably affect the bulk liquid temperature, as confirmed by the temperature profiles in Fig. 9.12b, while having only a limited impact on the very near-wall temperature and so should not impact significantly the model results[4]. Nevertheless, this thermal effect would merit a more detailed analysis with a simpler numerical set-up and a better-resolved film, which is not feasible with the current configuration due to computational cost.

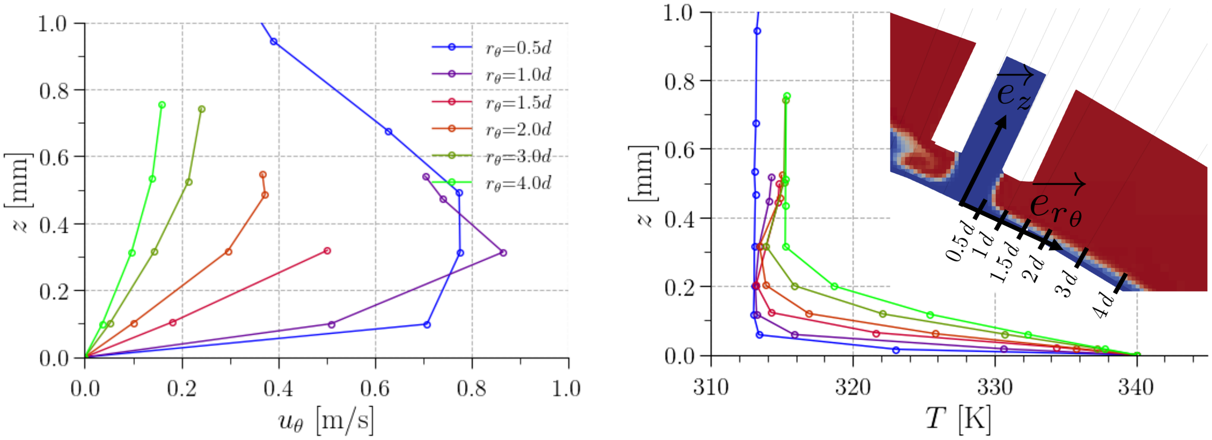

(a) Azimuthal velocity profiles.

(b) Temperature profiles.

Figure 9.12: Azimuthal velocity (a) and temperature (b) profiles, at several distances downstream of jet 2, inside the liquid film, for the wall-resolved configuration.

9.3 Grid sensitivity

To properly evaluate the TWM-cst, the mesh should under-resolve the near-wall temperature field while adequately resolving the velocity field. Notably, this ensures that the film thickness and its spatial extent are accurately predicted. The ratio of the surface covered

---

[4] The model assumes a single value of T_∞; any change in this value that alter the thermal boundary layer violate the model assumptions.

by the film, ξ, displayed for the upper part of the outer end-windings in Fig. 9.6, shows that all meshes yield similar values of ξ, all close to unity (indicating that the surface is almost entirely covered by the liquid film).

To assess the local sensitivity to mesh refinement, the near-wall shear stress τ_w is plotted in Fig. 9.13 as a function of the azimuthal position. As expected, τ_w reaches its maximum very near the jets and approaches zero near the film collision point. The results indicate that the shear stress distribution is only weakly dependent on the mesh, except in the downstream region of the outer surface ($\theta \in [0, 0.5]$), where higher variability is observed. However, this variability primarily arises from temporal fluctuations of the film, which exhibits oscillations likely related to Kapitza-type instabilities [38], as commonly observed in falling liquid films on vertical planes. Nevertheless, even the wall-resolved mesh may not be sufficiently refined to fully capture these phenomena.

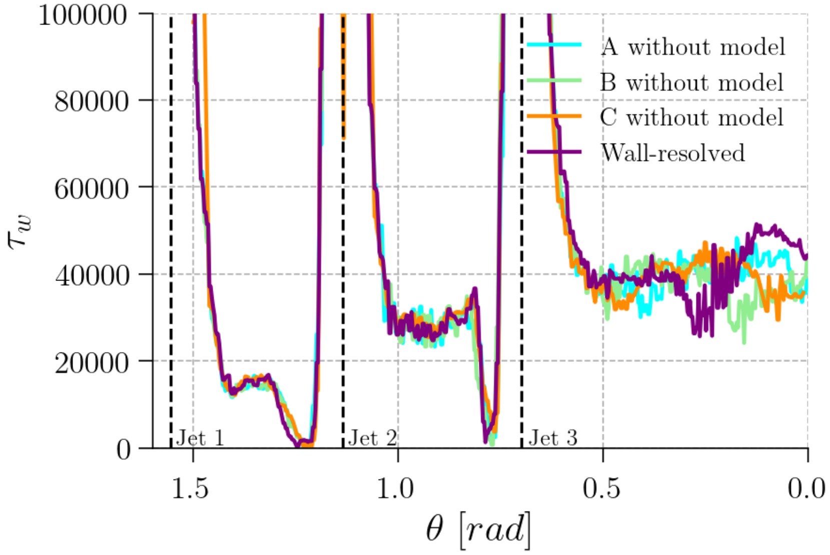

Figure 9.13: Azimuthal evolution of near-wall shear stress τ_w along the outer surface for different mesh refinements.

To complete the local investigation, u_θ profiles are compared at several positions. The u_θ profile very near jet 2, at $r_\theta = 1d$ from jet 2, shown in Fig. 9.14a, exhibits good agreement between all meshes and the wall-resolved reference. The coarsest mesh C shows a slightly larger deviation, which can be attributed to the near-wall cell height being comparable to the dynamic boundary layer thickness (defined as the distance between the wall and the location of maximum u_θ, see chapter 5). Further downstream, at $r_\theta = 4d$ (see Fig. 9.14b), the flow velocity decreases significantly, and all meshes capture correctly the parabolic-like shape of the velocity profile. Conversely, in the recirculation zone (see Fig. 9.14c), the velocity profiles display noticeable differences between meshes. This region remains mesh dependent, and the TWM-cst may be influenced by inaccuracies in the local velocity profile.

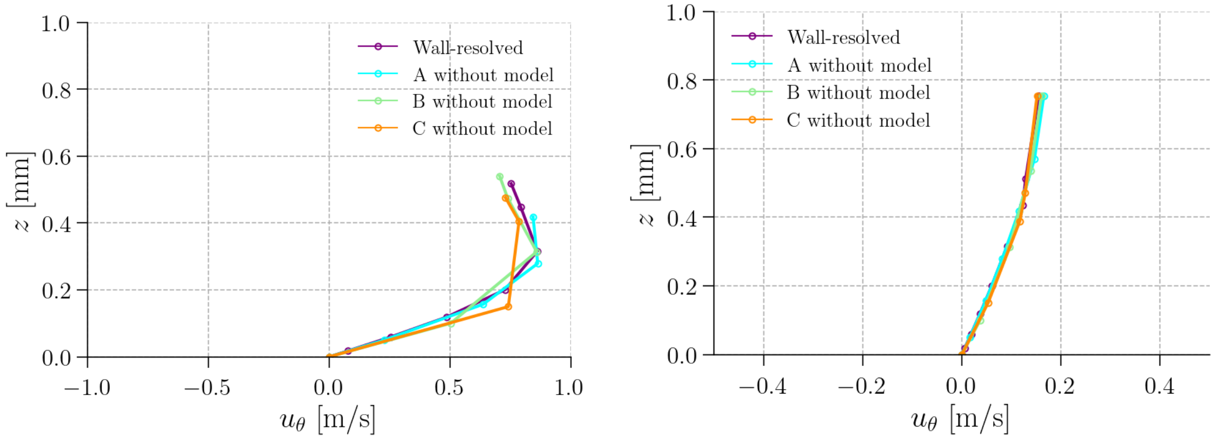

(a) Velocity profiles near jet 2 at $r_\theta = 1d$.

(b) Velocity profiles downstream of jet 2 at $r_\theta = 4d$.

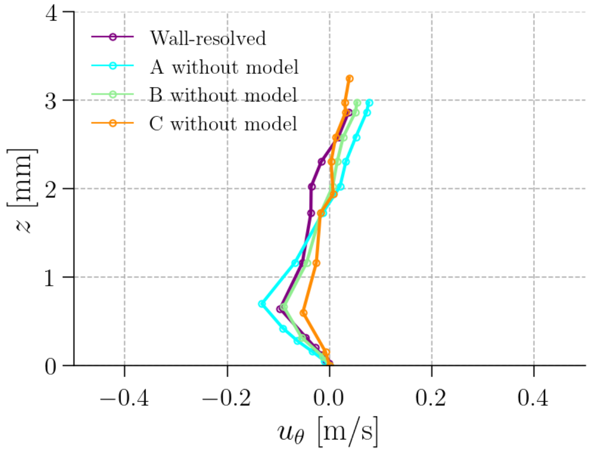

(c) Velocity profiles in the recirculation zone, upstream of jet 2 at $r_\theta = -2d$.

Figure 9.14: Azimuthal velocity profiles inside liquid film, obtained with different mesh resolutions at several distances from jet 2.

9.4 Model assessment

The TWM-cst is now assessed for all coarse mesh configurations by considering $Q_w(r < 3d)$ and $Q_w(r > 3d)$. $Q_w(r < 3d)$ is the integral of the surface heat flux over a disk of radius $r = 3d$ around each jet and $Q_w(r > 3d)$ is defined as the heat flux integral on the remaining part of the upper outer surface. They allow us to distinguish the errors on the total integral heat flux Q_w between different zones and to avoid compensation effects between them. $Q_w(r < 3d)$ can be approximated by

$$Q_w(r < 3d) \approx \sum_{jets} \int_0^{3d} q_w \, 2\pi r \, dr \tag{9.4.1}$$

where r denotes the radial distance from a given jet. The curvature of the outer surface is neglected in Eq. 9.4.1 as $3d \ll R$. $Q_w(r > 3d)$ is computed as $Q_w(r > 3d) = Q_w - Q_w(r < 3d)$. Both surfaces used to calculate Q_w are depicted in Fig. 9.15. The near-jet region $(r < 3d)$ includes both the stagnation zone, where the thermal boundary layer is thinnest, and part of the recirculation zone. The results, shown in Fig. 9.15, demonstrate that, as previously observed for the academic impinging jet configuration (see chapter 5), the model significantly improves the prediction of wall heat transfer near the jets, where the thermal boundary layer is thin and under-resolved. For mesh A, however, this improvement is less apparent since the integral wall heat flux $Q_w(r < 3d)$ is already well predicted.[5] In the remaining part of the upper outer surface ($Q_w(r > 3d)$), where the thermal boundary layer is thicker, the TWM-cst still provides a noticeable improvement. Overall, the results obtained for the different meshes indicate that the model's performance is only weakly dependent on mesh resolution and flow characteristic.

The model results are now analyzed in terms of the absolute relative error of the local wall heat flux, $|q_w^{\mathrm{error}}|$, as defined in Eq. 4.2.1, and recalled here:

$$q_w^{\mathrm{error}} = \frac{q_w - q_w^{\mathrm{ref}}}{q_w^{\mathrm{ref}}} \tag{9.4.2}$$

where the superscript "ref" refers to the wall-resolved case. The results in terms of $|q_w^{\mathrm{error}}|$ are presented for the least refined mesh (mesh C) in Fig. 9.16. It is observed that, without the model, the error exceeds 50 % near the impingement points (the color scale saturates above this limit), where the thermal boundary layer is the thinnest. Large errors are also visible in the recirculation regions, likely due to an under-resolved velocity field. A

---

[5] Mesh A without model seems to predict correctly the heat flux in the near-jet region. In fact, error compensations hide a local underestimation in the stagnation zone [31].

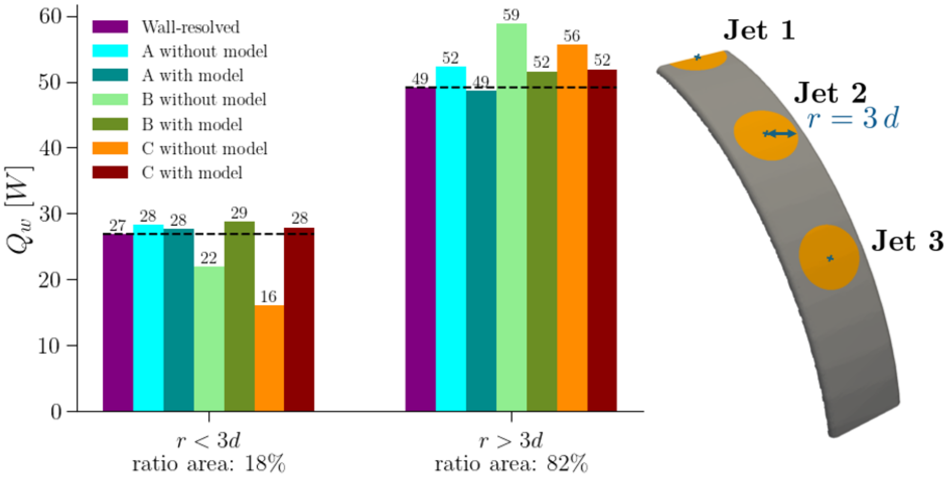

Figure 9.15: Integral wall heat flux Q_w (see Eq. 9.4.1) in the near-jet region ($r < 3d$ displayed in orange in the scheme) and the remaining part of the outer surface ($r > 3d$ displayed in gray), comparing the TWM-cst and non-modeled cases for different mesh resolutions.

ring of near-zero error (appearing as a blue circle around the impingement zones) is also noticeable: this corresponds to a border between an underestimated q_w inside the ring and an overestimated q_w outside it (to illustrate this, Fig. 5.11a for a single jet shows a similar trend). Once the TWM-cst is activated, $|q_w^{\text{error}}|$ is globally reduced across the entire outer surface. However, high errors persist in the recirculation areas, only slightly mitigated by the model. These residual errors may be attributed to the under-resolved velocity field (see Fig. 9.14c), which deteriorates the prediction of TWM-cst. In addition, the assumption of negligible wall-normal velocity across the near-wall cell height, an underlying premise of the model, is not fully satisfied in these regions.

The Nu distribution along a line passing through the jets for mesh C (see Eq. 5.3.2 for the definition of Nu), shown in Fig. 9.17, corroborates the observations discussed above. The TWM-cst allows a substantial recovery of the Nu prediction near the jet in the stagnation zone (which explains the large improvement in Fig. 9.15 for $Q_w(r < 3d)$), although a non-negligible error remains. A similar behavior was already observed in the academic impinging-jet configuration (see chapter 5), particularly at higher Reynolds numbers (see Fig. 5.11b). In that case, the discrepancy could be attributed to an under-resolved dynamic boundary layer in the stagnation zone. In the present configuration, the velocity profile shown in Fig. 9.14a confirms that mesh C under-resolves the near-wall velocity field, which may explains the residual errors observed with and without the model

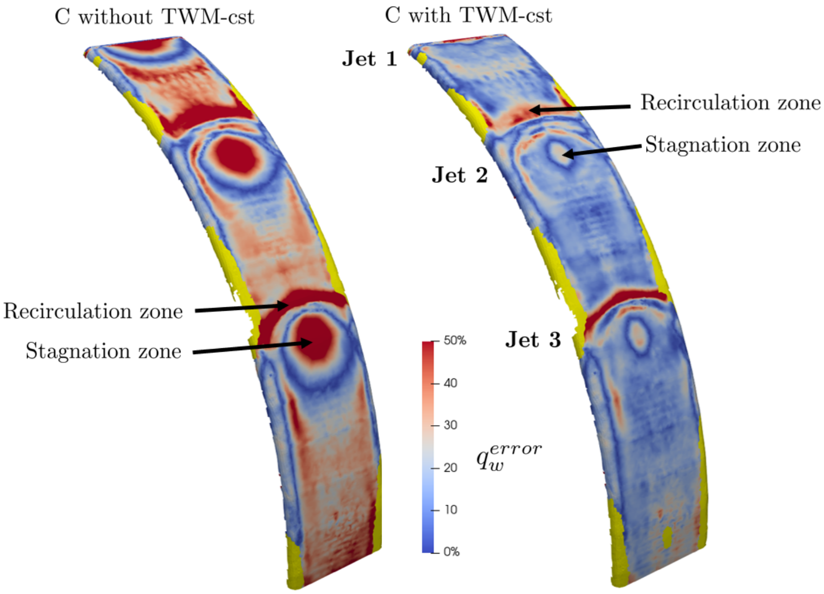

Figure 9.16: Relative surface heat flux error $|q_w^{\text{error}}|$ over the outer surface of the end-windings for the coarsest mesh C, with and without the TWM-cst. The color scale saturates for $|q_w^{\text{error}}| > 50\%$. The yellow part of the surface depicts dry zones.

in this region.

The same results, expressed in terms of the relative heat flux error q_w^{error}, are shown in Fig. 9.18. In the stagnation zones, the coarse mesh has a minimum n_{δ_T} of 0.2. Without the model, the error peaks at approximately 80 % for each jet, a large error that is consistent with the results obtained under Lévêque conditions (see Fig. 4.5). The TWM-cst reduces this error to about 25%. Outside the stagnation regions, except within the recirculation areas, the model reduces the local error by roughly 20 percentage points, bringing it down to values between 10% and 25%, depending on position. In the downstream region exhibiting flow instabilities ($\theta \in [0, 0.5]$), the model still improves the prediction, as the amplitude of film thickness oscillations remains smaller than the mean film thickness (see Fig. 9.10) and therefore does not strongly affect the near-wall heat flux. It is worth noting that fully developed Kapitza instabilities can significantly influence wall heat transfer unless the thermal boundary layer is sufficiently thin [82, 83, 84]. However, this region may not be correctly resolved in the present simulations, and the corresponding results should be interpreted with caution.

The TWM-cst has shown encouraging results in a complex configuration representative of the targeted industrial application. The model results exhibit trends that are close to

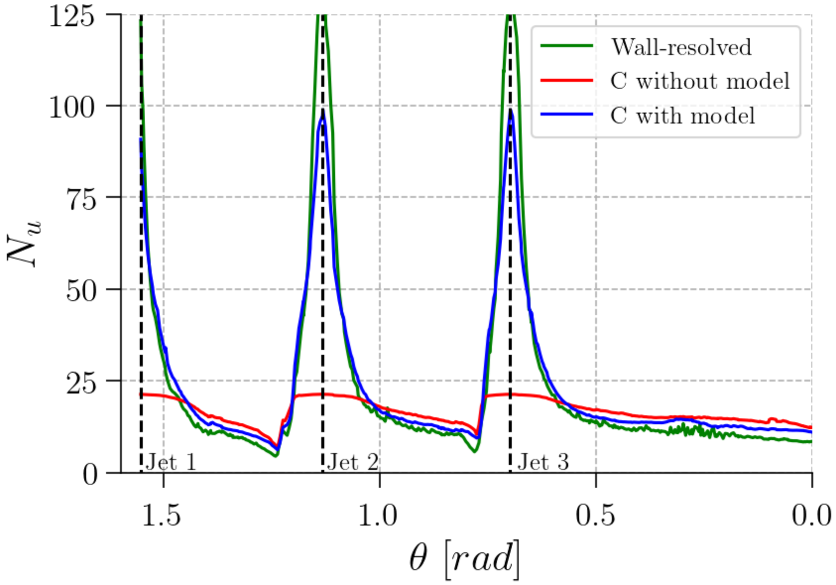

Figure 9.17: Azimuthal evolution of the local Nusselt number along the upper outer surface for the coarsest mesh C, with and without the TWM-cst, compared to the wall-resolved case.

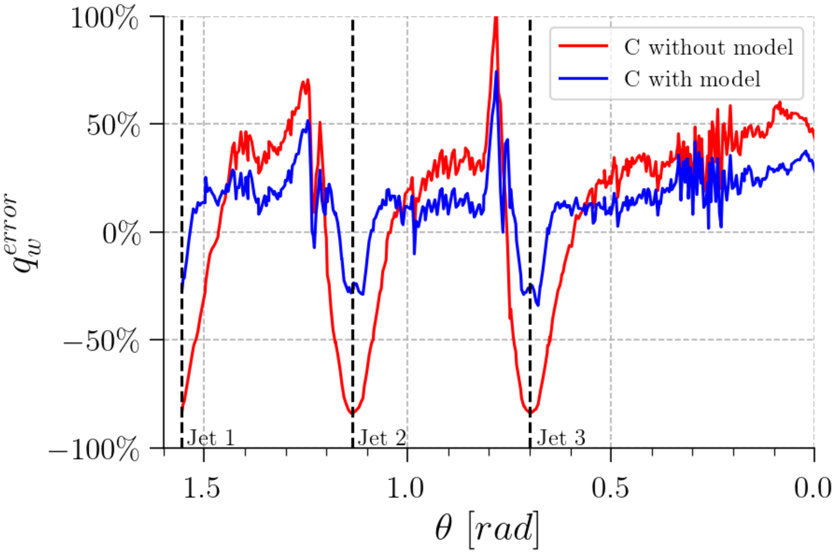

Figure 9.18: Azimuthal evolution of relative heat flux error q_w^{error} along the outer surface for the coarsest mesh C, with and without the TWM-cst.

those obtained for the simpler configurations, namely in Lévêque conditions (see chapter 4) and for the academic jet (see chapter 5). In particular, there is a strong improvement on coarse meshes, very close to the jet, where n_{δ_t} is lowest, and no noticeable deterioration further from the jet (finer meshes with higher n_{δ_t}). Interestingly, the model shows improvements further from the jet, except in the recirculation zones. Further investigation of the model behaviour in these regions would be an interesting perspective, especially using a similar but simpler configuration with a more refined wall-resolved reference case.

The improvement provided by TWM-cst is expected to be more significant for higher-Prandtl-number fluids, as the coarse mesh will be even coarser relative to the thermal boundary layer (while still resolving the flow). However, in such cases the corresponding wall-resolved simulations, requiring the resolution of much thinner thermal boundary layer, would become prohibitively expensive in terms of computational cost.

The gain in computational efficiency is summarized in Tab. 9.3 for all mesh configurations. The results show that activating the TWM-cst introduces no additional computational overhead. Therefore, with only a limited degradation in q_w prediction accuracy, results can be obtained at a lower computational cost compared to the wall-resolved mesh. For instance, with mesh C, the total computational time is reduced by approximately 18%. This reduction is smaller than might be expected, since the time step is found to be identical for all configurations. With a limitation imposed by the CFL and Fourier numbers, the time step is likely constrained by a relatively small cell outside the near-wall boundary layer mesh. Hence, coarsening the very thin near-wall boundary layer mesh does not permit a larger time step, contrary to expectations. Further investigation is needed to identify this limiting cell and adjust the mesh accordingly in order to increase the allowable time step.

Mesh	**TWM-cst**	**CPU time (days)**
Wall-resolved	without	556
A	with / without	519
B	with / without	491
C	with / without	455

Table 9.3: CPU time required for each mesh configuration, with and without the TWM-cst.

Part V

Conclusion and perspectives

This thesis proposes a thermal wall model designed for high Prandtl number cases in the laminar regime, where the thermal boundary layer is extremely thin, necessitating a near-wall model to mitigate excessive computational costs. The proposed model is based upon Lévêque theory [45], which analytically resolves the dimensionless temperature profile. Given user-prescribed wall and free stream temperatures, the model assigns a wall heat flux to each near-wall cell based on local information. To this end, a scaling based on the thermal boundary layer thickness links the near-wall cell temperature and height to the corresponding wall heat flux.

A first version of the thermal wall model, denoted TWM-cst, is tailored to handle fluids whose viscosity is only weakly dependent on temperature. Building on this, an extended version, denoted TWM-var, is proposed to handle fluids with strong viscosity–temperature dependence, leading to a coupling between the velocity and temperature fields. This extension relies on a dimensionless velocity profile that provides an accurate approximation in the limit of a thin thermal boundary layer. The extended model enables the prediction of wall shear stress in addition to wall heat flux, through an additional scaling, again based on the thermal boundary layer thickness, that relates the near-wall cell velocity to the associated wall shear stress. Implementation is straightforward, as both versions of the model require only the information from the first off-wall cell, in addition to user-prescribed wall and free stream temperatures. The numerical context in which the models are applied, namely the finite-volume method, is explicitly accounted for by adapting both dimensionless profiles to the approximations inherent in this framework.

The underlying assumptions of both models include the classical laminar boundary layer hypotheses: steady, incompressible, laminar, and two-dimensional flow, with negligible pressure gradients, viscous dissipation, and absence of variations in thermophysical properties except for the viscosity. In addition, it incorporates the specific assumption from the Lévêque's theory of a uniform shear stress across the thermal boundary layer. Further assumptions arising from the finite-volume method are introduced.

The initial assessment of the model tailored for uniform viscosity is conducted on a two-dimensional thermal boundary layer configuration under conditions that satisfy its underlying assumptions (see chapter 4). Substantial gains are obtained on coarse meshes: for example, with only 0.2 cells across the thermal boundary layer ($n_{\delta_t} = 0.2$), the wall-heat-flux error is reduced from 75 % to nearly 0 %. For finer meshes (about 2.5 cells across the boundary layer), a slight over-correction appears, with a maximum error of $\approx 10\,\%$, which decreases as the resolution is further refined.

For a two-dimensional thermal boundary layer with temperature-dependent viscosity (see chapter 7), the extended model shows significant improvements on coarse meshes for both wall shear stress and wall heat flux, with errors reduced to nearly zero. For finer meshes (approximately 2.5 cells across the thermal boundary layer), a slight over-correction of the wall heat flux is observed: the maximum error remains below 10 % and decreases further as the mesh is refined. Improvements are observed in the near-wall velocity, which is consistent with the enhanced prediction of τ_w.

A second evaluation on an academic impinging jet configuration, more representative of the intended industrial application, yields promising results (see chapter 5). The uniform-viscosity model exhibits low sensitivity to mesh resolution, flow regime, and to the ratio of thermal to dynamic boundary layer thicknesses. The wall heat flux predictions are strongly improved in regions where the thermal boundary layer is under-resolved (fewer than 1.5 cells across δ_t). Conversely, the model performance remains unchanged, or deteriorates only marginally (the error remains below 10 %), in regions where the thermal boundary layer is already sufficiently resolved. This slight deterioration is intrinsic to finer meshes and shares the same origin as the behavior observed in the two-dimensional thermal boundary layer assessment. It may also result from flow configurations that do not fully satisfy the model assumptions. In terms of computational cost, reductions of about 90% for $Pr = 1000$ and 70% for $Pr = 158$ are obtained while maintaining wall heat flux predictions close to the wall-resolved reference.

With temperature-dependent viscosity (see chapter 8), the uniform viscosity model provides only marginal improvement when the viscosity variation is significant (e.g., a kinematic viscosity up to five times lower inside the thermal boundary layer). In contrast, the extended model yields improvements in all regions or only slight deterioration. The film thickness error is reduced from about 10% at the minimum thickness location to 1.0% and the maximum error on wall shear stress decreases from 14% to 5% at the wall shear stress peak for a $Re = 317$ and $Pr = 111$. The improved near-wall velocity field further enables an accurate prediction of the wall heat flux by the model. Over a wide range $Re \in [220, 2844]$ and $Pr \in [1, 292]$, wall heat flux predictions are significantly improved where the thermal boundary layer is under-resolved and only marginally affected by the magnitude of the viscosity variation.

Finally, the model tailored for uniform viscosity is evaluated on a geometry representative of the targeted industrial application, featuring multiple jets and a partially wetted surface. Results are encouraging, with a substantial reduction in wall–heat–flux error, especially near the impinging jets where the thermal boundary layer is thinnest. However, in film collision zones the model assumptions are violated, and the method neither improves nor degrades the predictions.

Perspectives for future work are presented below. They include depicted improvements to the thermal wall model to enhance flexibility and accuracy. We then introduce numerical aspects related to robustness improvement. Finally, assessments that are mandatory before advancing the model toward the final industrial application are proposed.

A first avenue of improvement of the model is enhancing flexibility by removing reliance on an unique free stream temperature, i.e., the temperature outside the thermal boundary layer, which is taken as identical in all simulations. So far it is provided by the user as the inlet coolant. A two–point reconstruction in the near–wall grid (e.g., using the first two near–wall cells) could infer the local free stream temperature. This strategy previously used in subgrid–scale modeling (see section 2.2.3) and detailed in [67], allows a non–uniform free stream temperature which is especially beneficial in recirculating zones where the free stream temperature may varies. However, such an implementation may reduce robustness and increase model complexity.

Another improvement, specific to TWM-var, is to extend its use to configurations with non-uniform wall temperature, since the dimensionless velocity profile depends on the wall temperature. Two approaches can be considered: precomputing the dimensionless profiles for a discrete set of wall temperatures, or computing and regularly updating a dedicated profile for each near-wall cell.

A further refinement would be to correct the flux at the wall and between the first and second off-wall cells. This correction is expected to reduce the $\approx 10\%$ error observed for a medium refinement of the thermal boundary layer, at the cost of a more complex implementation. Finally, the model may be deactivated when the thermal boundary layer is sufficiently resolved (using a threshold based on the number of cells inside the thermal boundary layer) to mitigate the slight deterioration observed on moderately resolved meshes.

Additional assessment of the model is required to address aspects related to more complex numerical setups. An evaluation on Cartesian meshes using cut–cells at the wall is required, as this is a widely used technique. Moreover, particular attention should be paid to the model activation near the liquid–gas–solid contact line on partially wetting surfaces. The interaction of the model with the interface could trigger numerical instabilities (particularly for the TWM-var model, as the correction of the wall shear stress could impact the contact line velocity). So far, activation thresholds based on the volume fraction in VoF methods have been used on partially wetting surfaces for TWM-cst (see chapter 9), and no instabilities have been observed.

Evaluating the range of applicability of the model beyond the canonical impinging jet configurations and closer to the industrial objective of end–winding cooling is mandatory.

Addressing these related complexities will be a critical focus for future development of the thermal wall model. To date, the model has been assessed with a uniform wall temperature under steady–state conditions. Testing the model on non–uniform and unsteady configurations is therefore required to approach the targeted application. The model should also be evaluated on more complex flows than the "supercritical" part of the jet (upstream the hydraulic jump). The "subcritical" region downstream of the hydraulic jump, where recirculation occurs, should be investigated. Prior to this, a canonical separated configuration such as a backward–facing step would quantify sensitivity to recirculation. Interactions between multiple jets on a flat plate should be examined to characterize accuracy in film–film collisions, as chapter 9 indicates that model assumptions may not hold in this type of flow. Applications to non–smooth walls, such as corrugated plates that may induce periodic recirculation and local stagnation pockets, would probe robustness on geometrically complex surfaces representative of a realistic end–winding. Finally, the present evaluation has covered impinging jets and the resulting stable liquid films, while excluding falling–film regimes in which Kapitza waves develop [38], a regime often encountered in film–cooling applications. Even so, prior works [83, 82] shows that, when the thermal boundary layer is sufficiently thin, the influence of Kapitza waves on wall heat transfer is negligible.

The potential applicability of the thermal wall model extends beyond the present configuration. By replacing the thermal diffusivity with a species diffusivity, the same framework can be applied to near-wall mass transfer characterized by large Schmidt numbers. Near-wall heat or mass transfer in laminar flows with high Prandtl or Schmidt numbers arises in many industrial and natural settings, for example in reactive-surface and surface-cooling applications [62], as well as in geophysical and biological flows [70].

APPENDIX A

Near-wall cell temperature error with TWM-cst under Lévêque conditions

Activating TWM-cst modifies q_w, which in turn affects the near-wall cell temperature T_1 on coarse meshes. As for q_w^{error} (see Fig. 4.5), the dimensionless near-wall cell temperature T_1^*, with and without the model, depends primarily on n_{δ_t}; the results are shown in Fig. A.1. The numerical results, with and without TWM-cst, are compared with the exact flow temperature in the near-wall cell, $\widetilde{T_1^e}^*$ (see Tab. 3.2), which is the expected value if q_w and all inter-cell fluxes are correct (see section 3.3). They are also compared with the exact temperature at the cell center, T_1^{e*}. Both reference values depend only on n_{δ_t} and are computed from the analytical solution (see Eq. 2.1.31).

With the model, T_1^* agrees well with the expected $\widetilde{T_1^e}^*$ over the range of n_{δ_t} tested, with a slight degradation for $n_{\delta_t} > 2$. This offset from theory is also visible in Fig. 4.6b and underlies the $\sim 10\%$ error observed for q_w in Fig. 4.5. Without the model, T_1^* tends to overlap T_1^{e*} for $n_{\delta_t} > 2$, concomitant with a good prediction of q_w. The same phenomenon appears in Fig. 4.6b for $n_{\delta_t} = 2$, where T_1 without model nearly superimposes the exact local value at the cell center T_1^{e*} ($T_1^{e*} = P_T(y_1^*)$). Although it may seem surprising to recover an accurate q_w with an inaccurate T_1, this is expected on sufficiently fine meshes without model correction: the exact profile $P_T(y^*)$ across the near-wall cell is nearly linear, so if T_1 coincides with T_1^{e*}, the default linear finite–volume approximation yields the correct

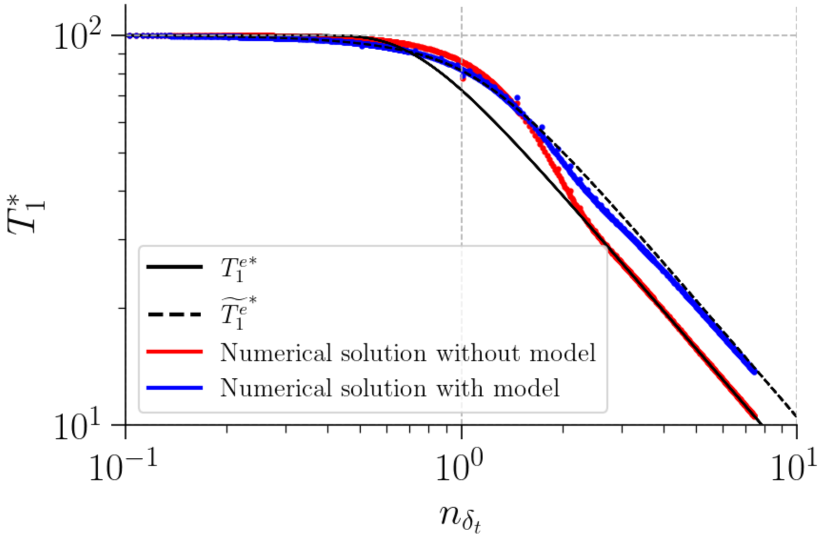

Figure A.1: Dimensionless near-wall cell temperature T_1^* as a function of n_{δ_t} (log–log scale), with and without the model, compared with the exact temperature at the near-wall cell center T_1^{e*} and the exact flow temperature in the near-wall cell $\widetilde{T_1^e}^*$ (see Tab. 3.2). The curves are constructed from the cases used in section 4.3, with different mesh resolutions and thermal diffusivities. The exact solutions (black lines) are built from the analytical solution given in Eq. 2.1.31.

q_w (see Eq. 2.2.4). Nevertheless, the fact that $T_1 \approx T_1^{e*}$ must due to q_w being misestimated upstream[1] of cell$_1$; a correct q_w would instead give $T_1 = \widetilde{T_1^{e}}^{*}$. Consequently, the no-model results can still deliver a good q_w prediction for $n_{\delta_t} \approx 2$, even without requiring a mesh thin enough so that $\widetilde{T_1^{e}}^{*} \approx T_1^{e*}$.

It is worth noting that the asymptotic dependence of $\widetilde{T_1^{e}}^{*}$ and T_1^{e*} on n_{δ_t} can be expressed analytically. For $n_{\delta_t} \gg 1$, the cell lies within the linear portion of the temperature profile, which can be approximated by

$$P_T(y^*) \approx \left.\frac{\partial T^*}{\partial y^*}\right|_{y^*=0} y^* \;\approx\; 1.572\, y^* \tag{A.0.1}$$

Since $n_{\delta_t} = \delta_t/(2y_1)$ and $y_1^* = y_1/\delta_t$, the exact center value is

$$T_1^{e*} \approx \left.\frac{\partial T^*}{\partial y^*}\right|_{y^*=0} y_1^* \;\approx\; \frac{1.572}{2}\, n_{\delta_t}^{-1} \tag{A.0.2}$$

As the velocity profile is also linear in this region for a high Prandtl number, Eq. 3.3.7 together with Eq. A.0.1 gives

$$\widetilde{T_1^{e}}^{*} \approx \frac{\int_0^{2y_1} y\left(1.572\,\frac{y}{\delta_t}\right) dY}{\int_0^{2y_1} y\, dY} \;\approx\; 1.572\,\frac{2}{3}\, n_{\delta_t}^{-1} \tag{A.0.3}$$

Thus both T_1^{e*} and $\widetilde{T_1^{e}}^{*}$ scale as $n_{\delta_t}^{-1}$ (or $\sim y_1$ for fixed δ_t), and their difference decreases as the near-wall cell is refined:

$$\widetilde{T_1^{e}}^{*} - T_1^{e*} \;=\; \frac{1.572}{6}\, n_{\delta_t}^{-1} \tag{A.0.4}$$

while their ratio remains constant,

$$\frac{\widetilde{T_1^{e}}^{*}}{T_1^{e*}} \;=\; \frac{4}{3} \tag{A.0.5}$$

On the log–log plot of Fig. A.1, this constant ratio appears as a fixed vertical offset between the two black curves (representing $\widetilde{T_1^{e}}^{*}$ and T_1^{e*}) for sufficiently large n_{δ_t}. Finally, for very coarse meshes ($n_{\delta_t} \ll 1$), the thermal boundary layer is much thinner than the near-wall cell, and both T_1^{e*} and $\widetilde{T_1^{e}}^{*}$ approach T_∞, as also seen in Fig. A.1.

---

[1] The temperature T_1 in a given near-wall cell is determined by the upstream wall heat flux q_w.

APPENDIX B

Wall heat flux error with TWM-cst under Lévêque conditions

The slight degradation in the TWM-cst prediction of q_w observed for $n_{\delta_t} > 2$ (see Fig. 4.5) can be attributed to the deviation of T_1 from its theoretical value $\widetilde{T_1^e}^*$ (see Fig. 4.6b for $n_{\delta_t} = 2$), which in turn results from the error on $q_{1\to 2}$ (see Fig. 3.3).

We define $q_{2\to 1} \equiv -q_{1\to 2}$. A positive $q_{2\to 1}$ (or q_w) indicates heat entering cell_1. The operator error used for q_w (see Eq. 4.2.1) is generalized to any flux q as

$$q^{\text{error}} = \frac{q - q_{\text{ref}}}{q_{\text{ref}}} \tag{B.0.1}$$

where q_{ref} denotes the corresponding reference (exact) flux. Applying Eq. B.0.1 to $q_{2\to 1}$ yields $q_{2\to 1}^{\text{error}}$. Fig. B.1 shows $q_{2\to 1}^{\text{error}}$ (orange) together with q_w^{error} (blue), with and without TWM-cst, as a function of n_{δ_t}. Both errors are of comparable magnitude and, over most of the n_{δ_t} range, have opposite signs. Hence, they exert counteracting effects on the evolution of T_1: the error on $q_{2\to 1}$ tends to increase the deviation of T_1 from $\widetilde{T_1^e}^*$ across almost the entire range, whereas the error on q_w tends to reduce it.

For example, at $n_{\delta_t} = 2$ with $q_w > 0$ (a heated bottom wall), Fig. 4.6b shows that T_1^* is underestimated, i.e., T_1 is closer to T_w than expected. From Fig. B.1, the error on q_w at $n_{\delta_t} = 2$ corresponds to an underestimation of q_w. This underestimation of q_w increases the difference between T_1 and T_w and thus reduces the T_1 error. Conversely, the error on

$q_{2\to1}$ leads to an overestimation of the heat flux entering the near-wall cell (equivalently, an underestimation of the heat leaving it), thereby increasing the T_1 error. Consequently, the error on $q_{2\to1}$ is the primary source of the discrepancy in T_1 and, indirectly, contributes to the residual error on q_w.

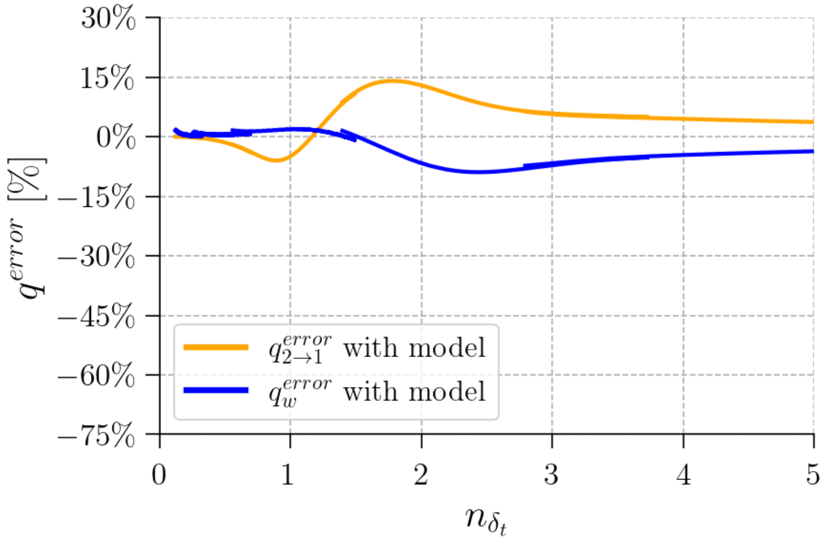

Figure B.1: Comparison of q_w^{error} and $q_{2\to1}^{\text{error}}$ with the TWM-cst as a function of n_{δ_t}. The curves are constructed from cases used in section 4.3 with different meshes and thermal diffusivities.

APPENDIX C

Wall shear-stress error with TWM-var under lévêque conditions

The relative error τ_w^{error} is defined analogously to q_w^{error}:

$$\tau_w^{\text{error}} = \frac{\tau_w - \tau_w^{\text{ref}}}{\tau_w^{\text{ref}}}\,, \tag{C.0.1}$$

where the superscript "ref" denotes the WR-var reference solution (see Tab. 7.1). Fig. C.1 summarizes τ_w^{error} across all meshes listed in Tab. 7.1.

For the cases without a model and with TWM-cst, the results do not collapse onto a single curve when plotted against n_{δ_t}, indicating that the error on τ_w is not solely dependent on mesh resolution. Nevertheless, the error tends to decrease as the mesh is refined. The maximum error for these two approaches (without model and with TWM-cst) remains modest compared with q_w^{error} in Fig. 7.13, staying below about 20%. TWM-cst has little effect on τ_w^{error} because it modifies only q_w; any influence on τ_w is indirect, via changes in the near-wall cell temperature T_1. In contrast, TWM-var (blue curves) reduces the τ_w error to values near zero over the entire range of n_{δ_t} tested.

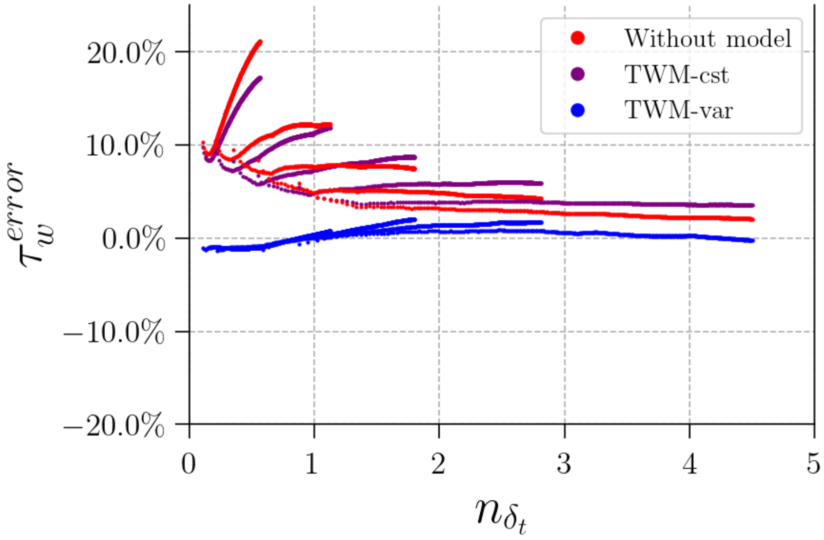

Figure C.1: Relative error in τ_w versus n_{δ_t}, with and without model corrections. Curves combine results from meshes A–E (see Tab. 7.1).

Bibliography

[1] Tanguy Davin. *Refroidissement des moteurs électriques : Exploration des solutions à huile de lubrification*. Phd, Université de Valenciennes et du Hainaut Cambresis, 2014.

[2] Ekta Meena Bibra, Elizabeth Connelly, Shobhan Dhir, Michael Drtil, Pauline Henriot, Inchan Hwang, Jean-Baptiste Le Marois, Sarah McBain, Leonardo Paoli, and Jacob Teter. Global ev outlook 2022: Securing supplies for an electric future. *IEA*, 2022.

[3] Merve Yildirim, Mehmet Polat, and Hasan Kürüm. A survey on comparison of electric motor types and drives used for electric vehicles. In *2014 16th International Power Electronics and Motion Control Conference and Exposition*, pages 218–223. IEEE, 2014.

[4] Jacek F Gieras and Nicola Bianchi. Electric motors for light traction. *EPE journal*, 14(1):12–23, 2004.

[5] Volkswagen AG. The electric drive system of the volkswagen id.3, volkswagen media, accessed 26 november 2025. `https://media.volkswagen.fr/le-systeme-de-propulsion-electrique-de-la-volkswagen-id-3`.

[6] Emmanuel Agamloh, Annette Von Jouanne, and Alexandre Yokochi. An overview of electric machine trends in modern electric vehicles. *Machines*, 8(2):20, 2020.

[7] Branko Ban, Stjepan Stipetić, and Mario Klanac. Synchronous reluctance machines: Theory, design and the potential use in traction applications. In *2019 International*

Conference on Electrical Drives & Power Electronics (EDPE), pages 177–188. IEEE, 2019.

[8] Oguzhan Ocak and Metin Aydin. A new hybrid permanent magnet synchronous motor with two different rotor sections. *IEEE Transactions on Magnetics*, 53(11):1–5, 2017.

[9] Carole Hénaux. *Contribution à la définition de moteurs à aimants permanents pour un véhicule électrique hybride routier*. PhD thesis, Toulouse, INPT, 1996.

[10] Nasser Hashemnia and Behzad Asaei. Comparative study of using different electric motors in the electric vehicles. In *2008 18th international conference on electrical machines*, pages 1–5. IEEE, 2008.

[11] Ivano Cornacchia. *Development of an Experimental Methodology for Characterising Liquid Cooling Systems for Electric Motor*. Phd, Universität of Duisburg Essen, 2023.

[12] Yinye Yang, Berker Bilgin, Michael Kasprzak, Shamsuddeen Nalakath, Hossam Sadek, Matthias Preindl, James Cotton, Nigel Schofield, and Ali Emadi. Thermal management of electric machines. *IET Electrical Systems in Transportation*, 7(2):104–116, 2017.

[13] Edison Gundabattini, Ravi Kuppan, Darius Gnanaraj Solomon, Akhtar Kalam, DP Kothari, and Rosli Abu Bakar. A review on methods of finding losses and cooling methods to increase efficiency of electric machines. *Ain Shams Engineering Journal*, 12(1):497–505, 2021.

[14] IEC. *Rotating electrical machines*. IEC, 2019.

[15] NEMA. *Motors and Generators*. National Electrical Manufacturers Association, 2016.

[16] Boris Bochenkov and Sergey Lutz. A review of modern materials of permanent magnets. In *Proceedings. The 8th Russian-Korean International Symposium on Science and Technology, 2004. KORUS 2004.*, volume 1, pages 201–203. IEEE, 2004.

[17] Bishal Silwal, Abdalla Hussein Mohamed, Jasper Nonneman, Michel De Paepe, and Peter Sergeant. Assessment of different cooling techniques for reduced mechanical stress in the windings of electrical machines. *Energies*, 12(10):1967, 2019.

[18] L. D. Marlino. *REPORT ON TOYOTA PRIUS MOTOR THERMAL MANAGEMENT*. U.S. Department of Energy, Oak Ridge National Laboratory, 2005.

[19] J Emily Cousineau, Kevin Bennion, Doug DeVoto, Mark Mihalic, and Sreekant Narumanchi. Characterization of contact and bulk thermal resistance of laminations for electric machines. Technical report, National Renewable Energy Lab.(NREL), Golden, CO (United States), 2015.

[20] Yaohui Gai, Mohammad Kimiabeigi, Yew Chuan Chong, James D Widmer, Xu Deng, Mircea Popescu, James Goss, Dave A Staton, and Andrew Steven. Cooling of automotive traction motors: Schemes, examples, and computation methods. *IEEE Transactions on Industrial Electronics*, 66(3):1681–1692, 2018.

[21] Tanguy Davin, Julien Pellé, Souad Harmand, and Robert Yu. Experimental study of oil cooling systems for electric motors. *Applied Thermal Engineering*, 75:1–13, 2015.

[22] Noureddine Ghayoub. *Contribution à l'étude et à la modélisation de la thermique et de l'aéraulique couplées d'un moteur électrique asynchrone en vue d'une aide à sa conception*. PhD thesis, Poitiers, 1992.

[23] Ilya Petrov, Pia Lindh, Markku Niemelä, Eero Scherman, Oskar Wallmark, and Juha Pyrhönen. Investigation of a direct liquid cooling system in a permanent magnet synchronous machine. *IEEE Transactions on Energy Conversion*, 35(2):808–817, 2019.

[24] Yves Bertin. *Refroidissement des machines tournantes. Études paramétriques*. Ed. Techniques Ingénieur, 2006.

[25] Chiranth Srinivasan, Jingyi Wan, Rohit Saha, Sujan Dhar, Krzysztof Paciura, Shaohong Zhu, Varun Nichani, and Raj Ranganathan. Heat transfer analysis of an electric motor cooled by a large number of oil sprays using computational fluid dynamics. *SAE International Journal of Advances and Current Practices in Mobility*, 4(2022-01-0208):1431–1444, 2022.

[26] Ralph Sindjui, Gianluca Zito, and Shimin Zhang. Experimental study of systems and oils for direct cooling of electrical machine. *Journal of Thermal Science and Engineering Applications*, 14(5):051007, 2022.

[27] Taewook Ha and Dong Kyu Kim. Study of injection method for maximizing oil-cooling performance of electric vehicle motor with hairpin winding. *Energies*, 14(3):747, 2021.

[28] Dong Hyun Lim and Sung Chul Kim. Thermal performance of oil spray cooling system for in-wheel motor in electric vehicles. *Applied Thermal Engineering*, 63(2):577–587, 2014.

[29] Chiranth Srinivasan, Xiaofeng Yang, Jeff Schlautman, Deming Wang, and Srihari Gangaraj. Conjugate heat transfer cfd analysis of an oil cooled automotive electrical motor. *SAE International Journal of Advances and Current Practices in Mobility*, 2(2020-01-0168):1741–1753, 2020.

[30] Taewook Ha, Yerim Kang, Nam Seok Kim, So Hee Park, Sang Han Lee, Dong Kyu Kim, and Hong Sun Ryou. Cooling effect of oil cooling method on electric vehicle motors with hairpin winding. *Journal of Mechanical Science and Technology*, 35:407–415, 2021.

[31] Adèle Poubeau, Guillaume Vinay, Breno Mendes Alves, Xiaohan Bai, and Pierre Viot. Numerical simulations of direct liquid cooling of the end-windings of an electric machine. *Available at SSRN 4717873*, 2024.

[32] Qi Lu, Rajesram Muthukumar, Haiwen Ge, and Siva Parameswaran. Numerical study of a rotating liquid jet impingement cooling system. *International Journal of Heat and Mass Transfer*, 163:120446, 2020.

[33] Huihui Xu, Kunpeng Lin, Claas Ehrenpreis, Grégoire Roux, and Rik W De Doncker. Thermal modeling of electrical machines with advanced fluid cooling. In *2020 19th IEEE Intersociety Conference on Thermal and Thermomechanical Phenomena in Electronic Systems (ITherm)*, pages 491–496. IEEE, 2020.

[34] Ronald O Grover, Xiaofeng Yang, Scott Parrish, Lorenzo Nocivelli, Katherine J Asztalos, Sibendu Som, Yanheng Li, Cooper Burns, John Van Gilder, Nitesh Attal, et al. Cfd simulations of electric motor end ring cooling for improved thermal management. *Science and Technology for Energy Transition*, 77:17, 2022.

[35] Marposs S.p.A. Stator applications for electric motor production. `https://www.marposs.com/fre/application/stator`. Marposs, accessed 26 November 2025.

[36] Adèle Poubeau, Guillaume Vinay, Bidzina Kekelia, and Kevin Bennion. Numerical simulations of high prandtl number liquid jets impinging on a flat plate. *International Journal of Heat and Mass Transfer*, 205:123889, 2023.

[37] Zhengyu Liu, Thomas Winter, and Michael Schier. Direct coil cooling of a high performance switched reluctance machine (srm) for ev/hev applications. *SAE International Journal of Alternative Powertrains*, 4(1):162–169, 2015.

[38] Serafim Kalliadasis, Christian Ruyer-Quil, Benoit Scheid, and Manuel García Velarde. *Falling liquid films*, volume 176. Springer Science & Business Media, 2011.

[39] John H Lienhard. *A heat transfer textbook, 5th edition.* Phlogistron, 2019.

[40] John Lienhard. Liquid jet impingement. *Annual Review of Heat Transfer*, 6(6), 1995.

[41] Theodore L Bergman. *Fundamentals of heat and mass transfer.* John Wiley & Sons, 2011.

[42] H-H Fernholz. Boundary layer theory-(8th (english) revised and enlarged edition) by h. schlichting, k. gersten (springer-verlag berlin, heidelberg, new york, 2000, 799 pp.). *European Journal of Mechanics/B Fluids*, 1(20):155–157, 2001.

[43] Hans Dieter Baehr and Karl Stephan. *Heat and Mass Transfer.* Springer Berlin Heidelberg, Berlin, Heidelberg, 2011.

[44] H Blasius. The boundary layers in fluids. *Zeitschrift fixr Mathematik und Physik*, 56(1), 1908.

[45] Lévêque André. Les lois de la transmission de chaleur par convection. *Annales des Mines ou Recueil de Mémoires sur l'Exploitation des Mines et sur les Sciences et les Arts qui s y Rattachent*, Mémoires, Tome XIII:201–239, 1928.

[46] Suhas Patankar. *Numerical heat transfer and fluid flow.* CRC press, 2018.

[47] K J Richards, P K Senecal, and E. Pomraning. CONVERGE 3.2.4, 2023.

[48] David C Wilcox et al. *Turbulence modeling for CFD*, volume 2. DCW industries La Canada, CA, 1998.

[49] Brian Edward Launder and Dudley Brian Spalding. Lectures in mathematical models of turbulence. *(No Title)*, 1972.

[50] David C Wilcox. Comparison of two-equation turbulence models for boundary layers with pressure gradient. *AIAA journal*, 31(8):1414–1421, 1993.

[51] Jonas Bredberg. On the wall boundary condition for turbulence models. *Chalmers University of Technology, Department of Thermo and Fluid Dynamics. Internal Report 00/4. G oteborg*, pages 8–16, 2000.

[52] MM Rahman and Timo Siikonen. Compound wall treatment with low-re turbulence model. *International journal for numerical methods in fluids*, 68(6):706–723, 2012.

[53] Sanjin Saric, Andreas Ennemoser, Branislav Basara, Heinz Petutschnig, Christoph Irrenfried, Helfried Steiner, and Günter Brenn. Improved modeling of near-wall heat transport for cooling of electric and hybrid powertrain components by high prandtl number flow. *SAE International Journal of Engines*, 10(3):778–784, 2017.

[54] T Cebeci J Cousteix and J Cebeci. Modeling and computation of boundary-layer flows. *Berlin, Germany: Springer*, 2005.

[55] BA Kader. Temperature and concentration profiles in fully turbulent boundary layers. *International journal of heat and mass transfer*, 24(9):1541–1544, 1981.

[56] CVCV Jayatilleke. The influence of prandtl number and surface roughness on the resistance of the laminar sublayer to momentum and heat transfer. *Prog. Heat Mass Transfer*, 1:193–321, 1969.

[57] William Morrow Kays, Michael E Crawford, and Bernhard Weigand. *Convective heat and mass transfer*, volume 4. McGraw-Hill New York, 1980.

[58] Christoph Irrenfried and Helfried Steiner. Dns based analytical p-function model for rans with heat transfer at high prandtl numbers. *International Journal of Heat and Fluid Flow*, 66:217–225, 2017.

[59] Brian Edward Launder and Dudley Brian Spalding. The numerical computation of turbulent flows. In *Numerical prediction of flow, heat transfer, turbulence and combustion*, pages 96–116. Elsevier, 1983.

[60] Kazuhiko Suga. Computation of high prandtl number turbulent thermal fields by the analytical wall-function. *International journal of heat and mass transfer*, 50(25-26):4967–4974, 2007.

[61] K Suga and M Kubo. Modelling turbulent high schmidt number mass transfer across undeformable gas–liquid interfaces. *International journal of heat and mass transfer*, 53(15-16):2989–2995, 2010.

[62] S Šarić and B Basara. A near-wall model for heat transfer at high prandtl numbers. In *at 10th Int. Conference on CFD (ICCFD10), Barcelona, Spain*, 2018.

[63] Robert Bergant and Iztok Tiselj. Near-wall passive scalar transport at high prandtl numbers. *Physics of Fluids*, 19(6), 2007.

[64] D Bothe, M Kröger, and HJ Warnecke. A vof-based conservative method for the simulation of reactive mass transfer from rising bubbles. *Fluid Dynamics & Materials Processing*, 7(3):303–316, 2011.

[65] Dieter Bothe and Stefan Fleckenstein. A volume-of-fluid-based method for mass transfer processes at fluid particles. *Chemical Engineering Science*, 101:283–302, 2013.

[66] Kangbei Cai, Guangyuan Huang, Yuchen Song, Junlian Yin, and Dezhong Wang. A sub-grid scale model developed for the hexahedral grid to simulate the mass transfer between gas and liquid. *International Journal of Heat and Mass Transfer*, 181:121864, 2021.

[67] Andre Weiner and Dieter Bothe. Advanced subgrid-scale modeling for convection-dominated species transport at fluid interfaces with application to mass transfer from rising bubbles. *Journal of Computational Physics*, 347:261–289, 2017.

[68] Andre Weiner, Claire MY Claassen, Irian R Hierck, JAM Kuipers, and Maike W Baltussen. Assessment of a subgrid-scale model for convection-dominated mass transfer for initial transient rise of a bubble. *AIChE Journal*, 68(7):e17641, 2022.

[69] Moritz Schwarzmeier, Tomislav Marić, Željko Tuković, and Dieter Bothe. A two-sided subgrid-scale model for mass transfer across fluid interfaces. *arXiv preprint arXiv:2505.17036*, 2025.

[70] Kirk B Hansen and Shawn C Shadden. A reduced-dimensional model for near-wall transport in cardiovascular flows. *Biomechanics and modeling in mechanobiology*, 15:713–722, 2016.

[71] B Aboulhasanzadeh, S Thomas, M Taeibi-Rahni, and G Tryggvason. Multiscale computations of mass transfer from buoyant bubbles. *Chemical Engineering Science*, 75:456–467, 2012.

[72] Mathis Grosso, Guillaume Bois, and Adrien Toutant. Thermal boundary layer modelling for heat flux prediction of bubbles at saturation: A priori analysis based on fully-resolved simulations. *International Journal of Heat and Mass Transfer*, 222:124980, 2024.

[73] Rodolfo Ostilla-Mónico, Yantao Yang, Erwin P Van Der Poel, Detlef Lohse, and Roberto Verzicco. A multiple-resolution strategy for direct numerical simulation of scalar turbulence. *Journal of computational physics*, 301:308–321, 2015.

[74] Bidzina Kekelia, Kevin Bennion, Xuhui Feng, Gilberto Moreno, J Emily Cousineau, Sreekant Narumanchi, and Jeff Tomerlin. Surface temperature effect on convective heat transfer coefficients for jet impingement cooling of electric machines with automatic transmission fluid. In *International Electronic Packaging Technical Conference and Exhibition*, volume 59322, page V001T08A004. American Society of Mechanical Engineers, 2019.

[75] ROBERT S. BRODKEY. *The Phenomena of Fluid Motions*. Addison Wesley, 1967.

[76] Samir Muzaferija. A two-fluid navier-stokes solver to simulate water entry. In *Proceedings of 22nd symposium on naval architecture, 1999*, pages 638–651. National Academy Press, 1999.

[77] CF Ma, YH Zhao, T Masuoka, and T Gomi. Analytical study on impingement heat transfer with single-phase free-surface circular liquid jets. *Journal of Thermal Science*, 5:271–277, 1996.

[78] X Liu and JH Lienhard. Liquid jet impingement heat transfer on a uniform flux surface. *Heat Transfer Phenomena in Radiation, Combustion, and Fires*, 106:523–530, 1989.

[79] XS Wang, Z Dagan, and LM Jiji. Heat transfer between a circular free impinging jet and a solid surface with non-uniform wall temperature or wall heat flux—1. solution for the stagnation region. *International journal of heat and mass transfer*, 32(7):1351–1360, 1989.

[80] Robert Miller, Stephen J Garrett, Paul T Griffiths, and Zahir Hussain. Stability of the blasius boundary layer over a heated plate in a temperature-dependent viscosity flow. *Physical Review Fluids*, 3(11):113902, 2018.

[81] Yunpeng Wang and Roger E Khayat. The influence of heating on liquid jet spreading and hydraulic jump. *Journal of Fluid Mechanics*, 883:A59, 2020.

[82] DR Oliver and TE Atherinos. Mass transfer to liquid films on an inclined plane. *Chemical Engineering Science*, 23(6):525–536, 1968.

[83] A Miyara. Numerical analysis on flow dynamics and heat transfer of falling liquid films with interfacial waves. *Heat and Mass Transfer*, 35(4):298–306, 1999.

[84] Georg Dietze and Reinhold Kneer. Flow separation in falling liquid films. *Frontiers in Heat and Mass Transfer (FHMT)*, 2(3), 2011.

Un modèle proche paroi pour la prédiction des transferts thermiques dans les écoulements laminaires à haut nombre de Prandtl : application aux jets liquides impactants pour le refroidissement des moteurs électriques

Résumé : Un modèle de paroi thermique, destiné aux fluides à nombre de Prandtl élevé et aux écoulements laminaires, est proposé afin d'éviter de mailler finement la mince couche limite thermique laminaire au voisinage de la paroi. Le modèle est ensuite étendu pour prendre en compte la forte dépendance en température de la viscosité, comme c'est le cas pour les huiles utilisées pour le refroidissement des moteurs électriques. Le potentiel de l'approche, fondée sur la solution analytique développée par Lévêque en 1928, est d'abord évalué sur le développement bidimensionnel d'une couche limite au-dessus d'une plaque plane. Elle est ensuite testée sur la configuration d'écoulement diphasique d'un jet impactant, pour des nombres de Prandtl pouvant atteindre 1000. Les comparaisons avec des simulations complètement résolues montrent que le modèle permet de prédire avec précision les transferts de chaleur locaux, y compris sur des maillages sous-résolus et en présence de fortes variations de viscosité. Le temps de calcul peut ainsi être fortement réduit, en particulier lorsque le nombre de Prandtl augmente, tout en conservant un niveau de précision similaire. Enfin, la version à viscosité constante du modèle est appliquée à une configuration représentative du refroidissement des têtes de bobines par plusieurs jets d'huile impactants. Malgré la complexité de l'écoulement, les résultats sont prometteurs.

Mots-clés : Nombre de Prandtl élevé, Modèle de paroi thermique, Écoulement laminaire, Refroidissement à huile, Jet liquide impactant

Partie 1: Introduction

Chapitre 1: Motivation industrielle

Le secteur automobile connaît une transition rapide vers l'électrification sous l'impulsion de politiques publiques visant à réduire la dépendance aux énergies fossiles et les émissions de carbone. Dans ce contexte, les moteurs électriques (EMs) constituent des éléments clés. Leur rôle principal est de convertir l'énergie électrique en puissance mécanique tout en satisfaisant des exigences sévères : forte densité de puissance et de couple, réponse dynamique rapide, large plage de vitesse, rendement élevé, fiabilité et coût maîtrisé. Malgré des rendements supérieurs à 90 %, les EMs dissipent une quantité significative de chaleur qui doit être évacuée pour éviter des températures dommageables.

Des limites de température strictes s'appliquent à l'isolation des enroulements, aux aimants permanents, aux matériaux ferromagnétiques et aux lubrifiants ; les dépasser peut entraîner la dégradation de l'isolation, démagnétisation, augmentation des pertes ou réduction de la durée de vie. De plus, la répartition non uniforme des pertes engendre des champs de température hétérogènes et des points chauds, en particulier dans les enroulements, ce qui rend nécessaire la mise en place de stratégies de refroidissement ciblées. La gestion thermique devient ainsi une contrainte majeure de conception.

Deux grandes approches de refroidissement sont utilisées. Le refroidissement par le carter est la solution la plus simple et la moins intrusive ; il repose sur la conduction à travers la structure du moteur et la convection vers un circuit liquide (par exemple une chemise d'eau). Cependant, les conductivités thermiques anisotropes et les résistances de contact aux interfaces limitent fortement l'évacuation de la chaleur. Pour les moteurs de traction à forte densité de puissance, le refroidissement par le carter est souvent insuffisant, notamment pour des zones isolées comme les têtes de bobines. Cela motive le développement de solutions de refroidissement local, où un fluide diélectrique, typiquement l'huile de lubrification déjà présente dans le groupe motopropulseur, est amené au plus près des composants critiques.

Le refroidissement direct des têtes de bobines est particulièrement pertinent, car elles sont à la fois des sources de chaleur importantes et facilement accessibles, et la forte conductivité thermique axiale du cuivre permet de tirer profit de ce refroidissement sur l'ensemble de l'enroulement. Parmi les concepts de refroidissement direct, les jets d'huile impactant les têtes de bobines sont prometteurs en raison de leur efficacité. Cependant, développer ces technologies nécessite de trouver un compromis entre intégration, coûts et efficacité de refroidissement. Les études expérimentales sont complexes, coûteuses et ne permettent qu'une évaluation thermique partielle. Elles peuvent être complétées par des simulations CFD haute fidélité, souvent basées sur des méthodes Volume of Fluid (VoF) tridimensionnelles pour les écoulements diphasiques. Ces méthodes exigent des maillages très fins et des pas de temps réduits, ce qui conduit à des coûts de calcul prohibitifs dans un contexte d'optimisation industrielle.

Sur le plan de la modélisation, le refroidissement par jets d'huile des têtes de bobines implique de nombreux phénomènes complexes : interaction avec des écoulements d'air, interaction entre jets et géométries complexes, dynamique du film liquide, mouillage de surfaces hétérogènes. Deux caractéristiques des huiles constituent des défis majeurs : des nombres de Prandtl élevés ($10^2 < Pr < 10^3$) et une forte dépendance de la viscosité à la température. Un Prandtl élevé implique une couche limite thermique beaucoup plus fine que la couche limite dynamique, nécessitant des maillages très raffinés et des pas de temps faibles. Par ailleurs, la viscosité peut varier d'un facteur proche d'un ordre de grandeur sur la plage de températures de fonctionnement, de sorte que la température ne peut plus être considérée comme un scalaire passif : les équations de quantité de mouvement et d'énergie sont fortement couplées au voisinage de la paroi.

L'objectif de cette thèse est de développer un modèle de paroi thermique (TWM) capable de prédire avec précision les flux de chaleur pariétaux pour des écoulements à grand nombre de Prandtl et une viscosité fortement dépendante de la température, tout en réduisant drastiquement le coût numérique par rapport à un calcul entièrement résolu. L'approche s'inspire des fonctions de paroi turbulentes et des modèles de sous-maille proposés dans la littérature. Une première version (TWM-cst) est élaborée pour des fluides à variation de viscosité négligeable, puis étendue (TWM-var) au cas des liquides présentant une viscosité très sensible à la température. Les deux versions sont évaluées sur des cas canoniques de développement de couche limite thermique et de jet impactant. Le TWM-cst est ensuite appliqué à une géométrie proche du cas industriel, représentative du refroidissement des têtes de bobines.

Chapitre 2: Une revue de l'état de l'art de la modélisation de la couche limite

Ce chapitre présente les principaux aspects physiques des couches limites dynamiques et thermiques laminaires, ainsi que les approches numériques existantes pour modéliser des couches limites en écoulements laminaires ou turbulents. On s'intéressera en particulier aux écoulements à nombres de Prandtl élevés pour lesquels la couche limite thermique est beaucoup plus fine que la couche limite dynamique.

À partir des équations de Navier–Stokes incompressibles sous l'hypothèse de bas nombre de Mach, de variations modérées de température et de propriétés constantes, les équations de couche limite sont établies pour un écoulement bidimensionnel stationnaire au-dessus d'une plaque plane. La solution de Blasius fournit un profil de vitesse auto-similaire et montre que la couche limite dynamique croît comme $\delta \sim x\,Re^{-1/2}$. La couche limite thermique est également auto-similaire et sa structure dépend uniquement du nombre de Prandtl : pour $Pr = 1$ les profils de vitesse et de température coïncident, tandis que pour $Pr > 1$ la couche limite thermique est plus fine, avec un rapport d'épaisseurs bien approché par $\delta_t/\delta \approx Pr^{-1/3}$. Dans la limite de très grands nombres de Prandtl, la théorie de Lévêque est rappelée : en supposant un profil de vitesse localement linéaire dans la zone où se développe la couche thermique, la solution analytique de l'équation de l'énergie s'exprime via la fonction gamma incomplète. Finalement, les flux pariétaux de chaleur peuvent être exprimés comme une fonction inversement proportionnelle à l'épaisseur de la couche limite thermique.

La seconde partie du chapitre passe en revue plusieurs stratégies numériques pour traiter des couches limites minces sans maillage extrêmement raffiné. La méthode « par défaut » en volumes finis consiste à approximer les gradients pariétaux par interpolation linéaire entre la paroi et le premier centre de cellule, ce qui devient insuffisant lorsque la couche limite est beaucoup plus fine que la maille. Dans le cadre RANS, les fonctions de paroi turbulentes sont introduites : à partir des équations moyennées de Reynolds et de l'hypothèse de viscosité turbulente, les lois de paroi, c'est-à-dire des profils universels en $u^+(y^+)$ et $T^+(y^+)$, sont dérivées, combinant sous-couche linéaire, région logarithmique et couche tampon. Les fonctions de paroi standard reposent sur ces lois de paroi mais leur précision se dégrade pour des Prandtl très élevés. Des modèles récents, comme le modèle Prandtl Thermal-Layer (PRTL), améliorent la prédiction du flux de chaleur et réduisent la dépendance au maillage jusqu'à $Pr \sim \mathcal{O}(10^3)$.

Pour des écoulements laminaires à haut nombre de Prandtl, ces lois de paroi turbulentes ne sont toutefois pas directement transposables, car elles supposent la présence de diffusivité turbulente et d'un flux thermique normal à la paroi quasi uniforme à travers la cellule pariétale. Le chapitre explore alors plusieurs approches dédiées aux couches limites scalaires laminaires : (i) un modèle de sous-maille (SGS) basé sur un profil auto-similaire pour le transport de masse/chaleur le long de parois glissantes, (ii) une méthode qui résout une équation de transport surfacique pour une quantité égale à l'intégrale de la concentration ou de la température à travers la couche limite, (iii) une méthode de sous-résolution radiale (LRS) qui résout localement un problème unidimensionnel le long de segments normaux à l'interface, et (iv) des stratégies à double grille, où le champ de température est porté par une maille plus fine que celle de la vitesse.

En conclusion, sur la base de cet état de l'art, le chapitre motive le développement d'un nouveau modèle de paroi thermique (Thermal Wall Model, TWM) spécifiquement adapté aux écoulements laminaires à haut nombre de Prandtl au voisinage de parois non-glissantes. Deux variantes sont envisagées : TWM-cst, pour des propriétés thermophysiques quasi constantes, et TWM-var, qui prend en compte une viscosité fortement dépendante de la température. Ce modèle suit la philosophie des fonctions de paroi et des modèles SGS, pour proposer un modèle robuste avec une implémentation simple. Il s'appuie explicitement sur le profil de température de Lévêque et sur des données locales, ce qui en fait, à la connaissance de l'auteur, une contribution originale.

Partie 2: Loi de paroi thermique pour les fluides à viscosité constante

Chapitre 3: Description et implémentation de la loi de paroi thermique

---

Ce chapitre présente le modèle de paroi thermique à viscosité constante (TWM-cst), développé pour prédire le flux de chaleur pariétal q_w à partir d'une température de paroi imposée T_w, tout en réduisant fortement le nombre de mailles dans la couche limite thermique. La température du fluide extérieur à la couche limite, T_∞, est fournie par l'utilisateur et est considérée uniforme. Ce modèle constitue la base de l'extension ultérieure à viscosité variable (TWM-var).

La formulation mathématique s'appuie sur l'écoulement laminaire sur une plaque plane isotherme, en régime permanent, incompressible et bidimensionnel, avec des propriétés constantes et des gradients de pression négligeables. Dans la limite de grands nombres de Prandtl, la couche limite thermique est beaucoup plus fine que la couche limite dynamique et reste confinée dans une région où le profil de vitesse est linéaire sous l'hypothèse de viscosité uniforme. Ce cas limite conduit au régime asymptotique de Lévêque. La solution auto-similaire proposée fournit un profil universel de température adimensionnelle à l'intérieur de la couche limite thermique. En modifiant le *scaling* du profil de Lévêque et en combinant ce profil avec la loi de Fourier, on obtient une expression analytique du flux de chaleur pariétal, $q_w \approx 1.572\, k\, (T_w - T_\infty)/\delta_t$, qui s'exprime en fonction de δ_t et constitue le cœur du modèle.

L'implémentation numérique du TWM-cst est conçue pour une formulation aux volumes finis. L'utilisateur impose T_w comme condition de Dirichlet, et le modèle renvoie localement le flux de chaleur q_w à la paroi pour chaque maille adjacente au mur. Le modèle est écrit sous la forme d'une fonction $f_1(T_1, T_w, T_\infty, y_1, k)$, où T_1 est la température discrétisée au centre de la première maille et y_1 sa distance au mur. On introduit une température adimensionnelle T_1^*, puis une coordonnée normale adimensionnelle $y_1^* = y_1/\delta_t$, obtenue à partir de T_1^* en inversant un profil modifié. Celui-ci permet de relier T_1^* et y_1^* de manière cohérente avec la discrétisation en volumes finis. À partir de y_1^*, δ_t est déduit puis le flux q_w est calculé avec l'expression analytique du flux.

La dernière partie du chapitre montre que, dans une approche volumes finis, T_1 ne représente pas la température ponctuelle au centre de la maille, mais une température débitante $\widetilde{T}$: une moyenne spatiale de la température pondérée par la vitesse et imposée par la conservation d'énergie, en particulier sur des maillages sous-résolus. On définit donc une température d'écoulement $\widetilde{T}(x_1, y_1)$ et sa forme adimensionnelle $\widetilde{T}^*$, ainsi qu'un profil effectif obtenu à partir du profil de Lévêque. L'utilisation de ce profil garantit que la prédiction de y_1^*, puis de δ_t et de q_w, reste compatible avec la formulation en volumes finis, même lorsque la couche limite thermique n'est pas correctement résolue par la grille.

Chapitre 4: Vérification de la loi de paroi dans les conditions de Lévêque

Ce chapitre évalue le modèle de paroi thermique TWM-cst dans une configuration idéale vérifiant les hypothèses du modèle, à savoir dans les conditions d'une couche limite thermique se développant au-dessus d'une paroi plane dans un champ de vitesse linéaire en fonction de la coordonnée normale à la paroi. Ces conditions idéales sont rencontrées pour un fluide à $Pr \to \infty$. Le but est de disposer d'un cas de référence simple, pour lequel une solution analytique existe, afin de valider d'une part la résolution numérique sans modèle, puis d'autre part l'impact du modèle de paroi sur la prédiction du flux de chaleur pariétal q_w lorsque la couche limite thermique est sous-résolue.

La configuration numérique est bidimensionnelle rectangulaire. L'épaisseur maximale de couche limite thermique δ_t à la sortie du domaine garantit que la paroi supérieure du domaine n'interagit pas avec la couche limite. Un profil de vitesse linéaire est imposé, avec condition de non-glissement à la paroi et vitesse verticale nulle. Des conditions de Dirichlet sont spécifiées pour la température à l'entrée et sur la paroi chaude. Le fluide présente des propriétés thermophysiques constantes.

Les équations de masse, de quantité de mouvement et d'énergie sont résolues par une méthode des volumes finis dans le code CONVERGE, avec couplage pression–vitesse de type PISO et schémas d'ordre deux. Un maillage cartésien uniforme est utilisé, avec un cas de référence très raffiné, ainsi que trois maillages plus grossiers. La comparaison du cas de référence avec la solution de Lévêque montre un très bon accord dès lors que le critère $x/\delta_t(x) > 10$ est satisfait, ce qui valide la résolution numérique sans modèle.

Une analyse sans modèle de sensibilité au maillage est ensuite menée en introduisant un paramètre : le nombre de mailles dans la couche limite thermique, $n_{\delta_t} = \delta_t/(2y_1)$, où y_1 est la distance du centre de la première maille à la paroi. L'erreur relative sur q_w par rapport au cas de référence ne dépend essentiellement que de n_{δ_t}. Pour des maillages très grossiers ($n_{\delta_t} < 1$), l'hypothèse (sans modèle) de profil de température linéaire dans la première maille conduit à une très forte sous-prédiction ou sur-prédiction de q_w. À l'inverse, pour $n_{\delta_t} \approx 3$, l'erreur sur q_w reste inférieure à 1 %.

Dans la dernière partie, le modèle de paroi thermique TWM-cst est activé et testé sur l'ensemble des maillages, ainsi que pour différentes diffusivités thermiques α, afin de couvrir un large intervalle de n_{δ_t}. Lorsque la couche limite est sous-résolue ($n_{\delta_t} < 2$), le modèle corrige efficacement le flux pariétal : l'erreur sur q_w devient quasi nulle et les profils de température numériques se rapprochent de la solution de référence. Pour des maillages plus fins ($n_{\delta_t} > 2$), l'utilisation du modèle dégrade légèrement la prédiction de q_w, avec une erreur qui reste toutefois inférieure à 10 % et diminue avec le raffinement. Cette dégradation est attribuée à une incohérence entre un flux pariétal correctement corrigé et le schéma de discrétisation du flux conductif entre les deux premières mailles. Globalement, le chapitre montre que TWM-cst est particulièrement pertinent pour améliorer la prédiction des flux de chaleur lorsque la couche limite thermique n'est pas suffisamment résolue par le maillage ($n_{\delta_t} < 1$), ce qui motive son application à des écoulements plus complexes avec des couches limites thermiques fines.

Chapitre 5: Évaluation de la loi de paroi thermique dans une configuration jet impactant

Ce chapitre évalue le *thermal wall model* pour viscosité constante (TWM-cst) dans une configuration de jet liquide laminaire frappant une plaque chauffée, représentative du refroidissement d'un moteur électrique. Dans un tel écoulement, certaines hypothèses du modèle (profil de vitesse linéaire, vitesse parallèle à la paroi) ne sont plus strictement satisfaites, mais l'objectif est de vérifier si, dans l'esprit des fonctions de paroi classiques, le modèle reste néanmoins précis en dehors des hypothèses.

La configuration reprend le dispositif expérimental d'impact de jet d'huile sur une paroi plane chauffée, déjà étudié numériquement dans la littérature. Le jet est injecté par une buse et impacte une paroi chauffée, et sa température peut être considérée uniforme. Le domaine de calcul est simplifié en ne conservant que l'air ambiant, le jet et le film liquide, et seul un quart de la géométrie est simulé grâce à des plans de symétrie.

Les propriétés de l'huile dépendent de la température via des corrélations expérimentales (densité, tension de surface, capacité thermique, viscosité). Pour la validation numérique, un premier ensemble de cas est simulé avec des propriétés thermophysiques variables, et les résultats à paroi résolue sont comparés aux mesures expérimentales par le nombre de Nusselt moyen. L'accord obtenu sur une large plage de Reynolds et Prandtl valide la configuration numérique.

Pour l'évaluation du TWM-cst, les propriétés sont ensuite figées à la température de film $T_f = (T_\infty + T_w)/2$, à l'exception de la conductivité, ajustée pour couvrir $Pr \in [1, 1000]$. Le débit est également ajusté pour couvrir plusieurs nombres de Reynolds ($Re \in [225, 1348]$). Chaque configuration est calculée sur un maillage fin (paroi résolue) et sur un maillage grossier, ce dernier étant utilisé avec ou sans modèle. L'analyse détaillée du cas de référence avec maillage fin ($Pr = 158$, $Re = 898$) met en évidence les trois régions classiques de l'impact de jet laminaire : zone de stagnation, région de développement de couche limite, puis région de similarité visqueuse. On y montre qu'en dehors du point d'impact, le profil de vitesse parallèle à la paroi est quasi linéaire dans la couche limite thermique et que la composante normale reste faible, ce qui justifie globalement les hypothèses du TWM-cst.

Les comparaisons des profils locaux de Nusselt et du flux intégré montrent que, sur maillage grossier, l'erreur sans modèle peut atteindre 40 à 70 % pour des Prandtl élevés, alors qu'elle est fortement réduite avec le TWM-cst, en particulier lorsque la couche limite thermique est sous-résolue (nombre de mailles $n_{\delta_t} \lesssim 1$). Pour des couches limites plus épaisses ($n_{\delta_t} \gtrsim 3$), le maillage étant déjà suffisant, le modèle ne dégrade pas ou seulement marginalement les résultats. Le modèle se révèle peu sensible aux nombres de Reynolds et de Prandtl tant que le profil de vitesse est correctement capturé (ce qui est une condition au bon fonctionnement du modèle thermique) et à la résolution du maillage défini par n_{δ_t}. A l'inverse, l'apport du modèle par rapport au cas sous-résolu est en priorité dépendant du paramètre n_{δ_t}, avec des résultats similaires à l'évaluation dans les conditions de Lévêque.

Sur l'ensemble des cas, le TWM-cst permet d'atteindre une précision proche des cas complètement résolus avec un coût de calcul réduit de 50 à 90 %, principalement grâce à l'augmentation du pas de temps admissible et à l'allègement du maillage.

Enfin, le modèle est testé dans un cas plus réaliste avec une viscosité fortement dépendante de la température, où en particulier la viscosité varie d'un facteur ≈ 5 entre l'écoulement extérieur à la couche limite thermique et la paroi. Dans ce cas, le profil de vitesse près de la paroi devient nettement non linéaire dans la couche limite thermique et n'est pas bien résolu sur le maillage grossier. L'hypothèse clé du TWM-cst étant violée, le modèle n'améliore alors presque pas la prédiction de Nu. Cette limite justifie le développement d'une version étendue du modèle, TWM-var, capable de traiter explicitement une viscosité fortement variable en température.

Partie 3: Loi de paroi thermique étendue aux fluides avec une viscosité variable

Chapitre 6: Loi de paroi thermique pour une viscosité variable: description et implémentation

---

Ce chapitre présente l'extension du modèle de paroi thermique TWM-cst à des fluides dont la viscosité dépend fortement de la température. Dans le contexte d'huiles de refroidissement à nombre de Prandtl élevé, la viscosité peut varier d'un ordre de grandeur entre le cœur de l'écoulement et la paroi, ce qui couple fortement les équations de quantité de mouvement et d'énergie. Dans ces conditions, la vitesse ne peut plus être considérée comme linéaire dans la couche thermique (même si elle est très fine), et le modèle TWM-cst conduit à des erreurs significatives sur le flux de chaleur pariétal q_w et la contrainte de cisaillement pariétale τ_w. Pour traiter ce cas, un modèle étendu, noté TWM-var, est introduit.

La formulation mathématique repose sur la même l'hypothèse de couche thermique mince valide à Prandtl infini, logée à l'intérieur de la couche dynamique, permettant de négliger le terme convectif dans l'équation de quantité de mouvement à proximité de la paroi : la cisaillement est donc invariant perpendiculairement à la paroi, comme dans le cas des hypothèses de Lévêque. Cependant dans ce cas-ci, la viscosité n'est pas considérée constante. La viscosité dynamique locale $\mu(T)$ apparaît alors explicitement dans la relation entre τ_w et le gradient de vitesse, et la vitesse s'exprime comme une intégrale de $1/\mu(T)$ à partir de la paroi. Le profil de température adimensionné est supposé avoir la forme du profil de Lévêque, avec une coordonnée normale adimensionnée $y^* = y/\delta_t$, où δ_t est l'épaisseur de la couche thermique. On définit une vitesse caractéristique servant à adimensionner la vitesse et égale à la vitesse à la distance δ_t de la paroi. À partir de ce profil de température adimensionnée, de la vitesse caractéristique et de la loi de viscosité $\mu(T)$, un profil universel de vitesse adimensionné est construit, ainsi qu'une viscosité équivalente μ_{eq}, définie comme la moyenne harmonique de $\mu(T)$ à travers la couche thermique. Cette viscosité équivalente correspond à la viscosité qui reproduirait la même contrainte pariétale si le profil de vitesse était linéaire sur δ_t.

L'implémentation numérique dans un schéma aux volumes finis est organisée autour de deux fonctions : f_1 fournit le flux de chaleur pariétal q_w à partir des données dans la première maille (T_1, T_w, T_∞, y_1, k) et d'un profil de température universel adimensionné, de manière similaire à la version « viscosité constante » du modèle (TWM-cst). De plus, f_2 fournit la contrainte pariétale τ_w à partir de la vitesse de maille u_1, de μ_{eq} (préalablement calculé) et des données obtenues lors du calcul de q_w, à savoir δ_t, y_1^*, ainsi que du profil de vitesse universel adimensionné.

Pour rester cohérent avec l'approximation en volumes finis, des profils « effectifs » sont introduits : un profil de vitesse adimensionné moyenné et le profil de température adimensionné débitant. Ce dernier est calculé à partir de la moyenne du profil de température adimensionné (supposé être identique à celui de Lévêque) pondérée par le profil de vitesse universel. Ces profils relient des grandeurs locales adimensionnées de façon compatible avec les maillages très déraffinés dans un contexte volumes finis.

L'analyse asymptotique vérifie que TWM-var se réduit au comportement attendu dans plusieurs limites : viscosité uniforme (où l'on retrouve exactement TWM-cst et un profil de vitesse linéaire), maille très grossière (cellule bien au-delà de la couche thermique, pour laquelle τ_w est contrôlée par la viscosité de l'écoulement à l'extérieur de la couche limite thermique μ_∞) et maille très fine (cellule située profondément dans la couche thermique, où τ_w dépend de la viscosité pariétale μ_w). Ainsi, le modèle TWM-var fournit des corrections cohérentes de q_w et τ_w sur une large plage de variations de viscosité et de résolutions proches de la paroi.

Chapitre 7: Loi de paroi thermique pour une viscosité variable: vérification dans les conditions Lévêque

Ce chapitre vérifie le modèle de paroi thermique à viscosité variable (TWM-var) dans une configuration bidimensionnelle simple satisfaisant au mieux les conditions de Lévêque, sauf pour l'hypothèse de viscosité uniforme. On considère le développement d'une couche limite thermique au-dessus d'une paroi plane à température fixée, en écoulement laminaire monophasique, avec un cisaillement quasi uniforme et une viscosité dépendant de la température. Le *set-up* numérique tend à reproduire les conditions dynamiques très près de la paroi, profondément à l'intérieur de la couche limite dynamique, et ainsi être cohérent avec l'hypothèse de $Pr \to \infty$.

Un profil de vitesse linéaire est imposé à l'entrée, de sorte que la contrainte de cisaillement τ_{yx} est presque uniforme sur la hauteur. Les propriétés thermophysiques sont choisies de manière à obtenir un nombre de Péclet élevé, $Pe \approx 7 \times 10^5$, garantissant une couche limite thermique mince au regard de la hauteur du domaine et un gradient de pression négligeable. Le nombre de Reynolds reste modéré ($Re \leq 40$), ce qui permet de négliger les effets d'inertie par rapport à la diffusion visqueuse et de reproduire au mieux les conditions rencontrées profondément à l'intérieur de la couche limite dynamique. Toutes les propriétés sont supposées constantes, à l'exception de la viscosité dynamique, qui varie d'un facteur 5 entre le cœur de l'écoulement et la paroi chaude.

Un cas de référence entièrement résolu (WR-var) est d'abord comparé à un cas de viscosité constante (WR-cst). La diminution de μ au voisinage de la paroi réduit d'environ 25 % l'épaisseur de la couche limite thermique et augmente le flux de chaleur pariétal q_w, tandis que la contrainte pariétale τ_w diminue légèrement. Cette évolution résulte d'une augmentation de la vitesse dans δ_t tout en maintenant une contrainte de cisaillement $\tau_{yx} = \mu\, \partial u/\partial y$ pratiquement uniforme en direction normale à la paroi, conformément à l'esprit de la théorie de Lévêque.

Les hypothèses du TWM-var sont ensuite vérifiées à partir du cas WR-var. Les profils de température et de vitesse, rendus adimensionnels, présentent une auto-similarité marquée et se superposent presque parfaitement aux profils théoriques de température de Lévêque et de vitesse adimensionnée, avec toutefois un léger écart loin de la paroi pour $y > 2\,\delta_t$. La distribution spatiale de viscosité $\mu\big(T(y)\big)$ suit la loi attendue et la contrainte τ_{yx} reste quasi uniforme à travers δ_t mais montre de légères variations à travers des cellules pariétales très grandes par rapport à la couche limite thermique. Ces constats confirment la validité des hypothèses de base du modèle avec ce *set-up* numérique.

Le TWM-var est finalement appliqué à plusieurs maillages grossiers et comparé au calcul sans modèle et au modèle à viscosité constante TWM-cst. Pour des résolutions typiques

($0.1 < n_{\delta_t} < 1.5$), TWM-var restitue correctement la contrainte pariétale τ_w, la vitesse dans la première maille u_1 et le flux de chaleur q_w le long de la paroi. L'erreur relative sur q_w tombe à quelques pourcents seulement (environ 3.5 % pour $n_{\delta_t} = 0.5$), contre 30 à 50 % avec TWM-cst ou sans correction. De manière similaire au TWM-cst sur cas à viscosité uniforme, lorsque le maillage est de raffinement intermédiaire, une erreur inférieure à 10 % apparaît mais décroît en raffinant plus et la solution converge vers le cas entièrement résolu. Cette étude montre que TWM-var permet de capturer de façon fiable l'effet d'une viscosité variable sur le transfert thermique pariétal avec des maillages fortement sous-résolus en proche paroi, et n'augmente l'erreur que marginalement sur des maillages de raffinements intermédiaires.

Chapitre 8: Loi de paroi thermique pour une viscosité variable: vérification dans une configuration jet impactant

Ce chapitre évalue le modèle de paroi thermique à viscosité variable (TWM-var) dans une configuration académique de jet liquide axisymétrique impactant une plaque chauffée identique à celle du chapter 5. Contrairement à TWM-cst, qui suppose une viscosité uniforme, TWM-var repose sur une loi réaliste $\mu_l(T)$, cohérente avec les données expérimentales. Les cas numériques utilisés pour tester le modèle correspondent directement aux conditions des essais, tandis que des configurations supplémentaires, sans données expérimentales mais basées sur le *set-up* numérique validé, sont utilisées pour analyser la sensibilité du modèle aux nombres de Reynolds et de Prandtl, ainsi qu'à la variation de viscosité.

Deux types de maillages sont considérés : un maillage fin résolu, qui résout explicitement la couche limite thermique, et un maillage grossier, dans lequel la structure de vitesse et de température à l'intérieur de cette couche est sous-résolue.

L'effet d'une viscosité non uniforme est d'abord étudié en comparant un cas à viscosité variable (variation d'un facteur 5) à un cas à viscosité constante. La diminution de la viscosité au voisinage de la paroi réduit la contrainte de cisaillement, augmente la vitesse locale dans le film, amincit la couche limite thermique δ_t et la hauteur de film, et renforce la convection, d'où une augmentation du nombre de Nusselt. Les profils de vitesse deviennent nettement non linéaires dans la couche thermique.

Les hypothèses internes à TWM-var sont ensuite confrontées aux solutions avec maillages résolus. Le profil de température sans dimension suit de près la solution de Lévêque dans la couche limite thermique malgré le non respect de l'hypothèse de vitesse linéaire.

La contrainte de cisaillement τ_{yx} n'est pas parfaitement uniforme, surtout sous le jet, mais reste suffisamment constante à l'intérieur et à proximité de δ_t pour que le profil de vitesse théorique décrive correctement les profils numériques.

La validation du modèle montre que, sur un maillage grossier, TWM-var reproduit très bien les distributions locales de Nu et de τ_w, ainsi que l'épaisseur de film et les profils de vitesse, avec des écarts fortement réduits par rapport aux cas sans modèle ou avec TWM-cst. L'apport est maximal dans la zone proche du jet, où la couche limite thermique est très mince ($n_{\delta_t} \lesssim 1$) : des erreurs locales de l'ordre de 30–50 % sans modèle sont ramenées à quelques pourcents avec TWM-var. L'apport du modèle est donc largement défini par n_{δ_t}, de manière similaire à ce qui a été observé dans les conditions de Lévêque, ou avec le TWM-cst à viscosité constante, tout en présentant une faible sensibilité au maillage. Autrement dit, l'erreur du modèle reste faible quel que soit le raffinement du maillage.

Le flux de chaleur pariétal intégré est bien prédit sur toute la plaque et en bon accord avec l'expérience, tout en présentant une faible sensibilité au raffinement du maillage, au Reynolds, au Prandtl et au ratio de viscosité.

Des études de sensibilité confirment la robustesse du modèle. Pour des rapports de viscosité allant jusqu'à 15, TWM-var reste précis alors que TWM-cst se dégrade nettement ; dans la limite de viscosité constante, TWM-var se confond avec TWM-cst. Sur une plage de nombres de Reynolds allant d'environ $Re \approx 200$ à 1900, le modèle restitue correctement le transfert thermique, malgré quelques écarts localisés près du point d'impact à hauts Reynolds. Enfin, pour $Pr = 1$, où la couche limite thermique devient épaisse et bien résolue même avec le minimum de mailles nécessaire à la résolution du film, TWM-var ne détériore pas la solution. L'ensemble des résultats montre que TWM-var fournit une amélioration systématique ou, au pire, une dégradation marginale, sans surcoût CPU mesurable et avec des gains de temps de calcul pouvant dépasser 80 % par rapport aux simulations avec maillages résolus.

Partie 4: Cas d'application avancé du modèle de paroi thermique

Chapitre 9: Application industrielle

Ce chapitre applique le modèle de paroi thermique à propriétés constantes (TWM-cst) à un cas industriel représentatif : le refroidissement par jets d'huile des têtes de bobines d'une machine électrique. Seul TWM-cst est considéré dans ces travaux, par contrainte de temps, le cas à viscosité variable pour évaluer TWM-var étant une perspective de travail pour de futurs travaux.

La configuration numérique reprend une architecture de machine commerciale : cinq jets d'huile impactent la partie supérieure de la surface externe des têtes de bobines et génèrent un film entraîné par gravité. La géométrie est simplifiée (paroi lissée, conduction solide et rotation négligées), les têtes de bobines sont maintenues plus chaudes que le reste du carter tandis que l'huile est injectée à température contrôlée. Les propriétés thermophysiques conduisent à un régime laminaire avec un nombre de Reynolds faible pour chaque jet et un nombre de Prandtl élevé, proche d'un cas test effectué sur la configuration du jet impactant académique, et donnant de bons résultats avec le modèle. La différence avec le cas d'application industriel est que, dans le cas académique, le modèle n'est évalué que dans la partie supercritique, c'est-à-dire avant l'apparition d'un ressaut hydraulique.

L'écoulement diphasique huile–air est simulé avec la méthode Volume of Fluid dans le code CONVERGE, sur une grille cartésienne, avec raffinement adaptatif à l'interface liquide–gaz et maillage de couche limite près des parois (cellules allongées). Un cas résolu sert de référence et trois maillages grossiers sont définis en déraffinant uniquement le maillage de couche limite, de façon à sous-résoudre la couche limite thermique tout en conservant un champ de vitesse correctement capturé. Le TWM-cst est activé uniquement dans les cellules adjacentes au mur mouillées par le liquide, identifiées à partir de la fraction volumique de gaz du modèle VoF.

La convergence est évaluée via le taux de surface mouillée et le flux thermique moyen sur la partie supérieure de la surface externe des têtes de bobines : la zone d'impact des jets à partir de laquelle le modèle est évalué. Tous les maillages atteignent un régime stationnaire, et l'activation du modèle ne dégrade pas la convergence. L'analyse du cas de référence met en évidence une topologie d'écoulement complexe, avec une stagnation sous les jets, une zone de collision des films liquides entre les jets, formant des zones de recirculation épaisses, et un film présentant ce qui s'apparente à des instabilités dynamiques de surface (instabilité de Kapitza) en aval des jets, dans une zone où la paroi est verticale.

L'évaluation du modèle repose sur des bilans de flux intégrés par zone autour des jets et sur l'erreur locale de flux q_w par rapport au cas résolu. Sur les maillages grossiers, l'absence de modèle conduit à une sous-estimation marquée du flux dans les zones de stagnation (près des zones d'impact de jet), où la couche limite est très fine. L'utilisation de TWM-cst réduit nettement ces écarts dans et au voisinage des zones de stagnation et améliore également la prédiction sur le reste de la surface, sans dégradation notable là où la couche limite est déjà bien résolue. Les gains restent plus limités ou marginaux dans les zones de recirculation. Le modèle n'ajoute pas de surcoût numérique identifié, et l'emploi d'un maillage de couche limite plus grossier permet une réduction globale du temps de calcul d'environ 18 % par rapport au cas résolu, ce qui montre que TWM-cst est robuste et efficace pour cette configuration industrielle réaliste. Cependant, ce gain reste plus modéré qu'espéré, le pas de temps n'évolue pas entre les cas résolus et grossiers, laissant penser à un problème de maillage avec une cellule de taille réduite pilotant le pas de temps en dehors de la couche limite ; cela reste à investiguer.

Partie 5: Conclusion et perspectives

Cette partie conclut la thèse en récapitulant le développement et l'évaluation d'un modèle de paroi thermique dédié aux écoulements laminaires à nombre de Prandtl élevé, pour lesquels la couche limite thermique est extrêmement fine et difficile à résoudre numériquement. Le modèle, fondé sur la théorie de Lévêque, corrige le flux de chaleur à la paroi à partir de la température pariétale et de la température extérieure à la couche limite fournies par l'utilisateur, ainsi que d'informations locales dans la maille pariétale. Une première version, TWM-cst, est conçue pour des fluides à viscosité peu sensible à la température, tandis qu'une extension, TWM-var, prend en compte une forte variation de viscosité et permet de corriger à la fois le flux de chaleur et le cisaillement pariétal.

Les deux modèles reposent sur les hypothèses classiques de couche limite laminaire stationnaire, incompressible et bidimensionnelle, sans gradient de pression significatif ni dissipation visqueuse et, parce que la couche limite thermique est très fine, sur une contrainte de cisaillement uniforme dans la couche limite thermique. Pour le cas particulier du modèle à viscosité uniforme (TWM-cst), cela mène à l'hypothèse de profil de vitesse linéaire. Les profils adimensionnels utilisés par les modèles pour prédire les flux pariétaux sont adaptés au contexte numérique de la méthode des volumes finis.

Les évaluations sur une couche limite thermique bidimensionnelle montrent que, même lorsque la couche limite thermique n'est représentée que par une fraction de maille, l'erreur faite par un maillage grossier sur le flux de chaleur pariétal est presque annulée, alors qu'une très légère sur-correction apparaît uniquement pour des maillages de raffinement intermédiaire (de 2 à 5 mailles dans la couche limite). En présence de viscosité dépendante de la température, l'extension TWM-var améliore simultanément les prédictions de la contrainte pariétale, du champ de vitesse au voisinage de la paroi et du flux de chaleur. Il présente également une légère sur-correction pour des maillages de raffinement intermédiaire.

Sur une configuration de jet impactant académique, représentative de l'application industrielle visée, le modèle à viscosité uniforme (TWM-cst) améliore nettement la prédiction du flux de chaleur local, dès lors que la couche limite thermique est très sous-résolue (moins d'une maille dans la couche limite). Pour un maillage mieux résolu, la prédiction du flux pariétal présente une dégradation marginale du flux déjà bien résolu par le maillage. Cette légère dégradation est aussi liée aux conditions non respectées des hypothèses du modèle rencontrées dans ce type d'écoulement. L'apport du modèle est donc principalement piloté par le nombre de mailles dans la couche limite, tout en montrant une faible sensibilité du modèle au maillage et à l'écoulement en ce qui concerne l'erreur sur le flux. Le coût de calcul est réduit jusqu'à environ 70–90 % selon le nombre de Prandtl. Lorsque la viscosité varie fortement, seule la version étendue fournit des gains substantiels, en réduisant les erreurs sur l'épaisseur de film, la contrainte pariétale et le flux thermique sur une large plage de nombres de Reynolds et de Prandtl, mais aussi pour différentes résolutions de la couche limite.

Une géométrie plus complexe à jets multiples confirme l'intérêt du modèle à viscosité constante près des zones d'impact, tout en montrant ses limites dans les régions de collision de films où les hypothèses de base ne sont plus vérifiées, mais où le modèle ne dégrade pas la solution.

Enfin, plusieurs perspectives sont identifiées : relâcher l'hypothèse d'une température d'écoulement uniforme à l'extérieur de la couche limite en lisant les informations sur 2 cellules, corriger également les flux entre les 2 premières mailles pour limiter la sur-correction observée sur des maillages de résolution intermédiaire et désactiver le modèle lorsque la couche limite thermique est suffisamment résolue. Des investigations complémentaires sont nécessaires pour renforcer la robustesse numérique (maillages à cellules coupées, voisinage de la ligne de contact sur surfaces partiellement mouillées). Des études supplémentaires sont également nécessaires pour étendre le champ d'application vers des configurations plus proches de l'application industrielle, incluant des parois non isothermes, des régimes instationnaires, des écoulements avec recirculations et des parois non lisses.

Le modèle proposé est transférable à d'autres problèmes de transfert, notamment aux phénomènes avec transferts de masse à grand nombre de Schmidt, rencontrés par exemple dans de nombreux problèmes d'ingénierie ou phénomènes naturels, incluant des surfaces réactives.